NC-AFM high-resolution studies of the calcite(104) surface at low temperatures with and without submonolayer of CO and H_2O

Dissertation
zur Erlangung des Doktorgrades (Dr.rer.nat.)
des Fachbereichs Physik der Universität Osnabrück
vorgelegt von

Jonas Heggemann

Osnabrück, 2022

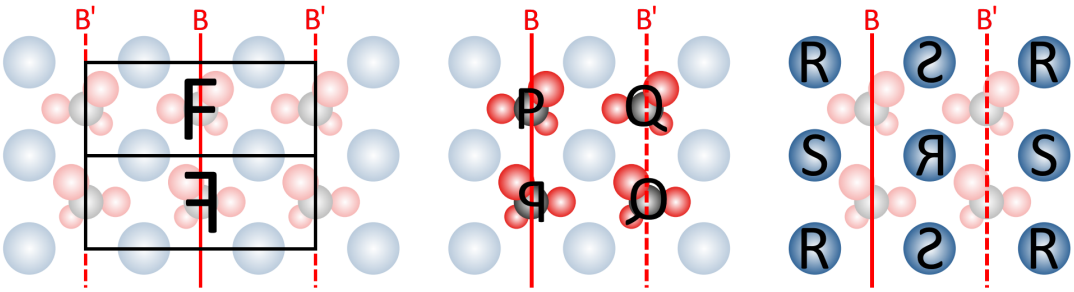

Gewidmet meiner Mutter,
die 2011 an Multipler Sklerose verstarb.

Erklärung über die Eigenständigkeit der erbrachten wissenschaftlichen Leistung

Ich erkläre hiermit, dass ich die vorliegende Arbeit ohne unzulässige Hilfe Dritter und ohne Benutzung anderer als der angegebenen Hilfsmittel angefertigt habe. Die aus anderen Quellen direkt oder indirekt übernommenen Daten und Konzepte sind unter Angabe der Quelle gekennzeichnet.

Bei der Auswahl und Auswertung folgenden Materials haben mir die nachstehend aufgeführten Personen in der jeweils beschriebenen Weise unentgeltlich geholfen.

1.) Abbildungen 19(a) und (b) wurde von Linda Laflör im Rahmen ihrer Messungen aufgenommen.

2.) Die technische Zeichnung in Abbildung 18(a) stammt von Holger Heine (Feinmechanischen Werkstatt, Universität Osnabrück)

3.) Die ICP-OES Ergebnisse in den Tabellen 3, 4, 5 und 6 wurden am Karlsruher Institut für Technologie (KIT) unter der Leitung von Dr. Thomas Bergfeldt durchgeführt.

4.) Die in Kapitel 7.3 behandelten NC-AFM Messungen von Wasser auf Kalzit wurden zusammen mit Simon Aeschlimann durchgeführt.

Weitere Personen waren an der inhaltlichen materiellen Erstellung der vorliegenden Arbeit nicht beteiligt. Insbesondere habe ich hierfür nicht die entgeltliche Hilfe von Vermittlungs- bzw. Beratungsdiensten (Promotionsberater oder andere Personen) in Anspruch genommen. Niemand hat von mir unmittelbar oder mittelbar geldwerte Leistungen für Arbeiten erhalten, die im Zusammenhang mit dem Inhalt der vorgelegten Dissertation stehen.

Die Arbeit wurde bisher weder im In- noch im Ausland in gleicher oder ähnlicher Form einer anderen Prüfungsbehörde vorgelegt. Osnabrück, den 17.06.2022

.....

Datum/Unterschrift

Contents

1 Introduction

Calcite is one of the most ubiquitous minerals in nature. It is prevalently found in most limestones, and is a constituent of biominerals in living organisms, including microlenses, bones and teeth, shells of molluscs, or sea urchin spines [1, 2, 3, 4, 5, 6, 7]. Due to its vast occurrence, non-toxicity, birefringence, and chemical properties, calcite is frequently used in the cosmetics industry as abrasive, in manufacturing as a polishing agent, and in pharmaceuticals as antacid, antidiarrhoeaic, or mineral supplement [8, 9, 10, 11, 12]. Additionally, calcite is a critical component in the design of environmentally friendly materials. In the last decade, significant efforts have been made to understand and control the mineralisation processes on the surfaces of calcite in living organisms, motivated by the strength and toughness of the resulting biominerals [7, 13, 14, 15, 16, 17]. Currently, calcite is discussed as a geological reservoir for long-term storage of atmospheric CO_2 with the aim to reduce the greenhouse effect [18, 19, 20].

Calcite belongs to the family of carbonates. The main characteristic of this family is the presence of a carbonate group (CO_3^{2-}) as an essential structural unit. The most common carbonates are magnesite ($MgCO_3$), calcium carbonate ($CaCO_3$), strontianite ($SrCO_3$), witherite ($BaCO_3$), copper(II) carbonate ($CuCO_3$), smithsonite ($ZnCO_3$), cerussite ($PbCO_3$), rhodochrosite ($MnCO_3$), siderite ($FeCO_3$), and dolomite ($CaMg(CO_3)_2$) [21]. Calcium carbonate occurs mostly in one of the three modifications calcite, aragonite, and vaterite. Calcite the most stable member and investigated in this thesis [1].

The (104) surface is the most stable cleavage plane of calcite and has intensively been studied over the last decades by using a number of experimental and theoretical methods [22, 23, 24, 25, 26, 27, 28, 29, 30, 31, 32, 33, 34, 35, 36, 37, 38, 39, 40, 41, 42, 43]. For example: Ohnesorge *et al.* [43] and Rachlin *et al.* [44] were one of the first researchers who presented AFM images of the calcite(104) surface explained by the model of the bulk-truncated calcite(104) surface. Using atomic force microscopy (AFM) measurements, Liang *et al.* [40] have found that the calcite(104) dissolves in a solution of water and NaOH (with pH 9) via the creation of rhombic pits (etch pits) and via the retreat of steps edges. These etch pits are delimited by two kinds of step edges, namely the $[4\,\overline{4}\,\overline{1}]$ and $[\overline{4}\,\overline{8}\,1]$ direction. Due to the rhombohedral structure of calcite, two inequivalent steps emerge for each direction. Nada *et al.* [45] and Hazen *et al.* [46, 47] related a preferred adsorption of aspartic acid to one of these two inequivalent steps.

Despite these intensive studies, there is so far no accepted structural model for the calcite(104) surface that describes the surface structure in all environments. In particular, two reconstructions have been found in some experimental studies of calcite(104), namely a (2×1)

reconstruction and a row-pairing reconstruction. Both are not in agreement with the structure of the bulk-truncated (1×1) surface [29, 48]. In contrast, there are also reports where a pristine (1×1) reconstruction has been found [39, 40, 49]. Furthermore, the row-pairing reconstruction has exclusively been found in AFM measurements and, therefore, it was repeatedly stressed that this reconstruction could rather be a tip-induced artefact instead of an inherent surface property.

The central aim of this thesis is to give further insights into the structural properties of the calcite(104) surface and especially to unravel its surface reconstruction by clarifying the contradicting reports of the (2×1) and row-pairing reconstruction. Within this thesis, the pristine as well as the CO and H_2O-covered calcite(104) surface is investigated for the first time with non-contact atomic force microscopy (NC-AFM) operated at 5 K. CO terminated tips are used in the measurements to benefit from the improved contrast capabilities and detailed understanding of contrast formation with these tips. The well-defined and characterised tip enables most reliable data interpretation [50, 51].

A key result of this thesis is the identification of a (2×1) reconstruction of the calcite(104) surface, the finding of a glide plane symmetry, and the localisation of the axes of glide plane symmetry to the positions of the carbonate groups. This result allows to derive conclusions for the geometrical structure of the (104) surface of calcite. Furthermore, it is demonstrated that the adsorption of CO molecules on calcite(104) is influenced by this (2×1) reconstruction as well as the glide plane symmetry. In particular, two different CO adsorption geometries within the (2×1) unit cell are identified. Finally, first steps in the field of studying the adsorption of H_2O on calcite(104) via NC-AFM are performed by experiments at 5 K and at temperatures of 110 K to 140 K. It is demonstrated that also the water molecules are influenced by the (2×1) reconstruction. In particular, the data point towards preferred water adsorption positions within the (2×1) unit cell at submonolayer water coverage.

This thesis is divided into six main chapters, in addition to introduction and conclusion. First, the bulk structure and the bulk-truncated (104) surface of calcite are described in chapter 2 introduced, and previous structural investigations summarised.

Chapter 3 introduces the experimental methods used to yield NC-AFM data of the calcite(104) surface. This includes the methodology of NC-AFM (subchapter 3.1), as well as a description of the experimental setup (subchapter 3.2), of the preparation methods to fabricate sharp and CO-terminated tips (subchapter 3.3), of a double sample holder designed for the high-resolution measurements (subchapter 3.4), of an optical method for the determination of the $[4\,2\,\overline{1}]$ direction (subchapter 3.5), and of the image editing processing steps (subchapter 3.6).

The preparation protocols of the metal and calcite surfaces are explained in chapter 4, together with a description of the CO and H_2O dosing (subchapter 4.3). This is followed by an overview over the used calcite crystals (subchapter 4.4).

The structure of the calcite(104) surface as imaged by NC-AFM is analysed in chapter 5. At first, it is shown that calcite(104) expresses a (2×1) reconstruction and a glide plane symmetry in the NC-AFM image data (subchapter 5.1). Second, the relation between the appearance of CO/Ag(111) and of the calcite(104) surface in NC-AFM images acquired with the same CO tip is discussed (subchapter 5.2). Third, conclusions for the orientation of the calcite surface species are derived from the NC-AFM results (subchapter 5.3). Last, the relation between impurities and imaged surface defects is investigated (subchapter 5.4).

In chapter 6 of this thesis, the properties of submonolayer coverage of CO on calcite(104) are investigated at 5 K. It is shown that CO molecules adsorb exclusively on the calcium atoms of the pristine calcite surface (subchapter 6.1). The geometry of the adsorption positions of the CO molecules follow the (2×1) reconstruction of the calcite surface. Two different CO adsorption geometries are identified (chapter 6.2) and further analysed by $\Delta f(z_p)$-curves. In particular, a different tilt of the CO molecules is visible in these $\Delta f(z_p)$-curves (subchapter 6.3). Image data of adjacent molecules can show apparent bonds if the distance between the molecules is smaller (0.49 ± 0.03) nm (subchapter 6.4).

Last, chapter 7 presents an outlook on investigating the adsorption properties of submonolayer coverage of H_2O on calcite(104) at low temperatures. At first, a concise summary of the adsorption literature describing the structure of water on calcite(104) is presented (subchapter 7.1). Second, preferred adsorption positions of the water molecules within the (2×1) reconstructed unit cell are found in NC-AFM image data acquired at water coverage up to 0.1 ML at 5 K with a CO tip (subchapter 7.2). In contrast, at temperatures between 110 K and 140 K and at water coverage of a full monolayer, the molecular structure resembles a (1×1) reconstruction.

In summary, this thesis demonstrates the existence of a (2×1) reconstruction and a glide plane symmetry in the NC-AFM image data of calcite(104) and shows the influence of the surface properties to the adsorption geometry of CO and water.

2 Properties of the calcite bulk structure and its unreconstructed (104) surface

The bulk structure of calcite belongs to the R$\bar{3}$c group and can be described by the rhombohedral unit cell that is shown in figure 1 [21, 26, 52, 53]. In this unit cell, the carbon atoms from the carbonate groups as well as the calcium atoms are arranged alternating, at equally spaced positions on the threefold rotational axis (red line in the centre of the hexagonal prism), whereby every second carbonate group is rotated by 180° around this axis. All four atoms of a carbonate group lie inside a plane that is perpendicular to the threefold rotational axis, and the distance between an oxygen atom and the carbon atom in the centre of a group is about 0.13 nm [52]. The rhombohedron has an unit cell size of about 1.7 nm along the threefold axis with an edge length of 0.64 nm (black lines in figure 1, one exemplar is marked by a black arrow) [21, 26, 52, 53].

The rhombohedral unit cell illustrates the calcite bulk structure. However, in most recent publications, the coordinates are given according to the hexagonal unit cell, which is presented in figure 2(a). The [0 1 0], and [1 0 0] axis are perpendicular to the [0 0 1] axis and intersect at an angle of 120° [12, 26, 45, 54, 55, 56, 57]. The red marked segment in the hexagonal prism in figure 1 indicates the position of the hexagonal unit cell of figure 2(a).

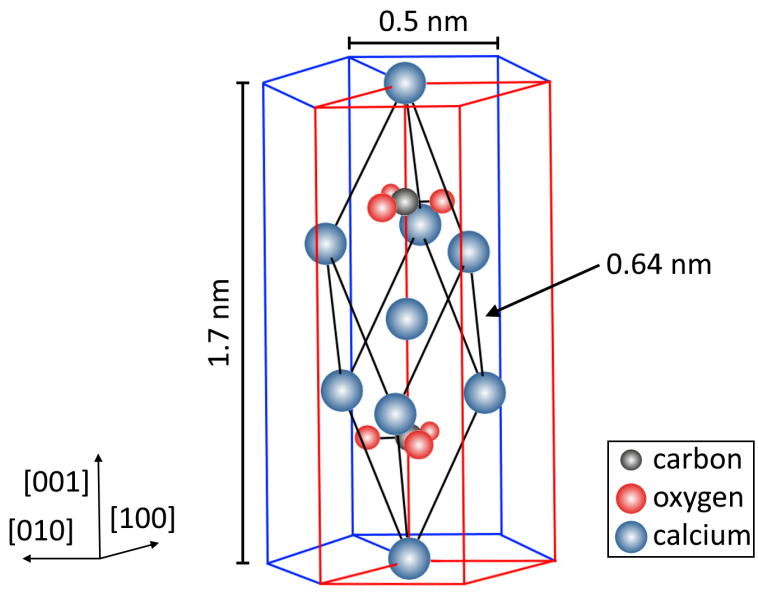

Figure 1: (a) Model of the rhombohedral unit cell of calcite following the references [21, 26, 52, 53]. All black lines have the same length of about 0.64 nm. The red marked segment in the hexagonal prism indicates the position of the hexagonal unit cell presented in figure 2(a), and the coordinate system is drawn according to this unit cell. Note: The planes restricted by four black lines and four calcium atoms do not represent the (104) surfaces.

The most stable surface of calcite is the (104) surface its position in the hexagonal unit cell is marked by dotted green lines in figure 2(a) [22, 23, 24, 25, 26]. The stability is explained by the finding that the fewest Ca–O bonds have to be broken to generate it. This plane is nonpolar, and has in the unreconstructed, bulk-truncated form a rectangular (1×1) unit cell with dimensions of $0.5\,\mathrm{nm} \times 0.81\,\mathrm{nm}$ containing two calcium atoms (Ca^{2+}) and two carbonate groups (CO_3^{2-}) as marked in figure 2(b) by a solid, black rectangle [30, 40, 44]. In this bulk-truncated geometry, the carbonate groups are rotated with respect to each other in $[4\,2\,\bar{1}]$ direction and with respect to the (104) surface plane, thereby intersects the plane of a carbonate group the (104) surface at an angle of 44.37° such that one oxygen atom of the carbonate group lies in the (104) surface, one protrudes out of the surface, and one lies below the surface [30, 44].

Mainly as a result of the different orientation of the carbonate groups, the bulk-truncated surface belongs to the two-dimensional crystallographic group (planar space group) *pg*, with a glide plane reflection as symmetry [34]. The glide plane symmetry operation is defined by a reflection on a line (m) and a translation (t) parallel to this line, whereby the distance of the translation amounts to half the unit cell size [58, 59]. An abstract example for a structure with a glide plane symmetry is shown in figure 3(a) and (b), where a structure is visible that is assembled of unit cells with two L-like patterns. There are two possibilities to position the axes of glide reflection, either along the unit cell edges (blue line S_1, figure 3(a)) or through the centre of the unit cell (red line S_2, figure 3(b)). Note: There are always two axes of glide

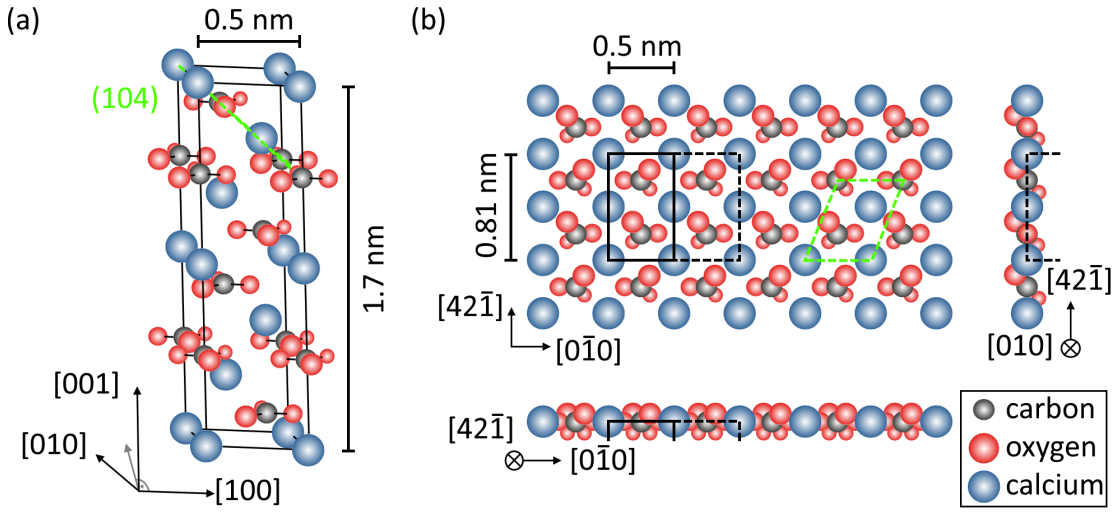

Figure 2: (a) Model of the hexagonal unit cell of calcite [26, 52, 53]. Marked by dotted, green lines is the position of the (104) cleavage plane. (b) Topmost layer of the bulk-truncated (104) surface of calcite with marked (1×1) (solid rectangle) and (2×1) (solid and dashed) unit cell. The surface species marked by the dotted, green parallelogram are associated to the species marked in (a) by the dotted, green lines.

reflection within the unit cell for a surface belonging to the planar space group *pg* [58, 59].

The glide plane symmetry can be found for the the bulk-truncated (1×1) calcite(104) surface as follow: Figure 3(c) shows the two axes of glide reflection running along the $[4\,2\,\bar{1}]$ direction and positioned on the rows of calcium atoms (blue line A) and on the rows of the carbonate groups (red line B).

After the reflection and translation the position and orientation of the calcium and carbonate groups matches to the original position and orientation as abstracted in figure 3(c).

The (1×1) structure visible in figure 3(c) applies to the bulk-truncated calcite structure. However, in most experimental studies of the calcite(104) surface, two reconstructions were found, namely the (2×1) and the row-pairing reconstruction that are not in agreement with the bulk-truncated surface [29].

In the (2×1) reconstruction every second (1×1) unit cell in $[0\,\bar{1}\,0]$ direction are imaged

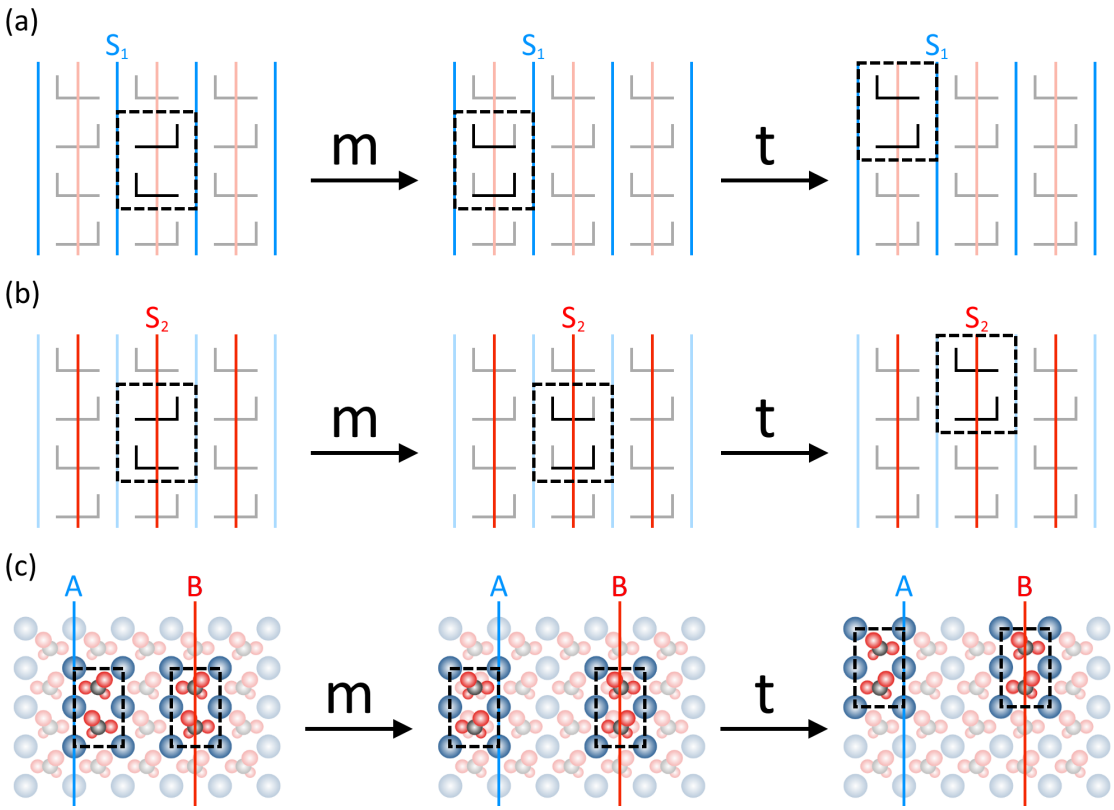

Figure 3: (a) and (b) Abstract illustration of the glide plane symmetry properties. Two symmetry axes are present, either positioned along the unit cell edges (blue line S_1, (a)) or running through the centre of the unit cell (red line S_2, (b)). The black, dotted rectangle has the size of one (1×1) unit cell. (c) Glide plane reflection symmetry operation applied to the bulk-truncated calcite$(104)-(1\times1)$ surface structure. The axes of glide reflection are running along the $[4\,2\,\bar{1}]$ rows of either calcium atoms (blue, A) or carbonate groups (red, B).

differently as abstracted by the orange and magenta rectangle in figure 4. This is in contrast to the bulk-truncated calcite(104) surface where (1×1) unit cells adjacent in $[0\,\bar{1}\,0]$ direction are imaged identically. Due to the difference in these (1×1) unit cells the unit cell length along the $[0\,\bar{1}\,0]$ direction is doubled resulting in a (2×1) unit cell. One of the first reports of this reconstruction have been given by Stipp *et al.* [39, 41, 49] who found in LEED pattern of calcite samples, which were prepared in atmosphere and then transferred to vacuum, extra reflections indicating a (2×1) reconstruction. Further evidence for this reconstruction has been given by AFM measurements that were performed in different environments and various AFM modes [29, 31, 39, 60]. The finding of the (2×1) reconstruction in the experiments is supported by several simulations: Rohl *et al.* [61] found in force field modelling a rotation of half of the surface carbonate groups resulting in a (2×1) reconstruction, Reksten *et al.* [62] and Wenk *et al.* [2] assume from transmission electron microscopy measurements that the (2×1) reconstruction is caused by foreign atoms periodically substituting Ca atoms in the calcite unit cell, and Kristensen *et al.* [22] found in modelling simulations that the (2×1) reconstruction is induced by surface steps of the calcite surface. Despite these experiments and simulations there is so far no agreed microscopic geometry available.

The second reconstruction is the row-pairing reconstruction that has so far exclusively been found in AFM measurements. Following Jin *et al.* [48], the appearance (especially the shape and signal intensity) of the upper and lower half of a (1×1) unit cell with respect to the $[4\,2\,\bar{1}]$ direction is imaged differently in this apparent reconstruction. Following the bulk-truncated calcite(104) surface structure, the structure of these halves are related by the glide plane symmetry. Hence, the row-pairing reconstruction violates the glide plane symmetry. The difference between (2×1) and row-pairing reconstruction can be confusing, because the row-pairing reconstruction can also have a (2×1) periodicity. The unit cell halves that are imaged differently in the (2×1) row pairing reconstruction are marked in figure 4 by

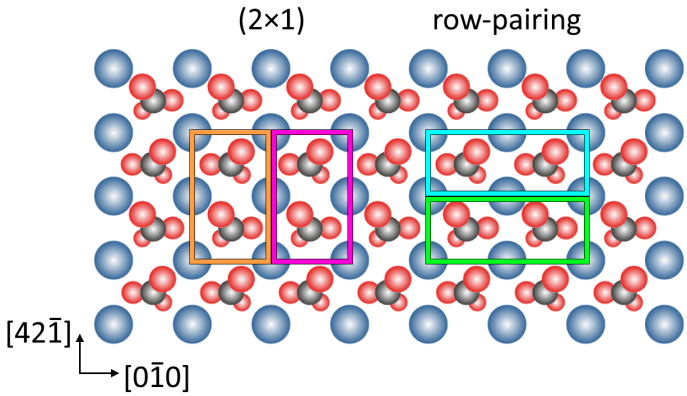

Figure 4: Sketch of the topmost layer of the bulk-truncated (104) surface of calcite. Two (2×1) unit cells that are separated into two sub cells are marked.

a blue and green rectangle. The row-pairing reconstruction of the calcite surface has been observed only in AFM acquired by different AFM modes operated under various conditions [29, 31, 40, 41, 42, 43, 44, 63, 64]. So far, there is no evidence from X-Ray reflectivity and diffraction experiments on calcite (104) [28, 33, 38, 65]. Therefore, it is widely assumed that this reconstruction is rather a tip artefact that affects imaging of the different orientations of the carbonate groups in AFM imaging than a true surface property [28, 29, 31, 40, 41, 42].

3 Methods

As mentioned in the introduction: NC-AFM with CO-terminated tips is nowadays established as a most important tool to obtain high-resolution images, especially in real space from non-conductive surfaces such as calcite [50, 51]. In this chapter the experimental setup and methods are explained that are used within this thesis to analyse the calcite(104) surface with an NC-AFM microscope and CO terminated tips. At first, the working principle and the experimental setup of the used NC-AFM system are described (subchapter 3.1 and 3.2), followed by the methods to obtain CO-terminated tips (subchapter 3.3). For the measurements in this thesis, a double sample holder was designed that is presented in subchapter 3.4. Additionally it is explained in this subchapter how the $[4\,2\,\bar{1}]$ direction can be determined by an optical method (subchapter 3.5), and how the obtained images were edited to highlight particular features (subchapter 3.6).

3.1 Non contact atomic force microscopy

In this subchapter the working principle and technical setup of an NC-AFM and a scanning tunnelling microscope (STM) in dynamic mode is explained, followed by an explanation of the method to determine the oscillation amplitude of an NC-AFM sensor.

3.1.1 Measurement of nanoscale forces and the working principle of NC-AFM

A sharp tip is mounted to a force sensor in AFM and brought to close proximity within a few nanometres to a surface. Due to this proximity, measurable forces act between the tip and the sample so-called tip-sample forces, that can be measured by the force sensor. An AFM image is basically acquired by rastering the tip across the sample, whereby the tip-sample force is measured at each raster point. Due to the force measurement in AFM, this technique can measure both conducting as well as insulating samples such as calcite. In contrast, the scanning tunnelling microscope (STM) uses the tunnelling-current between a tip and a surface and is, therefore, limited to conducting materials.

Mathematical description of the AFM measurement

The force sensor of an AFM can be described by an externally driven damped harmonic oscillator. In absence of tip-sample forces, the resonance frequency f_r of this resonator is described by:

$$f_r = f_0 \sqrt{1 - \frac{1}{2Q}}, \tag{1}$$

with the eigenfrequency $f_0 = \frac{1}{2\pi}\sqrt{\frac{k}{m^*}}$, the spring constant k, the effective mass of the oscillator m^*, and the quality factor Q. This quality factor is related to the intrinsic dissipation within an oscillating sensor and can be measured from $Q = \sqrt{3}\frac{f_0}{f_{FWHM}}$ with f_{FWHM} being the full width at half maximum of the amplitude response function $|G_{ho}(f)|$ [66, 67, 68]. This response function describes the response of the resonator under an influence of an external driving force at frequency f.

If the tip is brought in proximity to a surface, forces act between the tip and the sample that shift the resonance frequency of the resonator. It is prevalent practice to use the *harmonic approximation* for describing the oscillator with external forces. Within this approximation, the oscillation of the resonator influenced by external forces is assumed to be strictly harmonic, however, with adjusted oscillation parameters [66, 67].

According to reference [68], the frequency shift $\Delta f = f_r - f_0$ describes the difference between the resonance frequency at interaction and the eigenfrequency of zero tip-sample interaction and can be derived from considering the even tip-sample force gradient k°_{even} along the oscillation path. In particular, reference [68] derived following relation between this physical paramter and the measurement variables:

$$\langle k^{\circ}_{even}\rangle_{\cap}(z_c) = k_0(1 - \frac{f_r^2}{f_0^2}) - \frac{F_0}{A} \cdot cos(\varphi), \tag{2}$$

whereby F_0 is the excitation force amplitude and f_r the excitation frequency of the oscillator, while A describes the oscillation amplitude, z_c the centre position of the oscillation, and φ the phase shift between the excitation force and oscillator response.

$\langle k^{\circ}_{even}\rangle_{\cap}(z_c)$ is the cap-average of the force gradient $k^{\circ}_{even}(z_{ts}) = \frac{dF^{\circ}_{even}(z_{ts})}{dz_{ts}}$ along the oscillation path and is defined by:

$$\langle k^{\circ}_{even}\rangle_{\cap}(z_c) = \int_{-A}^{A} \frac{dF^{\circ}_{even}(z_c + z)}{dz_c} \cdot w_{\cap}(z)dz \tag{3}$$

with the cap-averaging function $w_{\cap}(z) = \frac{2}{\pi A^2}\sqrt{A^2 - z^2}$.

$F^{\circ}_{even}(z_{ts})$ describes the force contributions to the tip-sample force that are even with respect to the tip velocity, namely $F_{even}(z_{ts}, \dot{z}_{ts}) = F_{even}(z_{ts}, -\dot{z}_{ts})$.

Equation 2 can be simplified in two steps. First, a phase-locked loop (PLL, see section 3.1.2) working at optimum phase resonance ensures $\varphi = -\pi/2$, which is the optimum phase shift to drive an oscillator. The right term of equation 2 then reads

$$\langle k^{\circ}_{even} \rangle_{\cap}(z_c) = k_0(1 - \frac{f_r^2}{f_0^2}). \tag{4}$$

Second, the expression $f(x) = 1 - \frac{x^2}{f_0^2}$ is often approximated by a Taylor series at $x = f_0$, justified by small frequency shift values compare to f_0. This approximation allows the prevalent definition of the frequency shift Δf by the tip-sample interaction force gradient k°_{even}:

$$\Delta f = f_r - f_0 = -\frac{f_0}{2k_0} \cdot \langle k^{\circ}_{even} \rangle_{\cap}(z_c). \tag{5}$$

Forces in AFM

The forces acting on the sensor are usually separated into capacitive, Van der Waals, and short-range forces. Other contributions are possible, for example magnetic interactions are present if magnetic materials are investigated.

Capacitive forces have a long-range character and the cpacitive contribution can be written as $F_{ca} = -\frac{1}{2}\frac{\partial C}{\partial z_{ts}}(V_{DC} - V_{CPD})^2$ [69]. C is the tip-surface capacity, V_{CPD} is the contact potential difference between tip and sample, and V_{DC} is an external applied DC voltage.

Van der Waals forces are also of long-range character and describe the interaction of permanent or induced dipoles. For example, the force dependence of a spherical tip and a flat sample can be approximated by $F_{vdW} \approx -\frac{HR}{6z_{ts}^2}$, described by the Hamaker constant H and

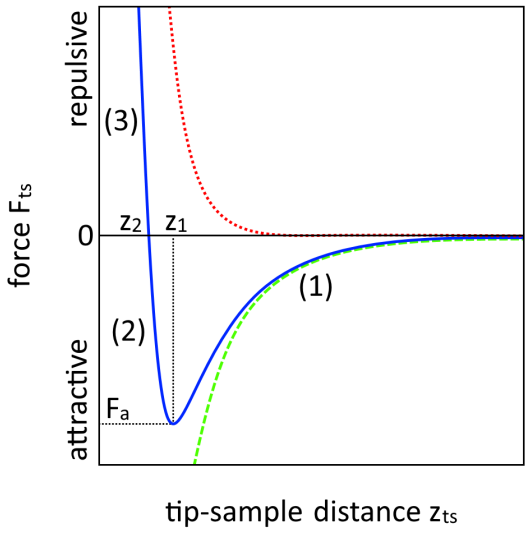

Figure 5: Simple generic tip-sample force curve. The blue curve is the sum from the dotted red (repulsive contributions) and the dashed green line (attractive contributions).

the tip radius R [70, 71].

Short-range forces result from the mainly chemical interaction of single atoms or molecules with each other. These forces can be either attractive or repulsive, for example by covalent bonds or by Pauli repulsion, and are mostly responsible for the high-resolution contrast in the NC-AFM images.

The total tip-sample force is the sum of all these forces, however, only the component parallel to the oscillation direction influences the sensor. In this thesis, this direction is assumed to be perpendicular to the surface plane.

A simplified generic tip-sample force curve is shown in figure 5 in blue. This curve is the sum from the attractive forces represented by the green dashed curve, and the repulsive forces represent by the red dotted curve. The generic tip-sample force can be separated into three parts along the z_{ts} axis: The first part is at tip-sample distances larger than z_1. In this regime the attractive forces dominate, with a maximum of F_a at z_1. In contrast, the forces approach zero for large tip-sample distances.

At distances in the range between z_1 and z_2 (second part) repulsive forces become stronger and the attractive tip-sample force is decreasing up to zero at z_2.

In the third part, at tip-sample distances smaller than z_2, the repulsive forces dominate and become stronger with further decreasing distance.

If the restoring force of the oscillator, which is given by $F_{r,max} = -k \cdot A$ using the spring constant k and oscillation amplitude A, is smaller than the maximum attractive force that acts on the tip, then a stable oscillation is not possible. In this case, the oscillation collapses and an unintentional sticking of the tip to the sample (known as snap-into-contact) occurs [67]. This can be avoided by two methods. First, the amplitude A is increased until the restoring force is larger than the maximum attractive force. However, an increased amplitude results into an averaging of the tip-sample force over a larger z_{ts}-range, especially in the regime of the long-range forces. This is not desirable, because the short range forces being the origin of the high-resolution contrast are becoming the minor contribution. Second, an oscillator with a larger stiffness k can be used to increase the restoring force of the oscillator. The last approach is chosen within this thesis.

Tuning fork sensor

An NC-AFM sensor with a reasonably high spring constant is a tuning fork sensor. This sensor is fabricated from quartz in form of a prong with a rectangular cross section that acts as the oscillator. The oscillation direction is approximately perpendicular to the sample

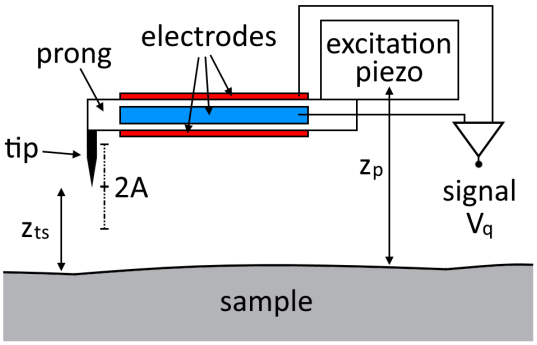

Figure 6: Sketch of a tuning fork sensor in side view. Opposite electrodes on the prong are connected to each other. Additional A, z_{ts} and z_p are marked in the image. A is the amplitude of the tip oscillation, z_{ts} is the distance between the tip apex and the surface, while z_p is the distance of the piezo to the surface.

surface. At one end of the prong the tip is attached, while the other end is mounted to a support (figure 6). This support is also an excitation piezo that provides the external excitation force for the oscillation. The prong[1] has a high stiffness of about $k = 1800\,\mathrm{N\,m^{-1}}$, a resonance frequency of $f_r = 25\,000\,\mathrm{Hz}$, and a quality factor of about $Q = 13000$ [72]. The quartz crystal is cut in such a way that f_r has a very low temperature dependency around room temperature [73].

If the prong is oscillated, an electric field is generated within the prong due to the piezoelectricity of the quartz crystal. The charges that are present at the surfaces, are measured electrically by a charge preamplifier and with contact via electrodes that are placed at the sides of the prong (marked in red and blue in figure 6). If the prong is oscillated, a voltage signal V_q is given at the output of the preamplifier, which is approximately linear to the deflection [74].

3.1.2 Technical setup of an NC-AFM microscope

The operation of an NC-AFM microscope requires three control loops: The amplitude controller, the phase-locked loop (PLL), and the distance controller (figure 7). These control loops keep the amplitude of the resonator and the phase shift between the excitation force and the oscillation of the resonator at a set value, and adjust the tip-sample distance so that the detuning of the resonator is kept constant in topography mode.

The three control loops are PI controller. The oscillating signal V_q, which has the frequency f_r and the voltage amplitude V_a, is fed into the amplitude controller and the PLL. The

[1]The tuning fork sensor without a tip has a resonance frequency of $f_r = 32\,768\,\mathrm{Hz}$ and a quality factor of about $Q = 200\,000$ [72].

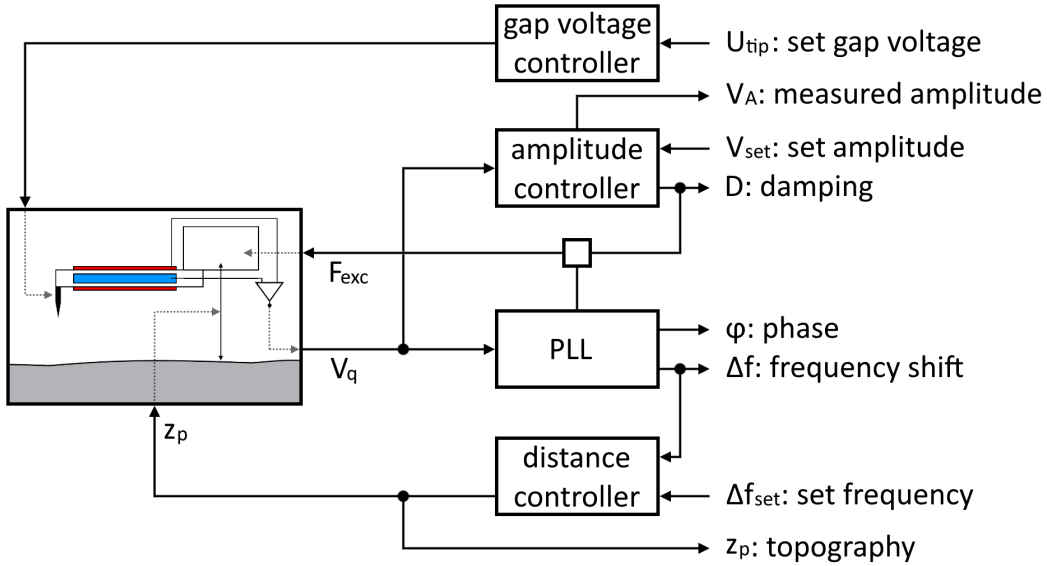

Figure 7: Sketch of the setup of an NC-AFM following reference [75]. Additional the gap voltage controller is drawn where the voltage between tip and sample can be set. The frequency signal coming from the PLL and the damping signal from the amplitude controller both determine the excitation force F_{exc} as abstracted by the square.

amplitude controller measures V_a, compares this amplitude with the set voltage amplitude V_{set}, and adjusts the amplitude A_{exc} of the excitation force (F_{exc}). If V_a is smaller than V_{set}, then A_{exc} is increased by increasing the amplitude of the voltage (D) that drives the external excitation force (excitation piezo), otherwise it is decreased. D is, therefore, assigned to the damping of the oscillator and is together with V_a available at the output of the amplitude controller.

In order to drive the oscillation of the prong at the current resonance frequency, F_{exc} and V_q must have a fix phase shift of φ_{set} to each other. The PLL determines the actual phase (φ) between V_q and F_{exc} and changes the momentous phase of F_{exc} in order to keep f_{exc} at the current f_r. Hence, the frequencies f_r and f_{exc} are identical. The PLL gives both the phase shift and the $\Delta f = f_{exc} - f_0$ as the output signal. The optimal phase shift φ_{set} between excitation and oscillation signal for a harmonic oscillator is usually close to $-\pi/2$. In practice, due to phase delay in the signal processing units and the wiring of the AFM, the set frequency-shift φ_{set} must be determined from phase-vs.-frequency and amplitude-vs.-frequency curves at the beginning of each NC-AFM experiment.

In topography mode, the Δf signal is fed into the distance controller that controls the z_p position of the piezo. If Δf is lower than a set frequency Δf_{set} the tip-sample z_p is increased, otherwise it is decreased. The data in topography images are, therefore, the z_p values from the distance controller. In constant-height frequency-shift mode, the distance controller is

switched off and the tip is moved along a plane. In this case, the image data containing the main information are the measured Δf values.

3.1.3 Technical setup of an STM microscope in dynamic mode

In addition to the force measurement, the NC-AFM setup with the tuning fork sensor can also be used to measure the tunnelling-current between the tip and a conductive sample as in scanning tunnelling microscopy (STM). The STM mode is used in the measurements of this thesis to prepare a sharp CO tip on a metal sample as explained in subchapter 3.3.

STM is based on the quantum mechanical tunnelling effect. If a voltage is applied between a conducting tip and a conducting sample and if the distance between them is only a few nanometre, electrons can be transferred between tip and sample via tunnelling. At a positive sample voltage, the electrons tunnel from the tip into the sample, and at negative voltages vice-versa. The current measured with a current amplifier is denoted as the tunnelling-current I_t. The magnitude of this current is dependent on the tip and sample electronic structure, the work function, and the tip-sample distance z_{tz}. To highlight the dependency on z_{tz}, I_t can be written as:

$$I_t(z_{ts}) = V_s \cdot K \cdot e^{-2 \cdot \kappa \cdot z_{ts}}, \tag{6}$$

whereby z_{ts} is the tip-sample distance, and V_s is the sample bias voltage K is a constant, and κ is the work function [76, 77]. $V_s \cdot K$ can be determined by experimentally acquired

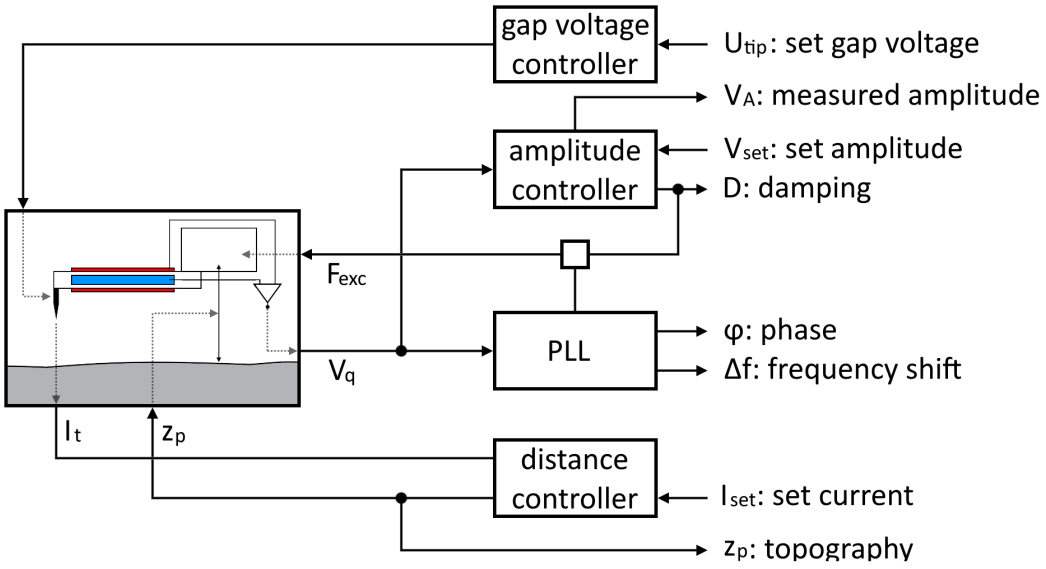

Figure 8: Sketch of the setup of an STM. See also explanations for figure 7.

$I_t(z_{ts})$ curves.

The signal path of a STM setup requires a current amplifier and one distance controller. This controller keeps the measured tunnelling-current to a set tunnelling-current I_{set} by adjusting the tip-sample distance.

Usually, the tip is not oscillated in STM. However, during the measurements within this thesis, the amplitude controller and the PLL were mostly switched on. Such STM measurement with an oscillating tip is called dynamic STM, and the setup is visible in figure 8, which is similar to the setup of the NC-AFM (figure 7). The amplitude controller and PLL work in the same way as in the NC-AFM mode, but the distance controller can now be used also with the measured tunnelling-current I_t as input signal. This I_t is not harmonically oscillating, but the distance controller uses the time-averages I_t as input signal $\langle I_t \rangle$, which is kept close to I_{set}.

In this thesis, the dynamic STM mode is mostly used during the tip preparation on Ag(111) surface whereby the frequency shift Δf is particular useful as an efficient probe for assessing the tip shape. A tip is modelled by three parts in the following: (i) The part spanning the foremost nanometres of the tip-apex have the strongest influence on the contrast formation in SPM. Here, this part is named "microscopic tip-apex". (ii) The section spanned by about the first micrometre from the tip-apex is here referred to as "mesoscopic tip apex", while (iii) the residual tip is identified as the macroscopic tip. The ultimate aim of tip preparation is to produce a CO-terminated tip that is suitable for high-resolution measurements of the calcite(104) surface. In several measurements within this thesis it is observed that a metal tip exhibiting a frequency-shift in the range of $-2.5\,\mathrm{Hz}$ to $0\,\mathrm{Hz}$ in dynamic STM at a bias of $U_{tip} = 5\,\mathrm{mV}$ and a tunnelling-current of $I_t = 5\,\mathrm{pA}$ is usually very suitable to pick a CO molecule up. Hence, tips that yield a small Δf in the dynamic STM mode are considered

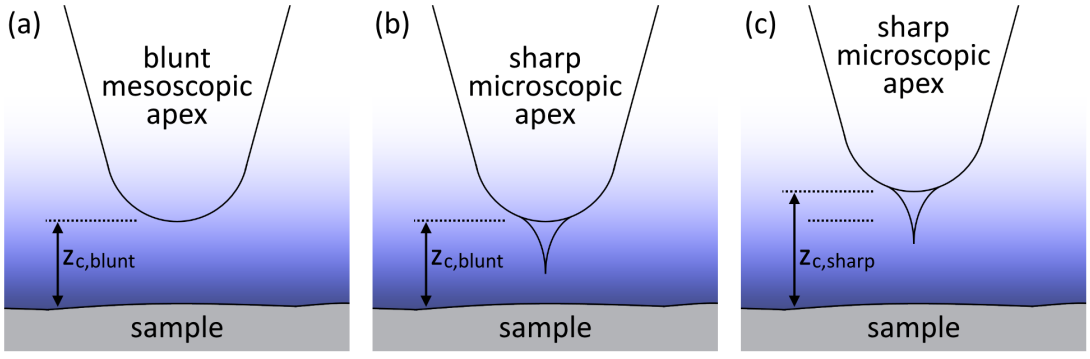

Figure 9: Illustration of a simple model of a tip with a blunt mesoscopic and a sharp microscopic apex. At closer tip-sample distances the tunnelling probability is higher as indicated by the gradient in the blue background.

to be sharp, while tips expressing large Δf values at aforementioned STM parameters are found to be blunt tips.

The reason for this observation is as follows: Assume that blunt mesoscopic tip apex is moved by the distance controller to the tip-sample distance $z_{c,blunt}$ to yield a tunnelling-current of I_{set} (figure 9(a)). Furthermore, the forces acting on this tip at this tip-sample distance cause a frequency-shift Δf_{blunt}. If a sharp tip would have the same mesoscopic tip apex as this blunt tip, but is equipped with a sharp microscopic apex as illustrated in figure 9(b), it will be moved further away from the sample to maintain the same tunnelling-current (figure 9(b)) at the larger tip-sample distance $z_{c,sharp}$. Consequently, the larger separation between the mesoscopic tip and the sample surface causes a reduction of the tip-sample forces and, therefore, a frequency-shift Δf_{sharp} being smaller than Δf_{blunt}.

This consideration is based on a strongly simplified structure of the tip apex, but motivated by observations in the experiments. Note that the crosstalk effect, which can lead to a coupling between the I_t and V_q signals, is not considered in this model [78]. Still, while this effect will influence absolute Δf values, the general order is expected to remain as discussed.

3.1.4 Determining the physical oscillation amplitude from the voltage signal V_q

The determination of the physical oscillation amplitude is of utmost interest in AFM, for example it is a required parameter for calculating the force from experimental $\Delta f(z_p)$-curves [79]. To convert the voltage amplitude V_a (determined from the deflection voltage V_q) into the physical oscillating amplitude A, a calibration factor S is necessary according to following formula [77, 80]:

$$A = S \cdot V_A. \tag{7}$$

There are four common methods to determine this calibration factor S: The force-based methods (a) *Constant normalised frequency-shift*, (b) *Force curve alignment*, as well as the current-based approaches (c) *Constant-height: $I_t(z_p)$ measurement*, and (d) *Normalised time-averaged tunnelling-current.*

(a) Constant normalised frequency-shift method

The *Constant normalised frequency-shift method* is a force based method that follows the idea of keeping the lower turning point of the oscillation at the same tip-sample distance for different oscillation amplitudes. The change of the piezo position z_p upon changing this amplitude would directly correspond to the change in the amplitude [66, 77, 80].

It is difficult to keep the lower turning point at the same tip-sample distance while changing the physical amplitude, because the observable used for the feedback loop depends on the amplitude. One approach to calculate an amplitude-independent quantity is the so called *normalized frequency-shift* $\gamma(z_{tip})$ introduced by Franz Giessibl [66] and defined by:

$$\gamma(z_{tip}) := \frac{\Delta f(z_{tip}, k_0, A_0, f_0) k_0 A_0^{3/2}}{f_0}, \tag{8}$$

with the distance between sample and lower turning point of the tip z_{tip}, frequency-shift Δf, the spring constant k_0, the physical oscillation amplitude A_0, and the eigenfrequency of the resonator f_0.

The $\gamma(z_{tip})$ on the left side of equation 8 represents the normalised tip-sample interaction, while the right side contains the parameters controllable by the microscopist.

At larger amplitudes the upper turning point of the tip extends into tip-sample distances where the tip-sample force is ever-decreasing up to zero (figure 5) [77]. Therefore, these larger distances are irrelevant for the normalised tip-sample interaction, while the contribution of the smaller tip-sample distances dominate the interaction. Consequently, at larger amplitudes the normalised tip-sample interaction depends only on the lower turning point but not on the amplitude.

The idea to determine S is to keep the normalised tip-sample interaction and thus also the lower turning point constant ($\gamma(z_{tip}) = const$); the changing in the oscillation amplitude would directly correspond to the change in z_p.

To determine S: The tip is first approached to a surface in NC-AFM mode with Δf_{Ref} and $V_{A,Ref}$ as initial settings. Next, $\tilde{\gamma} = \Delta f_{Ref} \cdot V_{A,Ref}^{3/2}$ is calculated and set constant to keep the lower turning point fix. Δf_i is set for a series of $V_{A,i}$ according to $\tilde{\gamma} = \Delta f_i \cdot V_{A,i}^{3/2}$, and for each Δf_i is $z_{p,i}$ measured. The plot of $z_{p,i}$ against $V_{A,i}$ results in a straight line with slope S.

The advantages of this method are a straightforward measurement protocol and applicability to conducting and non-conducting materials. The disadvantage is that this method needs large amplitudes to obtain sufficient exact results. Heile *et al.* [81] has shown that for initial physical amplitudes below 5 nm, which are commonly used in AFM, the *Constant normalised frequency-shift method* overestimate S.

(b) Force curve alignment

The *Force curve alignment method* is also a force based method. According to Sader *et al.* [79] the tip-sample force $F(z_{tip})$ can be calculated from the $\Delta f(z_p, A)$ curve by:

$$F(z_{tip}) = \frac{2k_0}{f_0} \int_{z_{tip}}^{\infty} \left\{ \left(1 + \frac{A^{1/2}}{8\sqrt{\pi(t - z_{tip})}}\right) \Delta f(t, A) - \frac{A^{3/2}}{\sqrt{2(t - z_{tip})}} \frac{d\Delta f(t, A)}{dt} \right\} dt. \quad (9)$$

For a set of $\Delta f(z_p, A_i)$, whereby A_i are different physical amplitudes and z_{tip} is the tip-sample distance at the lower turning point of the oscillation, the resulting force curve $F(z_{tip})$ must be the same for all used amplitudes. The idea in the *Force curve alignment method* is, to measure a set of $\Delta f(z_p, V_{A,i})$ curves with different voltage amplitudes $V_{A,i}$. With equation 7 and 9 the force curves $F_i(z_{tip}, S)$ are calculated while S is varied. The correct S is found if all $F_i(z_{tip}, S)$ curves are identical.

According to Heile *et al.* [81], the tip is first approached in NC-AFM mode to a surface, by using voltage amplitude $V_{A,Ref}$ and frequency-shift set point Δf_{Ref}. Then, $\Delta f(z_p, V_{A,i})$ curves are acquired with different $V_{A,i}$ (from smaller to larger amplitude and back). From the set of $\Delta f(z_p, V_{A,i})$ curves the $F_i(z_p, S)$ curves are calculated by using equation 9. S in turn is found via an optimisation routine where S is varied until all $F_i(z_p, S)$ curves are identical.

The advantages of this method are a high accuracy, a straightforward measurement protocol, and the possibility to use both conducting and non-conducting samples. The disadvantages are that this method needs a stable tip during the acquisition of the $\Delta f(z_p, A_i)$ curves and an advanced analysis with force deconvolution and optimisation routines.

(c) Constant-height: $I_t(z_p)$ measurement

The *Constant-height: $I_t(z_p)$ measurement* method uses the tunnelling-current to determine S.

The static $I_t(z_p)$ curve (without tip oscillation) can be described by equation 6 and can be acquired by measurement.

If the tip is oscillating, the movement of this tip can be written as $z_{ts} = z_c + A \cdot sin(\varphi)$, whereby z_c is the centre position of the tip movement, and A is the amplitude. The time averaged tunnelling-current can be written as [77]:

$$\langle I_t(z_p) \rangle = \frac{1}{2\pi} \int_0^{2\pi} V_s \cdot K \cdot e^{-2 \cdot \kappa \cdot (z_c + A \cdot sin(\varphi))} d\varphi. \quad (10)$$

The time averaged tunnelling-current is also the measured tunnelling-current of an oscillating tip. The idea in the *Constant-height: $I_t(z_p)$ measurement method* is, to measure the $I_t(z_p)$ curve, to calculate from this curve $\langle I_t(z_p) \rangle$ for a set of A_i and compare the results with the measured tunnelling-currents acquired with different $V_{A,j}$. The optimal S is found when the calculated tunnelling-currents are identical to the measured [67, 82].

For this method, the tip is approached in STM feedback without tip oscillation to a conducting surface, and a static $I_t(z_p)$ curve is measured. Then, the distance controller is switched off and the tip is moved up to z_0. This z_0 should ensure that for the largest chosen $V_{A,i}$ the corresponding lower turning point is within the z_p range of the static curve, otherwise a unintentional poking of the tip into the sample surface could occur. The oscillation is switched on and for a set of increasing $V_{A,i}$ is $\langle I_t \rangle_i$ measured. Next, from the static $I_t(z_p)$ curve, the cycle-averaged tunnelling-current $\langle I_t \rangle_j$ is calculated with a set of A_j with equation 10 and $z_c = z_0$. Then $V_{A,i}$ is converted with equation 7 into $A_{S,i}$. The optimal S is found if the amplitudes ($A_{S,i} = A_j$) as well as the measured and calculated tunnelling-currents are equal ($\langle I_t \rangle_i = \langle I_t \rangle_j$).

The advantage of this method is a straightforward measurement; but this method needs conductive samples, no drift, and an advanced analysis with cycle-average calculation and optimization routine.

(d) Normalised time-averaged tunnelling-current method

The method of using the *Normalised time-averaged tunnelling-current* is also a tunnelling-current based method, and mainly used in this thesis to determine the physical oscillation amplitude in NC-AFM experiments. This method keeps the lower turning point of the oscillation at the same height in topography mode. The change of the piezo position z_p corresponds to the change in amplitude [83]. This method is very similar to the *Constant normalised frequency-shift method*, but instead of using the normalised tip-sample interaction $\gamma(z_{tip})$, the amplitude-independent normalised time-averaged tunnelling-current $\beta = \langle I_t \rangle \cdot \sqrt{A}$ is used, with the time-averaged tunnelling-current $\langle I_t \rangle$ and the physical amplitude A.

In full analogy to the *Constant normalised frequency-shift method*: At larger amplitudes the upper turning point of the tip extends into tip-sample distances where the tunnelling-current is ever-decreasing up to zero (equation 6). These larger distances are irrelevant for the tunnelling-current, while the contribution of the smaller tip-sample distances dominate this. Consequently, at larger amplitudes the normalised time-averaged tunnelling-current depends only on the lower turning point but not on the amplitude.

To determine S: The oscillating tip is first approached in STM topography mode to a conducting surface with the initial settings $\langle I_t \rangle_{Ref}$ and $V_{A,Ref}$. From these settings the quantity $\beta = \langle I_t \rangle_{Ref} \cdot \sqrt{V_{A,Ref}}$ is calculated. Next, β is set constant to keep the lower turning point fix. $\langle I_t \rangle_i$ is set for a series of $V_{A,i}$ according to $\langle I_t \rangle_i = \beta \cdot V_{A,i}$, and for each $\langle I_t \rangle_i$ is $z_{p,i}$ measured. The plot of $z_{p,i}$ against $V_{A,i}$ results in a straight line with slope S.

The advantages of this method are a straightforward measurement, applicability to small

amplitudes, due to the exponential decrease of the tunnelling current smaller amplitudes compared to the *Constant normalised frequency-shift method* can be used, and reproducible results also after tip changes. The disadvantages are that this method requires conductive samples and $I_t = 0$ for large z_p.

3.2 Experimental setup

The experimental setup used within this thesis is a Multiprobe LT System from Scienta Omicron (Taunusstein, Germany) [84]. This system consists of three UHV chambers, namely the load-lock, the preparation, and the LT-SPM chamber.

The load-lock chamber is used to transfer sensors and samples from atmospheric conditions into ultra-high vacuum. The vacuum in this chamber is generated by a roughing pump and a turbomolecular pump.

The load-lock chamber is connected to the preparation chamber. In this chamber, the pressure is held below 1×10^{-10} mbar by an ion getter pump and occasional runs of a titanium sublimation pump. The pressure was measured by an ion gauge PVG 5 controlled by an IGC5: UHV System Controller both from VACGEN (Saint Leonards, UK).

Inside the preparation chamber is the manipulator that has two stages, one for supporting a tip (tip stage) and one for holding a sample (heating stage). The heating stage can be cooled by liquid nitrogen or heated by a resistive heater (PBN-heater, pyrolytic boron nitride ceramics) that is driven by a programmable DC power supply (Genesys (Gen30-50) from TDK-Lambda Germany GmbH, Achern, Germany). The temperature is measured by a thermocouple mounted at the base plate, but this measured temperature is in general different from the temperature of the sample. To convert the temperature measured by the thermocouple into the sample temperature the conversion scale given by Rostislaw Baurichter in his bachelor thesis is used within this thesis [85].

Cooling of the sample stage is done with nitrogen. The gas (at about 1.8 bar from a dry-nitrogen gas bottle) is cooled and partly liquefied by passing through a condensing coil that is immersed in liquid nitrogen. The cooled nitrogen is then directed through a thin pipe into the preparation chamber to the heat exchanger at the manipulator. A second return pipe transfers the nitrogen to the nitrogen exhaust. A high conductive Cu-braid connects the heat exchanger with the heating stage. With this cooling setup a minimum sample temperature of about 150 K can be reached.

Samples and tips can be sputtered by positioning the sample or tip stage, respectively, into the focal point of the ion beam of an ion source. An Ion Source IS 40C1 operated with

an IS40-PS (both fabricated by PREVAC, Rogów, Poland), and with argon 99.9999 % from (Westfalen AG, Münster, Germany) as sputter gas is used. The gas inlet of this ion source is done via a leak valve from VACGEN (Saint Leonards, UK).

The gas composition inside the preparation chamber can be analysed by a residual gas analyser; an e-Vision 2 General Purpose Residual Gas Analyser from MKS Instruments (Andoven, USA) is mounted to the preparation chamber.

Calcite crystals were cleaved by a sharp blade from TOOLCRAFT AG (Georgensgmünd, Germany) made from SK-5 steel. The blade is mounted on a wobble stick type ZWS075 from VACGEN (Saint Leonards, UK) using a home-build adapter piece. This cleaving method follows the method explained by Tröger *et al.* [86].

After the preparation process, the samples and tips were transferred by transfer via the manipulator and wobble stick (type WMG40 Dual Shaft Wobblestick from FERROVAC Zürich, Switzerland) into the low-temperature atomic force microscope (type LT qPlus gen.III instrument from Scienta Omicron) that is mounted into the LT SPM chamber. The base pressure in this chamber was at between 1×10^{-11} mbar to 2×10^{-10} mbar, depending on the LT temperature. An ion getter pump and a titanium sublimation pump are mounted to this chamber. The pressure in the LT SPM chamber is measured by an ion gauge (PVG 5 controlled by an IGC5: UHV System Controller both from VACGEN (Saint Leonards, UK))

The LT microscope consists of two nested cryostats, the outer one is filled with liquid nitrogen, while the inner one is filled with liquid helium. The latter one cools down the scan head to about 5 K. The temperature of the sample within the scan head is measured with a silicon diode that is mounted to the sample stage, and operated by a 335 Temperature Controller from Lake Shore Cryotronics (Westerville, USA) [87].

Sensors for STM and NC-AFM experiments are tuning fork sensors in the qPlus configuration [72, 74, 88]. Their stiffness is at about $k = 1800\,\mathrm{N\,m^{-1}}$, with eigenfrequencies around $f_0 = 25\,000\,\mathrm{Hz}$. Amplitudes in the range of 0.3 nm to 1 nm are chosen. The sensors, including electrochemically etched tungsten tips, were fabricated by Scienta Omicron. System control and data acquisition is performed by a MATRIX 3.2 unit [89]. During the measurements, the tip-sample distance was stabilised *in situ* by a home-build atom-tracking and feed-forward system [90].

3.3 Used methods to prepare the tip for NC-AFM measurements and CO pick-up

The shape and chemical composition of the tip apex has a strong influence on the imaging process in SPM experiments. With what is commonly referred to as a "blunt" tip, a larger area of the mesoscopic tip apex participates in the tunnelling contact (STM) or force measurement (AFM), consequently averaging over a larger area of the specimen. This results in a decreased resolution in the SPM images [91, 92]. Therefore, it is of utmost importance in SPM experiments to rather using a "sharp" tip for high-resolution imaging and reliable measurements. An example of an image acquired with a sharp tip is reproduced in figure 10. The images show an Ag(111)/mica surface with adsorbed CO molecules. The step edges (figure 10(a)) are imaged as sharp features between the terraces; the CO molecules (Figure 10(b)) are visible as small dark and rotational symmetric spots on the terraces.

The aim of *ex situ* and *in situ* tip preparation methods is to produce such sharp tips. Among the common *ex situ* methods to sharpen the tip are electrochemical etching and Focused Ion Beam (FIB) [93, 94].

In this subchapter, the different *in situ* methods that was used within this thesis are discussed together with the method used to terminate the tip with a CO molecule. All of these methods use the STM mode of the microscope and require, therefore, a metal sample. These methods are the cleaning and build-up method (section 3.3.1), stretching of the mesoscopic

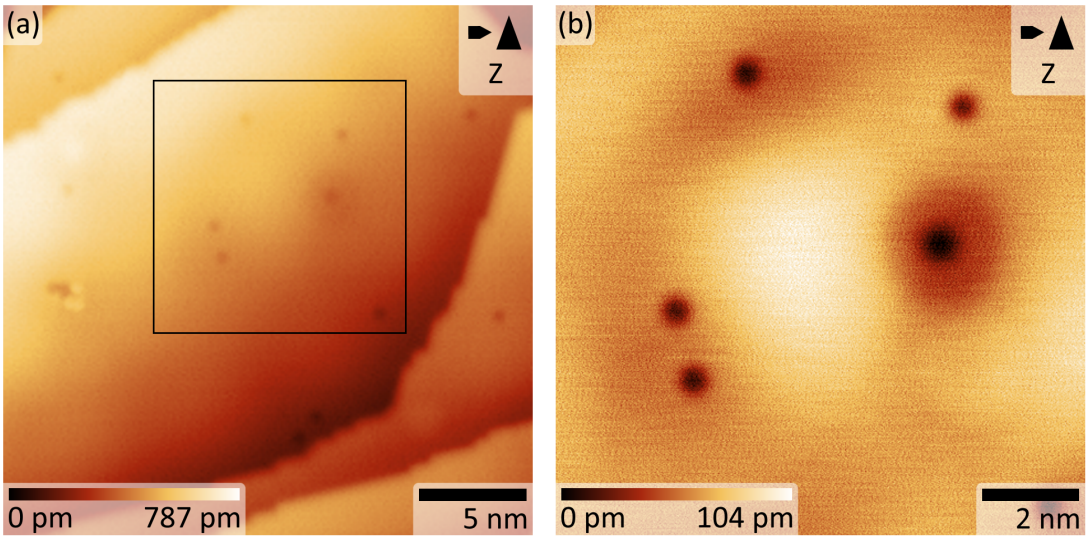

Figure 10: STM image of Ag(111) acquired at $U_{tip} = 5\,\mathrm{mV}$ and $I_t = 5\,\mathrm{pA}$. The dark spots are CO molecules adsorbed on the silver surface. (b) detail image of the area marked by a black rectangle in a). The larger black arrow in the upper right corner of the images indicate the slow scan direction in this image while the smaller black arrow indicate the fast scan direction.

tip apex (section 3.3.2), poking the tip into the metal surface (section 3.3.3), and voltage pulse (section 3.3.4). Then, a preparation protocol is given that is based on the experiences made during the tip preparations during this thesis (section 3.3.5).

3.3.1 Cleaning and build-up of the mesoscopic tip apex by using resistive heating and high electric fields

If the mesoscopic tip apex is very large or coated with impurity material possibly isolating such that the current conduction is inhibited, it can be cleaned and build-up on a metal sample by generating a high electric field. This method have been used in field emission microscopes (FEM). Later, it was transferred to STM experiments [95, 96].

A FEM is used to image the microscopic tip apex of a sharp metal tip [97]. A sharp tungsten tip is typically positioned a few centimetres in front of a fluorescent screen both build into an ultrahigh vacuum chamber. A voltage of several kilovolts is applied between the tip (cathode) and the screen (anode). As a result, the electric field at the microscopic tip apex is large enough to emit electrons (field effect) at the positions of low work function, because a low work function increases the Fowler-Nordheim tunnel probability [98]. The emitted electrons follow the lines of the electric field to the screen and causes emission of photons, collectively proceeding an image of the atomic positions of the microscopic tip apex there.

High voltages in the kilovolt regime as used in FEM experiments are usually not applied in STM. However, in order to produce high electric fields that cause field effect emission even at voltages of few volts, the tip is approached to a distance of a few nm to the sample. This effect can be approximated by a parallel plate capacitor where the electric field E is inversely proportional to the distance s between the plates: $E = U/s$ [96, 99]. If the applied voltage (U) becomes smaller the tip-sample/screen distance (s) must also become smaller to keep E constant.

According to reference [96]: At a tip-sample bias of a few ten volts and a tip-sample distance of a few nanometre, the electric field is large enough that electrons are emitted from the tip (field emission) and guided by the electric field to the surface. The occurring current is called the field emission current. This current heats the mesoscopic tip up due to the resistive heating [100]. Two effects are now possible that influences the shape of the mesoscopic tip apex.

The first effect is due to heating of the mesoscopic tip apex by the field emission current to a very high temperature. The tip apex melt at these temperatures and thermal evaporation of material from the foremost 100 nm of the tip occurs [96, 100]. At the same time, some of the tip atoms on the surface of the mesoscopic tip apex are polarised by the high electric

field and migrate to the tip apex due to the electric force gradient, which is determined by the shape of the tip. The thermal evaporation of tip material and the migration of the tip atoms blunt the tip rapidly [95, 96, 100, 101]. This effect can be used to remove impurity material from the mesoscopic tip apex.

The second effect occurs at mesoscopic tip apex temperatures of about one-third of the melting point of the tip material (for tungsten about 1250 °C [96]). At this temperature, no thermal evaporation occurs, but the migration of the surface tip atoms to the apex take place [95, 96, 101, 102]. The migrated tip atoms incorporate into crystal surfaces of low surface energy at the microscopic tip apex [102]. This growth of the tip in the direction of the electric field is called build-up and leads to a rather pyramidal mesoscopic tip apex, compared to the bluntening caused by the first effect [95, 103]. Thus, this second effect is suitable to sharpen very blunt tips. For example, the microscopic tip apex of a tungsten tip with [111]-orientation evolves into a shape of a flat pyramid with {011} and {112} facets after the build-up process [95, 103].

For the STM and NC-AFM experiments within this thesis, the cleaning and build-up process was performed at voltages in the range of 40 V to 55 V and at tip-sample distances of several nanometres. At first, the tip is approached in STM mode on the Ag(111) surface until a tunnelling-current of $I_t = 5\,\mathrm{pA}$ at $U_{tip} = 5\,\mathrm{mV}$ is reached. Then, the tip-sample distance is increased to about 20 nm and the excitation of the tip is switched off. As the scan controller is not able to provide a tip-sample bias larger than 10 V an external regulated power supply was used and connected to the microscope (sample positive, tip grounded) while the tip is located about 20 nm above the surface. A current meter is included into the circuit as well as a resistor of 20 MΩ to limit the current to 2.5 µA while the terminals for tuning fork sensor and the Kolibri sensor are short-circuited.

The cleaning and build-up processes itself include three steps. In the first step, a bias of 40 V is applied between tip and sample (sample positive, tip grounded) and the tip-sample distance is reduced until the measured current is at about 2.1 µA. This tip-sample distance is held for 2 min. In the second step, the voltage is increased to 45 V while the tip-sample distance is increased until the current is stable at 1.5 µA. This distance is also held for 2 min. The third step is similar to the second step, but with a voltage of 55 V and a tip-sample distance yielding a current of about 1 µA. After the third step, the tip-sample distance is increased until no current is measured. Then, the original connection of the wires is resumed, the gap-voltage is set to $U_{tip} = 5\,\mathrm{mV}$ again, and the tip is moved to a new sample position far away from the build-up position. The moving is necessary to avoid a sample position that is contaminated with tip material.

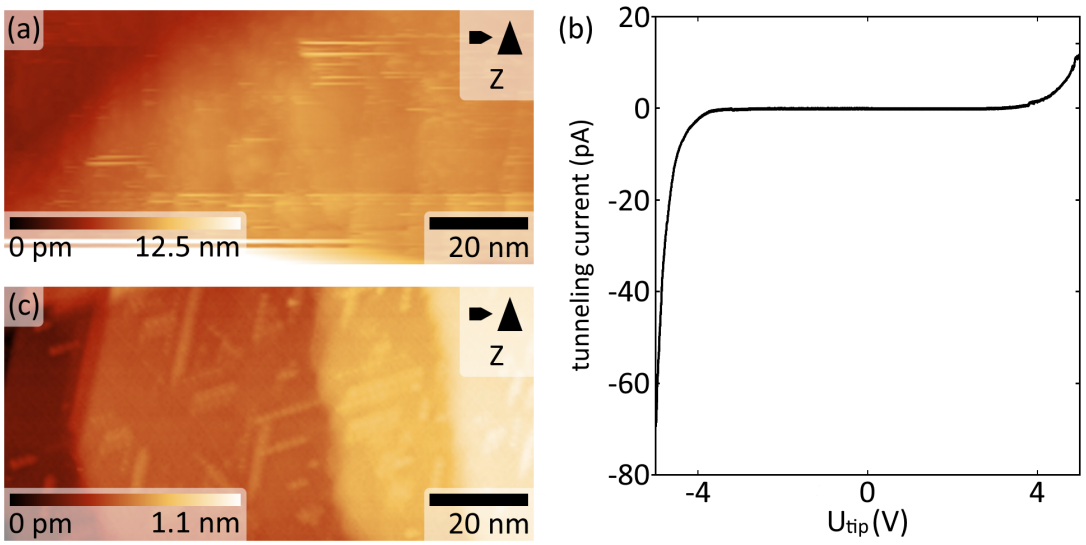

Figure 11: (a) STM image of Ag(111)/mica with a tip previously ramped deep into the sample and which is, therefore, probably coated with mica ($U_{tip} = -1\,\mathrm{V}$ and $I_t = 5\,\mathrm{pA}$). (b) The tip used for the image in (a) shows a diode-like $I_t(U_{tip})$ curve. (c) STM image of the Ag(111)/mica surface after cleaning and build-up the tip ($U_{tip} = -1\,\mathrm{V}$ and $I_t = 5\,\mathrm{pA}$).

An example for this cleaning and build-up process is presented in figure 11. An STM image of a molecule-covered[2] Ag(111)/mica surface is reproduced in figure 11(a), acquired with a tip which was previously ramped deeply into the Ag/mica sample. Only blurry structures are visible in the image. The mesoscopic tip apex is likely coated with mica due to the previous deep indentation of the tip into the specimen as indicated by the diode-like character of the $I_t(U_{tip})$ curve (figure 11(b)). Instead, a metallic surface measured with a metal tip should present a rather linear $I_t(U_{tip})$ dependence [104]. An STM image acquired after the cleaning and build-up process is shown in figure 11(c). The resolution of the image is significantly improved, single terraces and molecules forming elongated features of different length are clearly visible and indicating a tip that is clean and sharper.

The cleaning and build-up protocol used within this thesis starts with a lower voltage of 40 V and a high current of about 2.1 µA and ends with a high voltage of 55 V and a lower current of about 1 µA. However, the cleaning and build-up effect could probably be further enhanced by first applying a high voltage of 55 V at a current of about 2.1 µA to increase the thermal evaporation of impurity material, and then decreasing the voltage to 40 V while the tip is slowly retraced. Because of the reduced electric field in the last step, the field emission current decreases and causes a cooling of the mesoscopic tip apex. At an apex temperature of about 1250 °C (for tungsten tips [96]), the build-up process starts and the tip forms a

[2]It is unknown what kind of molecule was on the surface. Probably the preparation chamber and the manipulator were contaminated by protoporphyrin IX (PPIX). This PPIX could got onto the Ag(111) surface during the preparation of the calcite(104) surface and arranged in elongated structures there.

sharper apex delivering a better resolution in STM mode than the tip used for figure 11(a). This modified protocol could be tested in future experiments.

3.3.2 Changing the shape of the microscopic tip apex by stretching the tip

One approach to shape the microscopic tip apex is realised by stretching the tip [105, 106, 107]. This stretching is usually performed by impressing the tip several nanometres into the metal surface and then slowly pulling it out. The aim of the stretching is that a nanowire is formed by the sample material between tip and surface. This nanowire becomes thinner during stretching until it breaks. The residual wire element produces a new and sharp tip apex [106, 107]. Usually, the tip stretching does not directly improve the resolution power of the tip, but the purpose is to bring the microscopic tip apex into a new state that allows to continue tip shaping by other tip sharpening methods, which are discussed in the following sections.

The stretching process used within this thesis can be divided into seven steps. The time intervals of these steps are marked by numbers and different background colours in figure 12(a). The course of the vertical movement of the tip during these steps is drawn as a black line and the measured tunnelling-current is presented by a red line in figure 12(a). A tunnelling-current of 333 nA is used as an indicator for a point-contact between tip and surface. In the first step, the tip must be in tunnelling contact, here usually at $U_{tip} = 5\,\mathrm{mV}$ and $I_t = 5\,\mathrm{pA}$. Using these conditions, the tip is then located at a clean and flat position on the sample and retracted along Z by 20 nm. In the second step, the excitation of the sensor is switched of, the gap voltage is set on the $\pm 10\,\mathrm{V}$ range, a gap-voltage is set to 10 V, and the tunnelling-current preamplifier is set on maximum range (333 nA). The switch to maximum current range is causing a small electronic peak in the current signal (blue dotted circle in figure 12(a)). In the third step, the tip-sample distance is slowly decreased until the current saturated at 333 nA. It is assumed that a point-contact is established between tip and sample and that the mesoscopic tip apex starts melting due to the high current at this point. To increase the part of the microscopic tip apex that is reshaped, the tip can additionally be indented by a few nanometres into the metal surface. Here, the impressing depth is chosen up to 20 nm (fourth step). In the fifth step, the tip is slowly pulled out until the current is reduced to zero. In this step, stretching of the tip is expected to occur while the reduction of the current indicates the break of the nanowire. Sometimes the retraction length is less or equal to the impressing depth. In this case, an increase of the impressing depth or a change of the gap-voltage sign was sometimes necessary to reform the microscopic tip apex. In the sixth step, the tip is fully retracted, all settings are switched back to the settings of step one, and a new position on the sample far away from the stretching position is accessed. In the seventh and final step, the tip is approached to the surface and data acquisition is started.

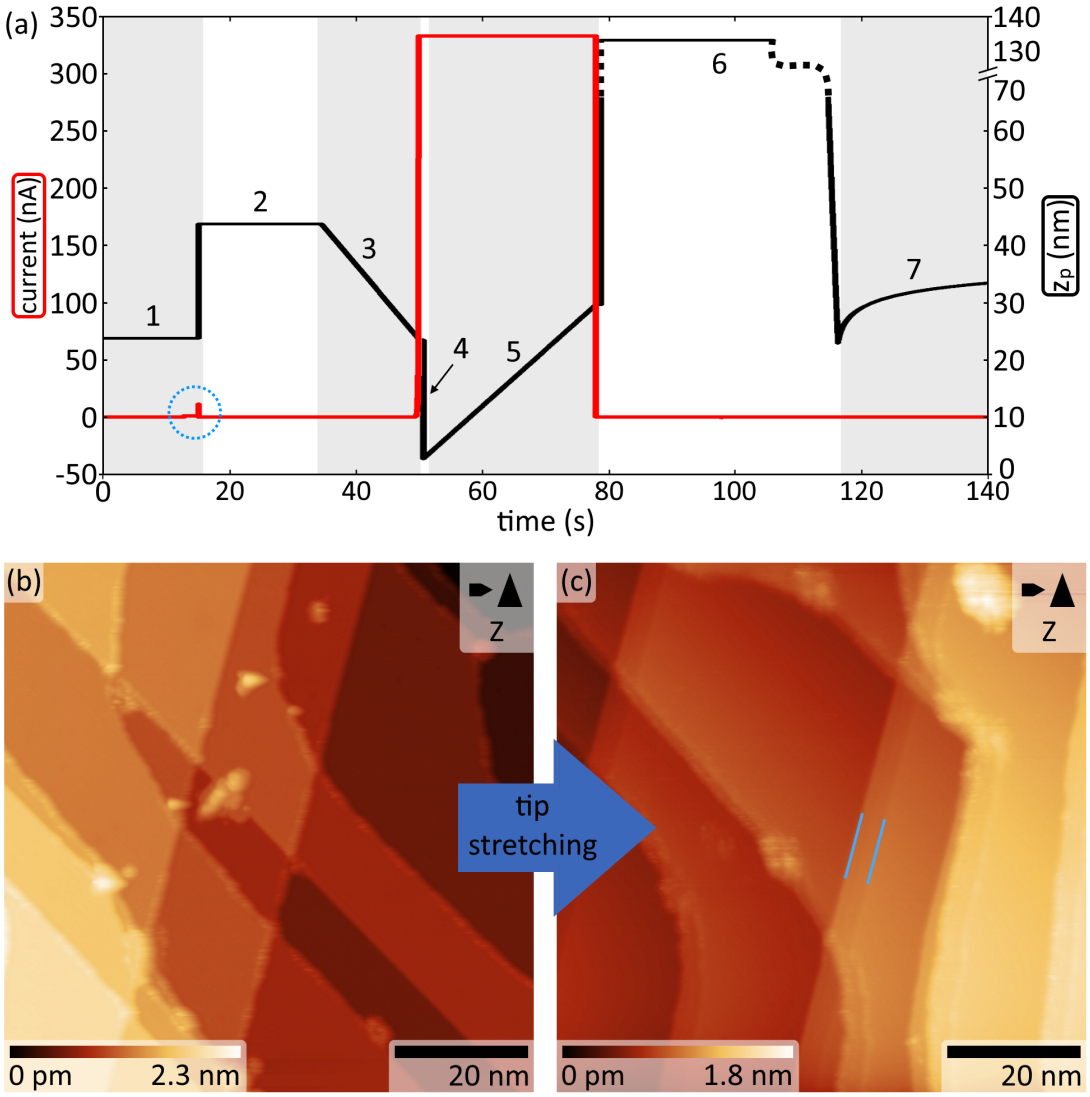

Figure 12: (a) Course of the horizontal movement of the tip (black) and of the measured current (red) during the tip stretching process. (b) STM image of Ag(111)/mica before the stretching process. (c) STM image of the sample after the stretching process. Both STM images were acquired at $U_{tip} = 1\,\mathrm{V}$ and $I_t = 50\,\mathrm{pA}$.

Exemplary data acquired before (figure 12(b)) and after (figure 12(c)) one stretching procedure is presented in figure 12. Between the images, the tip was stretched with an impressing depth of 20 nm and at $U_{tip} = 10\,\mathrm{V}$ (figure 12(a)). After the stretching process, the tip expressed a double tip character as indicated by blue lines at an step edge in figure 12(b). Such a double tip character was not observed in figure 12(b). This change in imaging indicates a reshaped microscopic tip apex.

3.3.3 Preparation of the tip apex by poking the tip into the metal surface

One of the most prevalent practice to modify the tip apex is to poke the tip into a metal surface [92, 108, 109, 110]. Pokes can roughly be separated into two types, namely: Strong and gentle pokes [92]. If the tip is indented into the metal surface in such a way that a crater in the specimen is produced, a strong poke has been performed [92]. Strong pokes coat the tip apex with sample material and can reform the mesoscopic tip apex to a shaper and more symmetric tip [108].

In contrast, a gentle poke leads to a change of the microscopic tip apex [92, 111]. Three effects of gentle pokes were mostly observed [92]: (i) the tip deposits material on the surface, (ii) the tip picks material from the surface up, or (iii) no material exchange occurs but the shape of the tip apex changes. To perform a poke, it is necessary to bring the tip in tunnelling contact with the surface. Then, the tip is further moved towards the surface with specified ramp time and maximum depth and then retraced immediately afterwards [92].

Gentle poke (i): Deposition of tip-material

In most cases, a gentle poke causes material transfer from the tip to the metal surface. This material is then visible as a bump on the surface [92, 108, 109].

An STM image of Ag(111)/mica is reproduced in figure 13(a). The tip was approached 0.5 nm to the surface during the acquisition of the scanning line that is marked by a green arrow. A bright bump (marked by a light blue arrow) appears at the position of the approach. As this bump is not imaged completely but rather appears above the active scan line, it is indicated that the bump was not there before the tip was approached 0.5 nm to the surface (scan direction is upwards in this image). Hence, this tip approach can be identified as a gentle poke with deposition of tip-material on the surface.

The resolution power of the tip is increased after this gentle poke as apparent from the step

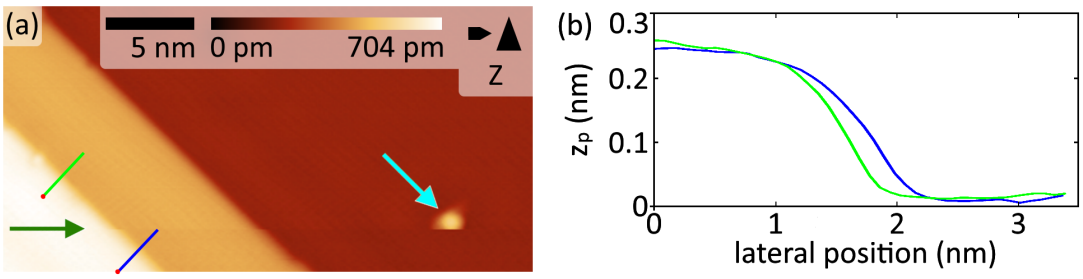

Figure 13: (a) STM image of Ag(111)/mica measured at $U_{tip} = 1\,\mathrm{V}$ and $I_t = 50\,\mathrm{pA}$. (b) Line scans extracted at the position of the blue and green lines. The red points mark the starting point of the line scans. The line scans were averaged over a line thickness of 5 pixel.

edge image in figure 13(a) that became more sharper after the poke. When inspecting the line scans extracted at the position before the gentle poke (blue line) and after the gentle poke (green line) it is apparent that the tip gives a sharper image. The profile extracted after the poke is slightly steeper in the range of 1.5 nm to 2 nm than the profile before indicating that the resolution in the image is enhanced indeed.

Gentle poke (ii): Termination of the tip with a CO molecule

The second effect of a gentle poke is the material transfer from the surface to the tip apex [92]. This ability of gentle pokes to pick-up material is not limited to atoms of the substrate, but it is also possible to pick adsorbed molecules and atoms from the substrate up [112, 113, 114]. In particular, the gentle pokes were used to terminate the tip apex with a CO molecule for the experiments in this thesis. Such CO-terminated tips significantly increase the resolution in NC-AFM images [50, 115, 116]. A detailed discussion of the contrast mechanism with CO-terminated tips is given in subchapter 5.2.

Originally, the CO pick-up has been performed by a combination of height- and voltage ramps such as the three-step procedure in one of the first approaches [117]. First, the tip is positioned directly over the molecule at $U_{tip} = 2\,\mathrm{V}$ and $I_t = 1\,\mathrm{nA}$. Second, the voltage was increased to 3 V followed by the third step, a decrease to 0 V while simultaneously approaching the tip to

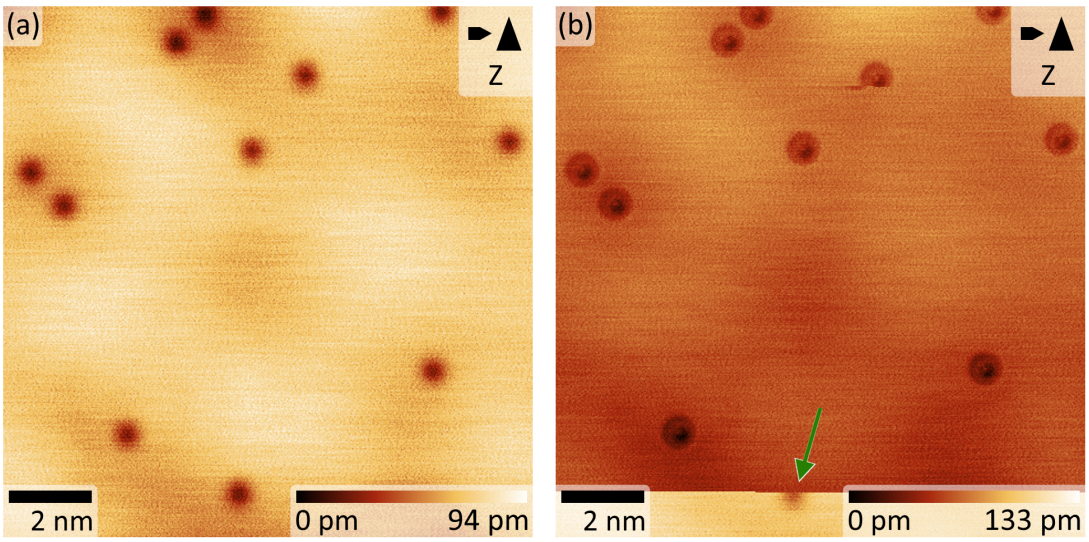

Figure 14: (a) STM image of CO molecules on Ag(111)/mica acquired with a metal terminated tip. The dark features are identified as CO molecules. The averaged frequency-shift in this image (acquired in dynamic STM mode) is $-2.25\,\mathrm{Hz}$. (b) Same position as in (a). The molecule marked by a dark green arrow was picked up with a gentle poke of $-0.8\,\mathrm{nm}$. The successful pick-up is visible in the disappeared CO molecule and in the change of the appearance of the other CO molecules. Both images were acquired at $U_{tip} = 5\,\mathrm{mV}$ and $I_t = 5\,\mathrm{pA}$

the surface at 0.1 nm.

Gentle pokes without a change in the voltage are used to pick-up CO molecules for the experiments in this thesis. It was found that a tip that yields strong contrast, a high resolution, and measures a frequency-shift between −2.5 Hz to 0 Hz at $U_{tip} = 5\,\mathrm{mV}$ and $I_t = 5\,\mathrm{pA}$ in dynamic STM, is very suitable for CO pick-up, resulting in a high probability of a CO-terminated tip.

First, an overview image of a group of CO molecules on a flat Ag(111) terrace is acquired. An example of such an image is shown in figure 14(a). The dark features in this image are identified as single CO molecules as they appear after dosing CO. Second, a gentle poke was executed with the tip located at the site of a CO molecules for pick-up. A gentle poke with a tip-sample approach of initially −0.1 nm is executed. If no change in the contrast is observed, the depth of the poke is increased by steps of −0.1 nm until a change is observed. The pick-up process is always performed when the actual scan line is over the selected CO molecule. If the CO molecule disappeared in this scan line after a poke and a change in the contrast was apparent, transfer of the CO molecule to the tip likely occurred.

For the example in figure 14, the CO molecule disappeared from the actual scan line after a gentle poke of −0.8 nm and a significant change of the appearance of the other CO molecules from dark features to features with a finer structure occur (figure 14(b)). A further discussion regarding the appearance of CO molecules on Ag(111) measured with a CO-terminated tip is given in section 5.2.4.

Gentle poke (iii): Recrystallisation of the tip without modification of the sample surface

The third effect of a gentle poke is a reordering of the tip that is apparent as a different imaging of the tip without a modification of the sample surface [92].

An example of a tip change without an effect on the sample surface is presented in the image sequence in figure 15(a–c). Figure 15(a) shows an STM image of four CO molecules on Ag(111)/mica. Figure 15(b) presents the same area, however, a gentle poke of −0.7 nm was performed at the position of the CO molecule that is marked by a light green cross between the acquisition of the scanning line that is marked by a green arrow. The aim was to terminate the tip apex with this CO molecule. However, instead of picking this CO molecule up, the contrast of the image changed, the calcite surface is imaged about 65 pm higher, while no change in the arrangement of the molecules and no crater or deposited material is visible. Figure 15(c) was acquired directly after figure 15(b) and shows the same CO molecules as in figure 15(a). The imaged shape of the CO molecules in the images is different. The CO molecules are imaged slightly less dark in figure 15(c) compared to figure 15(a) as can be

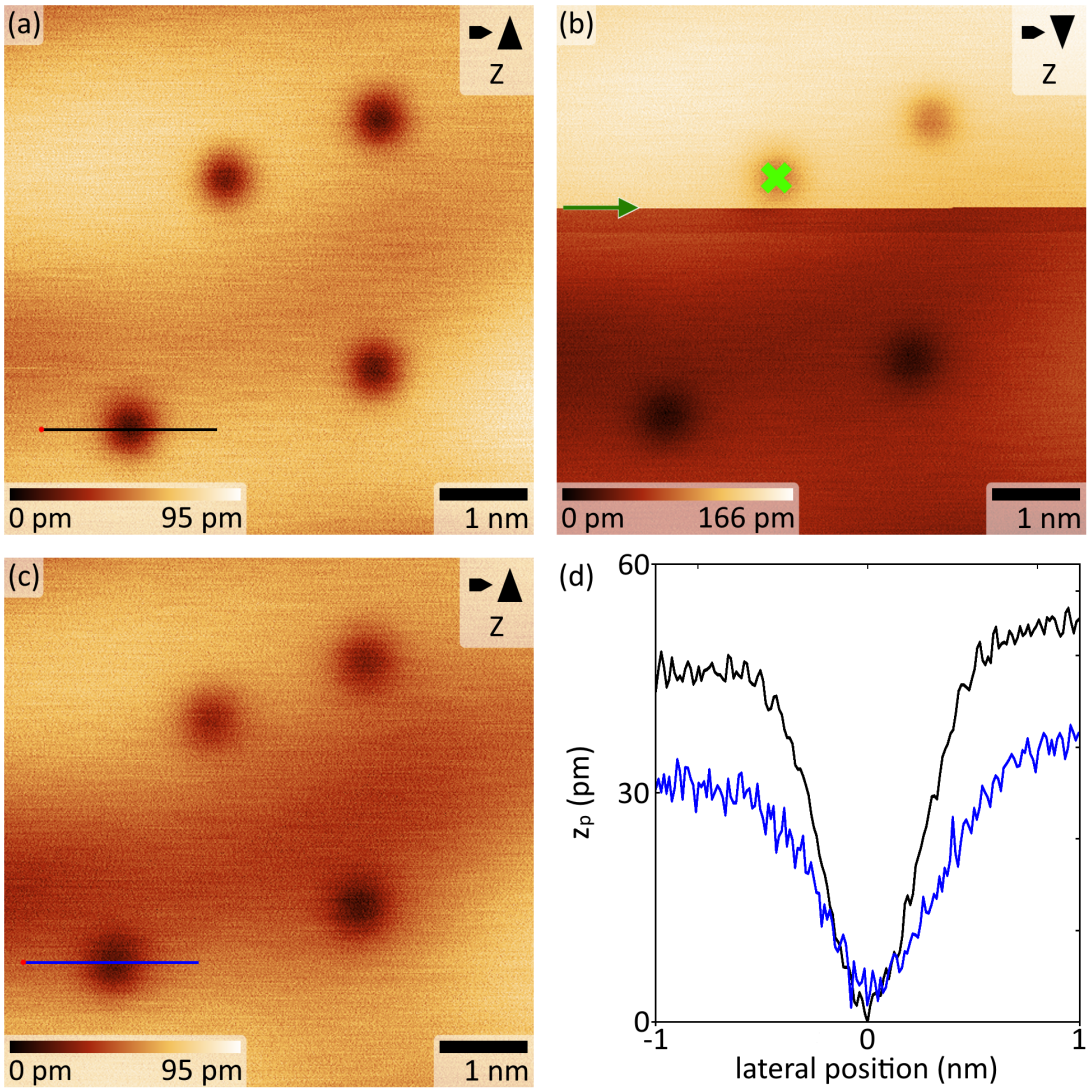

Figure 15: (a) STM image of four CO molecules on Ag(111)/mica. (b) Same area as in (a). A gentle poke of $-0.7\,\mathrm{nm}$ was performed. (c) Same area as in (a) imaged after the poke. All STM images were acquired at $U_{tip} = 5\,\mathrm{mV}$ and $I_t = 5\,\mathrm{pA}$. (d) Line scans extracted from (a) (black) and (c) (blue) indicating a change of the tip apex. The line scans were averaged over 5 pixel.

seen from the line scans in figure 15(d) extracted at the positions of the black and blue line in figure 15(a) and (c), respectively. The line scan extracted from figure 15(a) (before the poke) shows that the tip approaches the surface closer at the centre of the CO molecule than in figure 15(c) (after the poke). This difference in imaging indicates that the tip apex changed during the gentle poke.

3.3.4 Modification of the microscopic tip apex structure by a voltage pulse

A voltage pulse in STM experiments is a temporary change of the gap-voltage while the tip-sample distance is kept fix. The magnitude, the duration, and the polarity of voltage

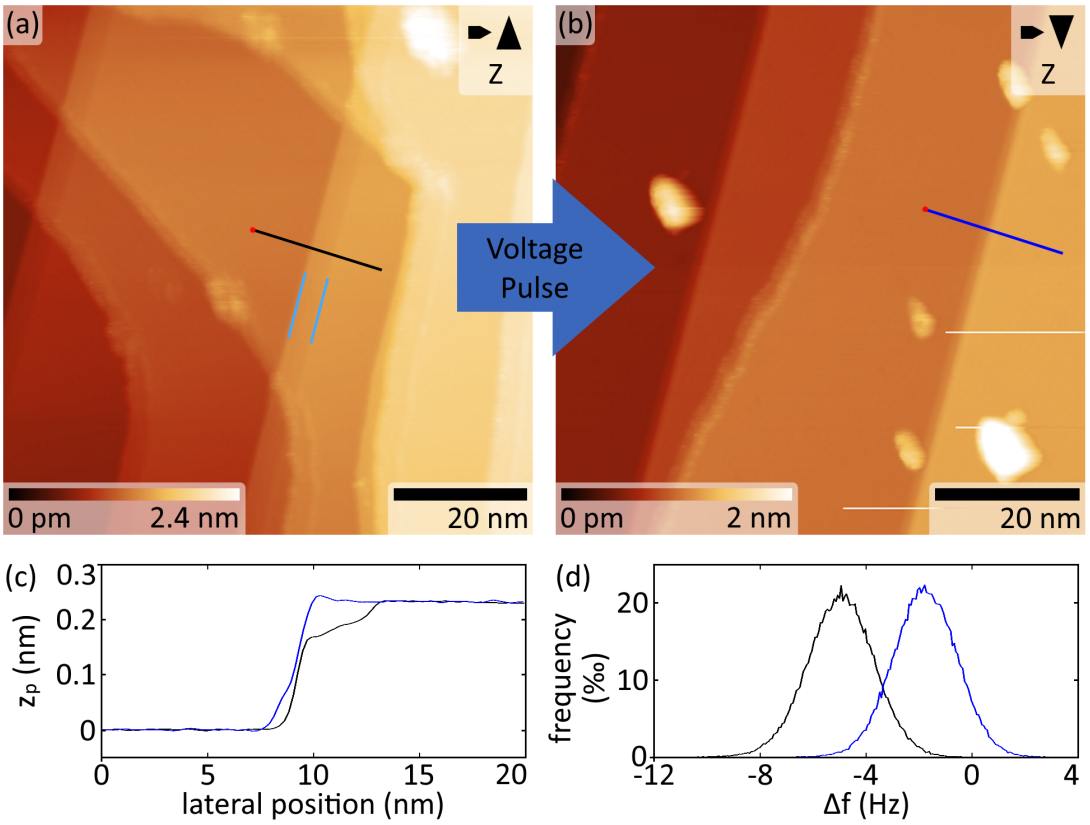

Figure 16: (a) STM image of Ag(111)/mica before the voltage pulse. Same image data as in figure 12(c). (b) STM image of the sample after a voltage pulse of 8 V, 500 ms and an increasing of the tip-sample distance by 1 nm. Both STM images were acquired at $U_{tip} = 1\,\mathrm{V}$ and $I_t = 50\,\mathrm{pA}$. (c) Line profiles extracted at the positions marked by the black and blue line in (a) and (b), respectively. In the range of 0 nm to 6 nm each line profile was linear approximated, and this linear approximation was subtracted from the whole line scan. (d) histogram of the frequency-shift in the corresponding frequency-shift images of (a) and (b).

pulse are free parameters to be chosen by the experimenter. Voltage pulse are commonly used to pick-up or deposit atoms, molecules or tip material and are combined in many cases with gentle pokes [117, 118, 119]. However, when using tuning fork sensors, it is known that voltage pulses may temporarily excite the oscillation, thus effective causing a poke at the same time.

The effects that modifies the microscopic tip apex structure are the same as discussed for the cleaning and build-up protocol discussed in section 3.3.1. However, the lower voltage range of $-10\,\mathrm{V}$ to $10\,\mathrm{V}$ and the much shorter duration of the voltage pulse limit the strength of the two effects of the pulse (thermal evaporation and migration of tip atoms) here.

An example of an improvement of the resolving power of a tip after a voltage pulse is presented in the successive images in figure 16(a) and (b) (figure 16(a) is the same image data as in

figure 12(b)). Between these images, a voltage pulse of 8 V was applied for 500 ms. To prevent thermal evaporation of the mesoscopic tip apex (section 3.3.1), the tip-sample distance was increased before the voltage pulse to $\Delta z = 1\,\text{nm}$ with the aim to keep the field emission current small and, consequently, also the temperature of the microscopic tip apex.

In figure 16(a) the tip expressed a double tip character as indicated by the double occurring step edges (blue lines) and in the kink at about 10 nm in the line profile in figure 16(c) (black line). The double tip character is not observed in figure 16(b) and in the line scan (blue line in figure 16(c)) after the pulse. This change in imaging indicates a reshaped microscopic tip apex. This is also supported by the frequency-shift that is averaged $-1.7\,\text{Hz}$ in figure 16(b) and significant smaller than in figure 16(b), where it is averaged $-4.9\,\text{Hz}$ (see also histograms in figure 16(d)).

3.3.5 Tip preparation protocol based on the experiences made in the experiments

In this section, a tip preparation protocol is presented that evolves from the experience of tip preparation on Ag(111)/mica performed during this thesis. The ultimate aim of this protocol is to produce a CO-terminated tip with a symmetric CO geometry. A flowchart of this protocol is presented in figure 17. The different tip preparation methods, which are explained in the previous sections, are written in bold in the right column. These methods are sorted according to their ability to change the tip apex. The most impacting method "Cleaning an Build-up" is at the bottom and the less impacting method "CO Pick-up" is at the top. The left panels represent different states of the tip, here classified by grades. The course in this flowchart is from panel "Start" to the panel "Characterisation and Measurement".

At the beginning (black arrow), the current state of the tip is evaluated and assigned to one of the six grades. This current tip state determines the first preparation method when starting the protocol. If the tip is CO-terminated (grade 1) it can directly be characterised (see section 5.2.3) and used for measurements. An example of an image acquired with such a tip is shown in figure 14(b). A metal tip that yields strong contrast and high resolution capability in the images, and express furthermore a frequency-shift in the range of $-2.5\,\text{Hz}$ to $0\,\text{Hz}$ in dynamic STM ($U_{tip} = 5\,\text{mV}$, $I_t = 5\,\text{pA}$, grade 2), can be used to attempt pick-up of CO molecules with a gentle poke (see section 3.3.3). Figure 10 and 14(a) are acquired with such a tip of grade 2. For tips that yield a strong contrast and high resolution capability, but express frequency-shift values outside of the range of $-2.5\,\text{Hz}$ to $0\,\text{Hz}$ (grade 3), voltage pulses (see section 3.3.4) can be used to bring the frequency-shift in the desired range. If the tip shows a reduced contrast, low resolution capability, or consists of multiple microscopic

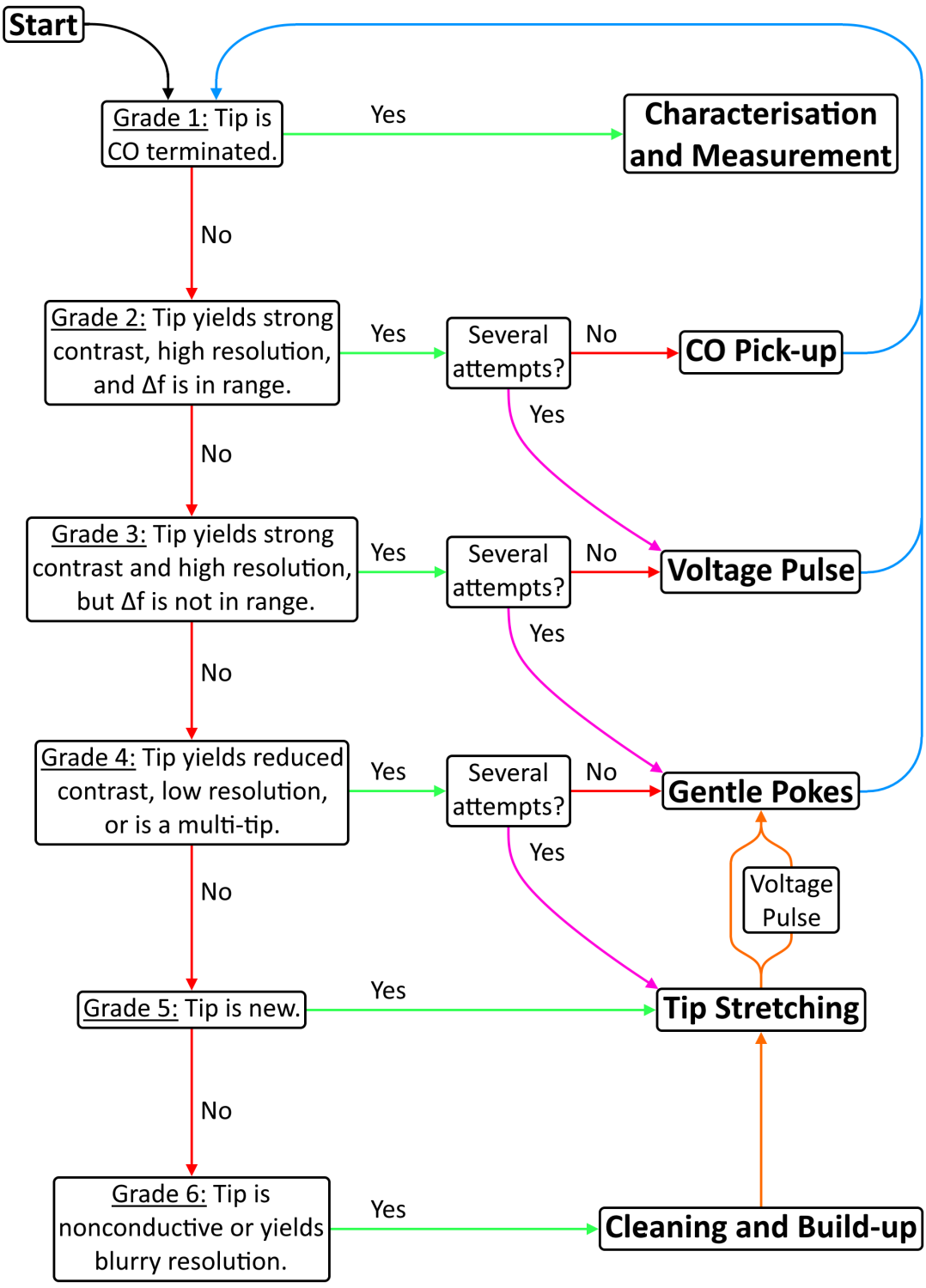

Figure 17: Flowchart of the tip preparation protocol developed within this thesis.

tip apexes apparent as image "ghosts" (grade 4, example shown in figure 12(c)), gentle pokes (section 3.3.3) can be used to remove additional tip apexes and to bring the tip into a state where a stronger contrast and a higher resolution capability might be achieved. A new tip (grade 5) is usually covered with foreign material. To remove these materials and to cover this tip with a pristine silver layer, the stretching method explained in section 3.3.2 can be used. A tip that is covered with nonconductive material or yields a blurry contrast (grade 6, one example shown in figure 11(a)) is cleaned and build-up following the cleaning and build-up method explained in section 3.3.1.

After performing a specific preparation step, the current state of the tip is determined again (blue arrow). The aim of each preparation step is to bring the tip into a state of higher grade. Exceptions from this rule are the "Cleaning and Build-up" and "Tip Stretching" steps. These methods are executed only once and then the next less impactful method is used (orange arrows). After stretching of a tip, a directly following voltage pulse can be used for removing double tips as shown in figures 16(a)–(b). If a method did not improve the tip despite several attempts, a more impacting preparation method can be used (magenta arrows) or the parameters of a preparation method can be adjusted. For example, the impact of the tip stretching method can be increased by choosing a larger indentation depth or the polarity of the gap voltage can be inverted. The impact of a gentle poke and a CO pick-up can be increased by increasing the indentation depth. Adjustable parameters of a voltage pulse are the magnitude, the duration, and the polarity.

After performing this tip preparation protocol, the tip is CO-terminated. The adsorption geometry of a CO tip influences its contrast formation. Therefore, the tip is characterised before the measurements on calcite on Ag(111) as discussed in section 5.2.4.

3.4 Double sample holder for efficient high-resolution studies of an insulator and a metal surface

The content of this subchapter is reproduced from [Jonas Heggemann, Linda Laflör, and Philipp Rahe, Double sample holder for efficient high-resolution studies of an insulator and a metal surface, Rev. Sci. Instrum. **92**, 053705 (2021)], with the permission of AIP Publishing. The technical drawing in figure 18(a) were made by Holger Heine (Feinmechanische Werkstatt, Universität Osnabrück), and the images in figure 19(a) and (b) were acquired by Linda Laflör.

A double sample holder supporting both a metal sample and an insulator crystal for high-resolution scanning probe microscopy experiments is described. The metal sample serves as a substrate for tip preparation and tip functionalisation

to efficiently and reliably enable high-resolution studies of the adjacent insulator surface. Imaging of Ag(111)/mica, Au(111)/mica, CaF_2(111), and calcite(104) surfaces is demonstrated at 5 K, including images on calcite(104) produced with a CO-terminated tip which was prepared on the adjacent metal sample.

Scanning probe techniques are now established as a gateway to the nanoworld [120, 121, 122]. In particular, non-contact atomic force microscopy (NC-AFM) has proven to be one of the major tools for the analysis of surfaces, molecular structures, or functional nanosystems [123]. With specifically functionalized tips, it is now possible to reliably quantify tip–surface interactions [124] or to image the molecular bond structure [125]. Currently, the relevance of this measurement approach for the study of insulator surfaces with their particular applications in catalysis [126] or information processing devices [127] is steadily growing.

Tip preparation strategies usually require several steps including *ex situ* electrochemical etching [93] or Focused Ion Beam (FIB)-based shaping [94], followed by *in situ* formation of the microscopic apex [92, 95, 106, 108], and finally the controlled pickup of a probe molecule [108, 117, 128]. The *in situ* tip preparation protocols commonly employ scanning tunnelling microscopy (STM) and, thus, require a metal sample, ideally with a small coverage of probe particles, such as CO or Xe. Consequently, these protocols are not directly applicable on insulator samples and it is instead common practice to switch between the metal and the insulator sample of interest. Yet, this sample holder exchange is usually a time-consuming procedure and bears especially in a low-temperature environment the risk of sample degradation.

Here, we describe a double sample holder supporting both a metal and an insulator sample. The metal sample enables tip preparation and characterization for subsequent studies of the insulator surface. Fast repositioning of the tip without the need to exchange the sample holder is possible, which is especially advantageous in a low-temperature environment as the heat load is significantly reduced by avoiding a sample transfer. We demonstrate the usage for Ag(111)/mica and Au(111)/mica mounted adjacent to crystals of calcium fluoride (CaF_2) and calcite ($CaCO_3$), exposing the CaF_2(111) and calcite(104) surfaces, respectively. In particular, we investigate possible contamination of the metal surface due to the cleaving process of the insulator surface.

The double sample holder is fabricated using the geometry of a commonly used base plate (type Specs/Omicron); see figure 18(a) for an exploded-view drawing and figure 18(b) for a photographic picture. Both the insulator crystal and metal sample are mounted such that large parts of the sample surfaces lie within a central area of 5 mm × 5 mm. This area is taken as a common range of SPM coarse positioners. The metal sample (size ∼ 3 mm × 6 mm, metal film (mica substrate) thickness about 300 nm (about 200 µm)) is clamped at both

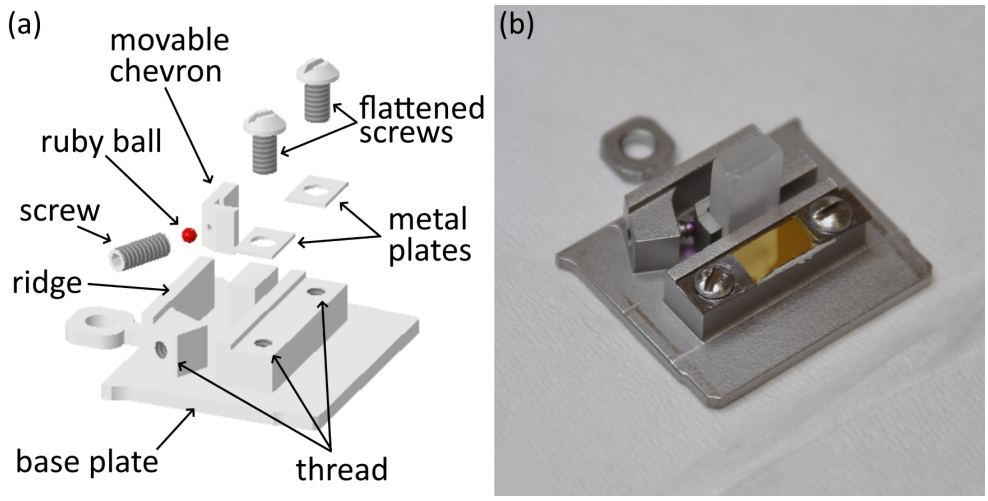

Figure 18: (a) Exploded-view drawing of the double sample holder (insulator and metal samples not shown). (b) Photographic picture of the double sample holder fabricated from stainless steel, a Au(111)/mica and calcite sample are mounted. The calcite crystal is uncleaved and, thus, protruding the sample holder.

sides using small tantalum pieces, which are tightened with screws to the protruding cuboid joined with the base plate. The screws are flattened to ensure optical access to the metal sample even at flat viewing angles. The dimensions of the protruding cuboid ensure that both sample surfaces are at the same vertical position. The support of the insulator crystal (size 2 mm × 4 mm × 3 mm) is based on a previous concept [86]: The crystal is pressed by a chevron piece against elements joined with the base plate. To enable the preparation by cleaving with a sharp blade [86], a ridge running along the front sample holder side (see figure 18) is here included to guide the cleaving blade during the cleaving process. This reduces in particular the pressure on the movable chevron.

Metal samples were prepared by common sputter and anneal cycles before cleaving the adjacent insulator crystal. We commonly sputter Au(111)/mica or Ag(111)/mica with Ar^+ at about 3×10^{-6} mbar for 15 min, followed by annealing at a sample temperature of about 400 °C for 15 min. The insulator samples were prepared by cleaving. The calcite(104) (CaF_2(111)) sample was additionally heated at about 200 °C (about 100 °C) for 90 min (60 min) after cleavage. This succession in sample preparation steps is important as sputtering the metal sample after cleaving the insulator crystal would damage the insulator surface.

Application of this double sample holder is particularly useful in a low-temperature environment. For a tight support of the crystal, the crystal's thermal compression has to be smaller than the shortening of the holder. As an example, we consider the thermal expansion across the 2 mm × 4 mm calcite(104) sample face. Calcite is strongly anisotropic [129, 130]. Within the (104) plane, the directions with the largest thermal expansion coeffi-

cients $\alpha_{\mathrm{calcite},[010]} = 180$ and $\alpha_{\mathrm{calcite},[42\bar{1}]} = -143.3$ are the [010] and $[42\bar{1}]$ directions, respectively [129, 130]. For cooling from 300 K to 5 K, we thus calculate the total length changes Δl of 8 µm and −6 µm along the [010] and $[42\bar{1}]$ directions, respectively. These numbers have to be compared to the thermal compression of the sample holder material. Double sample holders were fabricated out of stainless steel ($\alpha_{\mathrm{StSt}} = -308$ [131]), while a high-temperature variant for annealing at $T > 400\,^{\circ}\mathrm{C}$ can be produced out of tantalum ($\alpha_{\mathrm{Ta}} = -147$ [131]). Both materials compress when cooling to 5 K with $\Delta l = -13$ µm for stainless steel and $\Delta l = -7$ µm for Ta across the diagonal of a 2 mm × 4 mm rectangle. Consequently, by comparing the thermal compression and expansion, we find that the crystal is tightly supported also at 5 K. (The ruby ball (diameter: 1 mm, $\alpha_{\mathrm{ruby}} = -83.65$ [132]) does not affect this conclusion due to the negligible shortening of about 0.8 µm.) For crystals with a thermal compression larger than the holder, we note that the compressive stress from turning the screw (thread pitch 300 µm) by up to 20° after tightening could enable a length difference of up to 17 µm.

STM and NC-AFM data were acquired on Ag(111)/mica, Au(111)/mica, CaF_2(111), and calcite(104) surfaces using a combined low-temperature AFM/STM instrument (type LT AFM/STM qPlus gen.III, Scienta Omicron, Taunusstein, Germany) operated at 5 K. Electrochemically etched tungsten tips mounted to tuning fork sensors in the qPlus configuration [88] as supplied by the manufacturer were used for imaging. *In-situ* tip apex formation and tip functionalization were performed on metal surfaces

First, we investigate in figure 19 the cleanliness of the metal sample after the cleaving step for preparation of the insulator surface. While the Au(111) and Ag(111) surfaces adjacent to CaF_2(111) were covered with a sub-monolayer of extraneous material (figure 19(a)), these metal surfaces were found to be mostly clean when mounted adjacent to calcite(104) (see also the Au(111) surface in figure 19(c)). The effect of cleaving on the quality of the adjacent metal sample was investigated in further detail on a Ag(111) sample mounted adjacent to calcite. Three positions that correspond to three different distances to the calcite sample were chosen along the short metal sample axis for STM imaging; see Figure 19(e-g). Although a small amount of deposit was found at the position closest to calcite, extensive and clean areas were identified at the other sample positions. A similar observation was made for Au(111)/mica mounted adjacent to calcite(104): A clean herringbone reconstruction was imaged in most areas on the sample (figure 19(c)).

Second, we investigate the quality of the insulator surfaces. Atomic resolution was routinely achieved on both CaF_2(111) and calcite(104); see Figure 19(b) and (d), respectively. In agreement with earlier results on CaF_2(111) [133] and calcite(104) [27, 29, 31] using a similar clamping mechanism [86], extended terraces with a tiny fraction of defects were found. Further experiments at a number of surface areas give no evidence of contamination from

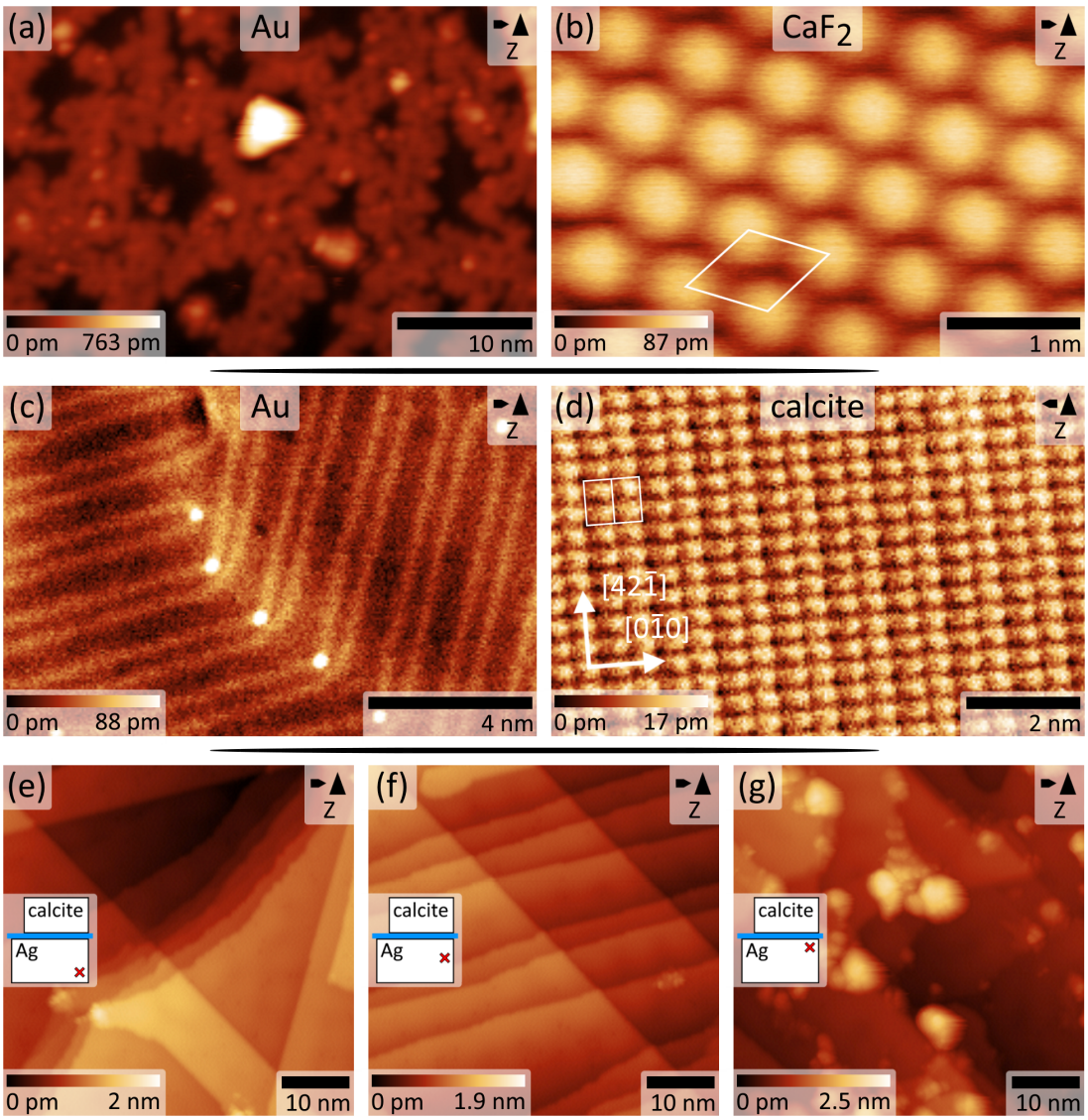

Figure 19: (a) STM image acquired on Au(111)/mica adjacent to CaF_2 (sample voltage $U_{\text{tip}} = 50\,\text{mV}$, tunnelling-current setpoint $I_t = 100\,\text{pA}$). (b) Atomic-resolution imaging on $CaF_2(111)$ in NC-AFM mode (unit cell marked in white, frequency-shift setpoint $\Delta f = -2\,\text{Hz}$). (c) STM image ($U_{\text{tip}} = 50\,\text{mV}$, $I_t = 5\,\text{pA}$) acquired on the far side of Au(111)/mica adjacent to calcite(104). (d) NC-AFM image acquired on calcite(104) with a metal tip ($\Delta f = -4.5\,\text{Hz}$ and $U_{\text{tip}} = 5\,\text{V}$ (Calcite-010, Ra crystal, see table 1)). (e-g) STM images acquired on a Ag(111)/mica sample mounted adjacent to a calcite(104) crystal ($U_{\text{tip}} = 5\,\text{mV}$, $I_t = 5\,\text{pA}$). Data were acquired at different positions as indicated by a red cross in the inset sketches (big (small) rectangle represents the surface area of the metal (calcite) sample).

the nearby metal sample or the double sample holder. Atomic contrast was in a number of experiments directly achieved after shaping the tip apex on the adjacent metal sample.

Finally, we demonstrate in figure 20 the preparation and usage of CO functionalized tips for imaging calcite(104). CO was dosed directly into the cold scan head for 120 s, yielding

a coverage of about 0.02 ML on the surfaces. CO pickup was performed by height ramps on Ag(111) after shaping a metal tip apex. Inverse imaging by a surface-adsorbed CO was used to ensure a symmetric tip [134]; see Figure 20(a). The tip was then approached on calcite(104) in the NC-AFM mode, and exemplary data are shown in figure 20(b) and (c). In the topography image (figure 20(b)), CO/calcite(104) is imaged by the CO-terminated tip as a dark depression surrounded by a bright rim. Imaging in the constant-height mode (figure 20(c)) avoids feedback instabilities at the molecule center and resolves single CO molecules as bright protrusions (white arrow in figure 20(c)) as well as the calcite lattice structure. Further details of the CO/calcite(104) system can be found in Ref. [55]. Inverse imaging on CO/Ag(111) after scanning calcite(104) (data not shown) yielded virtually similar CO images to that in figure 20(a). We conclude that a CO tip is stable during moving from one sample to the other and during the careful approach in both NC-AFM and STM modes.

The most important aspect to consider for a double sample holder is the mutual contamination of the sample surfaces. Cleanliness of the insulator surfaces is expectedly not an issue as the cleaving of the insulator crystal is performed as the last preparation step. Material deposited on the metal surfaces during the cleaving process of CaF_2, however, restricts the tip preparation sites to the areas within the void pores. In contrast, extensive areas on the metal samples are available after cleaving an adjacent calcite crystal. As the same *ex situ* cleaning protocol was used for both crystals, we account this difference to the different

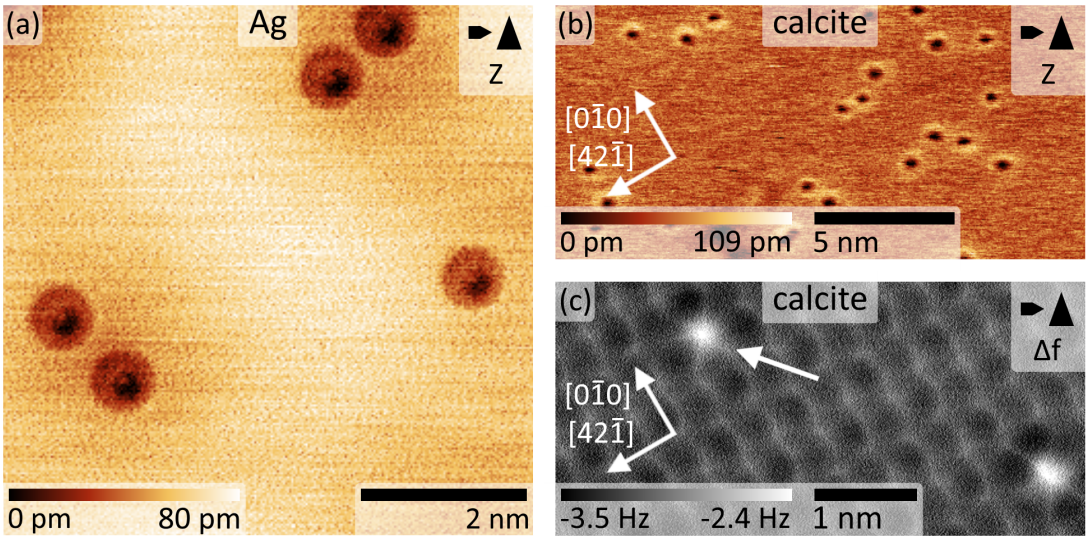

Figure 20: (a) CO/Ag(111)/mica imaged with a CO-functionalised tip in STM ($U_{\text{tip}} = 5\,\text{mV}$, $I_t = 5\,\text{pA}$). (b) CO/calcite(104) image acquired with a CO-functionalised tip in NC-AFM mode ($\Delta f = -1.4\,\text{Hz}$ and $U_{\text{tip}} = -10\,\text{V}$). (c) Constant-height frequency-shift NC-AFM image of CO/calcite(104) acquired with a CO-functionalised tip in NC-AFM ($U_{\text{tip}} = -10\,\text{V}$ (Calcite-012, Ku crystal, see table 1)).

chemical reactivity of the insulator materials. In particular, our data suggest that a CaF_2 molecule has a much larger adhesion to a metal sample [135] when compared to the rather volatile carbonate group.

In conclusion, we presented a double sample holder as support for both a metal and an insulator sample for efficient NC-AFM measurements with functionalized tips. The preparation of clean metal and insulator surfaces was demonstrated for the combination of Au(111)/mica and Ag(111)/mica with calcite(104). We expect that the sample holder will be particularly useful for studying calcite(104) and generally applicable to further combinations of insulator/metal samples.

3.5 Determination of the $[4\,2\,\overline{1}]$ direction in the NC-AFM images

It is important to know the correct orientation of the coordinate system for the interpretation of the NC-AFM images acquired on calcite(104). Especially for simulations, the exact knowledge of the $[4\,2\,\overline{1}]$ and $[\overline{4}\,\overline{2}\,1]$ directions is important in order to compare simulated images with the NC-AFM images more accurately. Note that the $[4\,2\,\overline{1}]$ and $[\overline{4}\,\overline{2}\,1]$ directions are not related by a symmetry on calcite(104). According to reference [27, 136] the $[4\,2\,\overline{1}]$ direction within the (104) plane of calcite can be determined by using the birefringence property of the calcite crystal as explained in the following.

After the NC-AFM measurements, the edge of the used calcite crystal the movable chevron was pressed against is carefully marked on the upper calcite surface (position is indicated by the light green L in figure 21(a)). This L-marker is important to be able to trace back how the calcite crystal was mounted into the double sample holder. After removing the calcite crystal from the sample holder, the crystal is placed on a line intersection of a chequered sheet of paper in such a way that the intersection is visible through the crystal as shown in figure 21(b). The surface used for NC-AFM measurements has to face away from the paper. Due to the birefringence the intersection visible through the calcite crystal appears in form of two images barely distinguishable. One image is formed by the ordinary and the other by the extraordinary ray. Consequently, the light delivering the two images has a different linear polarization. With a linear polariser, one of the two images of the intersection can be filtered (figure 21(c)). To change between the two images, the filter must be rotated by 90° (figure 21(d)). If the image of the intersection that matches the chequered pattern around the calcite crystal is visible, the ordinary ray passes the linear polariser (figure 21(c)). Otherwise, the extraordinary ray passes the filter and the image shows an offset to the chequered pattern of the paper (figure 21(c)). The appearances are in agreement

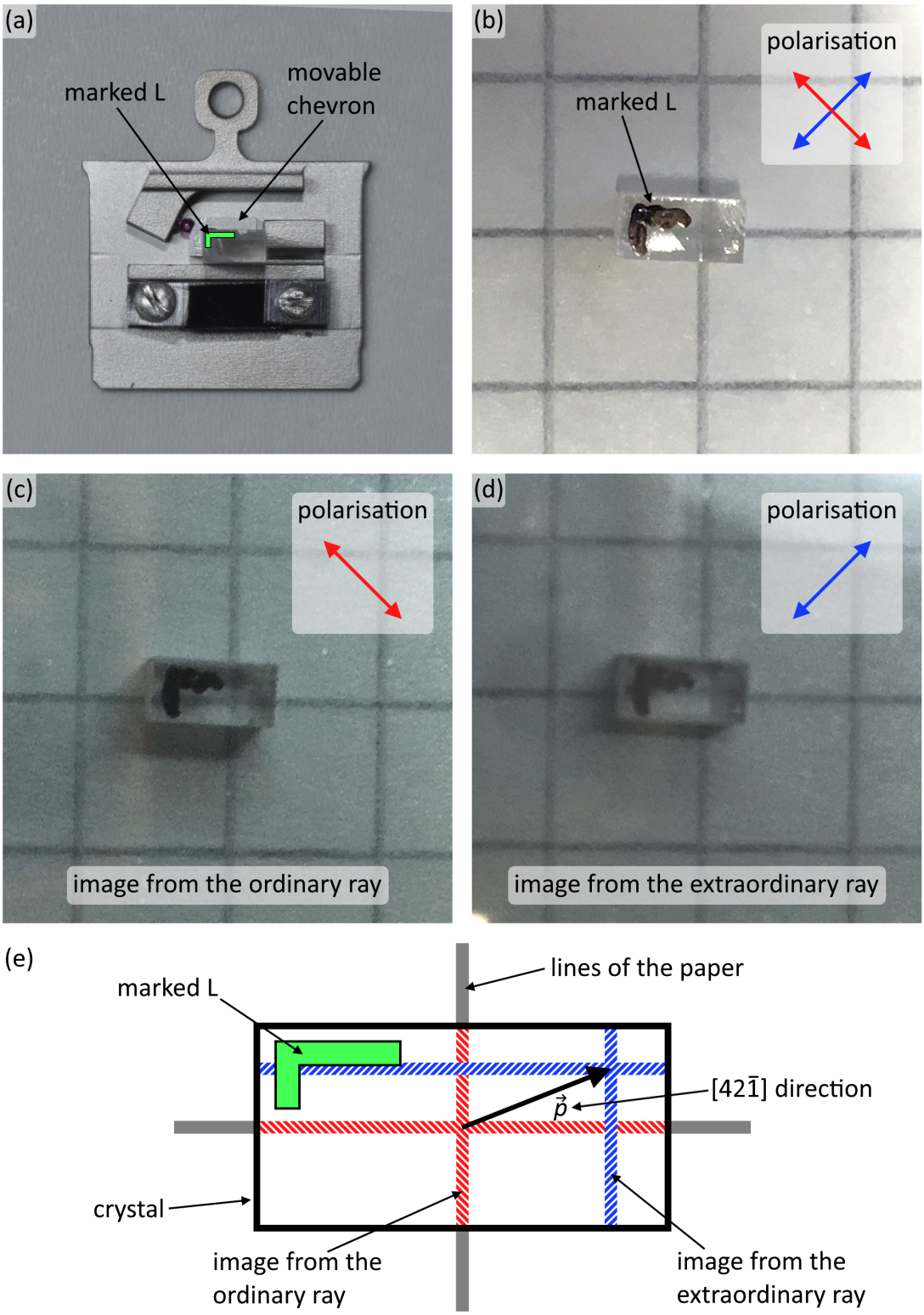

Figure 21: (a) Photographic picture of the double sample holder [137] with a calcite and an Ag(111)/mica sample. The green L indicates the crystal corner where the movable chevron is pressed against. (b–d) Calcite crystal with L-marker (black colour). The arrows indicate the polarisation at the linear polarising filter. (e) Sketch of the setup. The translation vector (split vector) between the images of the ordinary and extraordinary ray points along the $[4\,2\,\bar{1}]$ direction.

with the polariser direction. As a practical advice note that the viewing direction must be perpendicular to the paper plane in both cases. The translation vector between the image from the ordinary ray to the image of the extraordinary ray is called the split vector $\vec{p}$ that points in $[4\,2\,\bar{1}]$ direction [27], see also the sketch in figure 21(e). From the determination of this vector, the orientation of the calcite crystal is determined. In the example of figure 21 the $[4\,2\,\bar{1}]$ direction points upwards to the right.

For a reliable comparison to the NC-AFM data, the $[4\,2\,\bar{1}]$ direction of the calcite crystal must be transferred to the NC-AFM images in the next step. The result of the analysis using the birefringence property is shown in figure 22(a), where the double sample holder is

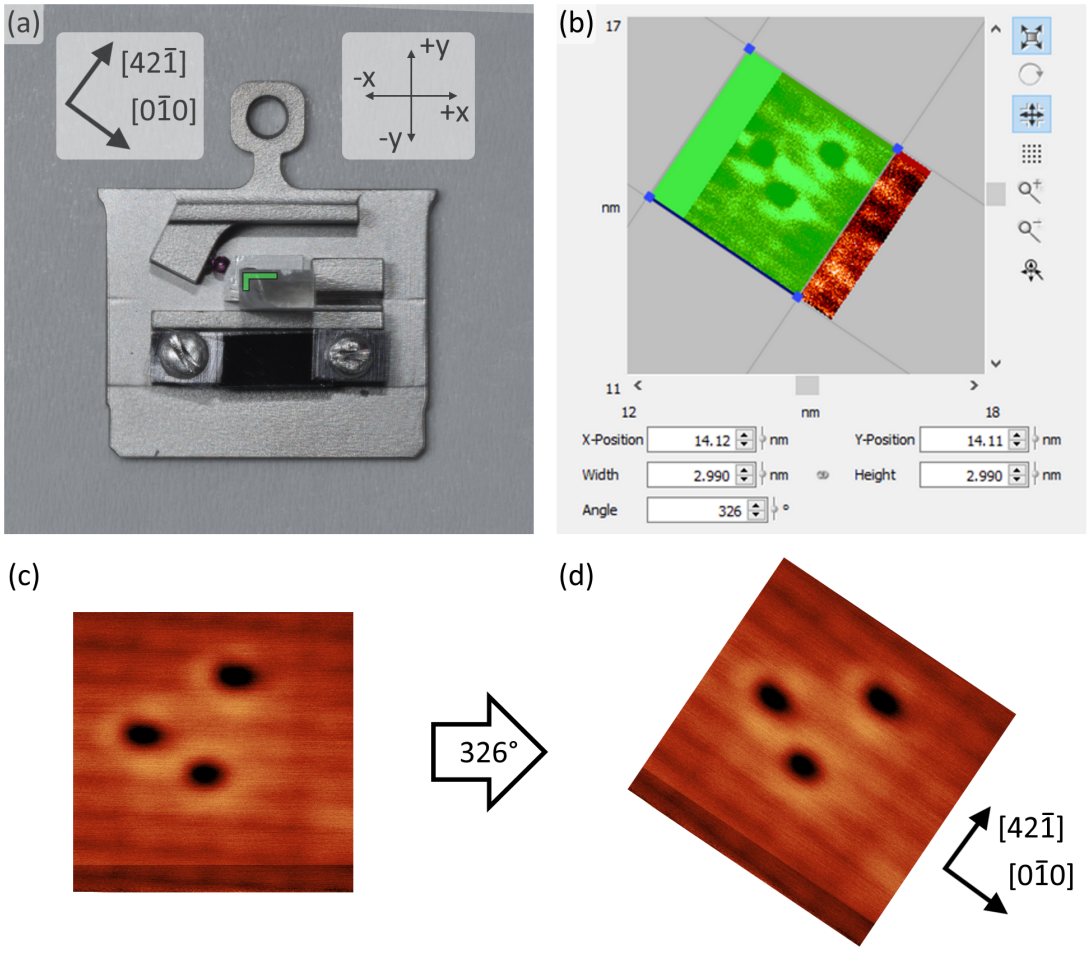

Figure 22: (a) Photographic picture of the Double sample holder with calcite and Ag(111)/mica sample. The upper left coordinate system is oriented following the determination of the $[4\,2\,\bar{1}]$ direction via the birefringence properties. The upper right coordinate system is the coordinate system from the measurement system [138]. (b) Screen capture presenting the "XYScanner" window of the measurement program. (c) "Raw" image data presented without considering the scan angle (i.e. with horizontal alignment of the fast scan direction). (d) Image data rotated using the scan angle.

visible with the marked $[4\,2\,\overline{1}]$ direction (upper left coordinate system). The $[0\,\overline{1}\,0]$ direction is derived from determining the $[4\,2\,\overline{1}]$ direction in a (104) plane. The internal coordinate system of the SPM measurement system is inserted in the upper right corner of figure 22(a), according to the specifications of this system [138]. The relation between these coordinate systems and the image frame follows from analysing the scan controller software. A screen capture of the window in the measurement program is shown in figure 22(b) where the scan parameters can be set. In this image, the shown scan area follows the internal coordinate system, which has the same orientation as indicated in the upper right of figure 22(a) [138]. A scan angle of 326° was set for the acquisition of the image data in figure 22(b). The green area indicates the scan area for a subsequent image with the same scan angle.

While the fast and slow scan direction are rotated with respect to the axes of the coordinate system in figure 22(a), this information is usually lost when presenting image data with the fast scan direction oriented horizontal an in figure 22(c). Therefore, the image must be rotated by the scan angle to fit to the coordinate system of the measurement system. As a result, the rotated image in figure 22(d) is aligned with respect to the internal coordinate system of the measurement system, and the $[4\,2\,\overline{1}]$ direction of the calcite crystal (upper left corner in figure 22(a)) can now be transferred to this NC-AFM image. As the final result, the $[4\,2\,\overline{1}]$ direction is determined in this image as indicated by the coordinate system in figure 22(d).

3.5.1 Calculating the image calibration factor of the measurement device by using 2D Fourier transform

The scan movement of the tip is performed by a piezoelectric scanner. This scanner is driven by an applied voltage; the scan software uses a generic factor to convert the applied voltage into a length. This length does not necessarily correspond to the physical length that the tip moves when the voltage is applied, hence, calibration factors are necessary that correct the length specifications of the scan software.

For the lateral calibration the (2×1) reconstruction of the calcite(104) surface is used. The dimensions of a (2×1) unit cell are 1 nm in $[0\,\overline{1}\,0]$ and 0.81 nm in $[4\,2\,\overline{1}]$ direction with an angle of 90° [43], and are, therefore, valuable as reference lengths. The lateral calibration factor is then derived by comparing the length informations and the angles of an unit cell given by the measurement device with the real unit cell dimensions. These length informations and the angles of the unit cells in the images are determined by 2D Fourier transform.

This method for the lateral calibration factor is shown for figure 23(a) as an example. This NC-AFM image shows a calcite(104) surface acquired with an unknown tip and with a scan angle of zero. Visible are bright protrusions arranged in $[0\,\overline{1}\,0]$ and $[4\,2\,\overline{1}]$ direction following

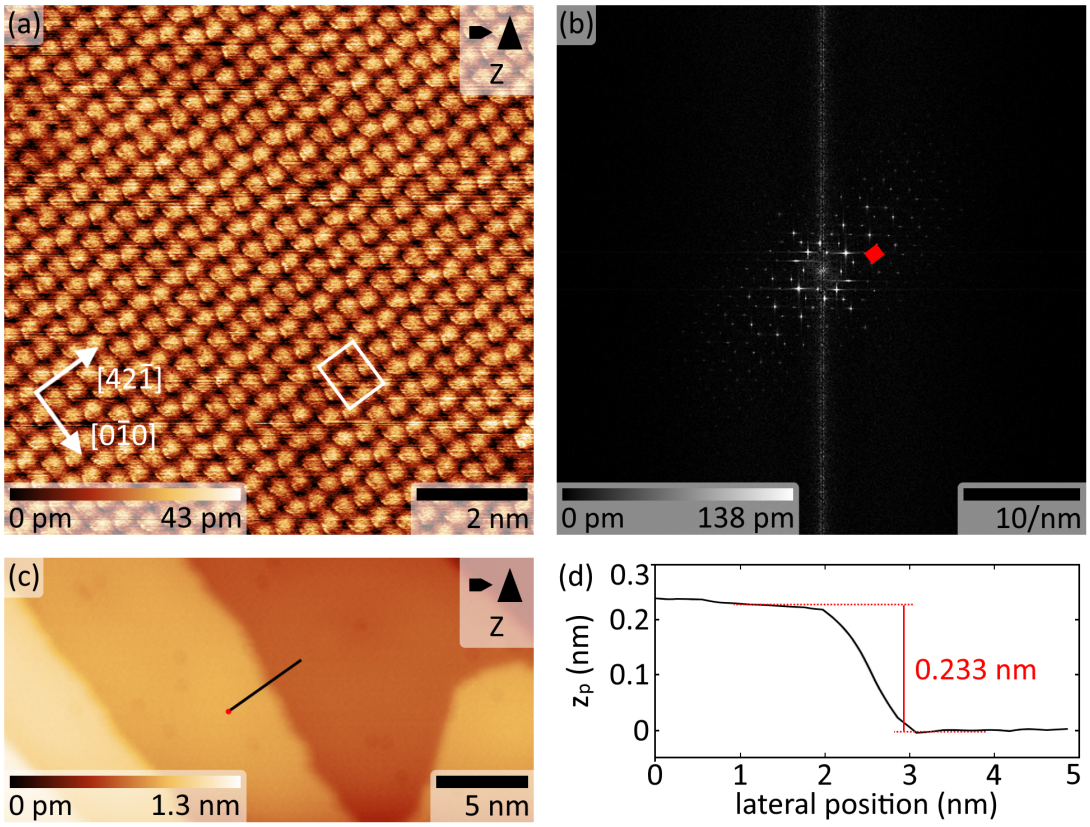

Figure 23: (a) Topography image of calcite(104) acquired with an unknown tip at $U_{tip} = -3\,\mathrm{V}$ and $\Delta f = -6.4\,\mathrm{Hz}$. The image data were line-by-line subtracted (Calcite-003, Ra crystal, see table 1). (b) Fourier transformation of the image in (a) as absolute value of the amplitude spectral density (ASD). The red rectangle indicate a reciprocal (2×1) unit cell. (c) Dynamic STM image of Ag(111) with step edges acquired at $U_{tip} = 5\,\mathrm{mV}$ and $I_t = 5\,\mathrm{pA}$. (d) Line scan extracted at the position of the black line in (c). The red dot marks the start. All lengths in this four images are the lengths informations given by the measurement device.

a (2×1) reconstruction, the white rectangle indicates a (2×1) unit cell of the calcite(104) surface. The directions are determined by the optical method explained in subchapter 3.5.

The 2D Fourier transform of figure 23(a) is visible in figure 23(b). Peculiar are the bright maxima, which represent periodical features in figure 23(a). The red rectangle indicate a reciprocal unit cell and can be, therefore, assigned to the (2×1) unit cells of figure 23(a). The length informations of this reciprocal unit cell are $1.08\,\mathrm{nm}^{-1}$ in $[0\,\bar{1}\,0]$ and $1.34\,\mathrm{nm}^{-1}$ in $[4\,2\,\bar{1}]$ direction, and the angle between the $[4\,2\,\bar{1}]$ and $[0\,\bar{1}\,0]$ direction is 90.3°. Consequently, in real space the unit cells have the dimensions 0.93 nm and 0.75 nm in $[0\,\bar{1}\,0]$ and $[4\,2\,\bar{1}]$ direction, respectively. This length informations of a (2×1) unit cells are slightly smaller than the real ones, and must be enlarged with the calibration factor of about 1.08 for both directions.

This analysis was applied to eleven images with different sizes. All of them were measured on the calcite-003 crystal with a scan angle of zero and at 5 K. For the unit cell length along the $[0\,\overline{1}\,0]$ direction an average calibration factor of 1.09 ± 0.04 was found, and for the $[4\,2\,\overline{1}]$ direction a factor of 1.09 ± 0.02. This two calibration factors for two linear independent directions are very similar. Therefore, the lateral calibration factor is set to 1.09.

The angle between the $[4\,2\,\overline{1}]$ and $[0\,\overline{1}\,0]$ direction is calculated from the eleven images to $91 \pm 1°$. The real angle of 90° is within the error interval and, therefore, the images are usually not angle corrected. The algorithmic symmetry test (described in section 5.1.3) needs 90° between the directions, hence, the images used for this algorithmic symmetry test are additional unit cell corrected.

The vertical calibration factor is determined from the height of step edges on the Ag(111) surface. This step edges have a height of 0.235 nm [139] and are, therefore, valuable as vertical reference length. The vertical calibration factor is then derived by comparing the height of a step edge in an NC-AFM image with the real height of a step edge.

In figure 23(c) an Ag(111) surface is visible with step edges and faintly visible CO molecules. The terraces were leveled by the Gwyddion tool "Level data by fitting a plane through three points" [140]. A line scan across a step edge was extracted at the position marked by the black line. This line scan is reproduced in figure 23(d). In this image the height profile of the step edge is visible. The height difference between the upper and lower terrace can not measured exactly because the terraces are not flat and have a small corrugation probably caused by electronic states. Hence, the step height is estimated to about 0.233 nm (red lines) that is slightly smaller than the height difference of 0.235 nm in the literature.

A total of 23-step edges on Ag(111) were measured acquired at 5 K on different samples. The average height of a step edge is determined to (0.24 ± 0.02) nm. Here, the standard deviation is used as error interval. The 0.235 nm is within this error interval, hence, no vertical calibration factor is used within this thesis, but the height data could have an uncertainty of about 8 %.

3.6 Explanation of the methods for image editing

The NC-AFM images shown in this thesis are processed using common methods as outlined in this subchapter. Practically, most processing steps are performed by using the open-source software Gwyddion [140].

Layout calibration

First, the height and width of STM and NC-AFM images are enlarged by the calibration factor of 1.09. This factor is determined from reference images as explained in section 3.5.1. It corrects the lateral calibration performed by the manufacturer.

Plane correction

Second, the mean plane is subtracted from the STM and NC-AFM topography data, to correct for the common misalignment between the sample surface plane and the scanner coordinate system. Additionally, a polynomial background of third degree along both axes is removed to compensate horizontal piezo creep. If terrace steps are present the plane substract is performed by aligning a single terrace. Single images with abrupt changes in the topography are coreccted using line-by-line subtraction instead of mean plane and polynomial background subtraction; These images are accordingly marked in the image caption. Utmost care is taken to not producing any artefacts in the images by this processing.

Drift and lateral piezo corrections

Due to imperfections of piezo scanners, the scanner coordinate system is not a precise orthogonal system. Consequently, angles in the images differ slightly from the physical angles of surface structures. As this imperfection does often not impact the image interpretation, it is usually neglected (section 3.5.1). In contrast the symmetry analysis in subchapter 5.1 requires perfect rectangular unit cells in the images. Therefore, the image data used for this analysis are sheared in a preprocessing step in a way that the unit cell in these images are rectangular with dimension of $1\,\mathrm{nm} \times 0.81\,\mathrm{nm}$. These corrections were performed by a first degree polynomial transformation as implemented in a specific computer programme [141].

A second strategy is used for correcting drift. The positions of features in sequential images (typically acquired in the up and down direction) are tracked and the drift velocity is calculated from the lateral shift. A polynomial transformation of the image can be performed from this velocity as is explained in detail in reference [142]. This approach is implemented in another specific computer programme [143].

Colour gradient

Fourth, all measurement data are lineary mapped to colour gradient with a selection of the minimum and maximum value according to the data range. Topography data are presented in a yellow-red colour gradient (Gwyddion.net) in Gwyddion, while a grey gradient is used for frequency-shift data.

4 Preparation of metal and calcite surfaces

The preparation of the metal and calcite samples for STM and NC-AFM measurements is explained in this chapter, including the deposition of CO and H_2O molecules on these samples. An overview over all calcite samples used within this thesis is given in the end of this chapter.

Before every measurement series, the double sample holder is equipped with a metal sample (either Ag(111)/mica or Au(111)/mica from Georg Albert PVD-Beschichtungen), as well as an uncleaved calcite crystal. The sample holder is then inserted into the load-lock chamber for bringing it into UHV. This chamber was closed and pumped with the roughing and turbomolecular pump. To reduce the amount of contaminating atoms and molecules, the load-lock chamber is baked by heating up to 110 °C for about 16 h. After the bake-out of the load-lock chamber, the double sample holder is inserted into the heating stage of the manipulator.

It is recommended to outgas this manipulator at about 750 °C for 1 h and subsequently run the titanium sublimation pump of the preparation chamber for several cycles before the double sample holder is inserted into the preparation chamber. Otherwise impurities, which were left behind from previous sample preparations, could contaminate the metal and calcite surface of the double sample holder during their preparation steps.

To further clean the double sample holder, it is heated up to about 380 °C by a resistive heating plate mounted at the sample reception. This heater is operable at 16 V (1 A) to reach this temperature. The temperature is slowly increased over 60 min to prevent a premature self-cleaving of the calcite crystal due to stress in the material at rapid temperature changes. The protocol is as follows: At first, the voltage is set to 10 V (0.4 A). After 10 min, the voltage is increased to 13 V (0.8 A). After further 10 min, the voltage is increased to 16 V. After about 40 min the temperature reached 380 °C. From this moment 90 min are waited until the voltage is ramped down with a rate of about 0.5 V per 30 s.

The preparation of the metal sample (described in the next subchapter) can be started as soon as the temperature of the double sample holder is less than 100 °C.

4.1 Preparation of clean metal surfaces

A standard sputtering and annealing method is used to prepare clean metal samples suitable for the tip preparation methods explained in subchapter 3.3 [144, 145].

For a new sample or a metal surface exposed to atmosphere, at least five sputter/anneal cycles are performed. Every cycle consists of a sputtering and an annealing part. At first,

the metal sample is sputtered by using the ion source with Ar^+ ions for 15 min at a current of 2 µA. The pressure in the preparation chamber was adjusted to about 2.2×10^{-6} mbar. After each sputtering procedure, the annealing step of the metal sample is performed. In this annealing step, the double sample holder is heated up to about 380 °C (16 V and 1 A). The temperature is slowly increased in the same way as explained previously. As soon as the temperature reaches 380 °C, annealing is performed for 15 min before the voltage is slowly decreased again at a rate of 0.5 V per 30 s. The next cycle can be started as soon as the temperature of the double sample holder is below 100 °C.

4.2 Preparation of a clean calcite surface

A clean calcite(104) is achieved by cleaving the calcite crystal in vacuum and subsequently annealing to about 160 °C [86].

The cleaving can be performed when the temperature of the double sample holder is below 50 °C. A sharp blade, which is guided by the ridge of the double sample holder (see figure 18), is used to scratch along the long side of the calcite crystal. The scratching is repeated until the crystal cleaved along a (104) plane and the upper part of the calcite crystal falls off. Then, a new calcite(104) surface is produced.

A fresh calcite surface, which is cleaved in UHV, usually exhibits large surface charges that prevent stable NC-AFM measurements due to erratic repulsion of the tip [39, 146]. To reduce the surface charge the sample is heated by applying 10 V (0.4 A) for 90 min to the resistive heater [147]. A temperature of about 160 °C is reached after about 90 min. The voltage is then decreased again at a rate of 0.5 V per 30 s.

The preparation of the calcite surface can partly degrade the metal surface adjacent to the calcite crystal as explained in subchapter 3.4. Nevertheless, a clean calcite(104) surface is produced and clean areas of the metal sample can be found at areas not directly adjacent to the calcite crystal.

4.3 Dosing of CO and H_2O on the calcite(104) surface

The setup and protocol for submonolayer deposition of CO and H_2O on calcite(104) is presented in this subsection. At first, the dosing of CO is treated, followed by dosing of H_2O.

4.3.1 Dosing of CO on the calcite(104) surface

CO is deposited on the sample while it is inside the scan head. As the desorption temperature of CO on Ag(111) and Au(111) is at around 50 K (measured in thermal desorption

spectroscopy (TPD) [148, 149]), it is necessary to use liquid helium cooling. At first, the valve between the preparation chamber and the turbomolecular pump is opened. Next, CO 99.997 % ((Westfalen AG, Münster, Germany) is leaked into the preparation chamber at a pressure of about 9×10^{-6} mbar by using the leak valve of the ion source. As soon as the pressure in the preparation chamber is stable, CO can be leaked into the LT chamber and dosed onto the cold sample. Practically, the valve between preparation and LT chamber as well as the shields around the scan head are quickly opened simultaneously. From this moment, CO is dosed on the sample and a specific time is waited before the shields of the scan head, the valve between preparation and LT chamber, as well as the leak valve are quickly closed again. The pressure in the LT chamber increases to about 5×10^{-8} mbar during CO dosing on the sample, while the pressure in the preparation chamber decreases to about 2×10^{-6} mbar. The temperature of the sample in the scan head rises to about 8 K due to the open shields. After dosing, the pressure in the preparation chamber decreases slowly. It is recommended to run the titanium sublimation pump of the preparation chamber about 1 h after the valve between preparation and LT chamber was closed in order to shorten the time that is used to settle to the original pressure value.

4.3.2 Dosing of H_2O on the calcite(104) surface

The deposition of H_2O required the construction of a water dosing unit and the determination of suitable parameters. This water dosing unit is similar to a dosing unit constructed by Dr. Ralf Bechstein [150] and explained in detail in this section, followed by the preparation protocol.

Components of the water dosing unit

The water dosing unit consists of a leak valve, a water reservoir, a bellow-seal valve, and a roughing pump as shown in figure 24. The leak valve (from VACGEN) is mounted to a flange at the preparation chamber with a direct line-of-sight from the valve to the sample mounted in the heating stage of the manipulator. Thus, the sample is directly exposed to a stream of water emanating from the leak valve. The bellow-seal valve connects the water reservoir with a roughing pump and is used for bake out the water dosing unit and cleaning the water (see figure 24(b)). Before first usage, the water dosing unit was roughly cleaned by opening the valve to the roughing pump and baking at 180 °C for about 30 h. Then, the water reservoir is dismounted and filled with a few millilitres of "Millipore water for molecular Biology" before mounting to the other parts again.

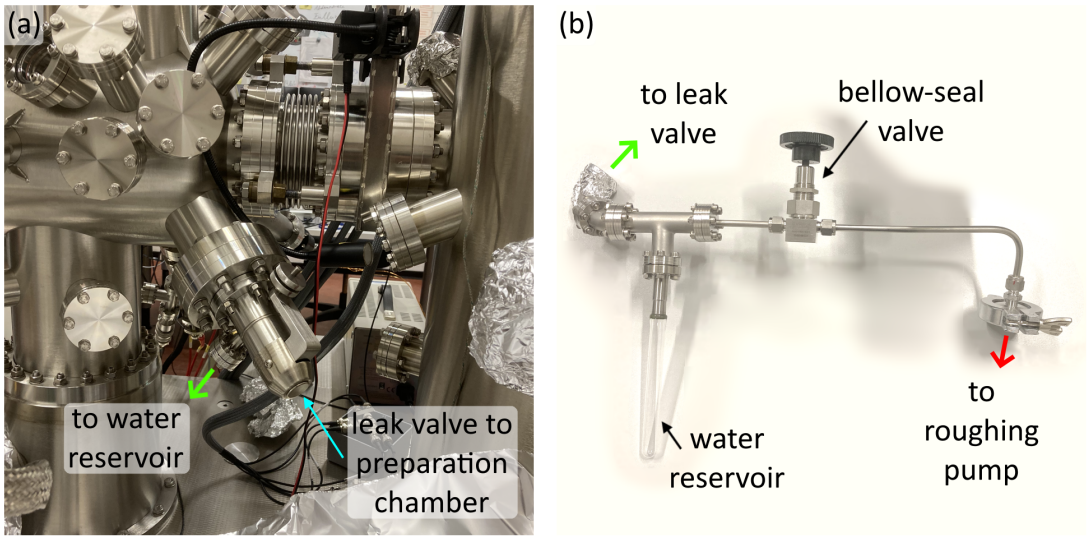

Figure 24: Water dosing unit. Consisting of (a) a leak valve mounted to the preparation chamber and (b) a water reservoir. The water dosing unit visible in (b) is connected to the leak valve as marked by the light green arrows. The bellow-seal valve separates the dosing unit from a roughing pump.

Water cleaning protocol

Dissolved gases such as CO_2 and N_2 as well as further containments need to be removed from the water to ensure clean sample preparation. Cleaning of water is usually performed with freeze-pump-thaw cycles. One cycle consists of three steps: In the first step, the water in the reservoir is frozen by immersion of the reservoir into liquid nitrogen (77 K). If the complete water is frozen, the bellow-seal valve is opened in the second step for about 3 min so that the pressure in the water dosing unit is reduced by the roughing pump. The pumping reduces the amount of contaminating gases in the reservoir. The frozen water allows to reduce the pressure in the reservoir much further, hence, the amount of contaminating gases that are removed is increased. In the third step, the bellow-seal valve is closed and the ice is melted by warming the water reservoir up. According to Henry's law [151], the amount of dissolved gas in water is proportional to its partial pressure in the gas phase. Due to the reduced partial pressures a larger amount of contaminants dissolved in the water escape into the gas phase in this step, and can thus be pumped during the next cycle.

In order to asses the water purity, the residual gas analyser is used to measure the gas composition when dosing water into the preparation chamber. The dosing is performed as follows. First, the valve between the preparation chamber and the turbomolecular pump is opened. Second, the leak valve of the water dosing unit is slowly opened until a specific chamber pressure between 1×10^{-10} mbar to 1×10^{-9} mbar is reached. Water is then dosed for a dosing time t_{H_2O} before the leak valve is closed again. The water purity is accessed after

N_{fpt} freeze-pump-thaw cycles by acquiring a measurement with the residual gas analyser. The resulting data of five m/z-spectra acquired after N_{fpt} = 4, 9, 19, and 24 numbers of freeze-pump-thaw cycles, are reproduced in figure 25(a).

The gas analyser works in three steps [152, 153]: First, the neutral particles of the residual gas are ionized by electron bombarding. This bombardment not only generates single and multiple charged ions of the particles but also fragments of these particles that in turn can also be single and multiple charged. Second, the generated ions are separated by a quadrupole mass spectrometer according to their mass-to-charge ratio m/z whereby m is the atomic mass of an ion and z is the charge number. Third, the amount of ions of a specific mass-to-charge ratio is determined by a microchannel plate detector [152]. The resulting m/z-spectrum consists mainly of single peaks that correspond to a specific mass-to-charge ratio and is called a mass spectrum because the charge number of the ions is usually $z = 1$, and m/z represents the atomic mass of the detected ions in this case.

In figure 25(a) the mass spectra of the five measurements are reproduced. The mass spectrum of the residual gas in the preparation chamber at a pressure of 1.1×10^{-10} mbar before water was dosed into the preparation chamber represents the black line. The other spectra represent the composition of the residual gas after N_{fpt} = 4 (dark blue), 9 (light blue), 19 (green), and 24 (orange) freeze-pump-thaw cycles during dosing at a pressure of 9.9×10^{-10} mbar, 2.2×10^{-10} mbar, 1×10^{-9} mbar, and 1.1×10^{-9} mbar, respectively.

In the spectra eight gases can be identified, namely: H_2, CH_4, H_2O, F, CO, N_2, O_2, and CO_2. These gases are also typical residual gases in UHV Systems [154, 155, 156]. The presence of hydrogen can be derived from the strong signal at $m/z = 2$ (H_2^+) and the much weaker signal at $m/z = 1$ (H^+) [157]. The signals at $m/z = 12$ (C^+), 13 (CH^+), 14 (CH_2^+), 15 (CH_3^+), and 16 (CH_4^+) indicate the presence of methane, which originates probably from lubricating oil [158]. Hydrocarbons with two or more carbon atoms are at or below the detection threshold as there are no clear peaks at $m/z = 24$ (C_2^+), 25 (C_2H^+), 26 ($C_2H_2^+$), and 27 ($C_2H_3^+$) [159]. Only the peak at $m/z = 28$ ($C_2H_4^+$) could indicate such hydrocarbons. But, due to the missing other fragments these peak is rather CO^+ and N_2^+ [160, 161]. Water is identifiable in a m/z-spectrum by a larger peak at $m/z = 18$ (H_2O^+), a about five times smaller peak at $m/z = 17$ (HO^+), and a much smaller peak at $m/z = 16$ (O^+); all these peaks are present in the spectra in figure 25(a). The presence of fluorine and hydrogen fluoride, probably originating from Viton gaskets (fluorocarbon-based fluoroelastomer), can be assumed from the peaks at $m/z = 19$ (F^+) and $m/z = 20$ (FH^+). The existence of nitrogen can be concluded according to the literature from a strong signal at $m/z = 28$ (N_2^+) and an about ten times smaller signal at $m/z = 14$ (N^+) [161], both peaks are found in the spectra of figure 25(a). Oxygen is visible in mass spectra as a large peak at $m/z = 32$ (O_2^+)

and a five times smaller peak at $m/z = 16$ (O^+) [162]. But, these peaks are only visible for the spectrum acquired during dosing at 1.1×10^{-9} mbar after twenty-four freeze-pump-thaw cycles (orange line). The presence of CO can be derived from the peaks at $m/z = 28$ (CO^+), 16 (O^+), and 12 (C^+) [160], and the presence of CO_2 from the peaks at $m/z = 44$ (CO_2^+), 28 (CO^+), 16 (O^+), and 12 (C^+) [163].

Isotopes, which shift the m/z ratio of a molecule, were neglected in the discussion of the mass spectra, because each of the five found elements consist to more than 98 % of only one isotope [164]. For example: $m/q = 18$ can not only originate from H_2O^+ but also from DO^+ (deuterium and oxygen). But only 0.015 % of the natural hydrogen is deuterium and can be, therefore, neglected in the discussion of the mass spectra [164].

Also neglected are the rare multiple charged ions. The mass-to-charge ratio of such an ion would be smaller than the ratio of a single ionized molecule. Typical are twofold ionized ions. The signal of twofold ionized ions with an odd atomic mass is particularly easy to find in a mass spectra. In this case the m/z-ratio of these ions is at an intermediate position between two atomic masses. For example: A single ionized fluoride atom has the mass-to-charge ratio $m/z = 19$ ($m = 19$ and $z = 1$), while a twofold ionized fluoride atom has the ratio $m/z = 9.5$ ($m = 19$ and $z = 2$) and would generate a peak at the intermediate position 9.5.

The half-integer intermediate positions are marked by vertical dashed lines in figure 25(a). No peak can be found at such a position and indicate, therefore, that the amount of twofold ionized ions is under the detection threshold. Another indication of rarely occurring twofold ionization are the peaks in the range of $m/z = 12$ to $m/z = 20$. These peaks were generated from typical residual gases in a UHV system [154, 155, 156] and can be, therefore, assigned to single ionized molecules. Peaks in the range of $m/z = 6$ to $m/z = 10$ would occur if some of these gas molecules would be twofold ionized. Except at a few positions no clear signal is visible in this range. Hence, the amount of these twofold ionized ions is also under the detection threshold.

As explained before, the aim of the freeze-pump-thaw cycles is to purify water before dosing into the preparation chamber. But it is difficult to conclude the purity from the mass spectra in figure 25(a) as the dosing pressure and number of freeze-pump-thaw cycles have been changed. However, it is expected that the ratio between the intensities of the signal at $m/z = 18$ and other m/z rations can be evaluated as a measure for the purity of the dosed water. Following this idea, each spectrum in figure 25(a) is normed to the height of its peak at $m/z = 18$. The resulting mass spectra are reproduced in figure 25(b) with the same colour code as in (a).

The peaks in the mass spectra acquired during water dosing after four freeze-pump-thaw cy-

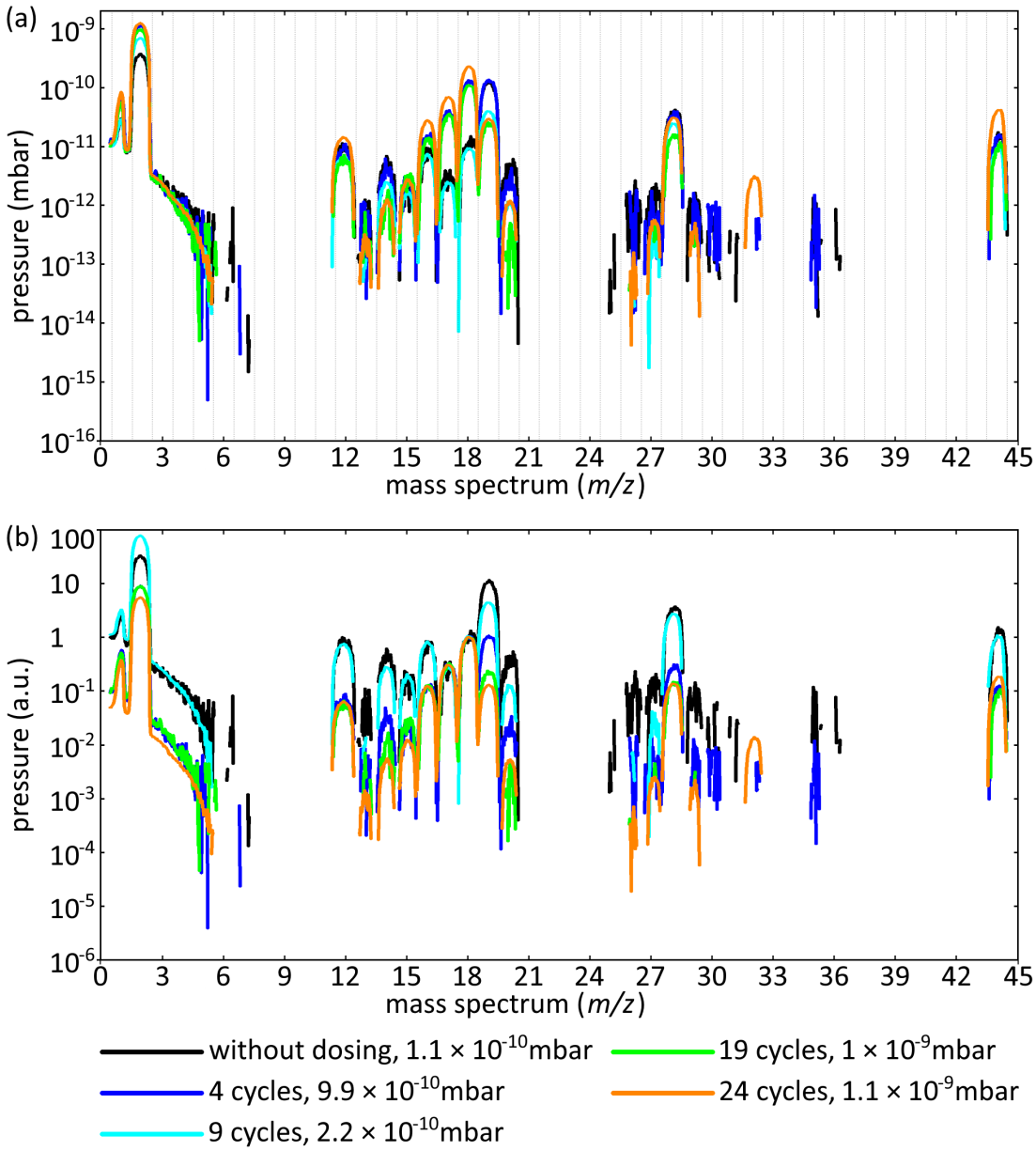

Figure 25: (a) Mass spectra of the atoms and molecules in the preparation chamber during water dosing. Black line: Spectrum at 1.1×10^{-10} mbar acquired before H_2O dosing. Dark blue line: Spectrum during dosing acquired at 9.9×10^{-10} mbar after four freeze-pump-thaw cycles. Light blue line: Spectrum during water dosing acquired at 2.2×10^{-10} mbar after nine freeze-pump-thaw cycles. Green line: Spectrum during dosing acquired at 1×10^{-9} mbar after nineteen freeze-pump-thaw cycles. Orange line: Spectrum during dosing acquired at 1.1×10^{-9} mbar after twenty-four freeze-pump-thaw cycles. (b) Same spectrum as in (a). Every spectrum is normed at its peak at $m/z = 18$.

cles and at a chamber pressure of 9.9×10^{-10} mbar (dark blue line in figure 25(b)) are mostly smaller than the peaks in the mass spectrum that was measured before water was dosed into the preparation chamber (black line). Exceptions are the peaks at $m/z = 17$ (OH^+) and

18 (H_2O^+). These peaks are typical for water [165] and indicate that water is indeed dosed into the preparation chamber.

The peaks in the spectrum after 9 freeze-pump-thaw cycles (light blue line) are very similar to the peaks in the spectrum without water dosing (black line). It is likely that this similarity is caused by the rather low pressure of 2.2×10^{-10} mbar, which is slightly higher than the chamber pressure without water dosing (1.1×10^{-10} mbar), and not by the number of freeze-pump-thaw cycles because the line for 4 freeze-pump-thaw cycles is clearly below the black line. Hence, it can be assumed that at a pressure of 2.2×10^{-10} mbar not enough water emanates from the leak valve and residual gases in the chamber pollute the water. Therefore, the water dosing at 2.2×10^{-10} mbar provides the most impure water of all four dosing pressures.

The peaks in the mass spectrum after 19 cycles and 1×10^{-9} mbar (green line) as well as the peaks in the spectrum after 24 cycles, 1.1×10^{-9} mbar (orange line) are very similar to each other. Different are the peaks at $m/z = 2$, 14, 15, and 19, where the orange line is particularly below the green line. This finding indicates that a purer water with less hydrocarbons and fluorine are dosed into the preparation chamber if 24 freeze-pump-thaw cycles are performed. In conclusion, the purity of dosed water is increased if the water is purified by 24 freeze-pump-thaw cycles dosed into the preparation chamber at a pressure in the range of 1.1×10^{-9} mbar.

It is further interesting to inspect the temporal evolution of the various contributions during dosing. This time-dependent behaviour of the peak height of $m/z = 2$, 4, 18, 28, 32, and 44 is shown in figure 26. The leak valve was opened at time index 5 min and the pressure in the preparation chamber was about 1×10^{-9} mbar during H_2O dosing. The leak valve was closed again at time index 15 min.

The traces for $m/z = 2$ (light green, H_2^+) and 18 (blue, H_2O^+) indicate successful water dosing at a nearly constant rate. The traces for $m/z = 4$ (black, He^+) is also very stable during dosing and indicate that the time depending increasing of the other peaks are indeed caused by an increasing of the related gas and not caused ba a measurement error of the residual gas analyser. In contrast, the traces for $m/z = 28$ (magenta, N_2^+), 32 (green line, O_2^+) and 44 (red line, CO_2^+) are increasing during H_2O dosing. The reason for this increase is unknown. A possible explanation could be a leak in the leak valve where atmospheric air, which contains nitrogen, oxygen, and carbon dioxide, enters the preparation chamber. To avoid larger amounts of this foreign gases, the maximum dosing time was set to 2.5 min. In this time range the dosed water is least contaminated with nitrogen, oxygen and CO_2.

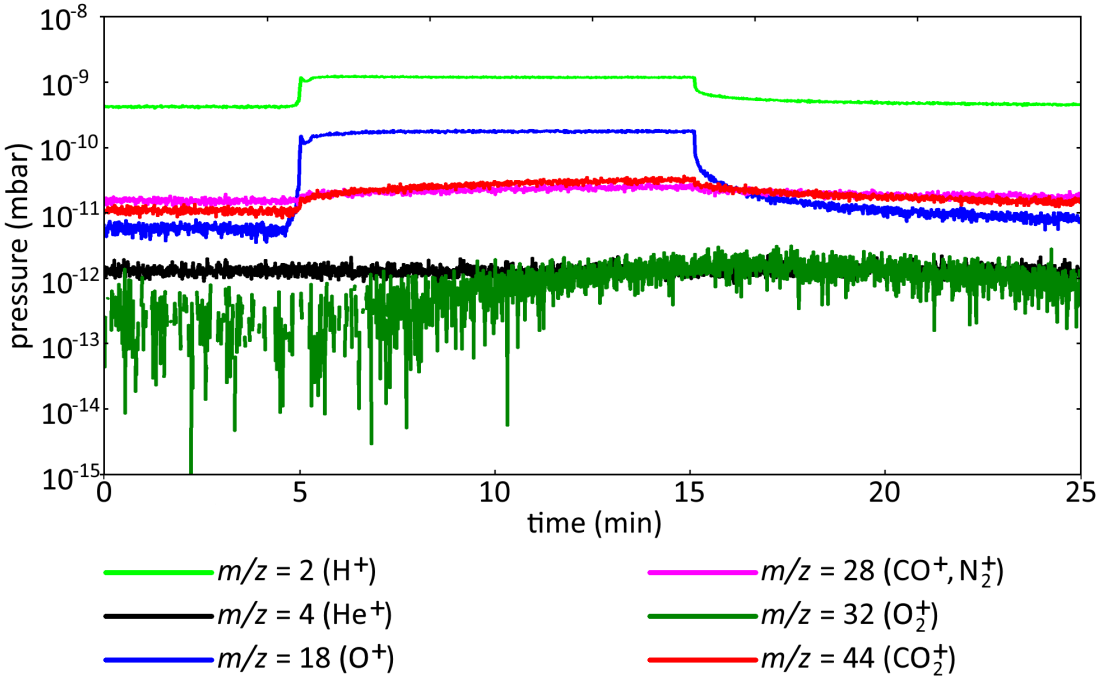

Figure 26: Time-dependent behaviour of the peak heights of $m/z = 2$, 4, 18, 28, 32, and 44 during dosing. The water leak valve was opened at time index 5 min and closed at time index 15 min. The total pressure in the preparation chamber was 6.3×10^{-11} mbar before H_2O dosing and about 1×10^{-9} mbar during H_2O dosing.

Protocol for dosing water on calcite(104)

Due to the desorption temperature of water on calcite(104) around $-10\,^{\circ}\mathrm{C}$ [57] the manipulator is cooled down before water dosing. The heating stage is placed in such a way, that the water stream from the leak valve is directed directly onto the double sample holder. Cooling is performed by flow of gaseous nitrogen from a dry-nitrogen gas bottle. The gas (at about 1.8 bar) is cooled by passing through a condensing coil that is immersed in liquid nitrogen. The cooled nitrogen is then directed through thin pipes to the heat exchange at the manipulator, while a second pipe acts as a nitrogen exhaust. A thermally highly conductive braid connects the heat exchange with the heating stage that is then cooled down to about 150 K. To dose water on the calcite sample, the double sample holder is inserted into the heating stage of the cooled manipulator, and the valve between preparation and LT chamber is closed, while the valve between preparation chamber and turbomolecular pump is opened. The water dosing itself is performed by quickly opening the leak valve until a chamber pressure of 1×10^{-9} mbar is reached. From this moment, a specific time (less than 2.5 min) is waited before the leak valve is quickly closed again. After water dosing, it is waited for about 10 min until the pressure in the chamber stabilized again. Then, the valve between preparation and LT chamber is opened to transfer the double sample holder back into the scan head of the microscope.

4.4 Overview over the calcite samples and their CO and H_2O dosages

Twelve calcite samples were used for the 5 K measurements within this thesis. A complete list is shown in table 1. The names of the samples are listed in the first column of table 1. The calcite crystals used for this thesis originate from different orders from Korth Kristalle (Altenholz, Germany). The as-delivered block of calcite was cut into smaller calcite crystals in all cases. The calcite blocks can be separated into the three groups Ra, Ku, and Os as marked in the second column ("Source"). An examination of the composition of these three samples is given in subchapter 5.4. In the first group (Ra) are blocks ordered before 2012. Unfortunately, it is no longer possible to trace whether there are one or two calcite blocks in this group. The second group (Ku) originate from one crystal block. Samples originating from this group are labelled with "Ku" in the second column of table 1.

CO was dosed on most of the calcite samples following the protocol described in section 4.3.1. The dosing time is given in column 3 together with the pressure in the LT chamber during

		CO dosing		H_2O dosing		Metal
Name	Source	Time (s)	Pressure (mbar)	Time (s)	Pressure (mbar)	sample
Calcite-003	Ra	30	5×10^{-8}			Ag(111)
		120	6.1×10^{-8}			
Calcite-004	Ra			60	1×10^{-9}	Ag(111)
				20	1×10^{-9}	
		20	4×10^{-8}			
Calcite-005	Ra			130	1×10^{-9}	Ag(111)
		25	4.7×10^{-8}			
Calcite-006	Ra	25	3.8×10^{-8}			Ag(111)
		25	4.1×10^{-8}			
		300	5×10^{-7}			
Calcite-007	Ra					Ag(111)
Calcite-009	Ra	30	3.5×10^{-8}			Ag(111)
		60	3.7×10^{-7}			
Calcite-010	Ra	50	3.1×10^{-8}			Ag(111)
Calcite-011	Ku	30	3.1×10^{-8}			Au(111)
Calcite-012	Ku	50	3×10^{-8}			Ag(111)
	Ku	70	3.5×10^{-8}			
Calcite-014	Ku	150	3×10^{-9}			Ag(111)
Calcite-015	Ku					Ag(111)
Calcite-016	Ku	60	9×10^{-7}			Ag(111)

Table 1: Overview over the calcite samples used within the 5 K measurements of this thesis and their CO and H_2O dosing parameters. Additional lines at a calcite crystal indicate multiple dosages. The calcite crystal used in subchapter 7.3 is not listed in this table.

CO dosing in column 4. H_2O was dosed on two samples as described in section 4.3.2. The water dosing time is listed in column 5 and the pressure in the preparation chamber during water dosing is in column 6. Several additional doses of H_2O or CO were performed on some samples as illustrated by additional lines for these samples. In the last column, the element of the metal samples are listed. Either Ag(111)/mica or Au(111)/mica was mounted next to calcite(104). No measurements were performed on a calcite sample of source OS.

5 High resolution imaging of the (2x1) reconstructed calcite(104) surface

This chapter investigates the surface properties of calcite(104). The aim is to clarify the surface reconstruction and to solve the contradiction between row-pairing and (2×1) reconstruction.

With an algorithmic symmetry test it is shown that the calcite(104) surface has a glide plane symmetry (subchapter 5.1). Next, the contrast formation when imaging calcite(104) with CO-terminated tips is discussed (subchapter 5.2). The usage of well-defined CO tips enables to clarify distinguishing between surface properties and imaging artefacts caused by asymmetric tips. While symmetric tips reveal a (2×1) reconstructed surface with a glide plane symmetry, evidence is given in this subchapter that the row-pairing reconstruction is caused by asymmetric tips and, therefore, not an inherent surface property. The existence of a glide plane symmetry allows to drawn conclusions for the structure of the calcite(104) surface, these conclusions are explained in detail in subchapter 5.3. Last, the composition of the used calcite samples and its influence on the (104) surface is investigated with inductively coupled plasma optical emission spectrometry (ICP-OES) (subchapter 5.4).

5.1 The structure of the calcite(104) surface

In this subchapter the symmetry properties of the calcite(104) surface is investigated optically and by an algorithmic symmetry test. It is shown that this surface has a (2×1) reconstruction with a glide plane symmetry.

5.1.1 Topography NC-AFM image on calcite(104) acquired with a sharp tip

A typical AFM topography image acquired at 5 K with a sharp tip is presented in figure 27(a). The surface is imaged in the form of bright protrusions that are arranged along the $[4\,2\,\overline{1}]$ and $[0\,\overline{1}\,0]$ directions. Every second protrusion is imaged with a different height (depicted by brightness) these different heights result in a chequerboard-like pattern in the image. The bright protrusions are separated by dark lines, which run along both surface directions and which form zig-zag patterns in $[4\,2\,\overline{1}]$ direction with different amplitude and alternating small (solid green line) and pronounced (dashed green line) intermediate minima. Mostly as a consequence of the position of these minima, the bright protrusions have a slight oval shape, which also leads to the appearance of a slight zig-zag pattern of the bright protrusions along $[4\,2\,\overline{1}]$. The different heights of the bright protrusions and the difference in the dark minima along $[0\,\overline{1}\,0]$ represent the (2×1) reconstruction; one (2×1) unit cell is marked by a black rectangle in figure 27(a).

The two dark features in this image, which are marked by dark green arrows, are CO molecules that appear after dosing CO and that substitute bright protrusions. In anticipation of sub-chapter 6.1, where CO on calcite(104) is discussed, the adsorption position of CO molecules on calcite(104) is on the calcium atom sites as found by IRRAS measurements and DFT calculations [55]. Therefore, the bright protrusions imaged in this image can be assigned to the positions of the calcium atoms, and consequently the carbonate groups are located at the positions of the intermediate minima (solid and dashed green line). From this result, the rows of the calcium atoms (blue lines *A* in figure 27(a)) and of the carbonate groups (red lines *B*) along the $[4\,2\,\bar{1}]$ direction can be identified. To consider the (2×1) reconstruction, every second row is named by *A'* and *B'*.

The finding that the bright protrusions are the sites of the calcium atoms contradicts the previous assumption from Ohnesorge *et al.* [43], that the topmost oxygen atoms, which protrude from the calcite(104) surface, dominate the AFM contrast and are, therefore, visible as bright protrusions. Instead, it is in agreement with the negative-tip model proposed by Foster *et al.* [166] where the positive calcium ions are imaged bright. Foster *et al.* simulated NC-AFM images of the bulk-truncated calcite(104) surface and have found that the contrast in the images is dominated by the interaction with the Ca^{2+} ions if the tip is terminated by a negative species. Due to the electric force between the surface species and the tip, the

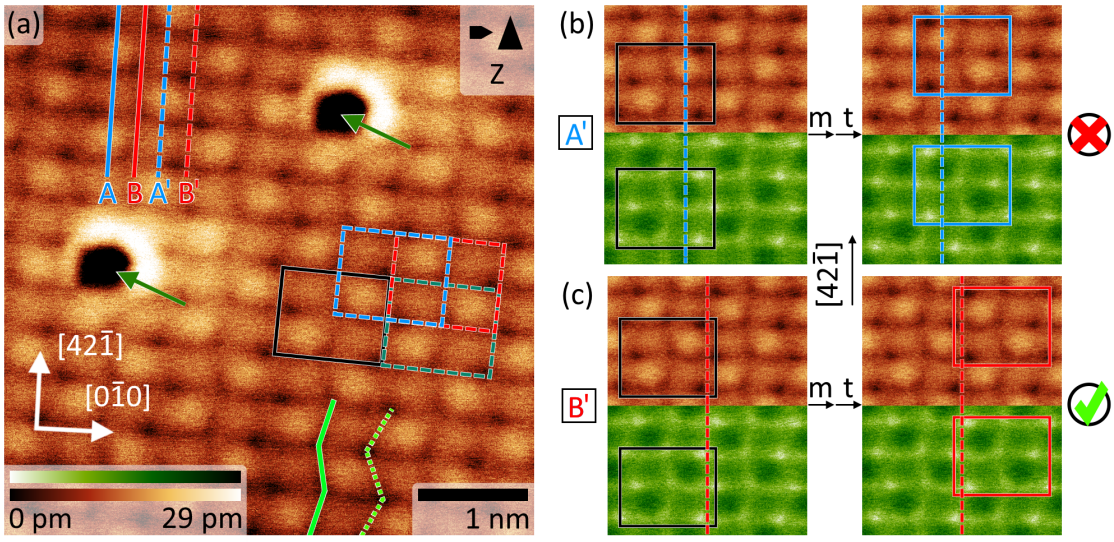

Figure 27: (a) High-resolution NC-AFM image acquired in topography mode on calcite(104) at 5 K with a sharp tip using one of the Ra crystals ($\Delta f = -1.67$ Hz and $U_{tip} = -6$ V, Calcite-006, Ra crystal). Two CO molecules (marked with dark green arrows) are identified at the bright (Ca) positions. (b, c) Simple glide plane symmetry test, applied to a single (2×1) unit cell with two possibilities of placing the axes of glide reflection. The glide plane symmetry is visually maintained for only one case. For a better visualisation, the rectangle indicating single unit cells are enlarged by 20 %. Image width is 2.5 nm in (b, c).

calcium atoms are slightly displaced out of the surface while the carbonate groups are slightly rotated and pushed into the surface in presence of a negative tip. Furthermore, when using a positive tip termination it was found that the interaction with the CO_3^{2-} group dominates at larger tip-sample distances the attractive contrast, while at shorter tip-sample distances the interaction localised at the topmost oxygen atom site. In the latter case, the oxygen atoms are visible as a zig-zag pattern in the images. Here, the electric force additionally pushes the Ca atoms into the calcite surface, while the carbonate groups are slightly rotated and strongly displaced out of the surface.

5.1.2 Simple visual symmetry test

In this section, the existence and position of the axes of glide reflection in the NC-AFM images calcite(104) surface is visually investigated. In the simple visual symmetry test, the presence of the glide plane symmetry is tested for an image data subpart covering one (2×1) unit cell. The operation of reflection (m) and translation (t) is performed with this subpart and the processed subpart is visually compared with the data at the glide plane related positions.

This procedure is applied to the topography data in figure 27(a), specifically for the unit cell marked by the black rectangle. This unit cell is chosen because neither the image edges nor the two CO molecules have a decisive influence on the symmetry test. To avoid systematic errors, which could be caused by thermal drift and imperfections of the piezo scanner, the image data are unit cell corrected with the aim to match the rectangular (2×1) unit cell with dimensions $1\,\text{nm} \times 0.81\,\text{nm}$ in the experimental data as explained in subchapter 3.6.

In the left column of figure 27(b) and (c), the image data around the black rectangle are reproduced with $[4\,2\,\bar{1}]$ pointing upwards. These data are also depicted with an inverted (green) colour map below each image to highlight the substructure of the dark depressions.

In figure 27(b), the axis *A'* is selected as axis of glide reflection. This axis runs along the rows of calcium atoms. The image subpart marked by a black rectangle is reflected and translated with respect to this axis and overlaid to the original data in the area marked by the blue rectangle in the right column. The position of this blue rectangle is also marked in figure 27(a) with a dashed blue rectangle.

The figure 27(c) is generated in analogy to figure 27(b), however, with the axis *B'* (carbonate groups) selected as symmetry axis. The processed image subpart is marked by a red rectangle in the right column of figure 27(c), and the reference subpart in figure 27(a) is marked by a dashed red rectangle.

By visual inspection it is obvious that the glide plane symmetry is violated in figure 27(b),

where the axis along the calcium atoms (*A'*) is chosen. Especially the bright protrusions do not match to the chequerboard-like pattern, and the positions of the small and pronounced intermediate minima are swapped in the area within the blue rectangle. Instead, when choosing the axis along row *B'* (carbonate groups, figure 27(c)), the processed image subpart matches to the original data very well. Thus, the glide plane symmetry is maintained. The symmetry operation is here only shown for one set of axes *A'* and *B'* as the operation delivers similar results for the respective other axes *A* and *B*. Choosing the corresponding second axis set effectively translates the glide plane processed subpart by the length of one (2×1) unit cell in $[0\,\overline{1}\,0]$ direction (see appendix figure 68).

While this analysis already points towards positioning the axes of glide refection on the rows of the carbonate groups, a more rigorous, and ideally quantitative method is required as developed in the next section.

5.1.3 Algorithmic symmetry test

The visual analysis from section 5.1.2 is now developed into an algorithmic symmetry test. The result of this test is twofold: (a) an image with the local deviation between the values at the original and glide plane equivalent positions for each axis will be calculated, and (b) a relative error that quantifies the presence of a glide plane symmetry is returned.

The algorithmic symmetry test calculates the local deviation between the image values $y(i, j)$ at all measurement positions $[i, j]$ within a single (2×1) unit cell and the values $y(i_{\mathrm{pg}}, j_{\mathrm{pg}})$ from the corresponding glide plane equivalent positions $[i_{\mathrm{pg}}, j_{\mathrm{pg}}]$ with the formula

$$\Delta_{i,j}^{\mathrm{pg}} = y(i, j) - y(i_{\mathrm{pg}}, j_{\mathrm{pg}}). \tag{11}$$

For an ideal surface with a glide plane symmetry and by using an axis of glide reflection, the values $y(i, j)$ and $y(i_{\mathrm{pg}}, j_{\mathrm{pg}})$ would be identical, and $\Delta_{i,j}^{\mathrm{pg}}$ would be zero for all image positions. The two coordinate sets $[i, j]$ and $[i_{\mathrm{pg}}, j_{\mathrm{pg}}]$ are linked by following formula 12. This formula describes a translation of the point $[i, j]$ to its mirror symmetric position related to the axis of glide reflection S by $\vec{r} = 2 \cdot \vec{d} = 2 \cdot d \cdot \frac{\vec{e}_{[0\overline{1}0]}}{|\vec{e}_{[0\overline{1}0]}|}$, and by a translation $\vec{t}$ by a half (2×1) unit cell size in $[4\,2\,\overline{1}]$ direction ($\vec{t} = \frac{\vec{e}_{[42\overline{1}]}}{2}$):

$$[i_{\mathrm{pg}}, j_{\mathrm{pg}}] = [i, j] + \vec{r} + \vec{t} = [i, j] + 2 \cdot d \cdot \frac{\vec{e}_{[0\overline{1}0]}}{|\vec{e}_{[0\overline{1}0]}|} + \frac{\vec{e}_{[42\overline{1}]}}{2} \tag{12}$$

whereby $d = \frac{|([i,j]-\vec{s}) \times \vec{e}_{[42\overline{1}]}|}{|\vec{e}_{[42\overline{1}]}|}$ defines the shortest distance from $[i, j]$ to the axis of glide reflection

(figure 28). The vector $\vec{e}_{[42\bar{1}]}$ ($\vec{e}_{[0\bar{1}0]}$) is a vector in $[4\,2\,\bar{1}]$ ($[0\,\bar{1}\,0]$)-direction with the length of one (2×1) unit cell size in $[4\,2\,\bar{1}]$ ($[0\,\bar{1}\,0]$)-direction, and $\vec{s}$ is a support vector to an arbitrary point on the axis of glide reflection S. Note that $\vec{e}_{[42\bar{1}]}$ and $\vec{e}_{[0\bar{1}0]}$ are defined in a cartesian coordinate system, while the $[4\,2\,\bar{1}]$ and $[0\,\bar{1}\,0]$ directions relate to the hexagonal crystal system [27].

$\Delta^{\mathrm{pg}}_{i,j}$ allows the calculation of the total RMS deviation $\Delta^{\mathrm{pg}} = \frac{1}{N}\sqrt{\sum_{i,j}\left(\Delta^{\mathrm{pg}}_{i,j}\right)^2}$, whereby N represents the total number of measurement points inside the (2×1) unit cell. Δ^{pg} quantifies the match between the (2×1) unit cells at the original and glide plane equivalent position.

To account for imperfections in positioning the axes of glide reflection in the experimental image, $[i_{\mathrm{pg}}, j_{\mathrm{pg}}]$ is shifted along the fast and slow scan direction inside a small square of 21×21 pixel as abstracted by the red square in figure 28. Effectively, this translates the coordinates as follows: $(i_{\mathrm{pg}}, j_{\mathrm{pg}}) \rightarrow (i_{\mathrm{pg}} + m, j_{\mathrm{pg}} + n)$.

The smallest deviation $\Delta^{\mathrm{pg}}_{\mathrm{min}} = \min_{m,n} \frac{1}{N}\sqrt{\sum_{i,j}\left(y(i,j) - y(i_{\mathrm{pg}} + m, j_{\mathrm{pg}} + n)\right)^2}$ gives the best match of the reference and glide plane equivalent unit cell data and quantify the presence of the glide plane symmetry, with the associated local deviation between the values at the original and glide plane equivalent positions: $y(i,j) - y(i_{\mathrm{pg}} + m, j_{\mathrm{pg}} + n)$.

For an ideal and noise-free image with glide plane symmetry and by correctly choosing an axis of glide reflection, the deviation $\Delta^{\mathrm{pg}}_{\mathrm{min}}$ would be zero. However, for real experimental image data, a small deviation in $\Delta^{\mathrm{pg}}_{\mathrm{min}}$ is always present due to noise in the measurement

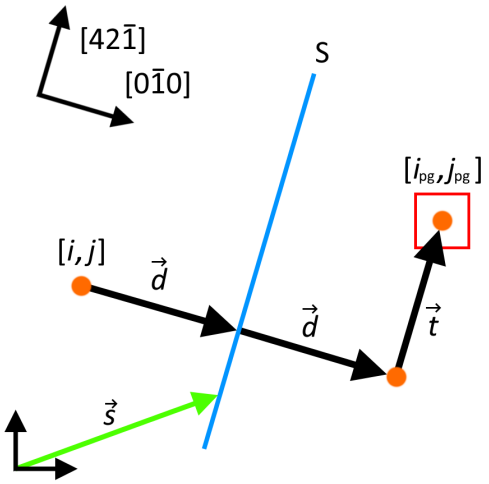

Figure 28: Abstraction of finding the glide plane equivalent position $[i_{\mathrm{pg}}, j_{\mathrm{pg}}]$ from $[i,j]$. S is the axis of glide reflection, $\vec{d}$ the shortest vector from $[i,j]$ to S. The length of d must be doubled to find the reflection of $[i,j]$. $\vec{t}$ represents the translation along the $[4\,2\,\bar{1}]$ direction.

data [75]. In an approach to determine a lower limit for the RMS deviation from the noise within the experimental data, the RMS deviation Δ^{t} is additionally calculated for the case of translating the data within one (2×1) unit cell by a multiple of the lattice vectors. The new coordinates $[i_{\mathrm{t}}, j_{\mathrm{t}}]$ after the translation are given by $[i_{\mathrm{t}}, j_{\mathrm{t}}] = [i, j] + \vec{a}$, whereby $\vec{a}$ is the integer multiple of the lattice vectors along the main surface directions ($\vec{a} = u \cdot \vec{e}_{[0\bar{1}0]} + v \cdot \vec{e}_{[42\bar{1}]}$, with $u, v \in \mathbb{Z}$). In full analogy to the formula for $\Delta^{\mathrm{pg}}_{\mathrm{min}}$, the minimum value $\Delta^{\mathrm{t}}_{\mathrm{min}} = \min_{m,n} \frac{1}{N} \sqrt{\sum_{i,j} \left(y(i,j) - y(i_{\mathrm{t}}+m, j_{\mathrm{t}}+n)\right)^2}$ is used as a lower limit for the glide plane symmetry check confidence. Again, m and n represent small shifts of the translation vector to consider imperfections of the axis positioning.

Finally, the algorithmic symmetry test calculates from $\Delta^{\mathrm{pg}}_{min}$ and $\Delta^{\mathrm{t}}_{min}$ the relative error β with the formula

$$\beta = (\Delta^{\mathrm{pg}}_{min} - \Delta^{\mathrm{t}}_{min})/\Delta^{\mathrm{t}}_{min}. \tag{13}$$

For an experimental image with glide plane symmetry and by choosing an axis of glide reflection, the deviation $\Delta^{\mathrm{pg}}_{\mathrm{min}}$ is close to zero, because $\Delta^{\mathrm{pg}}_{min}$ and $\Delta^{\mathrm{t}}_{min}$ would be very similar. Otherwise, for an experimental image without a glide plane symmetry or by choosing an axis that is not an axis of glide reflection, $\Delta^{\mathrm{pg}}_{min}$ and $\Delta^{\mathrm{t}}_{min}$ differ from each other and β would be larger than zero.

Figure 29 presents the results of the algorithmic symmetry test using the values of the unit cells marked by the rectangles in figure 27(a). The original unit cell (black rectangle) contains the values $y(i, j)$, the red and blue rectangle mark the area of the glide plane equivalent unit cell positions with the values $y(i^X_{\mathrm{pg}} + m, j^X_{\mathrm{pg}} + n)$ for using axes *A'* and *B'* (X is either *A'* or *B'*), respectively, and the green rectangle indicates the position of the translated unit cell

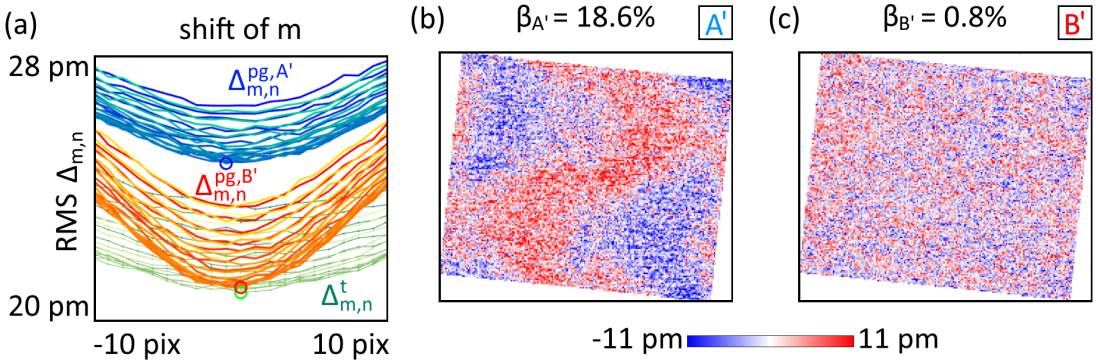

Figure 29: Results of the algorithmic symmetry test applied to the data marked by the black rectangle in figure 27(a).

position ($u = 1$ and $v = 0$) with values $y(i_\mathrm{t} + m, j_\mathrm{t} + n)$.

The resulting RMS deviations for shifts m and n of ± 10 pixel along the fast and slow scan direction are shown in figure 29(a) for three cases: (i) glide plane operation with the axis of glide reflection on row *A'* ($\Delta^{\mathrm{pg,A'}}_{m,n}$, blue curves), (ii) glide plane operation with axis on row *B'* ($\Delta^{\mathrm{pg,B'}}_{m,n}$, orange/red curves), and (iii) translation t along $[0\,\overline{1}\,0]$ by one (2×1) unit cell length ($\Delta^{\mathrm{t}}_{m,n}$, green curves). Each line of a family of curves in figure 29(a) corresponds to one shift n along the slow scan direction, while the shift m along the second direction is included as the abscissa. The minima of the three families of curves are $\Delta^{\mathrm{pg,A'}}_{\mathrm{min}}$, $\Delta^{\mathrm{pg,B'}}_{\mathrm{min}}$ and $\Delta^{\mathrm{t}}_{\mathrm{min}}$ and marked by a blue, red and green circle, respectively. The small difference between $\Delta^{\mathrm{pg,B'}}_{\mathrm{min}}$ and $\Delta^{\mathrm{t}}_{\mathrm{min}}$ indicates that the values $y(i, j)$ fit to the values at the glide plane related position $y(i^{B'}_{\mathrm{pg}} + m, j^{B'}_{\mathrm{pg}} + n)$ as good as the values $y(i, j)$ fit to the values at the translated position $y(i_\mathrm{t} + m, j_\mathrm{t} + n)$. In contrast, the larger difference between $\Delta^{\mathrm{pg,A'}}_{\mathrm{min}}$ and $\Delta^{\mathrm{t}}_{\mathrm{min}}$ indicates that the values $y(i, j)$ do not fit to the values $y(i^{A'}_{\mathrm{pg}} + m, j^{A'}_{\mathrm{pg}} + n)$ at the glide plane related positions. Hence, the axes *B'* is an axes of glide reflection.

To further substantiate the finding of an axes of glide reflection, the local deviation $\Delta^{\mathrm{pg,X}}_{i,j}$ is evaluated for each position $[i, j]$ inside the (2×1) unit cell, using the optimum shift values m, n found from the smallest deviation $\Delta^{\mathrm{pg,X}}_{\mathrm{min}}$. The results are presented in figure 29(b) and (c) for the axis *A'* and *B'* as axis of glide reflection, respectively. In figure 29(b) ($\Delta^{\mathrm{pg,A'}}_{i,j}$), areas of large deviation are seen roughly across the unit cell diagonal (red areas), in agreement with the mismatch of the chequerboard-like pattern as identified in figure 27(b), while in figure 29(c) ($\Delta^{\mathrm{pg,B'}}_{i,j}$) only uniform noise is visible in agreement with figure 27(c).

The relative errors β_X for figure 27(a) are calculated as $\beta_\mathrm{A'} = 18.6\,\%$ and $\beta_\mathrm{B'} = 0.8\,\%$ for using axis *A'* and *B'* as axes of glide reflection, respectively. These number quantify the conclusions from the visual analysis in figure 27(b) and (c): Using *A'* as the axis of glide reflection violates the glide plane symmetry, while a match of the imaged surface structure for the glide plane symmetry with selecting axis *B'* is confirmed.

In the following, the variation of β_X is analysed for different axes of glide reflection and for different (2×1) unit cells selected within figure 27 with the aim to exclude methodological artefacts of this analysis. These unit cells originate from the black cell in figure 27(a) by shift of an integer multiple of the half unit cell size in $[4\,2\,\overline{1}]$ and $[0\,\overline{1}\,0]$ direction. Care was taken to select only (2×1) unit cells where the two CO molecules and their brighter area around them do not influence the interaction data. A total of 22 cells are available as marked in figure 30. The relation between the position of a number and the position of the corresponding unit cell is included for the unit cell "22" as an example: The number denotes the lower right quadrant of a (2×1) unit cell. The algorithmic symmetry test is applied to every unit cell in the same

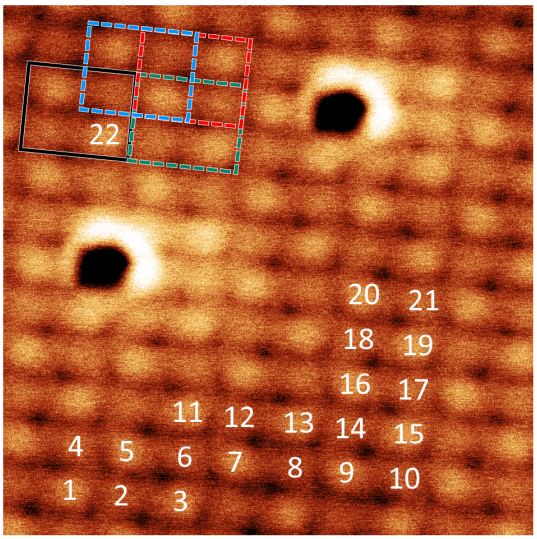

Figure 30: Same image data as shown in figure 27(a), but with positions of unit cells for the algorithmic symmetry test marked. The number indicates the lower right quadrate as shown exemplary for number 22. The results are listed in table 2

Unit cell	β (%)				Unit cell	β (%)			
number	A	A'	B	B'	number	A	A'	B	B'
1	18		-0.3		12		18.1		-0.6
2		15.3		-1.1	13	19.8		1.4	
3	16.8		-1.7		14		17.1		2.2
4	20.8		0.7		15	19		2.1	
5		17.3		-1.3	16		19.7		0.7
6	16.3		-2.5		17	17.6		0.2	
7		18.6		-0.6	18		18.6		0.8
8	18.8		4.2		19	18.9		0.2	
9		18.2		6.6	20		19.9		0.9
10	17.5		5.4		21	18.6		0.8	
11	22.3		-1.3		22	15.1		-1.1	
					Average	18 ± 2		1 ± 2	

Table 2: Results of algorithmic symmetry test applied to the unit cells marked in figure 30. The unit cell that is analysed in figure 27 corresponds to number 18.

way as explained before and the results are listed in table 2 separated for the different axes A, A', B, and B'. As is clearly visible, the algorithmic symmetry test produces similar relative error values for each pair of axes A or A' as well as B or B'. The test highlights a violation of the glide plane symmetry if the axes A or A' are selected. The average value with error from the standard deviation for these two axes is $\beta_{A,A'} = 18 \pm 2$. Instead, the relative error values β are around zero for the axes B or B', except for the unit cells 8, 9, and 10. It can only be speculated that these larger values are caused by some local defects that is hardly visible in the image. The average value for the relative error for these axes is $\beta_{B,B'} = 1 \pm 2$,

close to the ideal value zero. Therefore, it can be concluded, that the axes B and B' are the axes of glide plane symmetry.

Generally, β_{X} values that are in the range of $(0 \pm 1)\,\%$ likely indicate the presence of a glide plane symmetry with symmetry axis X. For calcite(104), this symmetry is consequently found for axes on the rows of the carbonate groups and when using sharp tips.

5.1.4 Examples for glide plane symmetry violations

This section discusses exemplary experimental results that apparently violate the glide plane symmetry as determined by the algorithmic symmetry test. Common to all results in this section is that the tips had several tip changes on the calcite surface. Hence, it can safely be assumed, that these tips are asymmetric and of unknown termination.

The NC-AFM image reproduced in figure 31(a) includes two bright features that are pairwise linked along the $[4\,2\,\overline{1}]$ direction within the unit cell. This pattern is typical for the row-pairing reconstruction [29, 31, 40, 41, 42, 43, 44, 64] and, consequently, these data deliver an example for this apparent surface reconstruction. The results for the local deviation of this image, which is generated by the algorithmic symmetry test applied to the marked unit cell, are presented in figure 31(b) and (c). Areas of larger deviation are clearly visible at the positions of the bright row-pairing features for all positions of the axes of glide reflection. Therefore, the symmetry test returns a violation of the glide plane symmetry with large relative errors of $\beta_{\mathrm{S}_1} = 26.2\,\%$ and $\beta_{\mathrm{S}_2} = 14.7\,\%$.

The strength of the algorithmic symmetry test to avoid a subjective assessment is shown with the example in figure 31(d). Although the tip, which has an unknown termination, delivers an exceedingly sharp contrast and the bright features appear to be glide plane related when positioning the axes of glide reflection on the bright rows (S_2, $\mathrm{S}_2^{'}$), the algorithmic symmetry test reveals that the glide plane symmetry is not maintained in these image data.

In particular, when performing the algorithmic symmetry test for the unit cell data marked in figure 31(d) by a black rectangle, the images of the local deviation (figure 31(e) and (f)) do present features at several positions. The presence of these features indicate a violation of the glide plane symmetry, in agreement with the large relative errors ($\beta_{\mathrm{S}_1} = 239.3\,\%$ and $\beta_{\mathrm{S}_2} = 30.0\,\%$).

In conclusion, in this subchapter it is shown that the calcite(104) surface shows a (2×1) reconstruction with a glide plane symmetry when sharp tips are used. The axes of this symmetry are on the carbonate groups in $[4\,2\,\overline{1}]$ direction (axes B and B').

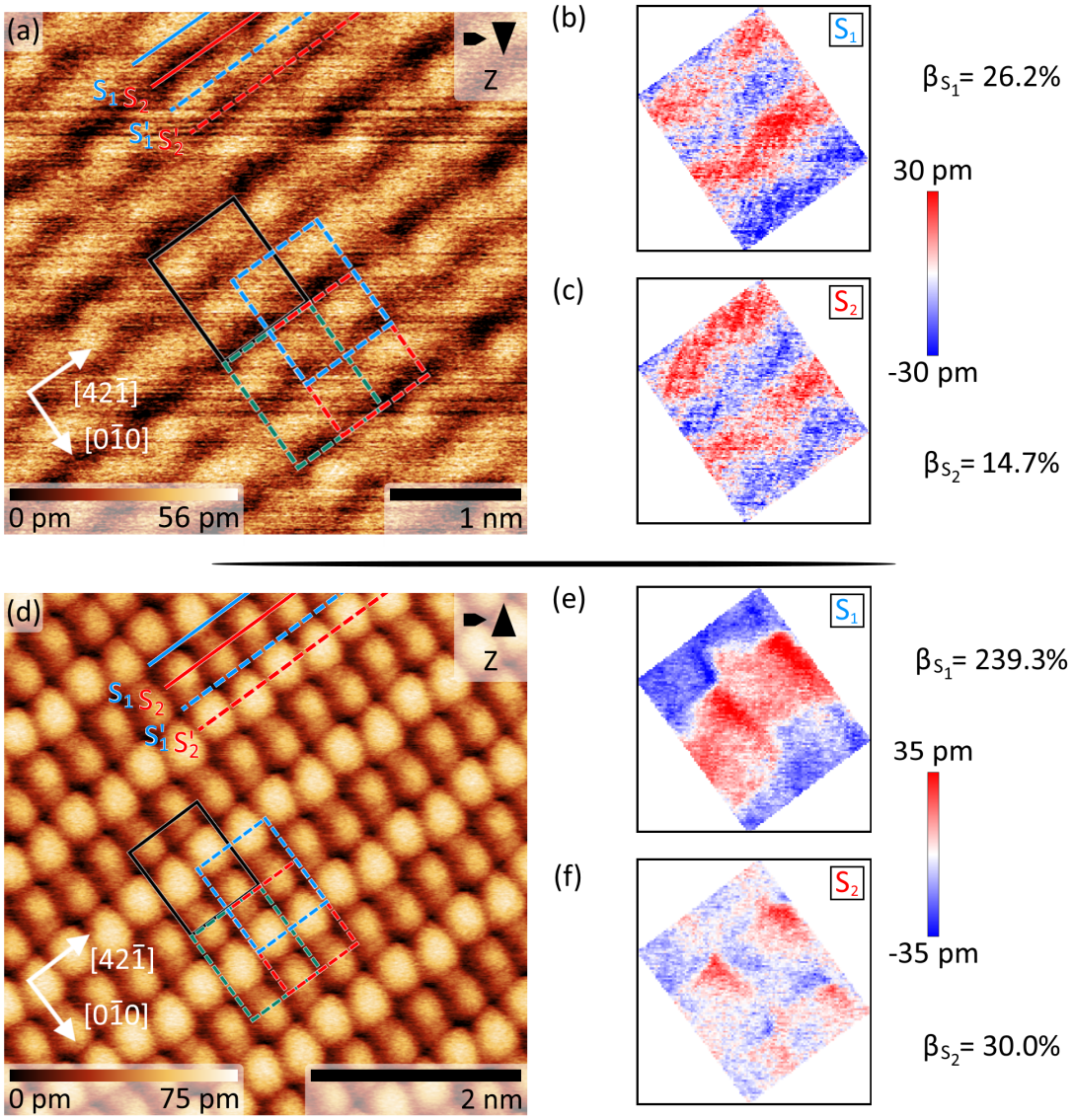

Figure 31: Examples of NC-AFM images acquired in topography mode on calcite(104) at 5 K with unknown tip terminations. (a) Typical example for the row-pairing reconstruction (Ra crystal, $\Delta f = -2.8$ Hz and $U_{tip} = 0$ V, (Calcite-003, Ra crystal). (b) and (c) local deviation from the symmetry test with axes of glide reflection S_1 and S_2 positioned on bright and dark rows, respectively. Reference (2×1) unit cell and boundaries of symmetry-tested positions marked with solid and dashed rectangles in (a). (d) High-resolution image achieved with an unknown tip (Calcite-003, Ra crystal, $\Delta f = -3.3$ Hz and $U_{tip} = -1$ V). (e) and (f) local deviation from the symmetry test with axes of glide reflection S_1 and S_2 positioned on dark and bright rows, respectively. Reference (2 × 1) unit cell and boundaries of symmetry-tested positions marked with solid and dashed rectangles in (d).

5.2 Contrast formation of the calcite(104) surface with CO-terminated tips

It is generally known that the shape of the microscopic tip apex strongly influences the contrast formation in NC-AFM [167, 168, 169]. In previous publications, a large number

of different contrast modes have been reported when imaging calcite(104) [29, 44]. Some examples for different contrast modes observed at 5 K are already presented in subchapter 5.1.

Thus, for a reproducible contrast and a reliable data interpretation, a tip with a well defined microscopic tip apex is required. One possibility is to terminate the tip with a CO molecule at low temperatures, building upon established preparation protocols [116, 170]. On the one hand, the CO molecule reduces the influence of the mesoscopic tip apex on the image by increasing the distance between sample surface and tip apex, thus providing a sharp tip termination. On the other hand, the contrast formation mechanisms are now well understood and can, in particular, be used to simulate NC-AFM images [116].

CO-terminated tips can provide resolution of individual atoms, when short range forces between CO tip and surface species are present [50, 116, 171, 172]. In particular, the localised interaction has been harvested to yield submolecular resolution of molecular systems by resolving chemical bonds between atoms as sharp lines in NC-AFM images. The resulting images firsthand remind of the appearance of the ball-and-stick models in chemistry [50, 170, 173, 174, 175]. This intermolecular contrast is especially enhanced by a deflection of the tip-CO from strongly repulsive positions that originate from the Pauli repulsion between the CO of the tip and a sample atom.

It is now understood that the appearance of bond-like features in NC-AFM images acquired with a CO-terminated tip does not necessarily identify a chemical bond, as a sharp bond-like line can also be visible between atoms that are not bonded but close together [176, 177]. In this case, the CO of the tip tilts away from the centre line as it is not able to enter the region between the atoms. As a result, the repulsive forces cause a sharp line in the NC-AFM images. Examples for such sharp lines are given in subchapter 6.4.

In the following, NC-AFM images of the calcite(104) surface acquired with CO-terminated tips are discussed. At first, the contrast formation of the pristine calcite(104) surface measured with CO-terminated tips is examined in detail (section 5.2.1). Then, it is shown in section 5.2.2 that the presented surfaces express glide plane symmetry in the (2×1) unit cell. Next, it is presented how CO tips were characterised by inverse imaging (section 5.2.3), and how the structure of such a CO tip influences the contrast formation of CO molecules on Ag(111) and of calcite(104) (section 5.2.4).

5.2.1 Contrast in NC-AFM images of calcite(104) acquired with CO-terminated tips

This section, extends the previous analysis from topography data to constant-height frequency-shift images acquired with CO-terminated tips at 5 K. CO molecules adsorbed

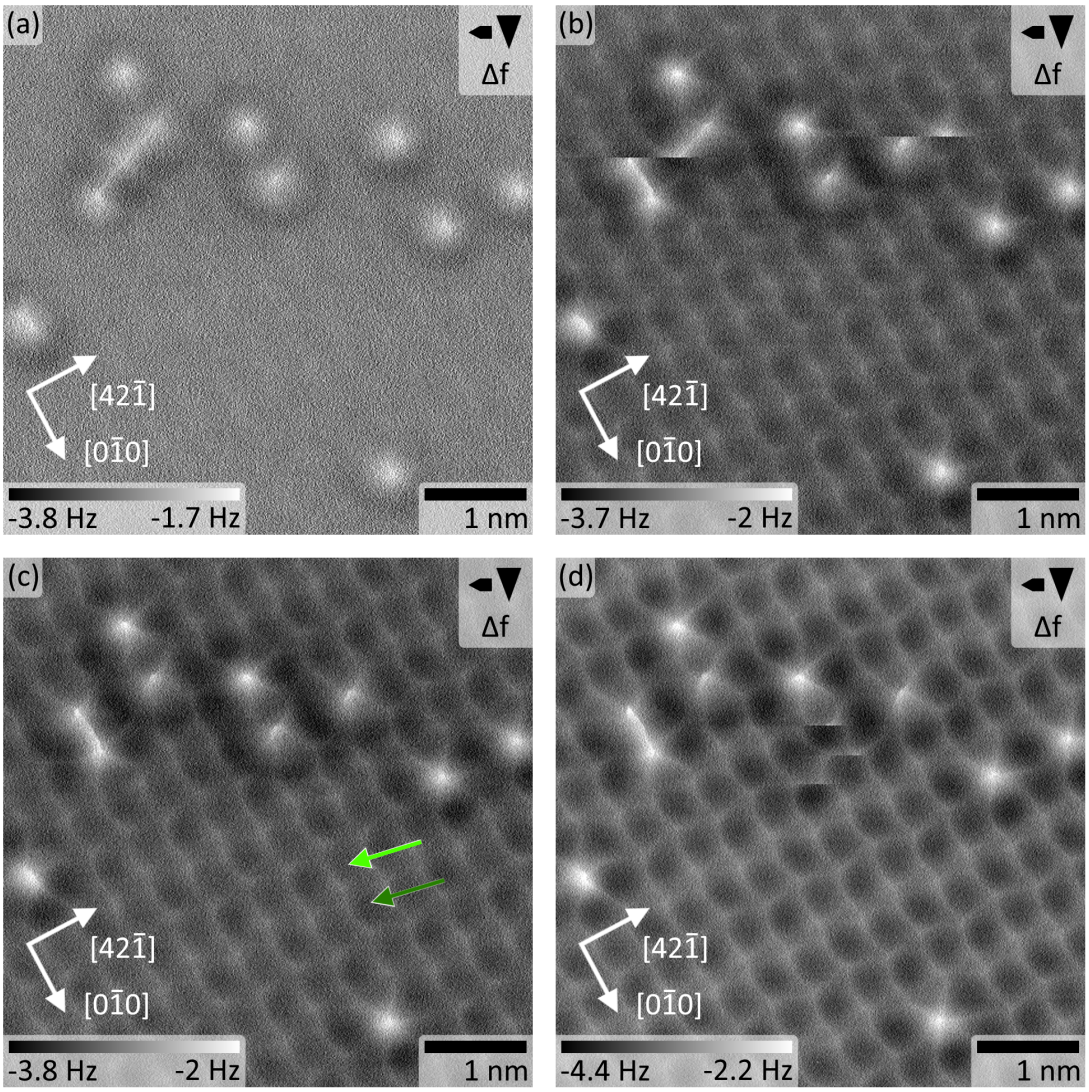

Figure 32: NC-AFM constant-height frequency-shift images acquired at different tip-sample distances (Calcite-012, Ku crystal, $U_{tip} = -10\,\mathrm{V}$).

on the calcite surface are again used as markers to determine the positions of the surface species. Imaging in topography mode was not successful at small tip-sample distances because strong repulsive interactions at the centre of the surface bound CO molecules prevented stable imaging (see subchapter 6.2).

A series of four images acquired at decreasing tip-sample distances is presented in figure 32. At larger tip-sample distance (figure 32(a)), the areas of the bare calcite surface is barely visible as blurry stripes in $[0\,\bar{1}\,0]$ direction. At smaller distances (figure 32(b) and (c)), the structure of the calcite lattice becomes apparent in the form of blurry bright lines that also run along the $[4\,2\,\bar{1}]$ direction. Additionally, differences in the dark pores recognizable as chequerboard-like pattern are visible in figure 32(c). One dark and one bright pore are

marked by a dark and a light green arrow, respectively. At the shortest tip-sample distance (figure 32(d)), the bright lines of the calcite lattice become sharper.

The CO molecules are imaged as round features with an attractive (dark) halo and a repulsive (bright) centre at larger tip-sample distances (figure 32(a)), while at smaller distances (figure 32(b)-(d)), the bright centres of the CO molecules evolve into a star-shaped appearance, and the dark halos almost disappear. The CO molecules are roughly centred in the dark pores, which can be assigned to the position of the calcium atoms [55]. Consequently, the positions of the carbonate groups are at the intersections of the bright lines of the calcite lattice.

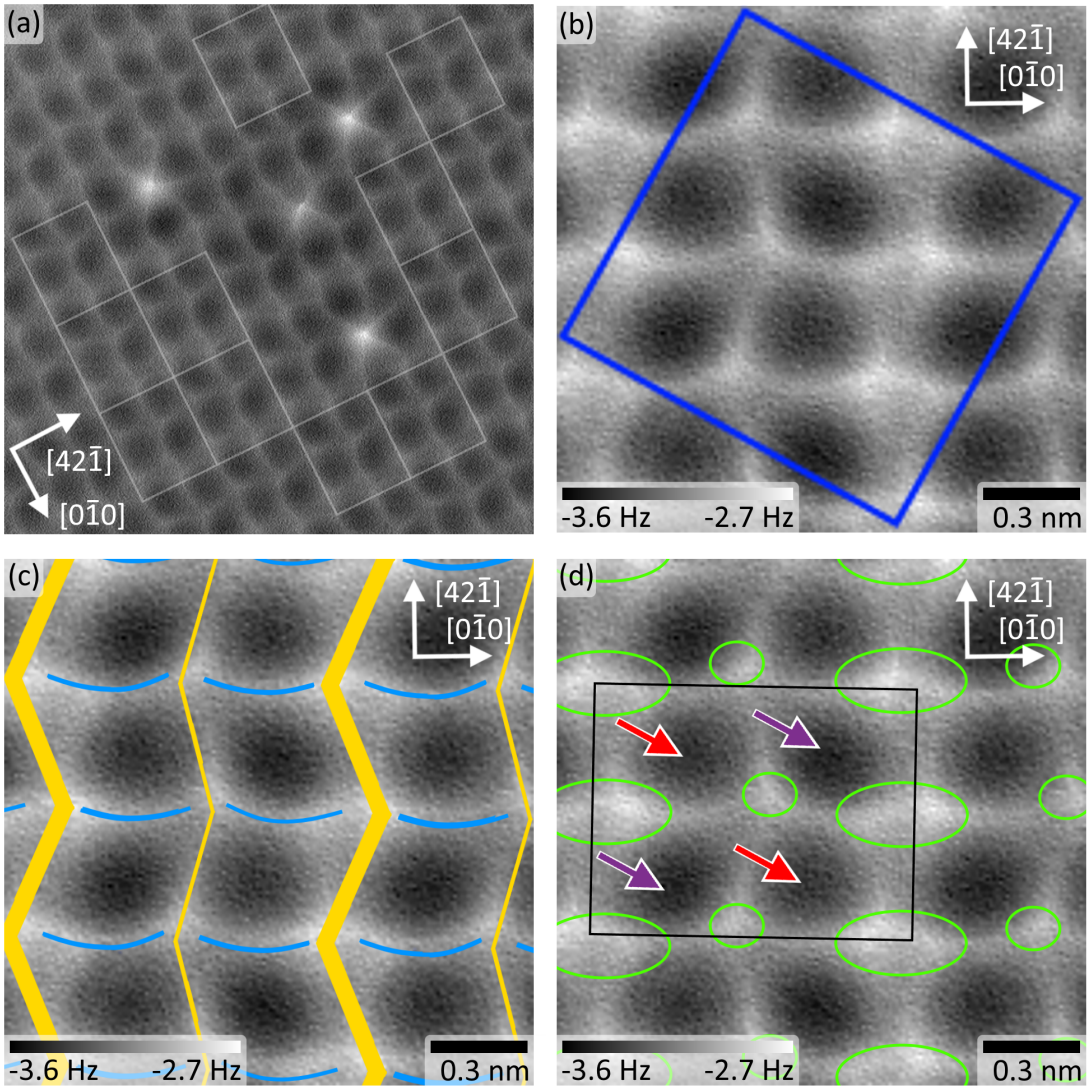

Figure 33: (a) Same image data as in figure 35(a) (Calcite-012, Ku crystal, $U_{tip} = -10\,\mathrm{V}$). The highlighted eleven (2×1) unit cells are averaged and the result is reproduced in (b). The images in (c) and (d) show the same data as in (b) but with markers for different features specific to the calcite(104) surface. The black rectangle in (d) indicates a (2×1) unit cell.

Next, the appearance of the calcite(104) surface is further investigated using figure 33(a) and figure 34(a). Figure 33(a) is acquired with the same tip as figure 32 at a different sample position but nomilally at the same height as figure 32(d), while for figure 34(a) another CO terminated tip is used.

In order to improve the signal-to-noise ratio, a total of eleven unit cells as highlighted in figure 33(a), are averaged. To obtain these unit cell averaged data, the raw data of figure 33(a) are first unit cell corrected (see subchapter 3.6) so that the unit cell dimensions are exactly $0.5\,\mathrm{nm} \times 0.81\,\mathrm{nm}$ [141]. In the next step the periodicity of the image data were used to separate the image into single unit cells. Care was taken to select only unit cells that do not contain any CO molecules or the CO-surrounding dark halo. The result of the averaging is presented in figure 33(b). The image data inside the dark blue rectangle are the result of the averaging. The data outside the rectangle are the image data from inside the rectangle periodically continued.

The improved signal-to-noise ratio in figure 33(b) allows the identification of a number of features specific to the calcite(104) surface:

(i) The calcite appearance is a lattice formed by bright, slightly buckled lines running in $[4\,2\,\overline{1}]$ and $[0\,\overline{1}\,0]$ direction as indicated by blue and yellow lines in figure 33(c). The lines running along the $[4\,2\,\overline{1}]$ direction have a different width, every second line along $[0\,\overline{1}\,0]$ appears wider as abstracted by the width of the yellow lines. This is a direct indication for the (2×1) reconstruction.

(ii) The vertical lines along the $[4\,2\,\overline{1}]$ direction show a zig-zag pattern, whereby the amplitude of the wider lines are larger as marked in figure 33(c) by the zig-zag lines.

(iii) The horizontal lines along $[0\,\overline{1}\,0]$ are slightly bent in $[\overline{4}\,\overline{2}\,1]$ direction, in consequence they appear arcuated (blue curved lines in figure 33(c)).

(iv) The vertical lines along $[4\,2\,\overline{1}]$ do not represent an uniform interaction strength as they are brighter at the intersection of vertical and horizontal lines. The brighter areas are marked by green ovals in figure 33(d).

(v) Diagonally adjacent dark pores have a similar appearance producing a chequerboard-like pattern. The red arrows in figure 33(d) point to pores brighter than the pores marked by violet arrows.

(vi) The (2×1) unit cell has a glide plane symmetry with axes of glide reflection positioned on the bright lines in $[\overline{4}\,\overline{2}\,1]$ direction. This will be analysed in section 5.2.2.

Figure 34 shows an image of calcite(104) acquired with a different tip as for figure 34. In full analogy to figure 33, the 17 unit cells marked in figure 34(a) are averaged and the result is presented in figure 34(b). The imaged calcite lattice in this image expresses few subtle differences to the lattice in figure 33(b). Similar to the lattice of figure 33(c), the lattice in figure 34(c) is also formed by bright lines running in $[4\,2\,\bar{1}]$ and $[0\,\bar{1}\,0]$ direction (blue and yellow lines), and the (2×1) reconstruction is visible in the different width of the lines running along the $[4\,2\,\bar{1}]$ direction. Furthermore, the bright lines are brighter at the intersection of

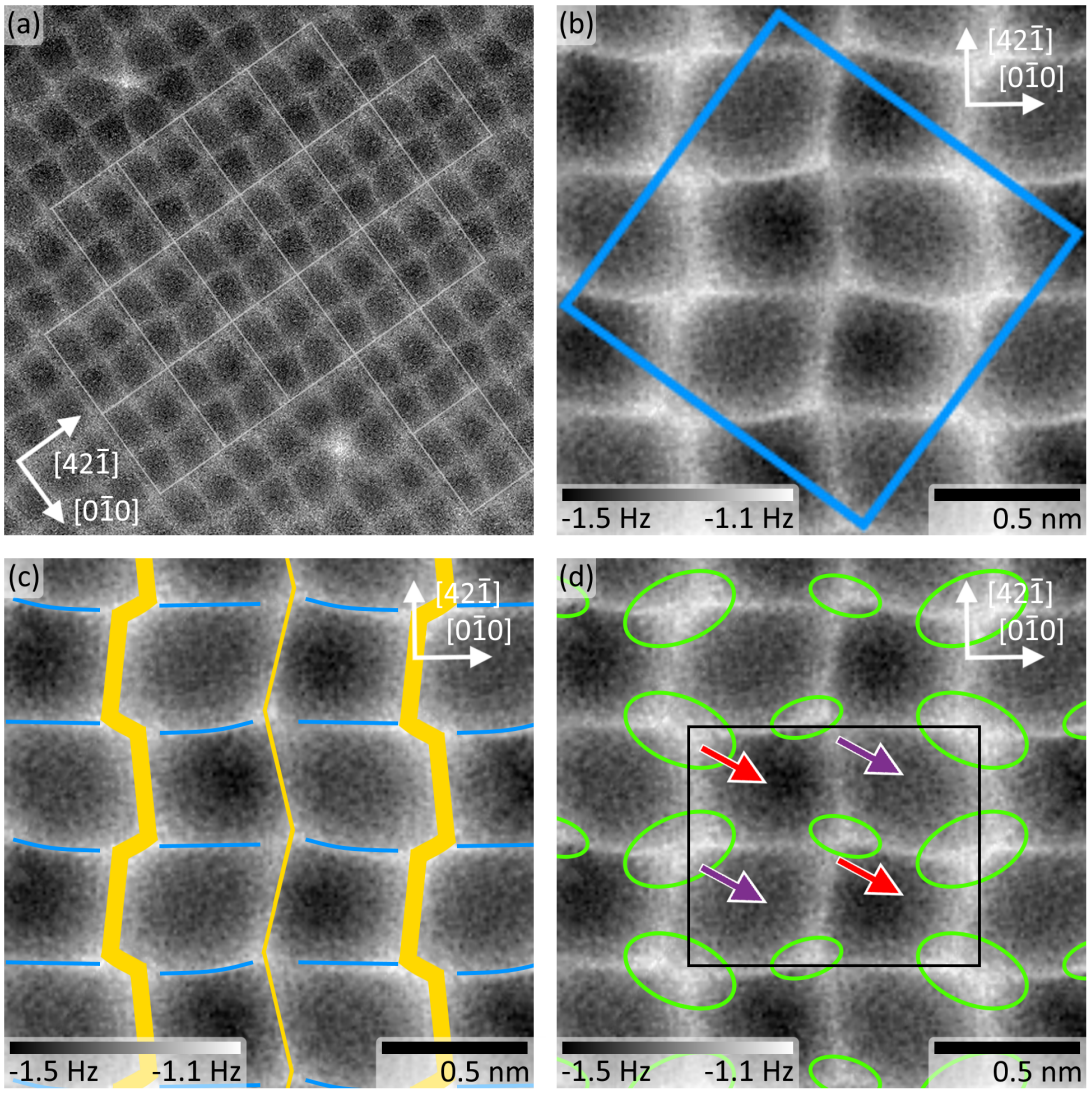

Figure 34: (a) Same image data as in figure 36(a) (Calcite-009, Ra crystal, $U_{tip} = 3\,\mathrm{V}$). The highlighted 17 (2×1) unit cells are averaged and the result is reproduced in (b). The image data inside the dark blue rectangle is the result of the averaging, while the data outside the rectangle are the image data from inside the rectangle periodically continued. (c) and (d) show the same data as in (b) but with markers for different features specific to the calcite(104) surface. The black rectangle in (d) indicate a (2×1) unit cell.

vertical and horizontal lines (figure 33(d), and figure 34(d)), and both images have a glide plane symmetry within the (2×1) unit cell as shown for figure 34(a) in figure 36. A slight difference to figure 33(c) is that the zig-zag pattern of the wider lines shows a more angular shape (figure 34(c)) and the horizontal lines along $[0\,\overline{1}\,0]$ are sharper and only slightly bent in $[\overline{4}\,\overline{2}\,1]$ direction. In particular, only every second horizontal line seems to be arcuated as marked in figure 34(c).

A more significant difference is visible at the positions of the dark pores in figures 33(d) and 34(d). One (2×1) unit cell is indicated by a black rectangle in both images. These cells are on equivalent lattice position as visible in the zig-zag pattern of the bright lines and the wider lines. The diagonal adjacent dark pores in both unit cells have a similar brightness. The lower left and upper right pore (violet arrows) in figure 34(d) are clearly brighter than the other two (red arrows). In contrast, in figure 33(d) the upper left and lower right pore are brighter than the other ones (violet arrows). Thus, the darker pores are located at different sites within the (2×1) unit cell.

A possible explanation for this brightness inversion of the dark pores in figure 34(d) could be caused by a different tip-sample distance. The bright lines that are marked in figure 33(c) are slightly blurrier than the lines in figure 34(c). Under the assumption that closer tip-sample distances result in sharper features in NC-AFM images it can be concluded that the tip-sample distance is smaller in figure 34 than in figure 33.

5.2.2 Algorithmic symmetry test applied to constant-height data

In this section it is demonstrated that the constant-height frequency-shift images in figures 33(a) and 34(a) express a glide plane symmetry. For this purpose, the symmetry test is applied to both images to the unit cell marked by the black rectangle by using the axes *A'* and *B'*. The glide plane symmetry is violated for both images when using *A'* (calcium atoms) as axes of glide reflection as shown in figure 35(b) ($\beta_{\mathrm{A'}} = 9.4\,\%$) and 36(b) ($\beta_{\mathrm{A'}} = 11.5\,\%$). This is also visible in the local deviation images that show larger areas of deviation. Instead, a match is found for both images by using axes *B'* (carbonate groups), see Figure 35(c), with $\beta_{\mathrm{B'}} = -0.6\,\%$, and 36(b), with $\beta_{\mathrm{B'}} = 0.5\,\%$. Only noise is visible in the associated images of local deviation. Therefore, it can be concluded for both images that the calcite(104) surface express a glide plane symmetry with axes of glide reflection running in $[0\,\overline{1}\,0]$ direction and located on the carbonate groups. This is in agreement with the result of the topography data (figure 27).

Thus, the glide plane symmetry and a (2×1) reconstructed surface are consistently found when using well-defined tips for imaging. The CO tip quality will be further investigated in the next section.

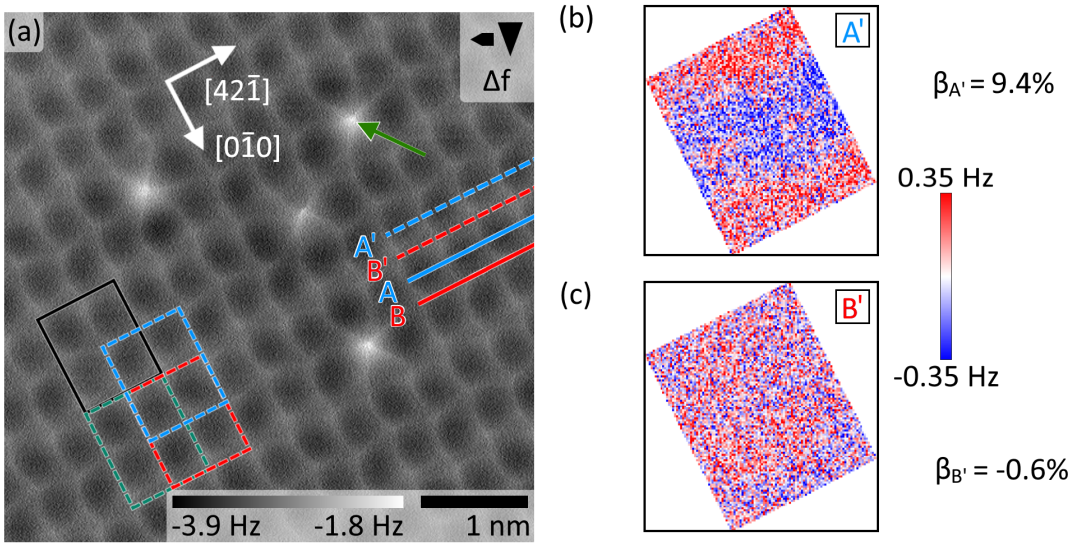

Figure 35: (a) Constant-height frequency-shift NC-AFM image acquired with a CO-functionalised tip (Calcite-012, Ku crystal, $U_{tip} = -10\,\mathrm{V}$). Several CO molecules (one is marked by a dark green arrow) are apparent as bright protrusions and replace a dark feature (Ca position). (b, c) glide plane symmetry test applied to the single (2×1) unit cell marked in (a) by a black rectangle.

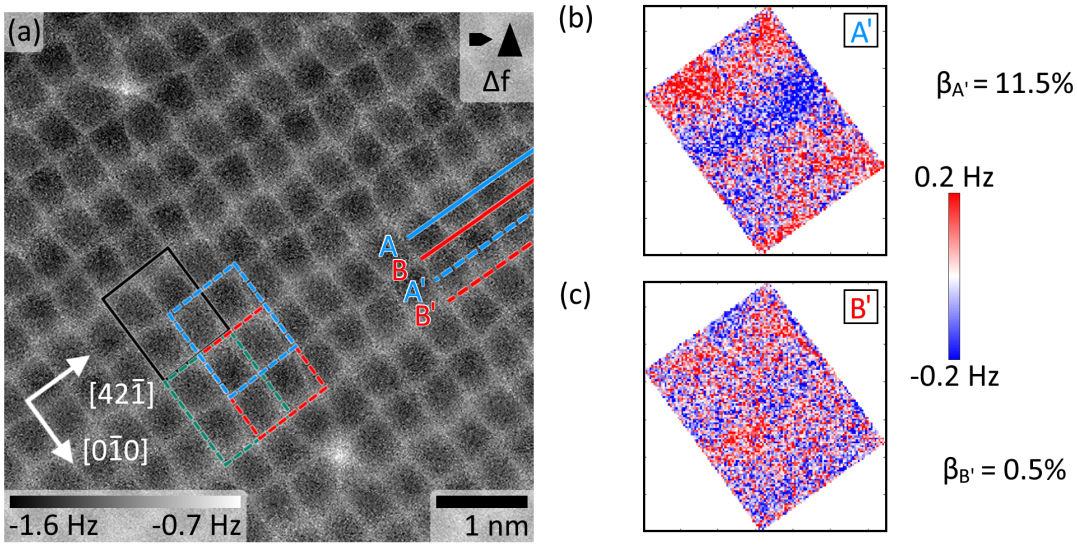

Figure 36: (a) Same image data in figure 34(a) (Calcite-009, Ra crystal, $U_{tip} = 3\,\mathrm{V}$). (b, c) Symmetry test applied to the single (2×1) unit cell marked in (a) by a black rectangle.

5.2.3 Characterisation of CO-terminated tips used for the acquisition of the NC-AFM images on calcite(104)

To ensure that the CO molecule of a CO-terminated tip is adsorbed perpendicular to the sample surface (rotational symmetric), the CO tip is characterised by inverse imaging using a single CO molecule on Ag(111) before and after the measurements on calcite. The idea

of inverse imaging is to image the microscopic tip apex by a sharp and well-defined feature on a surface [111, 167, 178]. In the measurements of this thesis a dynamic STM image of a CO molecule adsorbed on Ag(111) is acquired with a CO-terminated tip. The surface CO is adsorbed in a perpendicular geometry on the metal surface and, therefore, provide a well-defined feature with a sharp geometry that allows to characterise the tip-adsorbed CO [179, 180, 181, 182]. The appearance of the CO molecule in the image allows conclusions about the geometry of the microscopic tip apex [134, 183, 184].

Due to a lack of determining the exact geometry of the metal tip apex, the tip-CO can be adsorbed in rather different orientations at the tip. Therefore, CO inverse imaging fulfils two aims: First, imaging the tip before the calcite experiments allows to determine the quality of the tip and possibly to perform further tip optimisations (see subchapter 3.3). Second, inverse imaging after experiments on calcite enables to identify an unmodified tip. If the inverse images taken before and after the measurements on calcite are similar, it can be assumed that the CO tip did not change measurable during the measurement on calcite.

An example of this procedure is presented in figure 37. After pick-up of a CO molecule from

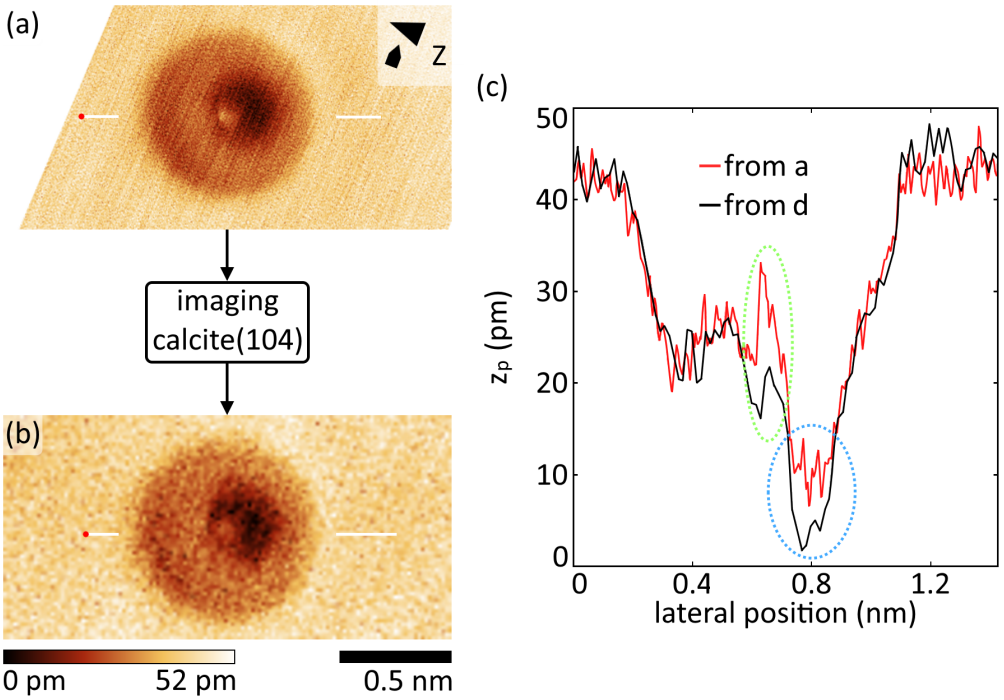

Figure 37: Inverse imaging of CO/Ag(111) before (a) ($U_{tip} = 5\,\mathrm{mV}$, $I_t = 5\,\mathrm{pA}$, and scan speed $v_s = 4.92\,\mathrm{nm\,s^{-1}}$) and after (b) ($U_{tip} = 5\,\mathrm{mV}$, $I_t = 5\,\mathrm{pA}$, and $v_s = 15.26\,\mathrm{nm\,s^{-1}}$) experiments on calcite(104). (c) Line profiles extracted at the position marked with white lines in (a) and (b), starting points are marked by a red dot. Due to visual reasons the white lines only indicate the start and the end of the line profiles. The black arrows show the chronological order of the images.

Ag(111) according to the protocol presented in subchapter 3.3, another surface-bound CO molecule is imaged in STM mode (figure 37(a)). This STM image allows for a characterisation of the CO tip. An explanation of the CO shape visible in this image is given in the next section 5.2.4. After the tip characterisation on the silver sample, the tip is moved on the adjacent calcite(104) surface for measurements on this surface. Two examples of calcite images acquired with the tip characterised in figure 37(a) are figure 32 and 33. During the measurements on calcite, no tip changes were noticed. This is further confirmed by the inverse imaging on the silver sample acquired after the measurements on calcite (figure 37(b)). The shapes of the CO molecules in the two inverse images agree exceedingly well with each other. The difference in the image quality is instead caused by a different scan speed. In particular, the line profiles in figure 37(c) extracted from figure 37(a) and (b) at indicated positions, show a good correspondence to each other. Two deviations are observed: The repulsive centre is of weaker strength (green dashed oval) and the dark area at the right is less pronounced (blue oval). Both effects are explained by a larger scan speed figure 37(b) that decreases the resolution of the CO molecule in the image. Hence, it can be concluded that the measurements on calcite(104) were acquired with a CO-terminated tip that did not modify during the measurements on calcite.

In other experiments, the tip-CO is often lost due to strong tip-sample interaction when imaging calcite. Although inverse imaging after the calcite measurement could not be acquired in these cases, it is still concluded that images with a similar appearance as in figure 32 and 33, have been acquired with a CO-terminated tip.

5.2.4 Relationship between inverse CO images and contrast formation on calcite(104)

In this section, relations between the properties of CO tips as determined by inverse imaging and the NC-AFM images of the calcite(104) surface including CO/calcite(104) are discussed. In particular, the appearance of CO molecules in the inverse images, which were acquired before the measurements on calcite, are correlated with the appearance of CO molecules on Cu(111) measured in the literature [134, 184, 185, 186]. Then, the properties of these tips are used to discuss the NC-AFM contrast of the calcite surface or CO/calcite(104). The literature about contrast formation of CO molecules adsorbed on Cu(111) and imaged with CO-terminated tips in dynamic STM mode is summarised in the following.

Literature review: Contrast formation of CO/Cu(111) imaged with different CO-terminated tips

Gustafsson *et al.* [134] have discussed the contrast formation of CO molecules adsorbed on Cu(111) imaged with CO-terminated tips in constant-height dynamic STM mode at three different tip-sample distances, namely 0 pm, −100 pm, and −200 pm. Initial (at tip-sample distances where no interaction between tip and surface occur), the surface CO as well as the tip-CO are orientated parallel to the surface normal vector of the sample surface.

If the tip-sample distance is reduced both CO molecules start to interact with each other. At a relatively large tip-sample distance (here named 0 pm) Gustafsson *et al.* have been found that the surface CO is apparent in the constant-height STM image as a circular dark feature with a slightly brighter halo while in the centre of this feature is a slightly bright spot. In the frequency-shift image the surface CO molecule is visible as a dark depression.

According to Gustafsson *et al.*, the circular dark feature is caused by a decrease of the tunnelling-current at the surface CO position [134, 185]. Furthermore, at this tip-sample distance, the tip- and surface-bound CO molecule attract each other as visible in the dark depression in the frequency-shift image. Due to this attractive interaction, both the surface and the tip-CO tilt toward each other. If the molecules are directly above each other both CO molecules are parallel aligned to each other [134, 185]. This parallel alignment causes an increased overlap of the p states of the two CO molecules and, therefore, an increased conductivity for the linearly arranged CO molecules. This increased conductivity is visible in the constant-height STM images in the slightly bright spot at the centre of the dark feature.

If the tip-sample distance is reduced to −100 pm, Gustafsson *et al.* have found that within the dark depression in the frequency-shift images a bright centre occur while the inside of the circular dark feature with the slightly brighter halo in the constant-height STM image becomes asymmetric, and a sharp and bright protrusion appear in the centre of this feature. The bright centre is explained by a repulsive interaction of the CO molecules at this tip-sample distance [134, 186]. Geometrically, this repulsive interaction causes a tilt of both CO molecules away from each other. Due to this orientation, the direct tunnelling from the tip-CO into the metal surface is enhanced and causes the sharp and bright protrusion in the constant-height STM image [134]. The slightly asymmetry in the dark feature with the slightly brighter halo is explained by changes of the overlap of the s and p states of the two CO molecules due to the bending of the CO molecules [134, 183, 186].

If the tip-sample distance is further reduced to −200 pm Gustafsson *et al.* have found that in the frequency-shift images the bright repulsive centre becomes a small sharp peak, and the inside of the dark feature in the constant-height STM image is further deformed while the

sharp and bride protrusion disappears. This observation is explained by a stronger repulsive interaction of the CO molecules that causes the sharp peak in the frequency-shift. This stronger repulsion causes an increased tilt of both the surface and the tip-CO. Due to this tilt the overlap of the s and p states of the two CO molecules is further changed causing a further deformation of the inside of the dark feature in the constant-height STM image and a disappearing bride protrusion.

Up to now CO molecules were considered that have an initial orientation parallel to the surface normal vector. Now, a tip-CO molecule is considered that has an initial tilt with respect to the surface normal vector of the sample surface. Such tips are discussed by Néel *et al.* [184]. They observed, that even at larger tip-sample distances the dark feature in the STM images is not circular and imaged asymmetric. Especially the bright and sharp protrusion appears further away from the centre of the dark feature if the CO molecule is tilted further [184].

In the following, three tips are presented with inverse images of the CO molecules on Ag(111) in dynamic STM mode, presenting different contrast pattern. It will be concluded that these three tips represent: (a) a CO tip with a rotational symmetric tip apex, (b) a CO tip with a sharp apex and a small tip-sample distance, and (c) a CO tip with an initial tilt angle.

In the measurements of this thesis the inverse images are acquired in constant-current mode. It is assumed in the following that the inverse images acquired in constant-current STM mode have a similar appearance than the constant-height STM images. The explanation is as follows: Bright areas in constant-height STM images indicate a higher tunnelling-current. In topography mode, the distance controller would increase the tip-sample distance at this position to maintain the tunnelling-current set point. Hence, also in topography mode, this area would be imaged brighter.

(a) CO tip with a rotational symmetrical tip apex

Image data acquired with the first tip on CO/Ag(111) (dynamic STM mode) and CO/calcite(104) are shown in figure 38(a) and (d), respectively. The CO molecule on Ag(111) is imaged as a circular dark feature with surrounding bright halo (figure 38(a)). Line scans extracted at the positions of the light and dark blue and green lines with the beginning always in the centre of the feature (red dot) and reproduced in figure 38(c). The four directions are chosen such that they are parallel to the $[4\,2\,\overline{1}]$ and $[0\,\overline{1}\,0]$ directions of the nearby calcite(104) surface. These line profiles are nearly identical, thus indicating a rotational symmetry in the imaging. At the origin of the abscissa, all line profiles express a small maximum (marked with a red dashed oval). The corresponding frequency-shift image to figure 38(a) is reproduced in (b). In this image the CO molecule is imaged as circular dark depression (red dashed circle)

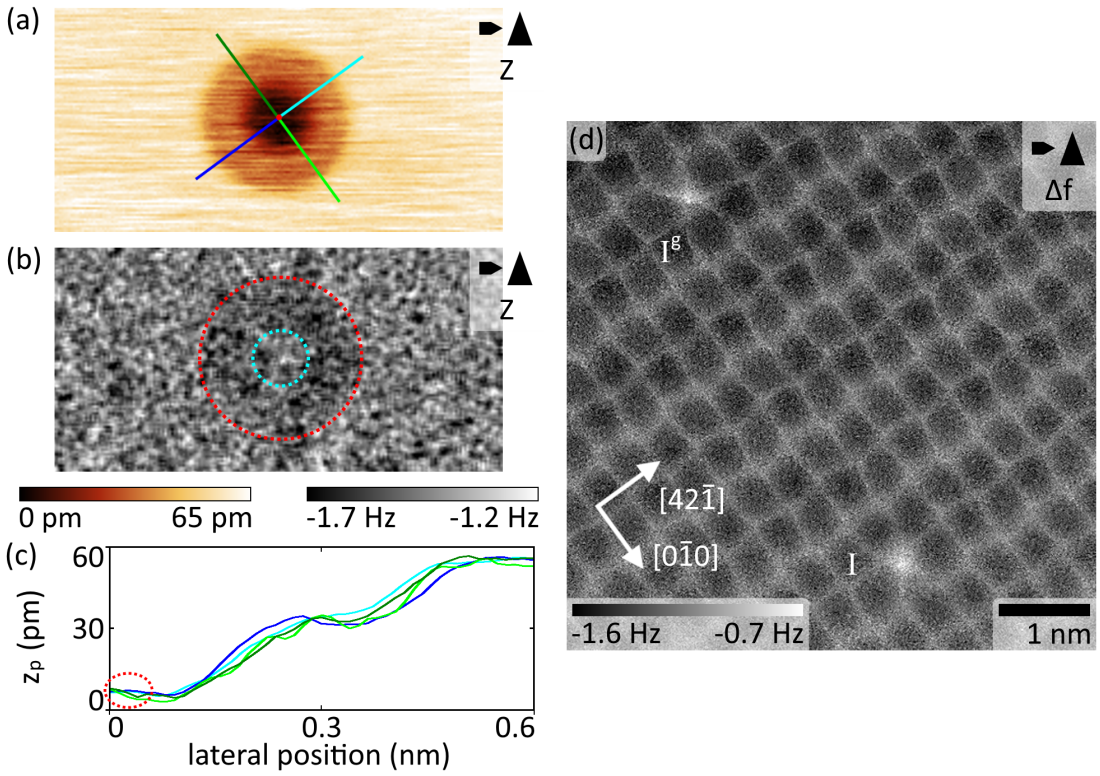

Figure 38: Characterisation of a symmetric CO tip with inverse imaging at larger tip-sample distance. (a) Inverse image of CO/Ag(111) before the experiments on calcite(104) measured with $U_{tip} = 5\,\text{mV}$ and $I_t = 5\,\text{pA}$. (b) Corresponding frequency-shift image to (a). The red and light blue circle are concentric. The image pixels are smoothed over an radius of 3 pixels with the Gwyddion filter "Basic filters: mean, median, denoise, ..." [140]. (c) Line scans extracted at the positions marked in (a). (d) unit cell corrected NC-AFM constant-height frequency-shift image of the calcite(104) surface with two CO molecules, same image data as in figure 34 and 36(a) measured with $U_{tip} = 3\,\text{V}$ (Calcite-009, Ra crystal). The names I and II of the CO molecules are explained in subchapter 6.2. The STM and NC-AFM images were measured under different scan angles, therefore, the STM images were rotated to provide a consistent orientation.

with a slightly brighter centre (light blue circle).

As mentioned in the literature review, a surface-adsorbed CO molecule imaged with CO tip at larger tip-sample distances (here 0 pm) is apparent as a circular dark feature with slightly brighter halo and a slightly bright spot in the centre. This description is in excellent agreement with the inverse image in figure 38(a): The circular dark feature with the slightly brighter halo is present and the small maximum at $x > 0$ in the line scans can be assigned to the slightly bright spot in the literature description. The dark depression in the frequency-shift image shows a slightly bright centre. This bright centre is probably caused by the smaller tip-sample distance at the centre of the surface CO molecule where the CO molecules start to have a repulsive interaction. Hence, it can be concluded that the inverse image in

figure 38(a) is acquired with a rotational symmetric tip-CO at a relatively larger tip-sample distance.

This tip is suitable for achieving atomic resolution in NC-AFM images of the calcite(104) surface (figure 38(d)). As already explained in section 5.2.1, the calcite surface is imaged in the form of sharp and bright lines running in $[4\,2\,\bar{1}]$ and $[0\,\bar{1}\,0]$ direction with a clear (2×1) reconstruction and a glide plane symmetry (see also appendix figure 36).

(b) CO tip with a rotational symmetrical microscopic tip apex at smaller tip-sample distance

STM and NC-AFM images acquired with another CO-terminated tip are reproduced in figure 39. The inverse image in figure 39(a) shows a slightly different shape of the CO molecule compared to figure 38(a): While the outer boundary of the halo in figure 39(a) is still rotationally symmetric, similar to figure 38(a), instead the dark area within this feature is at an off-centre position. Still, a sharp bright protrusion is clearly present and centred within the feature. In addition to the STM data the frequency-shift is recorded as shown in

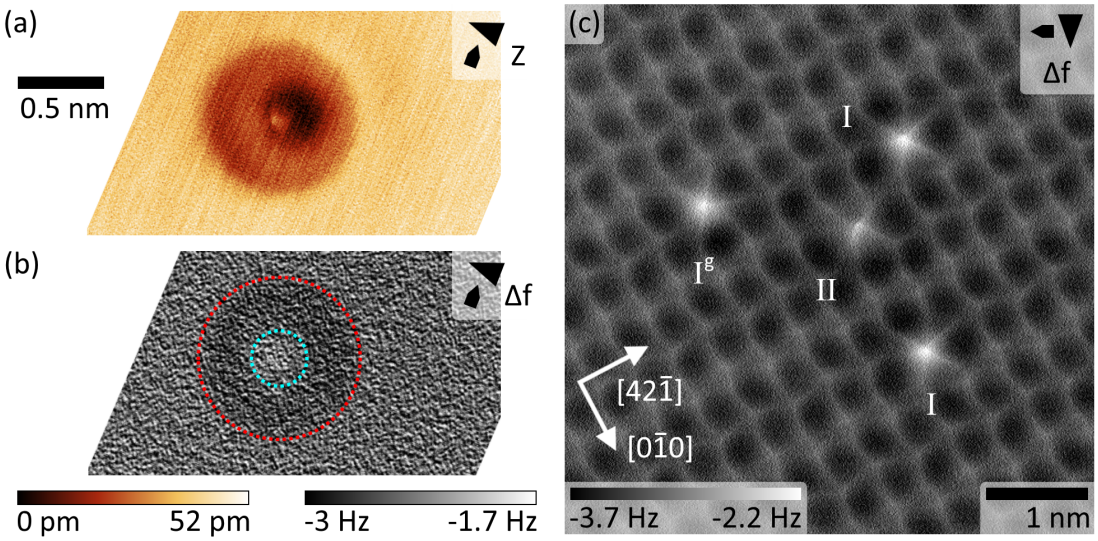

Figure 39: Characterisation of a symmetric CO tip with inverse imaging at larger tip-sample distance. (a) Inverse image of CO/Ag(111) before the experiments on calcite(104) measured with $U_{tip} = 5\,\text{mV}$ and $I_t = 5\,\text{pA}$. (b) Corresponding frequency-shift image to (a). The red and light blue circle are concentric. The image pixels are smoothed over an radius of 3 pixels with the Gwyddion filter "Basic filters: mean, median, denoise, ..." [140]. (c) unit cell corrected NC-AFM constant-height frequency-shift image of the calcite(104) surface with two CO molecules, same image data as in figure 33 and 35(a) measured with $U_{tip} = -10\,\text{V}$ (Calcite-012, Ku crystal). The names I, I^{g} and II of the CO molecules are explained in subchapter 6.2. The STM and NC-AFM images were measured under different scan angles, therefore, the STM images were rotated to provide a consistent orientation.

figure 39(b). In these data, a dark (attractive) depression with a bright (repulsive) centre is visible. This bright centre is in the centre of the dark depression as indicated by the red and light blue concentric circles. The observed pattern can be explained by a smaller tip-sample distance used for the inverse image and a CO molecule with a small initial tilt when compared to figure 38(a).

According to the literature review, repulsive forces between the CO molecules occur at closer tip-sample distances ($-100\,\mathrm{pm}$), which can be caused the bright centre in the frequency-shift image (figure 39(b)). Consequently, the bright spot in the centre of the feature in the topography STM image is assigned to the enhanced direct tunnelling into the metal surface if the molecules are directly above each other, while the off-centred position of the dark area can be assigned to the changes caused by the overlap of the s and p states of the CO molecules. Hence, it can be concluded that the tip is rotational symmetrical, and the tip sample distance in figure 39(a) is smaller than in figure 38(a). It is found that this tip is very suitable to image the calcite(104) surface. As mentioned in figure 33, the constant-height frequency-shift NC-AFM image in figure 39(c) shows a clear structure of the calcite surface following the (2×1) glide plane symmetry. The CO molecules are imaged sharp and show also a glide plane symmetry (further explanation in subchapter 6.2).

(c) Tilted CO tip

While the previous two tips expressed a strong rotational symmetry, a counter example for a tilted tip is discussed now.

The calcite surface in figure 40(d) is apparent in form of a blurry lattice that does not show a glide plane symmetry: For both axes S_1 and S_2, the algorithmic symmetry test delivers relative errors of $\beta_{S_1} = (3 \pm 1)\,\%$ and $\beta_{S_2} = (4 \pm 2)\,\%$ (the determination of the error is shown in appendix figure 69 and table 11), and the images of local deviation images (figure 40(e) and (f)) show larger values. Furthermore, all CO molecules in figure 40(d) have a shape that is elongated in the same direction within this image, one example is marked by a dotted rhombus. Such an elongation is not visible at the CO molecules in figure 38(d) and 39(c).

A likely explanation for this similar appearance of the CO molecules on the calcite(104) surface and the violation of the glide plane symmetry is a CO molecule adsorbed on the tip apex with an initial tilt angle. The inverse image of the CO molecule on Ag(111) acquired with this tip shows a dark feature with a slightly brighter halo (figure 40(a)). The inside of this dark feature is asymmetric as indicated by the concentric red and light blue circles. The asymmetry indicate that the tip CO molecule does not exhibit rotational symmetric geometry. This is further apparent when extracting line profiles (figure 40(c)) that have been extracted at the positions of the light and dark blue and green lines in figure 40(a)

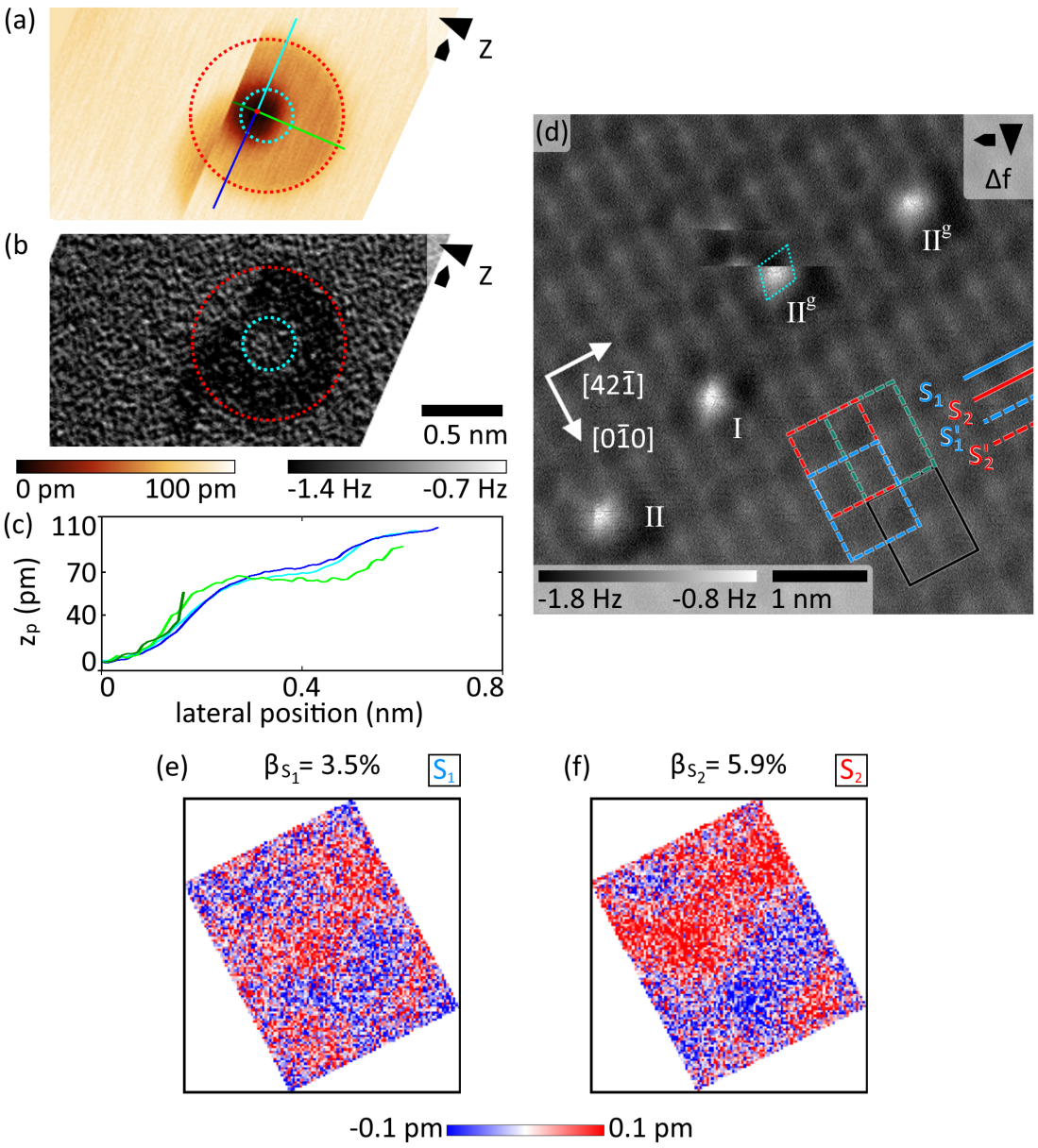

Figure 40: (a) Inverse imaging of CO/Ag(111) before the experiments on calcite(104) ($U_{tip} = 5\,\mathrm{mV}$ and $I_t = 5\,\mathrm{pA}$). The red and light blue circle are concentric. The image pixels are smoothed over an radius of 3 pixels with the Gwyddion filter "Basic filters: mean, median, denoise, ..." [140]. A small part of the halo is displaced due to a tip induced manipulation of the surface CO. (b) Corresponding frequency-shift image to (a). The red and light blue circle are concentric. (c) Line profiles extracted at the positions marked with dark and bright green and blue lines in (a). All line scans have the same starting point that is marked by a red dot. (d) NC-AFM constant-height frequency-shift image of four CO molecules on calcite(104) acquired with $U_{tip} = -10\,\mathrm{V}$ (Calcite-012, Ku crystal). (e) and (f) results of the algorithmic symmetry test applied to the black rectangle in (a). The STM and NC-AFM images were measured under different scan angles, therefore, the STM images were rotated to provide a consistent orientation.

always starting at the position marked by the red dot. The blue lines are very similar to each other, while the light and dark green line does not. Due to a tip induced manipulation of the surface-adsorbed CO, the green line is shorter than the other lines. A bright spot is not visible in the centre of the feature or in the line scans, and the frequency-shift image shows a similar appearance as figure 38(b), hence, a similar tip-sample distance as compared to figure 38(a) is likely.

Conclusion

In conclusion, the examples highlight that the usage of symmetric and well-characterised CO tips is an important requirement for the measurements of calcite(104). To obtain NC-AFM images of the calcite(104) surface that express a glide plane symmetry care must be taken to use tips with a tip CO adsorbed parallel to the surface normal vector of the sample surface. The finding that a tip with an initial tilted CO violates the glide plane symmetry is a further evidence that the row-pairing symmetry is caused by the shape of the tip and represents not a surface property. This is in accordance with previous publications [28, 40, 44].

5.3 Conclusions for the geometry of the calcite(104) surface derived from symmetry considerations

In subchapter 5.1 and 5.2 it is demonstrated that NC-AFM images from the calcite(104) surface acquired with symmetric tips show a (2×1) reconstruction with a glide plane symmetry, whereby the axes of glide reflection are located on the rows of the carbonate groups in $[4\,2\,\bar{1}]$ direction. This experimental finding does not only clarify the standing questions regarding the surface structure, but furthermore leads to considerable conclusions for the structure of the (2×1) unit cells that will be discussed in this subchapter.

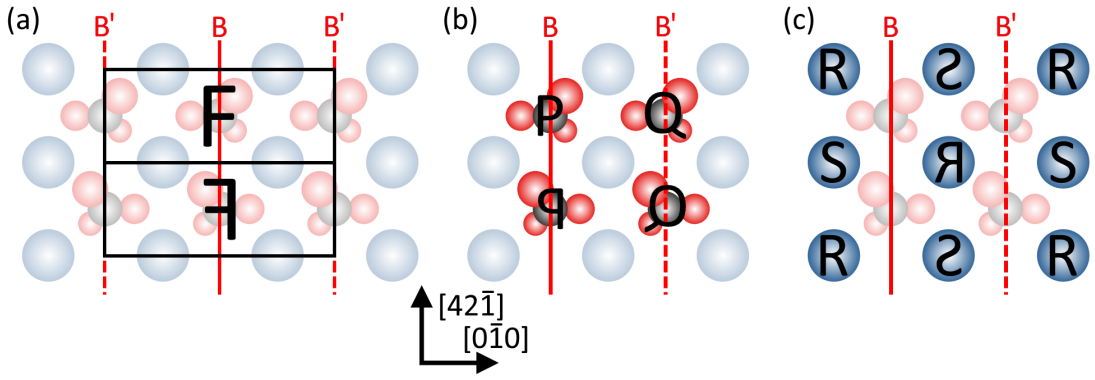

Figure 41: (a) Abstraction of the conclusions for the geometry of a (2×1) unit cell with glide plane symmetry. Implications for (b) the carbonate group and (c) the calcium atom properties.

A (2×1) unit cell separated into two sub-cells of the same size is shown in figure 41(a). The unit cell is drawn such that the axes of glide reflection are located at the centre and at the edges of the (2×1) unit cell. The positioning of the axes follow the experimental results from subchapter 5.1. To satisfy the glide plane symmetry, the upper and lower sub-cell of the (2×1) unit cell must be related to each other by reflection as abstracted by the letters F and Ꟊ.

This alignment of the sub-cells F and Ꟊ requires that the orientation of the two carbonate group pairs adjacent in $[4\,2\,\overline{1}]$ direction are each connected via the glide plane symmetry, as abstracted by the alignment of the respective characters P, Ꟙ, Q and Ꝙ in figure 41(b). To give an example for illustration: If the carbonate group P is rotated by 20° around the surface normal, the carbonate group Ꟙ has to be accordingly rotated by −20° to be in agreement with the glide plane symmetry. The difference to the (1×1) surface (figure 3(c)) is the independence of the carbonate groups P and Q. If the carbonate group P (Q) changes its orientation, only the carbonate group Ꟙ (Ꝙ) must be changed to maintain the glide plane symmetry. In contrast, P and Q, as well as Ꟙ and Ꝙ, are independent due to the (2×1) reconstruction. Therefore, for the carbonate groups the (2×1) reconstruction leads to a pattern of rows along $[4\,2\,\overline{1}]$, which have an alternating structure along $[0\,\overline{1}\,0]$.

The conclusions for the calcium atom properties are derived in a similar way. An important difference to the carbonate groups, however, is the off-axis position of the calcium atoms compared to the on-axis position of the carbonate groups. To follow the glide plane symmetry of F and Ꟊ in figure 41(a), diagonally adjacent calcium atoms are related to each other by reflection as is indicated by the letters R, Ꭱ, S, and Ꞓ in figure 41(c). This relation delivers a chequerboard-like pattern. In analogy to P and Q in figure 41(b), the properties of R and S are independent.

The conclusions for the calcium and carbonate groups are in agreement with the experimental data in figure 27. While the (2×1) reconstruction is apparent in the form of lines along $[4\,2\,\overline{1}]$ on the carbonate group positions (carbonate groups P and Ꟙ, as well as Q and Ꝙ), a chequerboard-like pattern is identified at the positions of the calcium atoms (calcium atoms R and Ꭱ, as well as S and Ꞓ).

A glide plane symmetry in the (2×1) reconstructed surface is in accordance with Rohl *et al.* [61], who found in simulations a (2×1) reconstruction of the calcite surface with a glide plane symmetry. This finding is supported by Geissbühler *et al.* [34], who found in X-ray scattering experiments indications for a glide plane symmetry of the hydrated calcite(104) surface.

5.4 Composition of the calcite sample and the calcite(104) surface

In the previous subchapters it is shown that the calcite(104) surface express a glide plane symmetry with a (2×1) reconstructed surface. However, the origin of the (2×1) reconstruction is still unknown. Kristensen *et al.* [22] found in modelling simulations that the calcite(104) surface only express a (2×1) reconstruction in an areas 4.5 nm around step edges. Reksten *et al.* [62] and Wenk *et al.* [2] assume from transmission electron microscopy measurements that the (2×1) reconstruction is caused by foreign atoms periodically substituting Ca atoms (at least 16 % of the Ca atoms) in the calcite unit cell (figure 1). In contrast, Rohl *et al.* [61] found in force field modelling that the (2×1) reconstruction is a inherent surface property. Hence, this subchapter addresses the question how the composition of the calcite samples used within this thesis is and how impurities in the material are related to the defect density observed in the NC-AFM images.

Typical impurities in calcite are magnesium, iron, zinc, strontium, barium or rare earth metals [21, 187]. According to Menadakis *et al.* [188], especially magnesium (Mg) and zinc (Zn) are frequently found in calcite crystals, because the substitution of Ca^+ cations by these impurities is energetically favourable, while the substitution with strontium (Sr) and barium (Ba) is less favourable. Here, the amount of the impurities in the calcite crystals is investigated with X-ray fluorescence spectroscopy and inductively coupled plasma optical emission spectrometry (ICP-OES), both performed at the Karlsruher Institut für Technologie (KIT). X-ray fluorescence spectroscopy is used to determine the presence of foreign elements in the sample. Signals pointing towards the presence of magnesium (Mg), titanium (Ti), chromium (Cr), manganese (Mn), iron (Fe), copper (Cu), zinc (Zn), strontium (Sr), selenium (Se), barium (Ba), and thulium (Tm). Next, the concentration of these impurities in the crystal samples is quantified with ICP-OES.

Brief explanation of ICP-OES

A concise explanation about ICP-OES, based on a publication from Hou *et al.* [189], is given in the following.

The sample material must be present in liquid or gas form for an ICP-OES measurement. Hence, solid samples need extraction or acid digestion. Aqua regia, which consists of nitric acid (NHO_3) and hydrochloric acid (HCl), is used for calcite because this acid dissolves calcite while it does not contain any calcite elements except oxygen [190].

Inside the ICP-OES device, a nebulizer converts the liquid into an aerosol with very fine droplets (about 8 µm). This aerosol is then injected into an argon plasma. The plasma is generated by a copper coil that surrounds the end of the aerosol/gas inlet. This coil is

operated with an RF current that produces an oscillating electromagnetic field. Gas ions and electrons in the plasma are accelerated by this field and produce ionisation and excitation of other atoms by colliding with them. This cascade of ionization maintains the plasma.

Each atom in an excited energy state emits its characteristic radiation due to electronic transition of electrons in higher states to the ground state. This characteristic radiation consists of single emission lines in the visible and UV regime, is element-specific, and can thus be used as a fingerprint. Emission lines of different elements can be very narrow and, therefore, difficult to distinguish. Consequently, the radiation is analysed by a high-resolution spectrometer. The intensity of such an emission line is directly proportional to the concentration of the associated element. The absolute concentration is determined by comparison to standard solutions with known concentrations.

The ICP-OES spectrum includes not only the emission lines of the sample material, but also a background that consists of the argon emission lines, the lines of the used solution, and a continuum emission. If the intensity of an emission line is only slightly higher than the intensity of the background, then the assumption of a linear relationship between element concentration and emission line intensity is not valid any more. The minimum concentration of an element, where it is assumed that the linear relationship still exists, is called the detection limit. The common definition for this limit is that the minimum intensity of an emission line must be higher than the background noise by nine times the standard deviation of the background noise [191, 192].

The quantity of an element in a sample as measured by ICP-OES is usually given as a mass fraction. In this thesis, this quantity is related to parts per 1 000 000 Ca atoms (ppm_{Ca}). In particular, the number of atoms (n_X) of kind X relative to 1 000 000 Ca atoms in a sample can be written as follows:

$$n_\mathrm{X} = \frac{1\,000\,000 \cdot a_\mathrm{Ca} \cdot m_\mathrm{X}}{a_\mathrm{X} \cdot m_\mathrm{Ca}} \tag{14}$$

whereby a_X is the atomic mass of X, m_X is its mass fraction in percent measured by ICP-OES, m_Ca is the mass fraction of calcium and $a_\mathrm{Ca} = 40.078\,\mathrm{u}$ is the atomic mass of calcium. The derivation of this formula is straightforward and illustrated by an example. In one particular ICP-OES measurement, the mass fraction of Ca in a sample was given as $m_\mathrm{Ca} = 39.2\,\%$ and of Mg as $m_\mathrm{Mg} = 0.0106\,\%$. From these values, the number of Ca atoms in 1 kg of sample material can be calculated by $n_\mathrm{Ca} = \frac{1\,\mathrm{kg}\cdot 0.392}{40.078\,\mathrm{u}}$. In the opposite way (calculating the mass M for 1 000 000 Ca atoms), the mass (M) of sample material containing 1 000 000 Ca atoms can be calculated by $M = \frac{1\,000\,000\cdot 40.078\,\mathrm{u}}{0.392}$. With this mass and the atomic mass of Mg

($a_{\mathrm{Mg}} = 24.305\,\mathrm{u}$), the number of Mg atoms relative to 1 000 000 Ca atoms (ppm_{Ca}) can be calculated by $n_{\mathrm{Mg}} = \frac{M \cdot 0.000106}{24.305\,\mathrm{u}}$. In conclusion, the number of magnesium atoms relative to 1 000 000 Ca atoms can be written in one formula:

$$n_{\mathrm{Mg}} = \frac{1\,000\,000 \cdot a_{\mathrm{Ca}} \cdot m_{\mathrm{Mg}}}{a_{\mathrm{Mg}} \cdot m_{\mathrm{Ca}}} \tag{15}$$

This formula is identical to formula 14 for X = Mg.

The defect density in NC-AFM images is of particular interest and a gauge for the presence of foreign elements. Therefore, the results from the ICP-OES measurements are converted to a number of foreign atoms of one kind within the calcite(104) plane in a typical overview image of 20 nm × 20 nm. One calcite surface layer of this size contains about 1975 Ca atoms, therefore, it can be expected that the average number of atoms of kind X in this layer is given by $x_X^{20\times20} = \frac{x_{\mathrm{X}}}{1\,000\,000} \cdot 1975$. Here it is assumed that only the atoms in the topmost surface layer are visible in the images.

Results of the ICP-OES

The calcite crystals used for this thesis all originate from Korth Kristalle (Altenholz, Germany), are of natural origin [193], but were ordered at different times over several years. The material as-delivered consists of a block with dimensions of about 37 mm · 37 mm · 15 mm, which is then cut into smaller crystal samples. These samples have a (104) face size of 2 mm · 4 mm and a length between 8 mm and 15 mm.

The investigated crystal samples can be classified into three groups. The samples within the first group originate from a single calcite block, herein after named Ku. The composition was determined for two crystal samples from this block (Ku 1 and Ku 2). The second group contains samples from one or several blocks ordered before 2012. Unfortunately, it is no longer possible to trace from how many calcite blocks the samples within this group originate. Three crystal samples of this group were investigated by ICP-OES, herein named Ra 1, Ra 2 and Ra 3. The third group, ordered 2020, consists of two crystal blocks (Os 1 and Os 2). One crystal sample of each block was examined with ICP-OES.

The results of the ICP-OES measurements from the two crystals Ku 1 and Ku 2 are listed in table 3 as n_X in ppm_{Ca} in the left columns and rescaled to $n_X^{20\times20}$, namely to foreign atoms per 20 nm × 20 nm calcium layer, in the right two columns. Only the content of Mg and Sr is above the detection limit, and the concentrations of these two elements are similar for both samples. This indicates that the calcite block is very pure and has a homogeneous distribution of the foreign elements. In an NC-AFM image, acquired on a crystal of type Ku,

Element	n_X (ppm_{Ca}) Ku 1	n_X (ppm_{Ca}) Ku 2	$n_X^{20\times20}$ Ku 1	$n_X^{20\times20}$ Ku 2
Mg	445.9±0.2	434.4±0.2	0.8806±0.0004	0.858±0.0004
Ti	<0.854	<0.857	<0.01	<0.01
Cr	<0.393	<0.394	<0.01	<0.01
Mn	<0.931	<0.933	<0.01	<0.01
Fe	<1.648	<1.652	<0.01	<0.01
Cu	<0.321	<0.323	<0.01	<0.01
Zn	<1.251	<1.254	<0.01	<0.01
Se	<2.59	<2.596	<0.01	<0.01
Sr	26.25±0.08	27.14±0.02	0.0519±0.0002	0.0536±0.00004
Ba	<0.149	<0.149	<0.01	<0.01
Tm	<0.121	<0.121	<0.01	<0.01

Table 3: Result of the ICP-OES measurement for the two Ku crystals. The amount of the elements Ti, Cr, Mn, Fe, Cu, Zn, Se, Ba, and Tm are smaller than the detection limit (indicated by "<"). If the probability to find an atom of an element in one Ca layer of a 20 nm × 20 nm image is smaller than 1 %, then the exact value was neglected and only <0.01 was written into the corresponding cell.

one surface defect is expected in a calcium layer of a 20 nm × 20 nm. NC-AFM images taken on a crystal of this group are marked with "Ku" in the captions of the images.

The results for the three Ra crystals are listed in table 4 (unit ppm_{Ca}) and in table 5 (foreign atoms in a Ca layer of 20 nm × 20 nm). It is clearly visible that the crystals Ra 1 and Ra 2 are very similar and are probably from one calcite block, while Ra 3 has a markedly different composition. Compared to the the Ku crystals, the Ra samples contain further foreign elements, and a larger amount of Mg and Sr. Especially the amount of Mg and Sr is much higher in Ra 1 and Ra 2 than in Ra 3. A calcium layer of 20 nm × 20 nm from a sample of type Ra 1 or Ra 2 should contain about 10 foreign atoms, while for an image measured on a Ra 3 crystal about one foreign atom is expected. AFM images measured on a calcite crystal of the Ra group are marked with "Ra" in the captions of the images.

The results for the two Os crystals are listed in table 6. Compared to the other groups, the content of Mn and Fe are much higher. It is expected that in a Ca layer of 20 nm × 20 nm are 4–5 foreign atoms. However, no images were acquired for this thesis on these crystals.

Examples of NC-AFM images acquired on nominally pristine crystal samples of group Ku, Ra 1 or 2, as well as Ra 3 are reproduced in figure 42. Figure 42(a) shows an NC-AFM overview image of the calcite(104) surface acquired on a sample of group Ku. The calcite surface is imaged in the form of bright protrusions arranged in rows along $[4\,2\,\overline{1}]$ and $[0\,\overline{1}\,0]$ direction, while the rows in $[4\,2\,\overline{1}]$ direction form pairs. Two features are visible (red and orange arrows) that consist of a dark spot with a larger bright area at the left side. These

Element	n_X (ppm_{Ca}) Ra 1	Ra 2	Ra 3
Mg	5243±2	4735±2	313±2
Ti	<0.859	<0.859	<0.854
Cr	2.767±0.008	4.348±0.008	<0.393
Mn	51.81±0.05	46.76±0.05	<0.931
Fe	2.944±0.007	<1.656	18.674±0.007
Cu	<0.323	<0.323	6.114±0.006
Zn	<1.257	<1.257	<1.251
Se	<2.603	<2.603	<2.589
Sr	221.67±0.07	227.531±0.07	22.4±0.07
Ba	2.17±0.007	3.442±0.004	0.1489
Tm	<0.122	<0.122	<0.121

Table 4: Result of the ICP-OES measurement for three Ra crystals using the unit ppm_{Ca}. See also the explanations for table 3.

two features are not exactly similar. The bright area of the feature marked by a red arrow is much larger and brighter than the bright area of the other feature (orange arrow). In contrast, the dark spot is much larger and clearly visible at the feature with the orange arrow. It can be assumed that both features are impurities, and that these impurities are located in two different Ca layer. This would explain the different appearance of the features and would be in agreement with one foreign atom within a 20 nm × 20 nm Ca layer, which is the expected density of foreign elements (table 3).

In figure 42(b) an overview image acquired on a sample of the group Ra is presented. Bright protrusions arranged in $[4\,2\,\overline{1}]$ and $[0\,\overline{1}\,0]$ direction with a row-pairing reconstruction are

Element	$n_X^{20\times20}$ Ra 1	Ra 2	Ra 3
Mg	10.355±0.004	9.353±0.004	0.617±0.004
Ti	<0.01	<0.01	<0.01
Cr	<0.01	<0.01	<0.01
Mn	0.1023±0.0001	0.0924±0.0001	<0.01
Fe	<0.01	<0.01	0.03689±0.00001
Cu	<0.01	<0.01	0.01208±0.00001
Zn	<0.01	<0.01	<0.01
Se	<0.01	<0.01	<0.01
Sr	0.4378±0.0001	0.4494±0.0001	0.0442±0.0001
Ba	<0.01	<0.01	<0.01
Tm	<0.01	<0.01	<0.01

Table 5: Same results as in table 4 converted in number of atoms in the surface of a typical overview image of 20 nm × 20 nm. See also the explanations for table 3.

visible. At many positions, dark spots appear that can be separated into two kinds by their brightness. The first kind is a dark spot replacing a bright protrusion of the calcite surface. One of these spots is marked by a light blue arrow. The second kind is brighter than the first kind of spots, and seems to be located between two in $[0\,\bar{1}\,0]$ direction adjacent bright protrusions. One spot of the second kind is marked by a dark blue arrow. In this image, eleven dark spots of the first kind and eight spots of the second kind have been found. This number would be in agreement with the expected density of impurities (ten within a 20 nm × 20 nm Ca layer) of a sample of group Ra1 or 2, if the two kinds of dark spots were impurities in two different Ca layer. It is likely that the impurities of the first kind are in the topmost Ca layer, while the impurities of the second kind are in the second Ca layer due to their rather faintly appearance. It is unlikely that these two kinds of dark spots are assigned to two different kinds of impurities, because the ratio of 11:8 for the impurities does not fit to the ratio in the ICP-OES measurements (ratio Mg to Mn and Sr: about 20/1).

A further indication that in NC-AFM images the impurity atoms in the first two Ca layer are visible is found for the image in figure 42(c), which shows a typical row-pairing reconstruction. Dark features are visible at two positions, marked by bright and dark green arrows. The feature marked with the bright green arrow is larger and darker than the feature marked with the dark green arrow. Also these features are assigned to impurities in two different Ca layers, because of the different appearance, and their number would be in agreement with the expected impurity density of one foreign atom within a 20 nm × 20 nm Ca layer.

From the ICP-OES measurements it can be concluded that it is unlikely that the (2 × 1) reconstruction is caused by foreign atoms substitution periodic Ca atoms in the calcite unit cell as assumed by Reksten *et al.* [62] and Wenk *et al.* [2], because the amount of impurities

	n_X (ppm_{Ca})		$n_X^{20\times20}$	
Element	Os 1	Os 2	Os 1	Os 2
Mg	253.98±0.06	328.5±0.1	0.5016±0.0001	0.6488±0.0002
Ti	<0.87	<0.859	<0.01	<0.01
Cr	<0.4	<0.395	<0.01	<0.01
Mn	2198±0.2	1444.1±0.3	4.3411±0.0004	2.85202±0.0006
Fe	126.6±0.1	106.9±0.1	0.25±0.0002	0.2112±0.0002
Cu	<0.328	<0.323	<0.01	<0.01
Zn	<1.274	<1.257	<0.01	<0.01
Se	<2.636	<2.603	<0.01	<0.01
Sr	514.4±0.2	385.9±0.1	1.016±0.0004	0.7621±0.0002
Ba	<0.152	<0.15	<0.01	<0.01
Tm	<0.123	<0.122	<0.01	<0.01

Table 6: Result of the ICP-OES measurement for the crystal Os. See also the explanations for table 3.

found in the ICP-OES measurements are much smaller than the amount of impurities assumed by Wenk and Recksten. Also unlikely is the assumption of Kristensen *et al.* [22] that the calcite(104) surface only express a (2×1) reconstruction at a distance of 4.5 nm from step edges. In the images of figure 42 no step edges were found, the dimensions of the images are larger then 4.5 nm, and a clear (2×1) reconstruction is found in each image. Consequently, it is likely that the (2×1) reconstruction is a inherent surface property as assumed by Rohl *et al.* [61].

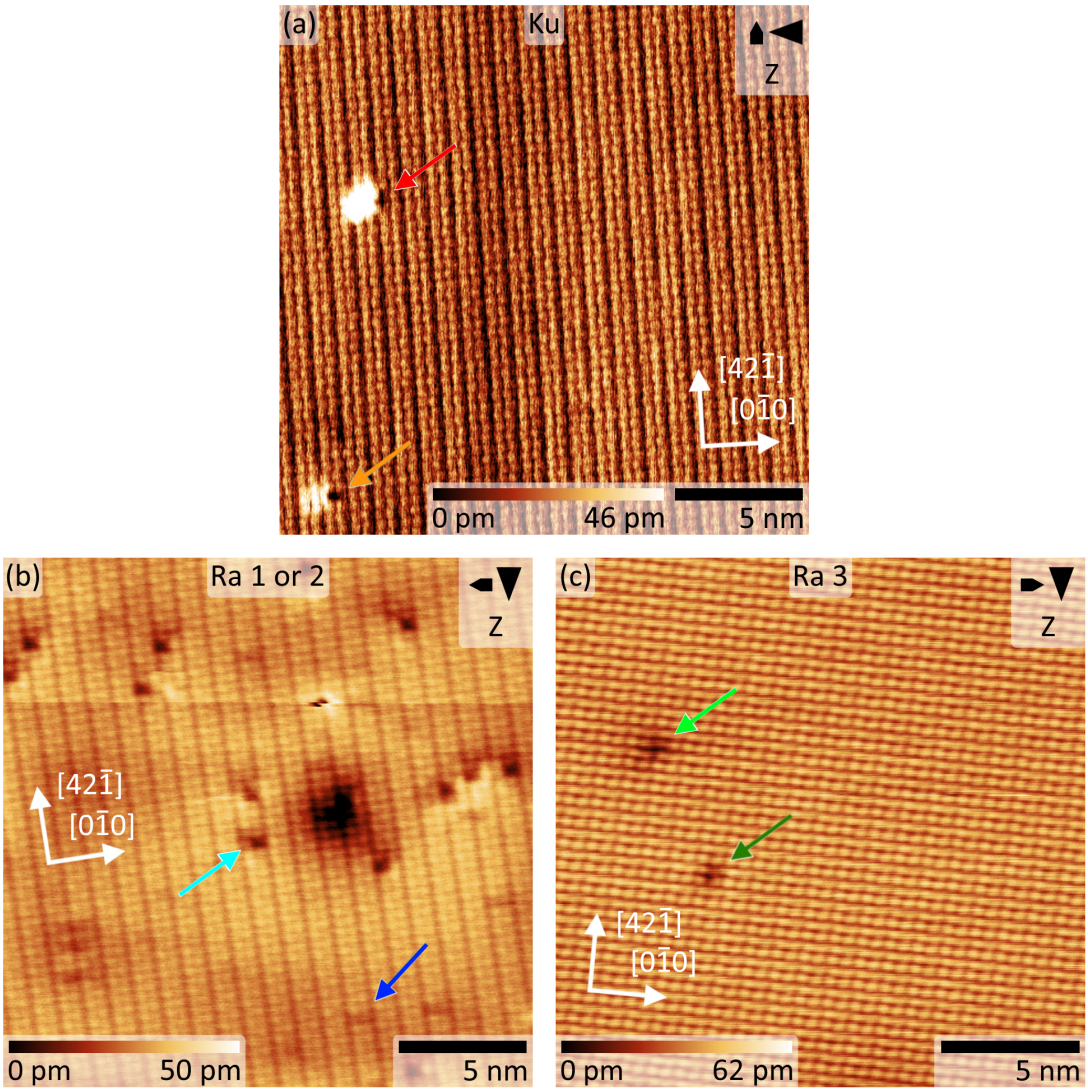

Figure 42: NC-AFM topography images acquired on calcite samples from different blocks. (a) (104) surface of a calcite sample from block Ku (Calcite-015), imaged with $\Delta f = -1.5$ Hz and $U_{tip} = -9$ V. (b) Calcite(104) sample of group Ra (Calcite-010), according to the defect density of Ra 1 or Ra 2 ($\Delta f = -4$ Hz and $U_{tip} = 10$ V). (c) (104) surface of a calcite sample from block Ra 3 (Calcite-006) acquired with $\Delta f = -1.7$ Hz and $U_{tip} = -4$ V.

5.5 Conclusion

In this chapter it is demonstrated that the calcite(104) surface shows a (2×1) reconstruction with a glide plane symmetry in NC-AFM images if sharp and well-characterised tips are used. The axes of glide reflection are on the carbonate groups along the $[4\,2\,\overline{1}]$ direction. From this symmetry property conclusions for the geometry of the calcite(104) surface could be derived. Carbonate groups adjacent in $[4\,2\,\overline{1}]$ direction are connected via the glide plane symmetry, while carbonate groups adjacent in $[0\,\overline{1}\,0]$ direction are independent. Diagonally adjacent calcium atoms are related to each other by reflection, while calcium atoms adjacent in $[4\,2\,\overline{1}]$ or $[0\,\overline{1}\,0]$ direction are independent resulting in a chequerboard-like pattern. The origin of the (2×1) reconstruction is still unknown, but it can be supposed that this reconstruction is a inherit surface property.

6 Adsorption properties of CO on calcite(104) at 5 K

In the chapter 5 it is shown that the calcite(104) surface has a glide plane symmetry within the (2×1) reconstruction. In this chapter the question is addressed if this reconstruction can affect the adsorption geometry of molecules. In the literature the adsorption geometries of rather larger molecules adsorbed on the bulk-truncated (1×1) calcite(104) surface is investigated [57, 194], and give, therefore, no answer. To answer this question the adsorption geometry of small molecules with well known properties are investigated in the measurements of this thesis. In particular, the adsorption geometry of the CO molecule on calcite(104) is examined in this chapter.

6.1 CO adsorption positions on calcite(104)

The central result in this subchapter is the determination of the adsorption positions of single CO molecules on the calcium atoms. This conclusion was reached in a collaboration with the group of Prof. Dr. Christof Wöll and Dr. Peter Thissen at the Karlsruher Institut für Technologie (KIT). IRRAS experiments and DFT calculations (both performed at the KIT) were combined with high-resolution NC-AFM experiments, that were performed within this thesis. The results published in [Tahereh Mohammadi Hafshejani, Weijia Wang, Jonas Heggemann, Alexei Nefedov, Stefan Heissler, Yuemin Wang, Philipp Rahe, Peter Thissen, and Christof Wöll, CO adsorption on the calcite(10.4) surface: a combined experimental and theoretical study, Phys. Chem. Chem. Phys. **23**, 7696 (2021)] are explained and summarised in the following.

Brief explanation of the IRRAS experiments performed at the KIT

Molecules have characteristic vibrational modes that allow to identify them [97, 195, 196]. Some of these modes have a changeable dipole moment and can, therefore, be excited by absorption of infrared light of certain frequency, also denoted as IR-active [97, 195]. Infrared reflection absorption spectroscopy (IRRAS) measures the absorption spectrum of adsorbates on a surface. The resulting IR-spectrum typically exhibits frequency ranges at that absorption by the specimen occurs. Such range is called an "absorption band" and has usually the shape of a downward pointing peak. The zenith of a single peak is located at the absorption frequency. The absolute value of the absorption frequencies can enable a detailed understanding about the surface structure, the geometry of the adsorbed molecules, and their bonding geometry [197, 198].

In the IRRAS experiments performed at KIT [55], the absorption band of the C–O stretch mode is measured to determine the adsorption structure of the CO molecules on the cal-

cite(104) surface. This band is chosen as it is known that the absorption frequency of this stretch mode varies with the bonding configuration of the molecule to the surface [179, 196, 197]. If the molecule-surface bonding weakens the C–O bond, the force constant of the internal C–O bond is weaker than the bond of a free CO molecule. Thus, redshift of the absorption frequency occurs. In contrast a blueshift occurs if the C-O bond is strengthened [197, 198].

The reason for this strengthening or weakening of the C-O bond can be explained by the Blyholder model that gives an explanation for the bonding structure of a CO molecule to a metal surface, and how this bonding structure influences the C–O bond. This model is also often used to explain the bonding structure of a CO molecule to a non-metal surface [55, 182, 198]. The Blyholder model considers how the bonding and antibonding orbitals of an adsorbed CO molecule are filled with electrons due to the interaction with the surface, and how this filled orbitals influence the C–O bond.

In the orbital diagram in figure 43(a) the ground state of the free CO molecule according to the energy scheme and the LCAO-method (linear combination of atomic orbitals) is drawn. The energy levels of the atomic orbitals of the carbon atom are visible at the right side and the energy levels of the oxygen atom on the left side; the levels of the CO molecule are drawn

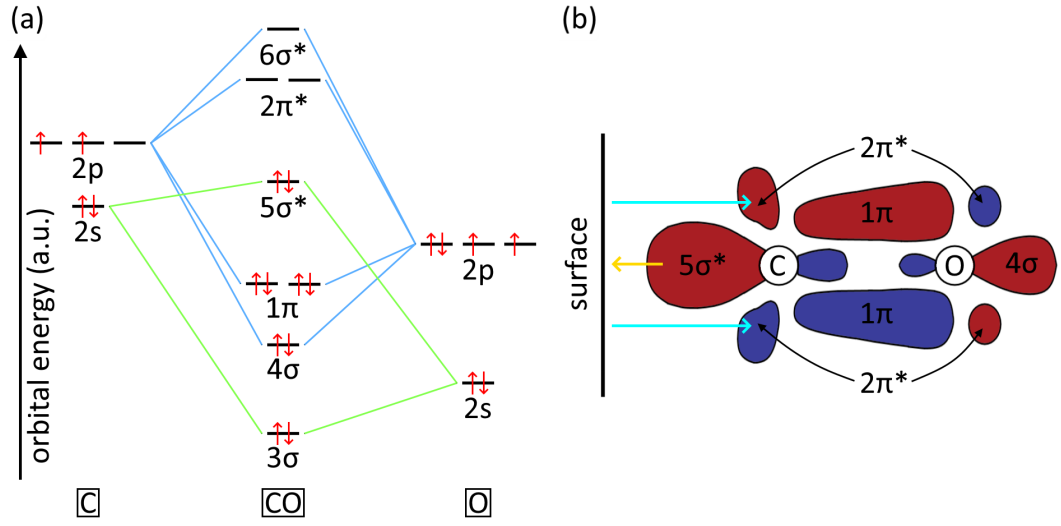

Figure 43: (a) Orbital diagram of a CO molecule in ground state according to the energy scheme and LCAO-method (linear combination of atomic orbitals) [181, 199, 200]. The "*" indicates antibonding orbitals. (b) Scheme of the coupling of a CO molecule to a surface (not to scale). It is drawn following the references [180, 181, 197, 200, 201]. The yellow arrow indicate the bonding of the filled $5\sigma^*$ orbital to empty orbitals of the surface, the blue arrows indicate π backbonding from filled states of the surface into the empty $2\pi^*$ orbital of the CO molecule. The $3\sigma^*$ orbital, which is mainly localized between the carbonate and oxygen atom, not drawn in this scheme for visual reasons.

in the image centre. The red arrows indicate the distribution of the electrons to the orbitals according to Hund's rules in the ground state. In a CO molecule, the combined electrons of the carbon and oxygen atoms can fill all orbitals up to the antibonding 5σ orbital that is located at the carbon site (figure 43(b)). The molecule is stable because the antibonding $2\pi^*$ and $6\sigma^*$ orbital are not occupied and the bonding orbitals 4σ and $1\pi^*$ outweigh the weakly antibonding 5σ orbital.

If the CO molecule is bound to a metal surface it is explained by the Blyholder model that charge transfer from the highest occupied molecular orbital (HOMO, $5\sigma^*$ orbital) into empty orbitals of a surface atom (figure 43(b) yellow arrow) occurs. This results in a CO molecule absorbed with the carbon side to the metal surface. The weakening of the antibonding 5σ orbital results in a strengthened C–O bond and, therefore, in a blueshift of the absorption frequency. The charge transfer from the CO molecule to the metal atom leads to a negative charge at the metal atom. To neutralise the system electron transfer from a metal d-orbital into the unoccupied and strongly antibonding orbital $2\pi^*$ occurs (figure 43(b), light blue arrows). This so-called π backbonding weakens the C–O bond and results in a redshift in the IRRAS measurements.

For example, the absorption frequency of the C–O stretch mode of CO molecules on Pd(100) is in the range of $1895\,\mathrm{cm}^{-1}$ (at 0.006 ML coverage) to $1997\,\mathrm{cm}^{-1}$ (at a coverage of 0.82 ML, 1 ML is defined as one CO molecule per Pd atom) and, therefore, shows a clear redshift compared to the absorption frequency of the free CO molecule of $2143\,\mathrm{cm}^{-1}$ [196, 197, 202, 203].

With IRRAS it is furthermore able to determine the tilt of a molecular dipole from a vibrational mode. A dipole that is positioned perpendicular to the surface normal can only adsorb p-polarized infrared light (polarized in the plane spanned by the incident ray and the surface normal), whereas tilted dipoles are also able to adsorb s-polarized infrared light (polarized perpendicular to the plane spanned by the incident ray and the surface normal) [179, 197, 198, 204].

In conclusion, from the shift of the $2143\,\mathrm{cm}^{-1}$ absorption frequency in IRRAS experiments conclusions about the bonding geometry of the CO molecule can be made via the Blyholder model. A tilt in the bonding geometry is visible in an adsorption of s-polarized infrared light.

Calcite(104) adsorption geometry determined by IRRAS measurements

The IRRAS experiments carried out at KIT were performed in UHV at 62 K, and the calcite surface was prepared by cleaving and annealing in vacuum before the experiments. The calcite surface was irradiated by infrared light at a grazing incidence angle of 80° (relative to the surface normal) and the reflected light was analysed by a spectrometer. Polarized light

was used to measure the tilt of the CO molecules.

Overall, the spectrum of the reflected light changes when CO molecules are deposited onto the calcite surface. Of particular interest in the spectrum of the reflected light is an asymmetric adsorption band at an absorption frequency of $2175.8\,\mathrm{cm}^{-1}$ when using p-polarized light. This absorption band occurs at small CO coverage, was not apparent on the pristine calcite surface, and is close to the absorption frequency of the stretch mode of a free CO molecule ($2143\,\mathrm{cm}^{-1}$) [179, 196, 197, 202]. Therefore, the apparent blueshift between the free and a surface-bound CO molecule indicates a strengthened C–O bond. The reason for this strengthening is assumed to be caused by a charge transfer from the weakly antibonding 5σ CO orbital into the unoccupied orbitals of the Ca^{2+} ions of the calcite surface similar to the bonding structure of CO on metal (Blyholder model) [181, 197, 198]. An electron-depleted 5σ orbital would result in a strengthened C–O bond and, therefore, in a blueshift of the absorption frequency compared to the frequency of the free CO molecule. Hence, the absorption band at $2175.8\,\mathrm{cm}^{-1}$ is assigned to the stretch vibrations of the CO molecules bound with the carbon atom to one of the surface calcium atoms.

The stretching vibration with an absorption band at $2175.8\,\mathrm{cm}^{-1}$ is also observed by s-polarized infrared light. As previously explained, this is only possible if the CO molecules are adsorbed tilted with respect to the surface normal [179, 197, 198].

With increasing CO coverage, the absorption band at $2175.8\,\mathrm{cm}^{-1}$ shifts to $2173.4\,\mathrm{cm}^{-1}$, but eventually further CO dosing did not cause further shifts of the absorption wavelength. The initial shift is interpreted as a growing CO monolayer with increasing CO-CO interaction, while the saturation of the shift indicates the absence of multilayer growth at 62 K [55, 197].

Upon increasing temperature of a 1 ML CO/calcite sample, the integrated band intensity remains constant up to 92 K. Upon further annealing to 100 K, the intensity of the absorption band decreases. This decrease indicates the onset of CO desorption. From the onset temperature of 92 K a binding energy of the adsorbed CO molecules of $-0.31\,\mathrm{eV}$ can be calculated using the Redhead equation [55, 205].

DFT calculations of submonolayer CO on calcite(104)

The results of the IRRAS experiments were supported by calculations with density functional theory (DFT) as performed at KIT. The calculations were carried out for a 4-layer slab of a (1×1) unit cell of the calcite(104) surface. The DFT calculations were performed with both one (0.5 ML) and two (1 ML) CO molecules per (1×1) unit cell. In both cases, stable configurations were found for CO molecules adsorbed on top of calcium atoms with the carbon atoms pointing downwards. In particular, the CO molecules are found to be tilted

with respect to the surface normal and absorption frequencies at 2177 cm^{-1} for 0.5 ML and 2161 cm^{-1} for 1 ML were determined. These are in good agreement with the IRRAS results. A tilt angle of 14.42° for a CO coverage of 0.5 ML was calculated, while tilt angles for the two CO molecules inside a (1×1) unit cell are different (14.57° and 15.14°). The binding energy for a single CO molecule is calculated to −0.216 eV (0.5 ML) and −0.21 eV (1 ML) [206].

The difference in the tilt, the binding energies, and the absorption frequencies as resulting from the DFT calculations for 0.5 ML and 1 ML are explained by repulsive adsorbate-adsorbate interactions. This interaction could explain the coverage depending shift of the adsorption band from 2175.8 cm^{-1} to 2173.4 cm^{-1} in the IRRAS measurements and suggests the absence of island or cluster formation

In conclusion, the IRRAS experiments and DFT calculations give indications that the CO molecules on calcite(104) adsorb tilted on the calcium atoms while no island or cluster formation is expected. These conclusions are now further confirmed by NC-AFM measurements.

Results of the NC-AFM measurements of submonolayer CO on calcite(104)

In order to investigate the lateral assembly of CO on calcite(104) NC-AFM images of a submonolayer coverage are at 5 K after deposition of different coverage of CO molecules; results are presented in figure 44: 0.006 ML in figure 44(a), 0.013 ML in figure 44(b, d) and 0.067 ML in figure 44(c). 1 ML is defined as one CO molecule per calcium atom. The calcite surface is apparent in all images in the form of four bright protrusions inside a (2×1) unit cell similar to figure 27(a). An exemplary (2×1) unit cell is marked by a white rectangle in every image. The dark depressions in the topography images (examples are marked by a green arrow) are only present after dosing CO and are more frequent with increased CO deposition time. Therefore, each of this dark depression is assigned to a single CO molecule.

The IRRAS measurements and DFT calculations indicate that the CO molecules exclusively adsorb on the calcium ions. This finding is in agreement with the NC-AFM images where it is clearly visible that the dark depressions in the topography images are only located on similar positions; for example in figure 44(d) the positions of the dark depressions are exclusively on bright features of the surface. Consequently, these features are assigned to the positions of the calcium atoms. As visible in the images of figure 44, the CO molecules are well separated on the surface, are often manipulated by the tip, and do not show indications of clustering or island formation. Hence, this is also in excellent agreement with the IRRAS and DFT results.

Some of the CO molecules have a slight off-centre position on the bright features (examples are marked by white circles in figure 44(b)). This observation hints towards the existence of two

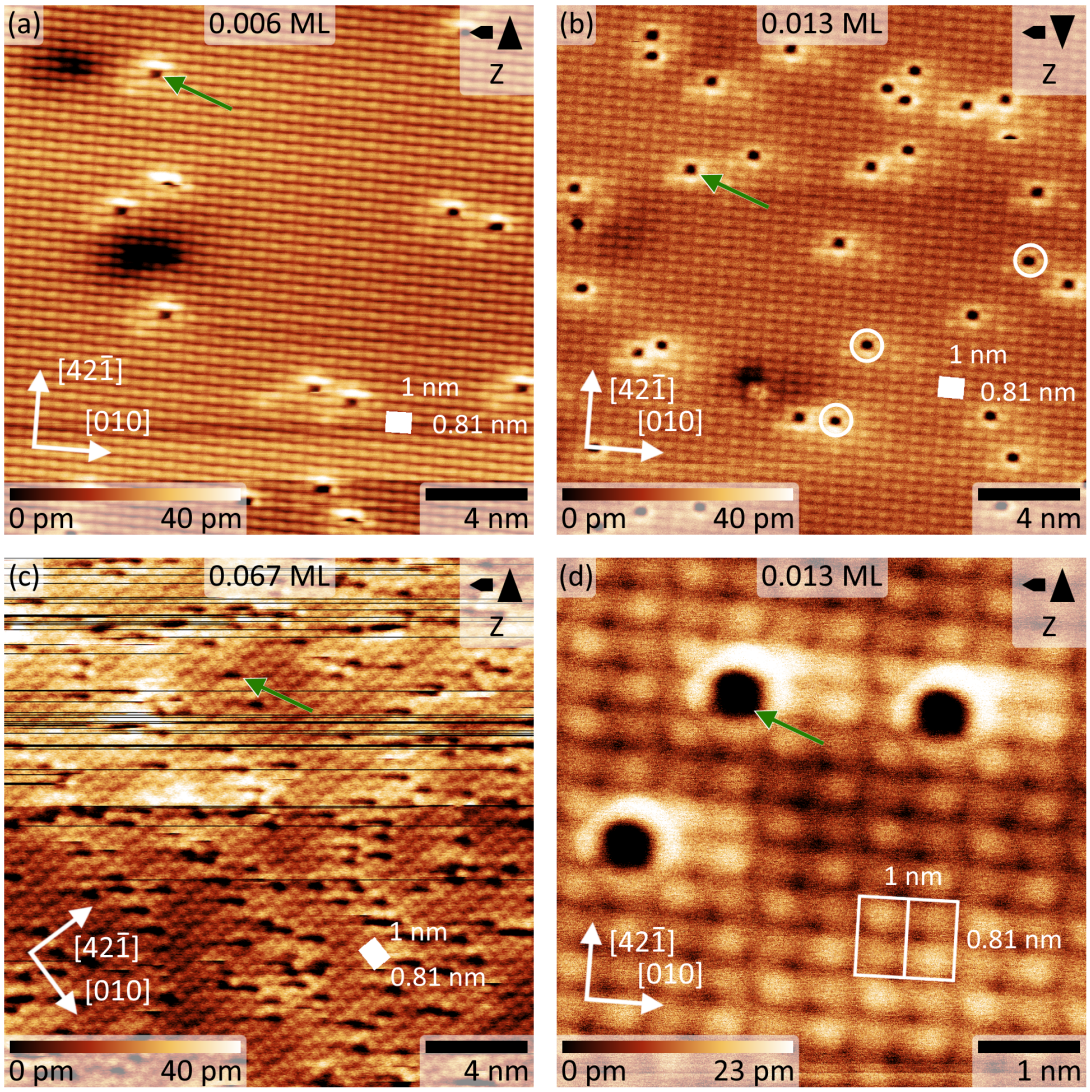

Figure 44: Topography NC-AFM images of calcite(104) (Ra crystals) at 5 K with different CO dosing times. The dark depressions are identified as CO molecules that substitute bright features of the surface. (a) 25 s CO deposition resulting in a coverage of 0.006 ML (Calcite-006, $\Delta f = -1.5$ Hz and $U_{tip} = -4$ V), (b and d) same sample as (a) with additional 25 s of deposition resulting in 0.013 ML ((b): $\Delta f = -1.35$ Hz and $U_{tip} = -6$ V. (d): $\Delta f = -1.67$ Hz and $U_{tip} = -6$ V.) (c) acquired after dosing for 25 s and additional 125 s resulting in 0.067 ML (Calcite-003, $\Delta f = -1.1$ Hz and $U_{tip} = -2$ V).

different CO adsorption positions as expected due to the presence of a (2×1) reconstruction. Although the presence of two different species was not revealed by the IRRAS measurements, this could be explained by the higher temperature of 62 K during the IRRAS measurements, possibly leading to a thermal averaging or a peak broadening, that clouds the presence of two species.

In conclusion, in this subchapter it is shown that CO molecules adsorb exclusively on the

calcium atoms of the calcite(104) surface. Features in the NC-AFM images of the calcite(104) surface can be assigned to the positions of the calcium atoms with the help of the adsorbed CO molecules. It seems that the CO molecules adsorb in two different types on the surface. A further investigation of these different CO types is topic of the following subchapter 6.2.

6.2 Differences between the adsorption positions of CO molecules on calcite(104)

This section will give experimental evidence for the existence of two different CO adsorption types on calcite(104) as suggested by the data in figure 44. These types will be investigated in further detail by comparing the NC-AFM images of CO molecules that are adsorbed at the four different positions inside a (2×1) unit cell.

6.2.1 Identification of two different CO adsorption types in the long-range interaction regime

An NC-AFM topography image acquired at 5 K of 0.025 ML CO on calcite(104) is shown in figure 45(a). The measurement was performed with a CO-terminated tip. To avoid manipulation of single CO molecules by the tip, the average tip-sample distance is chosen to be relative large by a moderate Δf set point. In this interaction regime, the calcite lattice is faintly visible as stripes running along the $[4\,2\,\overline{1}]$ direction, whereby the CO molecules are apparent as dark depressions surrounded by a bright rim. Clearly, two types of CO molecules can be distinguished: The first type (type I, green and blue arrow) is imaged with a smaller diameter than the second type (type II, red and violet arrow).

Figure 45(b) shows the same image as in (a) overlaid with a black grid. The grid lines are equidistant and represent the lattice of a (2×1) reconstructed surface with a periodicity of 1 nm in $[0\,\overline{1}\,0]$ direction and 0.81 nm in $[4\,2\,\overline{1}]$ direction. The grid was slightly sheared to take the imperfections of the piezo scanner into account. The lines of this grid are aligned by using 2D Fourier filtering and by matching the CO positions to equivalent locations inside the (2×1) unit cell as described by the following six steps and as illustrated in figure 46 [44, 207, 208].

In the first step, the raw image was corrected for linear drift by comparing the up and down scan as explained in subchapter 3.6. The result is reproduced in figure 46(a), which is identical to figure 45(a).

As the second step, the 2D Fourier transform (FT) of figure 46(a) was calculated with Gwyddion [140], the absolute value of the amplitude spectral density (ASD) is shown in figure 46(b). Two maxima with a distance of about $(1.04 \pm 0.05)\,\mathrm{nm}^{-1}$ from the centre of the coordinate

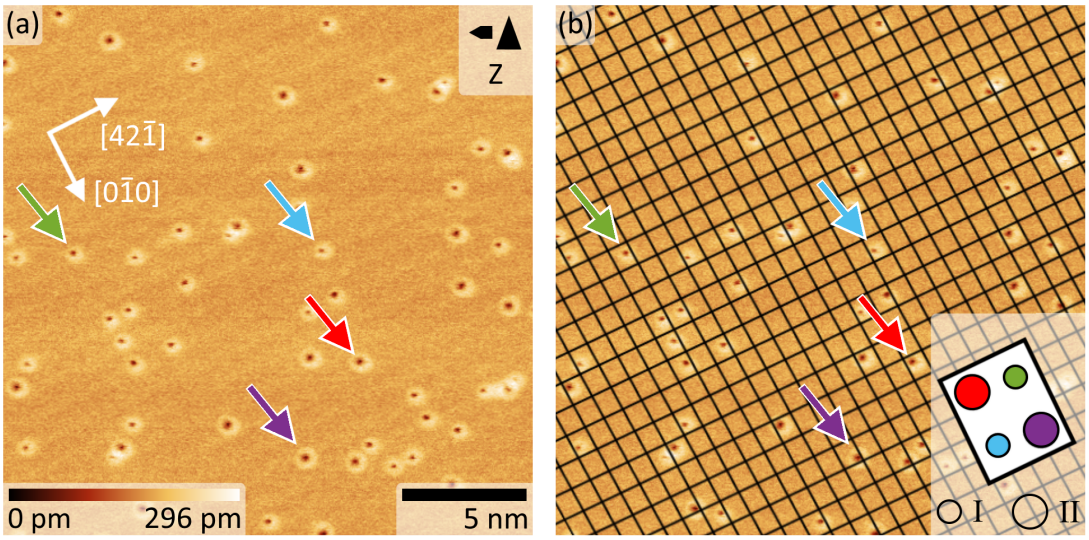

Figure 45: (a) NC-AFM topography image of calcite(104) covered by 0.025 ML (Calcite-012, Ku crystal, $\Delta f = -0.9$ Hz and $U_{tip} = -10$ V). Image data corrected for thermal drift. (b) Same data with a carefully-aligned (2×1) grid as overlay. Inset: Four positions inside the (2×1) unit cell: Green and blue (type I) as well as red and violet (type II). A total of 25, 18, 15, and 10 molecules are found in the green, blue, red, and violet positions, respectively, within this image.

system are marked, they represent lines in the original data (figure 46(a)) with a periodicity of about (0.96 ± 0.09) nm along $[0\,\bar{1}\,0]$. The orientation of the $[0\,\bar{1}\,0]$ and $[4\,2\,\bar{1}]$ directions was determined from the analysing of the birefringence property of the calcite crystal after the measurement, see subchapter 3.5 [27]. Hence, these marked maxima can be assigned to the 1 nm periodicity of the (2×1) unit cells in $[0\,1\,0]$ and $[0\,\bar{1}\,0]$ direction and are, therefore, labelled with (020) and $(0\bar{2}0)$.

In the third step, the amplitude of the periodicity described by the (020) and $(0\bar{2}0)$ coefficients is increased fivefold and the reverse FT image is calculated with the result presented in figure 46(c). The dark and bright stripes occurring in this image have a periodicity of 0.95 nm perpendicular to the $[0\,\bar{1}\,0]$ direction. From a comparison of figure 46(a) and (c) it is obvious that the faintly visible bright stripes in (a) are at the same position as the bright stripes in (c), thus allowing a more precise determination of the CO positions along $[0\,\bar{1}\,0]$ direction. It is clearly visible that some of the CO molecules are positioned on the lower side of the bright stripes while other molecules are on the upper side. These positions do, however, not coincide with the size of the molecules.

In the fourth step, the CO molecules in figure 46(c) are classified into two groups by their apparent size (type I or type II) and in further two groups by their position relative to the bright stripes (lower and upper side). For example, the position of the dark depression of the CO molecules marked by a blue or a violet arrow are on the lower edge of one of the bright

stripes, while the dark depression of the other CO types (green and red arrow) are positioned on the upper edge.

In the fifth step, the amplified striped pattern as well as the different types of CO molecules are used to orient the black grid lines running along the $[4\,2\,\bar{1}]$ and $[0\,\bar{1}\,0]$ directions (figure 46(d)). While the lines running along $[4\,2\,\bar{1}]$ can direct be placed on the bright stripes, another strategy is necessary for lines running along $[0\,\bar{1}\,0]$ as the periodicity along $[4\,2\,\bar{1}]$ is not apparent from the topography or 2D FT data. Instead, the lines running along $[4\,2\,\bar{1}]$ were slightly rotated and their periodicity was slightly reduced until they are running through

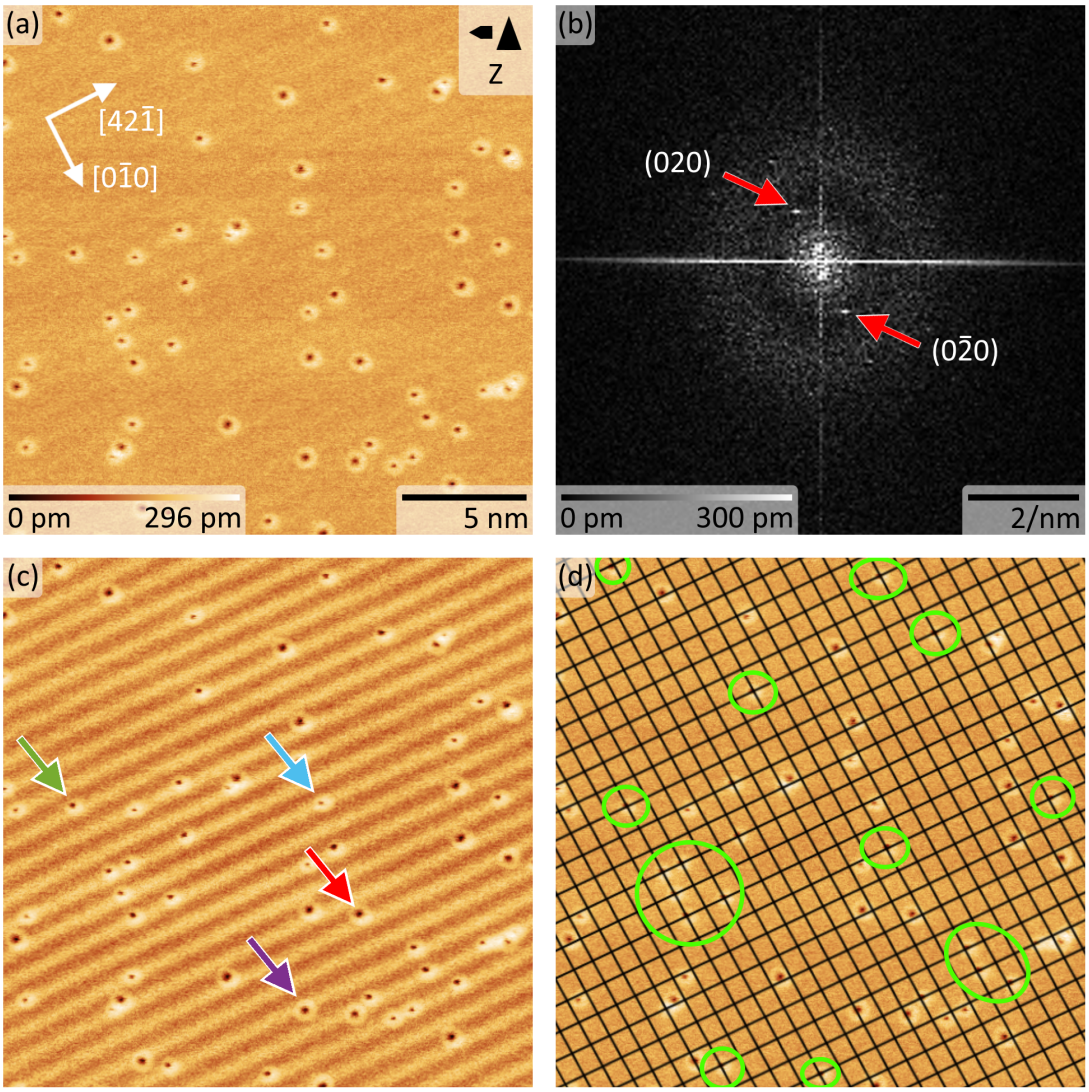

Figure 46: (a) Drift-corrected image of CO molecules on calcite(104) after aligning the up and down (not shown) scan. (b) 2D Fourier transform from (a) with marked (020) and (0$\bar{2}$0) maxima. (c) Data from (a) with fivefold increase of the (020) and (0$\bar{2}$0) components. (d) Data from (a) with a grid aligned to the bright stripes in (c) and with some of the small CO molecules marked by light green ovals.

the CO molecules of the same type as marked by the green ovals. In this placement, the lines have a distance of about 0.8 nm that is in excellent agreement with the unit cell size of 0.81 nm in $[4\,2\,\overline{1}]$ direction. Other rotations and scalings of the lines along the $[4\,2\,\overline{1}]$ direction were treated. However, they did not match either the expected unit cell size or the equivalent CO type.

In the last step, the whole grid is translated in such a way that the dark centres are always located in one of the grid cell corners with the result presented in figure 45(b). This translation reflects a positioning of the grid on the carbonate groups. The CO molecules in these corners are marked by green (top corner), blue (bottom corner), red (left corner), and violet (right corner) circles in the following. From a closer inspection of this image it becomes clear that CO molecules with a similar imaged size are always located in opposite corners within the (2×1) unit cell, namely type I (green/blue) or type II (red/violet). This is abstracted in the inset of figure 45(b), where the positions are indicated by green/blue (red/violet) circles. The same colour code is used for the arrows in figure 45(a).

In conclusion, this analysis gives evidence that there are at least two different adsorption geometries for CO molecules on the calcite(104) surface. CO molecules of the same type are located in opposite corners of the (2×1) unit cell, effectively adapting a chequerboard-like pattern. This arrangement pattern is in full agreement with the properties of Ca ions of the calcite(104)-(2×1) surface that are explained in subchapter 5.3. In the next section it is shown, that the CO molecules also follow the glide plane symmetry of the calcite(104) surface.

6.2.2 High-resolution constant-height measurements of CO/calcite(104)-(2×1)

The CO adsorption at the four positions inside the (2×1) unit cell is further investigated by high-resolution NC-AFM data acquisition with a CO tip. The images shown in figure 47 are measured with the same CO-terminated tip as used in figure 37 and figure 35. The central molecule in figure 47(a) is imaged larger than the other three molecules. In accordance with figure 45 is, therefore, identified as type II, while the others are identified as type I.

Due to the strong repulsive interaction at the dark molecule centres, the tip approaches the surface in topography mode closer than at equivalent positions on the pristine calcite surface. Especially when further reducing the tip-sample distance by increasing the frequency-shift setpoint, lateral manipulation of single CO molecules is frequently observed and the imaging becomes unstable as the tip approaches the CO molecule closely. A similar behaviour has been observed for CO atoms on Cu(111) at 5 K that shows a repulsive centre when measured with a CO-terminated tip [185]. Upon reducing the tip-sample distance, at a certain tip-CO distance the atom is manipulated. Therefore, in order to simultaneously image the calcite

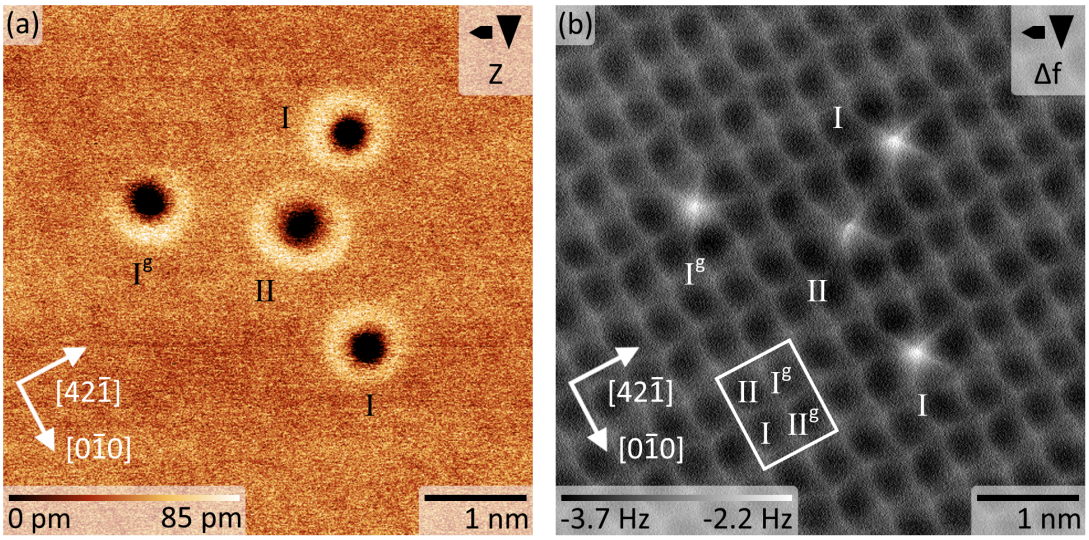

Figure 47: (a) Topography (Calcite-012, Ku crystal, $\Delta f = -2.1\,\mathrm{Hz}$ and $U_{tip} = -10\,\mathrm{V}$) and (b) constant-height frequency-shift data ($U_{tip} = -10\,\mathrm{V}$) of four CO molecules measured on a Ku crystal.

surface and the CO molecular structure while avoiding manipulation of the CO molecules due to feedback instabilities, images in constant-height frequency-shift mode are acquired.

Figure 47(b) shows a constant-height frequency-shift image of the same position on the calcite crystal as imaged in figure 47(a). The pristine calcite surface follows a glide plane symmetry in this frequency-shift image, as is confirmed by the algorithmic symmetry test (figure 35(a)). The four CO molecules are imaged as bright features roughly centred in the dark pores of the calcite lattice, which are assigned to the position of the calcium atoms as explained in subchapter 6.2. A (2×1) unit cell positioned on the carbonate groups is included as a white rectangle and four calcium atom positions I, $\mathrm{I^g}$, II, and $\mathrm{II^g}$ within the (2×1) unit cell can be identified as possible CO adsorption positions. The notation I and $\mathrm{I^g}$ (and II and $\mathrm{II^g}$) reflects the glide plane symmetry property of the unit cell.

The glide plane symmetry of the (2×1) surface predicts a chequerboard-like pattern for the properties at the calcium atom positions as explained in subchapter 5.3. To investigate whether the CO adsorption properties follow this glide plane symmetry of the calcite surface, image subparts around the two CO molecules adsorbed on the positions I and $\mathrm{I^g}$ are extracted from the images of figure 47(a) and (b) and presented in figure 48 with the $[4\,2\,\bar{1}]$ direction pointing upwards. The unit cells marked with white rectangles in figure 47(b) and figure 48(a) and (b) are on equivalent positions relative to the calcite lattice. By comparing the topography images from the CO molecules at adsorption positions I and $\mathrm{I^g}$ in figure 48(a) (blue and green frame), the asymmetry of the bright rim in the topography images follow the glide plane symmetry. In contrast, the bright rim of the CO molecule at position II is

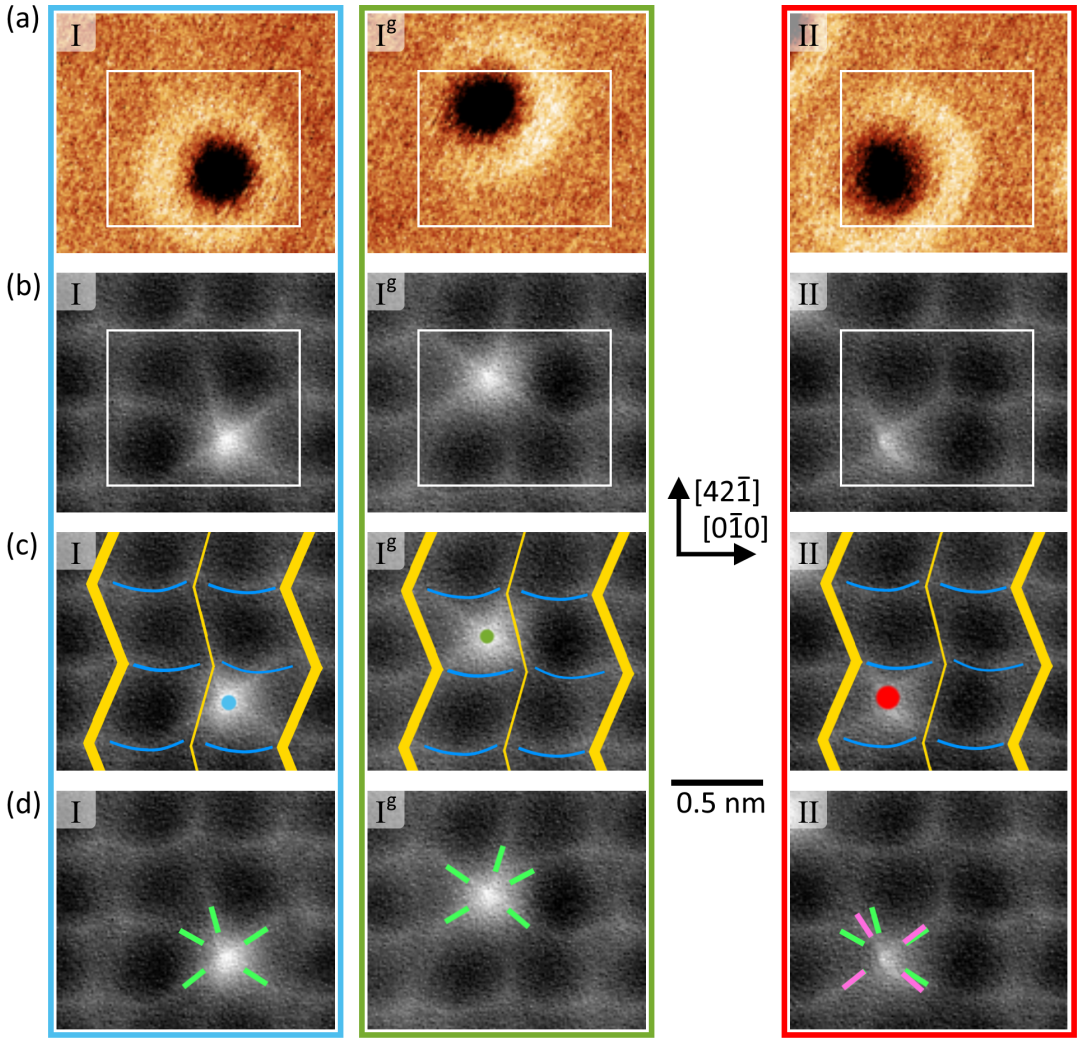

Figure 48: (a) Detailed images of CO molecules at positions I, I^g, and II extracted from figure 47(a), and (d-e) are extracted from figure 47(b). (c) and (d) are the same image data as in (b) but with markers for different features specific to CO molecules on calcite(104). The blue and yellow lines in (c) mark the same features as in figure 33(c). All images oriented with [4 2 $\bar{1}$] pointing upwards. The coloured frames connect detail images of the same CO molecule and follow the colour-code from figure 45.

larger and more homogeneous than the rim of the CO at position I.

The glide plane symmetry is also visible in the constant-height frequency-shift images in mainly three properties of the fine substructure of the CO molecules (figure 48(b-d)):

(i) The brightness of the CO molecules in the NC-AFM images are different. The molecules at adsorption positions I and I^g show almost the same brightness. In contrast, the CO molecule at position II is imaged slightly darker (figure 48(b)).

(ii) The positions of the centres of the imaged CO molecules are different. The centres for

the molecules at adsorption positions I and I^{g} are closer to a smaller line that runs in $[4\,2\,\overline{1}]$ direction, as marked by the blue and green point in figure 48(c). But, the centre of the CO molecule of type II (red point) is rather in the centre of a dark pore.

(iii) The sharp filaments of the CO molecule in the constant-height images follow the glide plane symmetry properties of the calcite(104)-(2×1) surface. The positions of these filaments for the CO molecule of type I are marked in figure 48(d) with light green lines. If these lines are glide reflected then they also fit to the positions of the filaments of the CO molecule of type I^{g}. In contrast, these green lines do not fit to the positions of the filaments of the CO molecule of type II that are marked by magenta lines.

On an unreconstructed (1×1) surface, position II would be identical to position I, consequently, there would be no difference in the properties of the CO molecules. However, the CO molecules at position I and II instead appear different. Therefore, it can be concluded that the (2×1) reconstruction of the calcite(104) surface influences the adsorption properties of the CO molecules.

Unfortunately, a comparison between the CO molecule on position II^{g} to the other three positions is not possible within this series as imaging a CO molecule at position II^{g} in constant-height mode with the same quality at the others did not succeed[3]. In most images, the CO molecules on position II and especially II^{g} are remarkable underrepresented. For example, in eight constant-height frequency-shift images, where no tip induced manipulation of the CO molecules was observed, 28 CO molecules of type I, 30 molecules of type I^{g}, 20 molecules of type II, but only 11 molecules on position II^{g} were found. Still, no violation of the glide plane symmetry relation is evident from positions II^{g} and II in figure 45. From now on, the CO molecules are, therefore, named according to their adsorption positions on the calcite(104) surface.

To identify the adsorbed CO molecules, a model sketch of the calcite(104) surface is introduced that is presented in figure 49(a). This sketch is based on the calcite lattice structure and the CO adsorption positions as identified before in figure 47(b) and repeated in figure 49(b) with the overlaid sketch. The black lines of the model sketch in figure 49(b) follow the bright lines of the calcite(104) surface. Every second zig-zag line in the sketch is drawn as a double line in order to reflect the (2×1) reconstruction, in particular the wider lines imaged along the $[4\,2\,\overline{1}]$ direction. Additionally, the adsorption positions of the CO molecules are marked in the sketch by dots. Their different colours and sizes follow the colour-code of the CO molecules introduced in figure 45(b) and the different diameters of the imaged CO molecules

[3] A constant-height frequency-shift image of a CO molecule of type II^{g} is visible in figure 57(c). However, due to reduced contrast likely caused by a non-optimum tip, the image is difficult to compare with the data presented in figure 47(c)

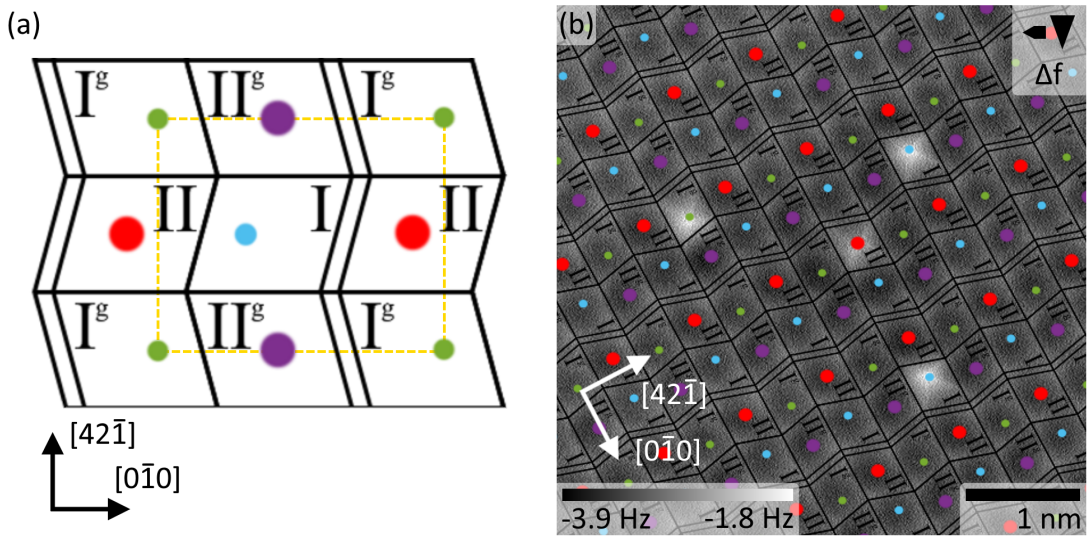

Figure 49: (a) Model sketch of the calcite surface with marked CO adsorption positions. The yellow rectangle indicates a (2×1) unit cell. The model is based on the calcite lattice structure and the CO adsorption positions identified in figure 47(b) as shown in (b).

in figure 45(a). The positions of the dots are named in the same way as the positions of the CO molecules in figure 47(b). For these positions, the maximum of the repulsive centres of the imaged CO molecules are used and periodically repeated as visible in figure 49(b). As visible in this image, the red and green (violet and blue) dots are aligned in a zig-zag pattern in $[4\,2\,\bar{1}]$ direction.

In conclusion, in this section it is shown that CO molecules adjacent in $[0\,\bar{1}\,0]$ direction are imaged differently, indicating that these molecules follow a (2×1) reconstruction (CO molecules of type I and II), while a glide plane symmetry is found between CO molecules of type I and I^{g}. Hence, CO molecules on calcite(104) follow the glide plane symmetry of the calcite(104) surface. This finding is further confirmed in the next subchapter, by investigating the tilt of these molecules.

6.3 Orientation and tilt of single CO molecules on calcite(104)

The difference between CO type I and II is most clearly apparent when investigating the interaction between the CO adsorbed on the calcite(104) surface and the CO at the tip apex with respect to the tip-sample distance and lateral position in so-called slice measurement. For the data acquisition of a slice, the start- and endpoint are specified in the measurement software and a total of N $\Delta f(z_p)$-curves are acquired at equidistant positions along the direct path. Results are shown in figure 50. Slice (A) consists of a total of 375 $\Delta f(z_p)$-curves acquired along the $[0\,\bar{1}\,0]$ direction using a lateral path where both molecules of type II and I

are crossed, as marked by the white line (A) in figure 51(a). Slices (B) and (C) consist each of a total of 200 $\Delta f(z_p)$-curves acquired along the $[\overline{4}\,\overline{2}\,1]$ direction, crossing the molecule of type II and I, respectively, as indicated by the white lines (B) and (C). In order to fulfil the convention regarding the orientation of the coordinate system in this thesis, data in slices (B) and (C) in figure 50 are mirrored along the horizontal axis such that $[4\,2\,\overline{1}]$ points to the right.

The three specified paths for the three slices are included as white lines in figure 51(a) and marked by the same capital letter as in figure 50. However, due to thermal drift, lateral piezo creep, and imperfections of the piezo scanner, the real lateral positions of the slices are usually slightly different to the specified path. To identify the real positions, a Matlab script was developed that searches for the smallest mean squared error between values extracted from the slice data (here at $z_p = 0\,\text{nm}$) and a family of curves extracted from the constant-height frequency-shift data (figure 51(a)). This family is generated by varying both the start and end point of each slice by ± 45 pixel in the fast and slow scan directions in the XY image.

The sample temperature measured during the acquisition of the image (figure 51(a)) and slice data (figure 50) is shown in figure 51(g). Throughout the measurement, the temperature changes only by about 2 mK. Therefore, due to this very small temperature change, no significant thermal drift is expected and, therefore, some degrees of freedom such as compression or non-linear behaviour of the $\Delta f(z_p)$-curve positions are not considered for the alignment. To reduce the calculation time, non-linear drift and a possible tilt of the slice was neglected, and only the start and end point of a slice was shifted, the intermediate points were interpolated using Bresenham's line algorithm [209].

The absolute tip-sample distance of the constant-height frequency-shift image (figure 51(a)) and of the slices at $z_p = 0\,\text{nm}$ would nominally be identical. However, due to piezo creep along the z_p axis caused by the repetitive movement of the tip in z_p direction during the acquisition of the $\Delta f(z_p)$-curves, the values nominally at $z_p = 0\,\text{nm}$ of the slices are acquired at a slightly larger distance than the image, resulting in slightly larger Δf values. To numerical compare between the profiles extracted from image and slice data the Δf values from the slices are reduced by an offset of 0.14 Hz, 0.19 Hz and 0.2 Hz for slice (A), (B) and (C), respectively, and for the tip-sample distance for the constant-height frequency-shift image $z_p = 0\,\text{nm}$ is used. This procedure has only a minor influence on the finding of the optimum slice positions, because the shape of the profiles extracted from the slices and of the values at the optimum lateral shift from the Δf image are similar as visible in the three images in figure 51(b)-(d).

The coloured lines in figure 51(a) represent the slice positions where the values from the constant-height image and the values extracted from the slices at $z_p = 0\,\text{nm}$ have the lowest

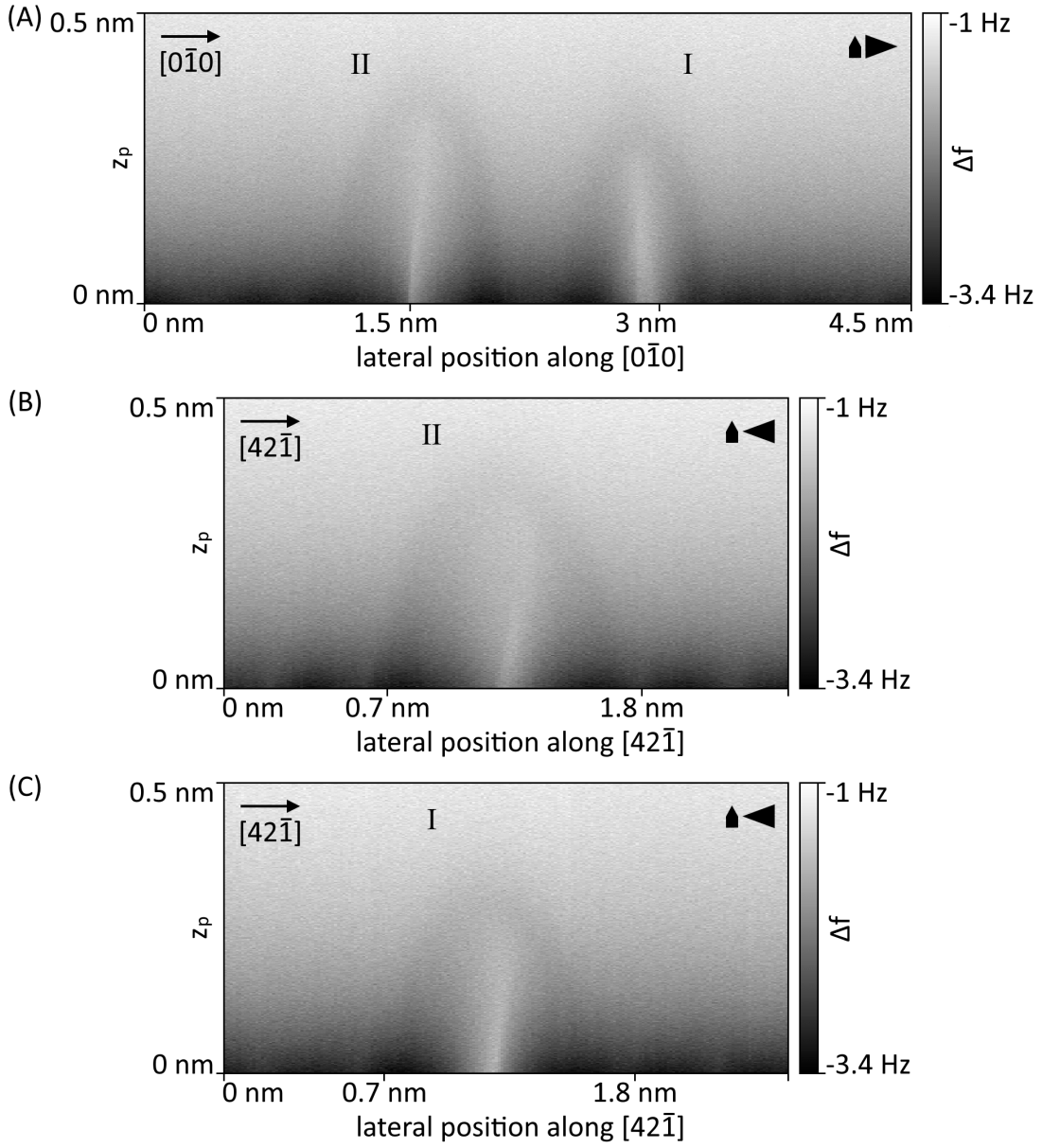

Figure 50: (A) Slice data acquired along the $[0\,\bar{1}\,0]$ direction across the different CO molecules of type I and II (total of 375 $\Delta f(z_p)$-curves). (B) Slice data along the $[4\,2\,\bar{1}]$ direction across a CO molecule of type II (total of 200 $\Delta f(z_p)$-curves). (C) Slice data along the $[4\,2\,\bar{1}]$ direction across a CO molecule of type I (total of 200 $\Delta f(z_p)$-curves). The positions of the slices are marked in figure 51(a) with white lines. (C) and (B) are flipped horizontally compared to the data acquisition order.

mean squared deviation from each other. Line (A) is shifted five pixels to the right with respect to the chosen coordinates, highlighted by the magenta line. Line (B) is shifted three pixels to both the right and up direction as highlighted by the blue line, and line (C) is shifted six pixels to the right and four pixels up, see green line. The values extracted from the slices at $z_p = 0\,\text{nm}$ (magenta, blue, and green lines) as well as the values extracted from

the image data at the position of the coloured lines in figure 51(a) (grey lines) are reproduced in figure 51(b–d) and show an excellent agreement.

To further confirm the accuracy of the slice position determination, a second criterion of comparing specific $\Delta f(z_p)$-curves is used. In particular, it is tested whether the $\Delta f(z_p)$-curves of the slice data at the intersections of the coloured lines in figure 51(a) are identical

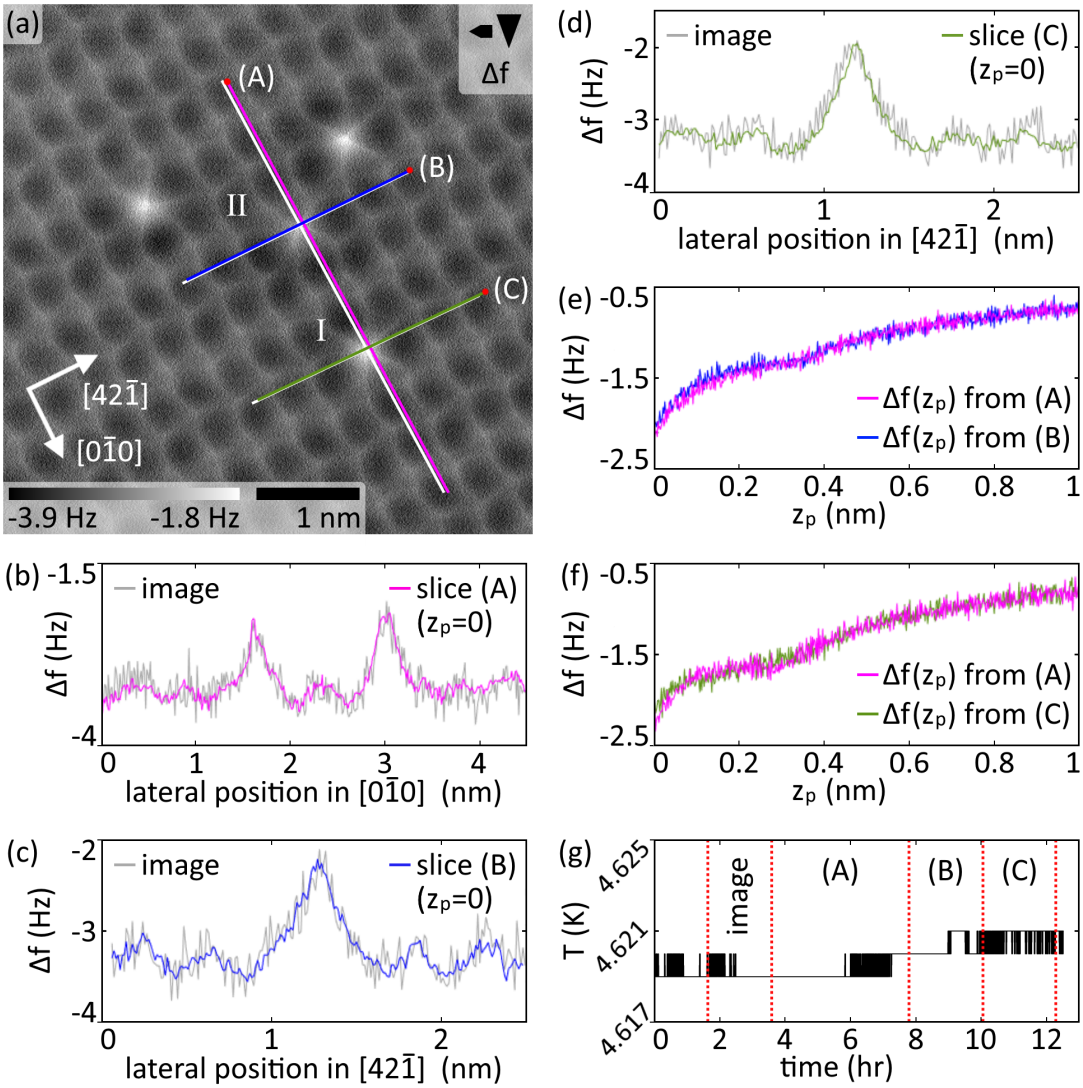

Figure 51: (a) Δf image with the specified slice data positions marked with white lines and the real positions with coloured lines. The red dots mark the data acquisition starting points of the slices. (b-d) comparison between the values extracted from the Δf image (grey) and the slice data at $z_p = 0\,\text{nm}$ (magenta for slice (A), blue for slice (B), and green for slice (C)). The values of the slice data are reduced by 0.14 Hz, 0.19 Hz and 0.2 Hz for (b), (c) and (d), respectively. (e and f) comparison between the $\Delta f(z_p)$-curves of the slice data at the intersection positions. (g) Temperature of the calcite sample during data acquisition of the calcite(104) image in (a) and of the slices. The steps are caused from the bit resolution of the temperature measurement. The capital letters inside all images are assigned to the capital letters of the images in figure 50.

as these $\Delta f(z_p)$-curves are acquired at the same lateral position. Thus, this comparison can reveal imperfections of the relative slice position determination. The $\Delta f(z_p)$-curves extracted at the intersection of slices (A) (magenta line in 51(e)) and (B) (blue line) as well as the curves extracted at the intersection of slices (A) and (C) (green line) are reproduced in figure 51(e) and (f), respectively. The excellent match of these curves relative to each other show that the slices are correctly aligned with respect to each other. Therefore, it can be concluded that the coloured lines clearly represent the real positions of the slice data.

Tilt of single CO molecules on calcite(104)

In all slice data in figure 50 a weak attractive regime around a strong and sharp repulsive centre is revealed at the places of the CO molecules. This finding is similar to previous measurements of CO/Cu(111), where the attractive regime is mostly assigned to van der Waals interactions between the CO molecules, while the repulsive forces in the centres are assigned to chemical repulsion [134, 185]. The appearance of molecule II in the slices appears higher and wider than molecule I, in agreement with the different CO sizes found in figure 45. The repulsive centre of both CO molecules in figure 50(A) shows a slight tilt with respect to the surface normal. Most important, the orientation of this tilt along $[0\,\overline{1}\,0]$ is different for the two molecules of type I and II. The apparent tilt of CO type I is in $[0\,1\,0]$ direction (to the left in the slice), while CO type II appears tilted in $[0\,\overline{1}\,0]$ direction (to the right). In figure 50(B) and (C), the repulsive centre of both CO molecules tilt in the same direction along the $[4\,2\,\overline{1}]$ direction. As the tilt orientation differs within the same data set (figure 50(A)) a measurement artefact due to an asymmetric CO tip can be excluded.

Assuming that the tilt of the repulsive interaction centre in the slice data of figure 50 represents the geometrical tilt of the physical CO molecule in $[\overline{4}\,\overline{2}\,1]$ and $[0\,\overline{1}\,0]$ direction, the geometrical tilt angle can be calculated from the measured tilt components. In the following, the coordinate system presented in figure 52(a) is used to calculate this geometrical tilt for the CO molecules. The $[\overline{4}\,\overline{2}\,1]$–$[0\,\overline{1}\,0]$ plane in this coordinate system is parallel to the calcite surface and represents the $z_p = 0\,\mathrm{nm}$ plane and, thus, the plane where $z_p = 0$ of the slices is located. The magenta arrow passes through the centres of the oxygen atom and of the carbonate atom of the surface adsorbed CO molecule. The point at $z_p = 0\,\mathrm{nm}$ on this magenta vector is selected as origin of the coordinate system and of the magenta vector. Θ is the angle between the surface normal vector ($\vec{n}$) and the magenta vector and represents, therefore, the inclination of the CO molecule. The angles α and β are the projections of Θ on the plane spanned by the $[\overline{4}\,\overline{2}\,1]$ direction and $\vec{n}$ and the plane spanned by the $[0\,\overline{1}\,0]$ direction and $\vec{n}$, respectively, and represent the tilt-components visible in the slice data with respect to the surface normal. Following conventions are used in the further procedure: The angle α and (β) is indicated positive if α (β) tilts in $[\overline{4}\,\overline{2}\,1]$ ($[0\,\overline{1}\,0]$) direction. The blue vector

in figure 52(a) is the projection of the magenta vector on the $z_p = 0\,\text{nm}$ plane. This vector encloses the angle φ with the $[\bar{4}\,\bar{2}\,1]$ axis, whereby φ defines the azimuth of the CO molecule orientation and is positive for counter-clockwise orientation.

The process to determine the orientation of the repulsive CO image in 3D is described by exemplary using the slice data of the CO type II shown in figure 50(B); the process itself is visualised in figure 52(c). Line profiles at the heights (z_p) of 0 nm, 0.05 nm, 0.1 nm, 0.15 nm and 0.2 nm (orange lines in figure 52(c)) are extracted and the centre of the features is determined by a total of four methods explained in the following. A section around the repulsive centre of the extracted line profile for $z_p = 0\,\text{nm}$ is shown in figure 52(b). In this

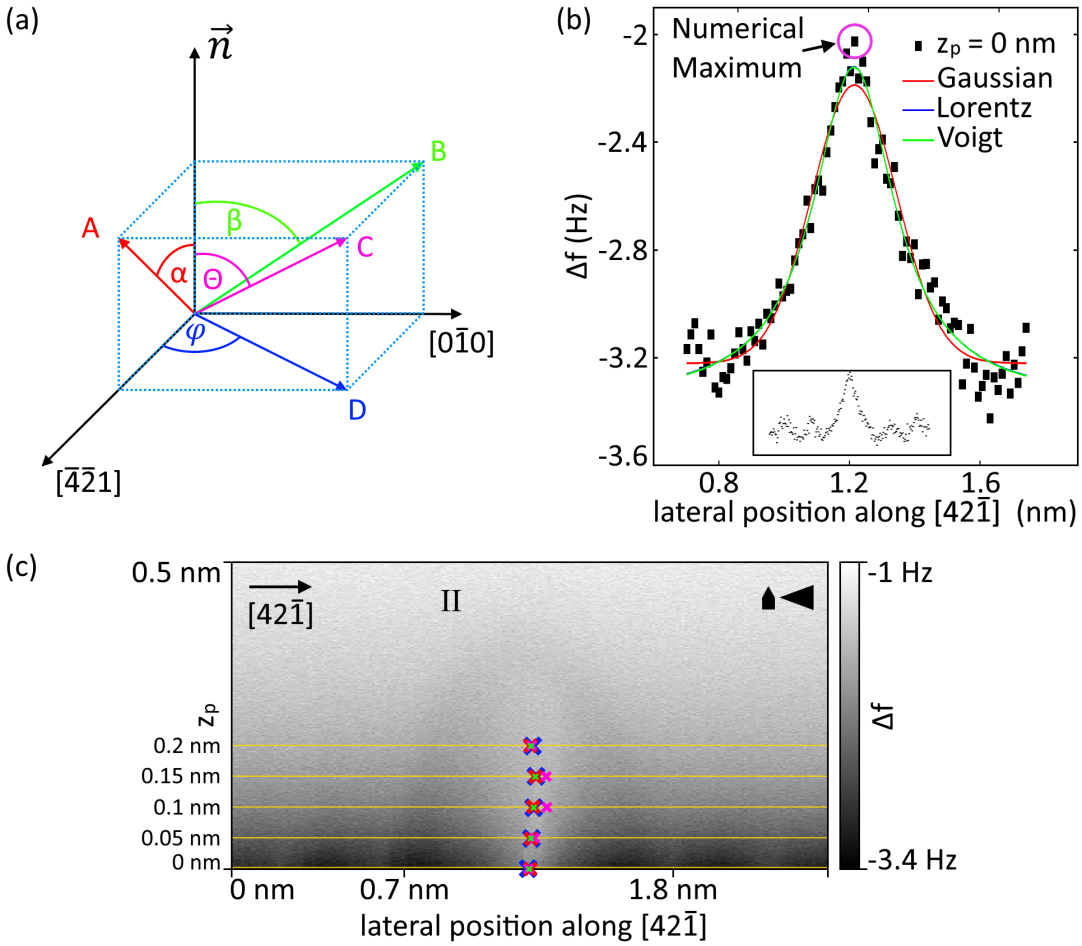

Figure 52: (a) Coordinate system used for the determination of the tilt angle of the CO molecule image. (b) Line profile from the slice in (c) at $z_p = 0\,\text{nm}$ with fitted Gaussian, Lorentz and Voigt distribution. Additionally, the numerical maximum is marked. The full line profile as extracted from the slice is visible in the inset. (c) Slice of CO type II (figure 50(B)). Heights where line profiles were extracted are marked with orange lines. The centre of the features determined by the different methods (red – Gaussian, blue–Lorentz, green–Voigt, magenta–numerical maximum) are marked by crosses.

plot, the repulsive centre of the feature in (c) is clearly visible as a maximum. With the aim to determine the lateral position of the maximum with lack of the functional description, Gaussian, Lorentz, and Voigt functions are used as approximations, included as red, blue and green curves. The centre positions of these functions after fitting to the data are then used as the lateral centre of the feature. Additionally, the numerical maximum (magenta circle) is used as fourth approach to approximate the feature centre. The results for all methods and for all heights are marked with crosses in figure 52(c) with the same colours for the different methods as used in (b). The Gaussian, Lorentz and Voigt functions produce very similar positions for the centre of the feature, likely because the shape of these three functions is very similar. Instead, the positions determined by the method of numerical maximum for the heights $z_p = 0.1\,\text{nm}$ and $0.15\,\text{nm}$ are slightly shifted in $[4\,2\,\overline{1}]$ direction, probably indicating a small asymmetry in the graph, which can not be considered by the three symmetric functions. Noticeable, the determined centres of feature are not on a straight, but on a slightly curved line that is bend in $[4\,2\,\overline{1}]$ direction for all methods. From the points marked in figure 52(c), the angle α_{II} can be calculated for all four methods. The lateral position at $z_p = 0\,\text{nm}$ is used as the origin and connected to the other points by vectors. Using the dot product, the angles between the surface normal an these vectors can be calculated and averaged for all four methods separately. The results, listed in table 7, are similar for three methods, while the numerical maximum delivers a larger α_{II}.

Together with the angle β_{II}, which can be determined from the slice data aquired for CO type II in figure 50(A) by the same strategy, the inclination and azimuth of the CO molecule type II can be calculated. For this, the points A (B) are introduced in figure 52(a) to be positioned in the plane spanned by the $[\overline{4}\,\overline{2}\,1]$ and $\vec{n}$ ($[0\,\overline{1}\,0]$ and $\vec{n}$) directions, defining the end points of the red (green) vector. The red vector is mainly defined by the angle α and can be written as $\vec{A} = [h \cdot tan(\alpha), 0, h]$, while the green vector is defined by β and can be written as $\vec{B} = [0, h \cdot tan(\beta), h]$. Here, h is the height of A and B along the direction of the normal vector, which can be chosen arbitrarily ($h \neq 0$) because h only affects the lengths of the vectors but not the angles between the vectors. Using the points A and B, a cuboid can be formed as drawn in figure 52(a) by the light blue dotted lines. The magenta vector ends on point C, which lies in one of the cuboid corners and can be defined from the components of $\vec{A}$ and $\vec{B}$ as $\vec{C} = [h \cdot tan(\alpha), h \cdot tan(\beta), h]$. The projection of C on the $z_p = 0\,\text{nm}$ plane is defined by point D, which is the end point of the blue vector, and can be written as $\vec{D} = [h \cdot tan(\alpha), h \cdot tan(\beta), 0]$. By using the dot product, the angle Θ can be calculated by

Method	Gaussian	Lorentz	Voigt	Numerical Maximum
α_{II} (°)	-9±2	-10±2	-8±3	-27±7

Table 7: Mean values of the results of the different methods for α_{II}.

the magenta vector ($\vec{C}$) and the surface normal $\vec{n}$ to:

$$\Theta = cos^{-1}\left(\frac{\vec{C}\cdot\vec{n}}{|\vec{C}|\ |\vec{n}|}\right). \tag{16}$$

Substituting $\vec{C}$ and $\vec{n}$ and simplifying the equation results in:

$$\Theta = cos^{-1}\left(\frac{|cos(\alpha)\cdot cos(\beta)|}{\sqrt{cos^2(\alpha)+sin^2(\alpha)\cdot cos^2(\beta)}}\right). \tag{17}$$

In full analogy to equation 16 and 17, the angle φ between the vector ($\vec{D}$, blue) and the $[\overline{4}\,\overline{2}\,1]$ axes can be calculated to:

$$\varphi = 90 - sign(cos(\alpha))\cdot sin^{-1}\left(\frac{sin(\alpha)\cdot|cos(\beta)|}{\sqrt{cos^2(\alpha)\cdot sin^2(\beta)+sin^2(\alpha)\cdot cos^2(\beta)}}\right). \tag{18}$$

Note that φ becomes to $360° - \varphi$ if β is negative, this is a result of using the dot product.

The results for Θ_{II} and φ_{II} are listed in table 8, together with Θ_I and φ_I are calculated from the features of the CO molecule of type I, which is visible at the right side of figure 50(A) and in figure 50(C). For nearly all methods, the angles show remarkable similarity, except Θ_{II} and its error calculated from the numerical maximum, which are significant larger than the others.

Θ_I and especial φ_I are again similar for all methods except Θ_I, which is significant larger when using the numerical maximum method.

An overview of the results using all four methods for CO molecules of type I and II is graphically represented in figure 53. In this figure, Θ and φ are abstracted by circular sectors. The bisection of the circular sectors indicates the direction of the CO tilt (φ), while the angular aperture gives the error of φ. The inclination of the CO molecule (Θ) is

	Gaussian	Lorentz	Voigt	Numerical Maximum
Θ_I (°)	17±2	18±2	18±2	27±9
φ_I (°)	227±7	227±6	227±6	230±20
Θ_{II} (°)	9±2	10±2	8±2	28±7
φ_{II} (°)	170±20	170±10	170±20	170±10

Table 8: Results for Θ and φ resulting from applying different methods for the CO molecules of type I and II.

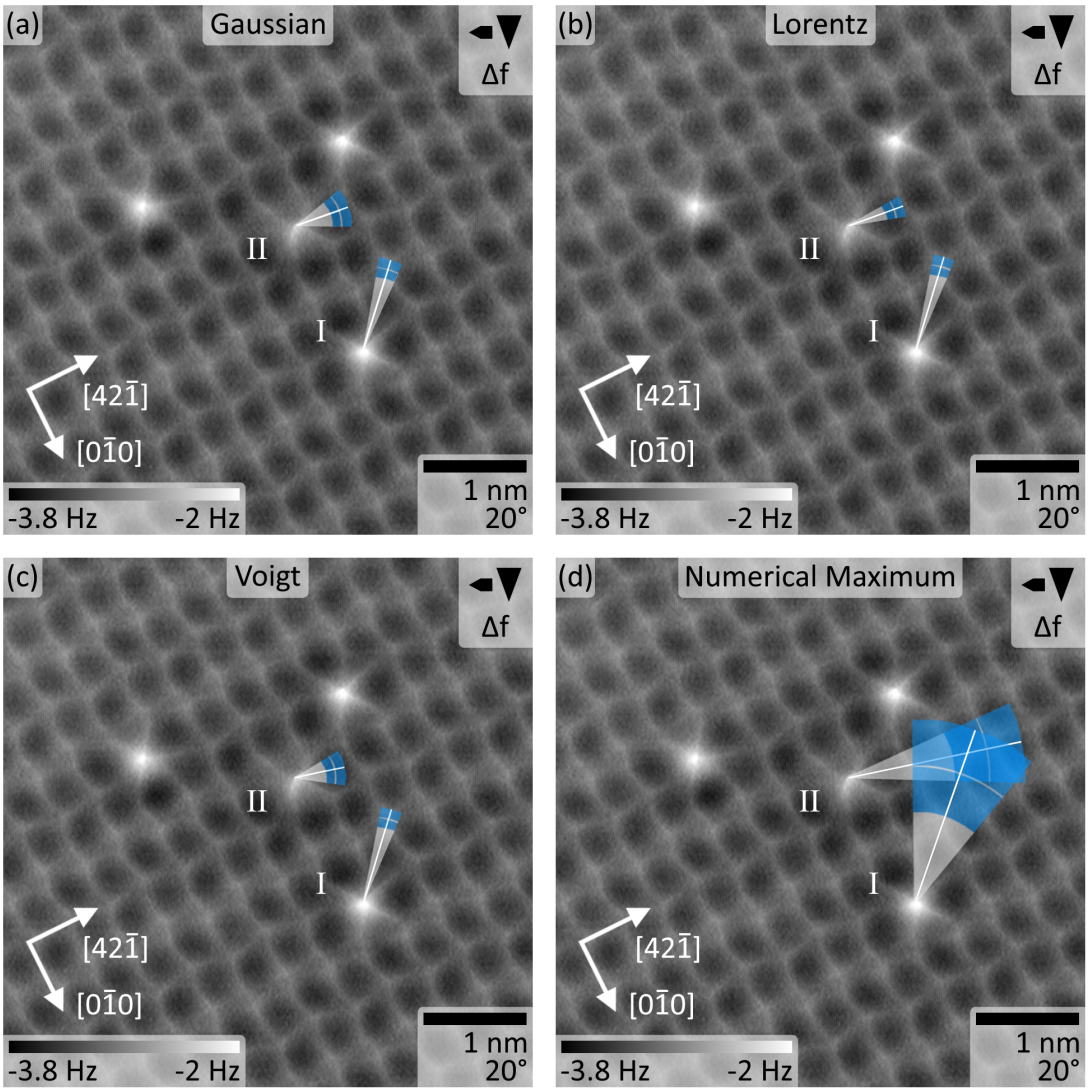

Figure 53: Overview over Θ and φ represented by circular sectors for the four methods.

represented by the radius (1 nm corresponds to 20°) of the white circular arc, whereby the error of Θ is indicated by the blue area. The similarity of the results for Θ and φ using the fits are directly apparent from figure 53(a–c), while the larger circular sector in (d) indicates larger errors for the method with the numerical maximum.

In conclusion, from the features in the slices of figure 50 it was able to calculate a tilt that is assigned to the physical tilt of the CO molecule, which is adsorbed on the calcite(104) surface. These tilt is different for the CO molecules of type I and II and further confirm the finding that these two molecules have a different adsorption geometry.

6.4 Apparent bonds between CO molecules on adjacent adsorption positions

Up to now, only CO molecules on calcite(104) are considered that are separated from each other. Now, a closer look is taken on CO molecules that are adsorbed on a dimer (adjacent adsorption positions) on the calcite(104) surface, whereby apparent bonds are visible in NC-AFM constant-height frequency-shift data. An example of such an apparent bond is given in figure 54(b), which is a detail image of the area marked by a yellow dashed rectangle in figure 54(a). In figure 54(b), two CO dimers are present, each formed by two CO molecules adjacent along the $[0\,\bar{1}\,0]$ direction. Both dimers are formed by one CO molecules of type I and one of type II. These types are determined by the sketch in figure 49(a). The lower dimer (types II–I along $[0\,\bar{1}\,0]$) shows an apparent bond connecting the two molecules, while the molecules are imaged separately in case of the upper dimer (I–II). In this subchapter it is shown that a II–I dimer is one of a few cases where an apparent bond is visible, and a possible explanation based on a distance argument is given.

Three representative constant-height frequency-shift images are reproduced as examples in figure 55(a), (c), and (e). Several dimers are present, and some of these dimers express an apparent bond. In figure 55(b), (d), and (f) the images from figure 55(a), (c), and (e) are reproduced overlaid with the sketch from figure 49(a). The sketches in the images (b) and (d) are oriented directly following the direction of the imaged $[4\,2\,\bar{1}]$ and $[0\,\bar{1}\,0]$ direction as well as the visible zig-zag lines in $[4\,2\,\bar{1}]$ direction. It would also be possible to position the model

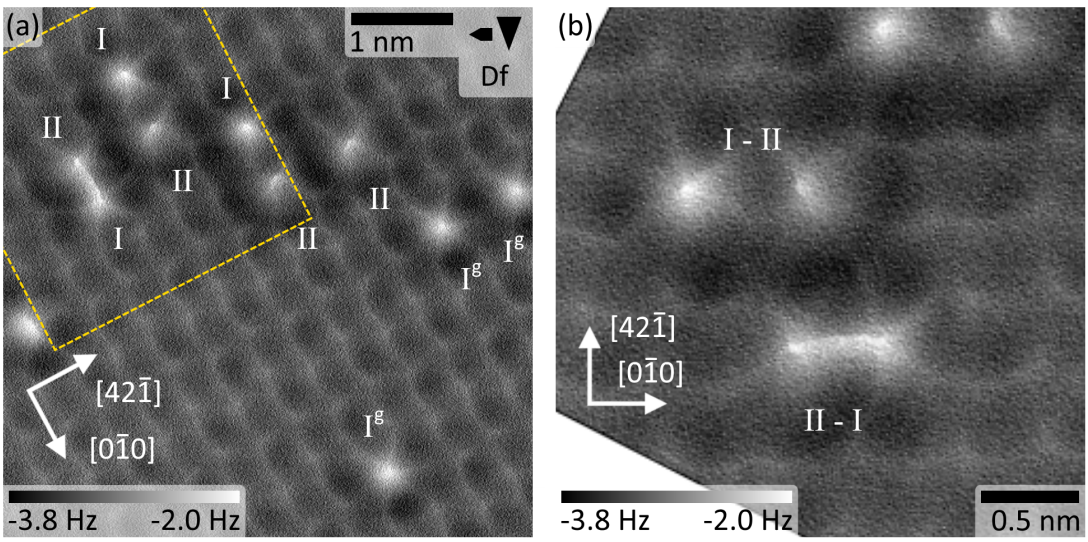

Figure 54: (a) NC-AFM constant-height image of single CO molecules as well as CO dimers on calcite(104) (Calcite-012, Ku crystal, $U_{tip} = -10\,\mathrm{V}$). (b) Detail image extracted from (a) showing dimers of type I–II and II–I.

sketch relative to the different CO molecules only, because the calcite(104) surface bequeaths the (2×1) reconstruction and the glide plane symmetry to the adsorbed CO molecules as shown in subchapter 6.2. In particular, the CO molecules on the four adsorption positions I, II, I^g, and II^g are distinguishable from each other by their imaged size and by their positions inside the zig-zag pattern of the CO molecules in $[0\,\overline{1}\,0]$ direction. While this assignment directly agrees with the positioning in (b) and (d) it is used to position the model sketch in (f), where only the imaged CO molecules with their different sizes are clearly revealed. In the next step, the CO molecular type and, thus, the dimer types can directly be identified with the model sketch. The name of the molecules that are participating in dimers are written next to the molecules. Additionally, the dimers are marked by green and red lines: A green line indicates the presence of an apparent bond, while a red line marks nearby molecules without an apparent bond. All dimers found in figure 55(b), (d), and (f) are marked in the model sketch in figure 56.

Following a naming system is introduced to name the dimers: A–B [direction], whereby A and B denote the CO type (either I, II, I^g, or II^g) and [direction] the direction along which the molecules are adjacent, namely $[\overline{4}\,\overline{8}\,1]$, $[0\,\overline{1}\,0]$, $[4\,\overline{4}\,\overline{1}]$, or $[4\,2\,\overline{1}]$. For example: The dimer without an apparent bond in figure 54(b) is called a I–II $[0\,\overline{1}\,0]$ CO dimer, while the dimer with an apparent bond is a II–I $[0\,\overline{1}\,0]$ CO dimer.

As can be seen in figure 56 a total of 14 dimers were found: Eight of them express an apparent bond, while six dimers do not. Three dimers were not found in the NC-AFM images and are, therefore, not marked with a line in figure 56. It is remarkable that apparent bonds are never found between adjacent CO molecules separated by a wider line of the calcite surface (figure 56, red lines on the right side). For example, the dimers I–I^g $[\overline{4}\,\overline{8}\,1]$ and I–II $[0\,\overline{1}\,0]$ are imaged without an apparent bond. Instead, apparent bonds are only measured at adsorption positions separated by a narrow line, two examples are the dimers I^g–I $[\overline{4}\,\overline{8}\,1]$ and II–I $[0\,\overline{1}\,0]$.

A possible explanation for these observations are the different dimer lengths. In case of the red marked dimers, the separation between the CO molecules are always larger than for the green marked ones. In particular, the CO molecules that are separated by a wider line of the calcite model are further away from each other. The distance between the two maxima of the repulsive centres is used for quantifying the distance between two CO molecules. An apparent bond is observed to always start (end) at one of these centres. The longest dimers that express an apparent bond are the two glide plane related dimers I^g–I $[4\,\overline{4}\,\overline{1}]$ and I^g–I $[\overline{4}\,\overline{8}\,1]$ with a length of (0.49 ± 0.03) nm (average of 15 dimers). The shortest dimers without an apparent bond are the dimers I–II $[0\,\overline{1}\,0]$ and II^g–I^g $[0\,\overline{1}\,0]$, also related via glide plane symmetry, with a length of (0.62 ± 0.07) nm (average of 12 dimers). This finding indicates that the presence

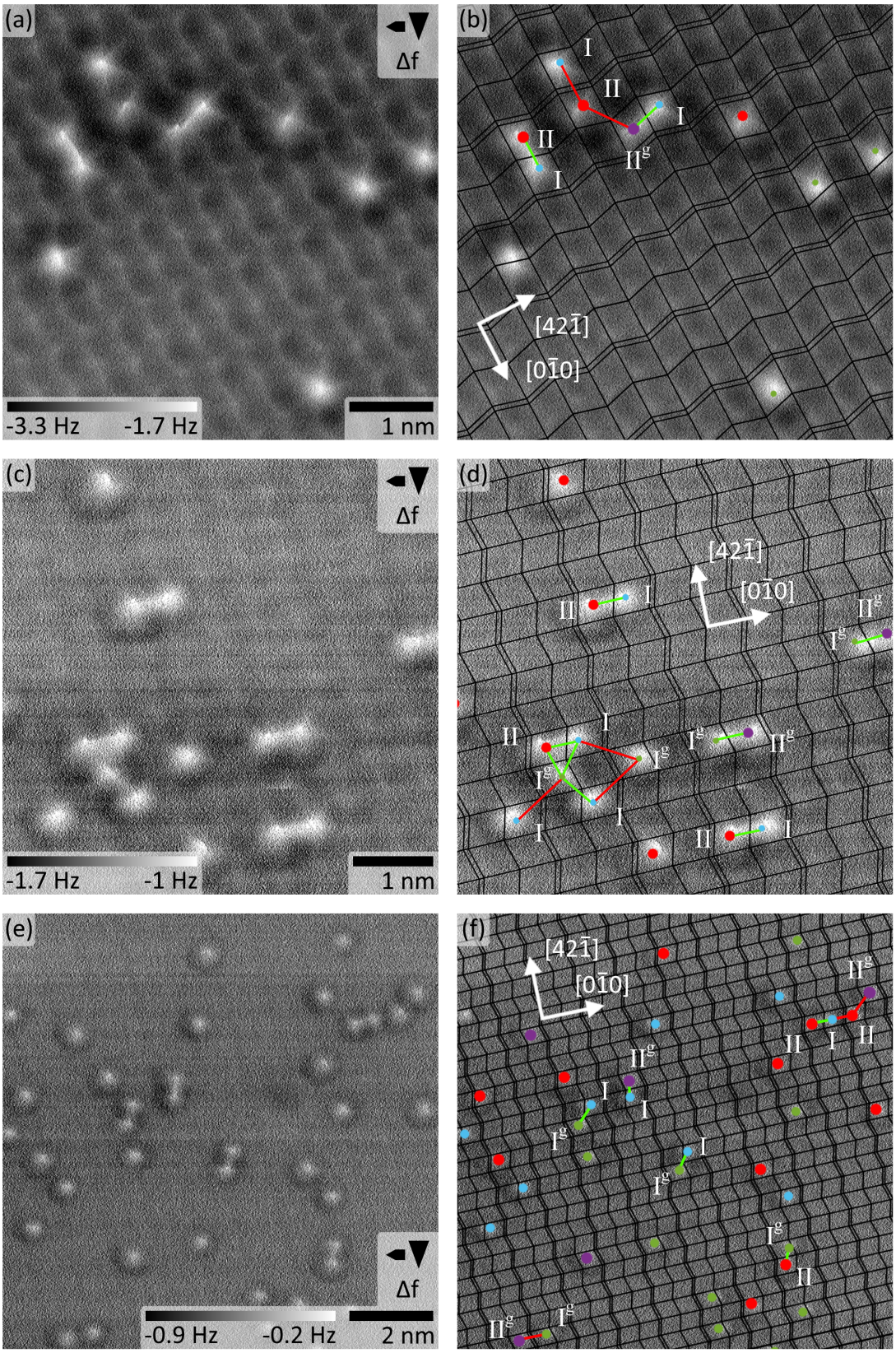

Figure 55: (a), (c) and (e) constant-height frequency-shift images of CO/calcite(104) (Ku crystal) acquired with CO functionalised tips. (b), (d) and (e) same images with overlaid sketch of the calcite surface. Dimers are marked green if they express an apparent bond and are marked red otherwise. Measurement parameters (a) $U_{tip} = -10\,\mathrm{V}$, Calcite-12, (c) $6\,\mathrm{V}$, Calcite-14, (e) $4.5\,\mathrm{V}$, Calcite-14.

of apparent bonds is mainly a matter of the distance between the two CO molecules. It is widely accepted that CO functionalised tips can indicate bonds between non-bonded features [176, 177]. The appearance of such a bond can rather be an effect of the proximity of two atoms and is not the result of a chemical bond. Therefore, it can be assumed that the apparent bonds of adjacent CO molecules on calcite(104) are only a CO tip induced effect, whereby CO dimers with a CO-CO distance shorter than (0.49 ± 0.03) nm appear with an apparent bond in NC-AFM.

This effect of the proximity of two atoms could be amplified by the tilt of the CO molecules. In figure 56, the blue arrows indicate the tilt direction and the tilt angle of the CO molecules as an average of the results listed in table 5 and 6 in subchapter 6.3. Between two wider lines, the CO molecules II and I^g tilt in $[0\,\bar{1}\,0]$ direction, while the molecules II^g and I tilt in $[0\,1\,0]$ direction. This effect could be especially relevant for the cases II–I $[0\,\bar{1}\,0]$, and I^g–II^g $[0\,\bar{1}\,0]$ dimers. In these cases, the tilt would bring the top oxygen atoms closer towards each other and could, therefore, enhance the effect of the proximity.

In the NC-AFM images at eight different positions a total of 41 dimers were found, but three types of dimers were not found, namely II^g–II $[\bar{4}\,\bar{8}\,1]$, II–II^g $[\bar{4}\,\bar{8}\,1]$ and II^g–II $[4\,\bar{4}\,\bar{1}]$. The reason for this seems to be the remarkable underrepresentation of the CO molecules of type II^g. However, based on the preset model, the three missing dimers are expected to not express apparent bonds in NC-AFM images due to three reasons. First, all these bonds have a larger CO-CO distance than the shortest dimer without apparent bonds. Second, the II^g–II $[\bar{4}\,\bar{8}\,1]$ and II^g–II $[4\,\bar{4}\,\bar{1}]$ dimers are separated by a wider line. So far, no bond was observed for dimers separated by the wider line. Third, as the II–II^g $[4\,\bar{4}\,\bar{1}]$ dimer is found and does

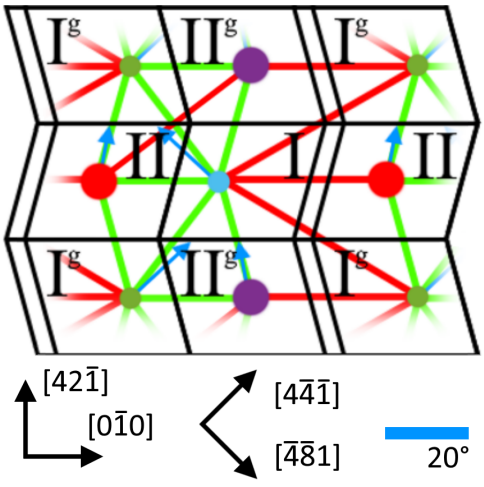

Figure 56: Model sketch of the calcite surface: All CO dimers observed in the measurements are marked: Green lines are for observed and red lines for not observed apparent bonds. The blue arrows indicate the tilt direction of the CO molecules as average from the analysis in figure 53.

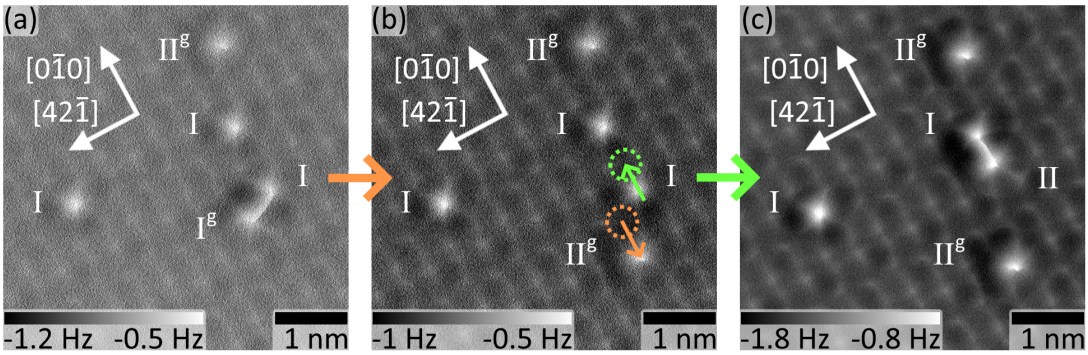

Figure 57: Breaking and forming of apparent CO-CO bonds (Calcite-12, Ku crystal) measured with $U_{tip} = -10\,\mathrm{V}$. The images are in chronological order.

not express an apparent bond, it can be assumed that the glide plane related counterpart to this dimer, namely II–II^g $[\bar{4}\,\bar{8}\,1]$, does also not express an apparent bond.

Last, to substantiate that the dimers are indeed formed by adjacent CO molecules, the consecutive image series in figure 57 gives evidence that these dimers can be formed and dispersed by the NC-AFM tip. In the first image (a), an I^g–I $[\bar{4}\,\bar{8}\,1]$ dimer is clearly visible. Due to the influence of the tip, the CO molecule of type I^g is manipulated (orange arrows) and the previous dimer is dispersed as shown in (b). In this image, all CO molecules are separated. One of the CO molecules of type I is again manipulated by the tip and forms with another CO molecule of type I a II–I $[0\,\bar{1}\,0]$ dimer (figure 57(c), green arrows). Thus, the assumption that the apparent bonds are no chemical bond but a tip induced effect is further supported.

In conclusion, in this subchapter the appearance of CO dimers in NC-AFM images were investigated. It is found that dimers with a CO-CO distance shorter than $(0.49 \pm 0.03)\,\mathrm{nm}$ appear with an apparent bond. But, the appearance of such a bond is rather an effect of the proximity of two atoms and not the result of a chemical bond.

6.5 Domain boundary on calcite(104)

To the best of my knowledge, there are so far no reports of a (2×1) domain boundary on the pristine calcite(104) surface. Still, their observation would give further evidence for the existence of a (2×1) reconstruction.

A large-scale NC-AFM image of a calcite(104) surface after dosing CO for 25 s is presented in figure 58(a) (same image as in figure 44(c)). The calcite surface is visible in this image in the form of bright protrusions arranged along the $[4\,2\,\bar{1}]$ and $[0\,\bar{1}\,0]$ directions. These bright protrusions are separated by dark rows running along both surface directions. Note that the

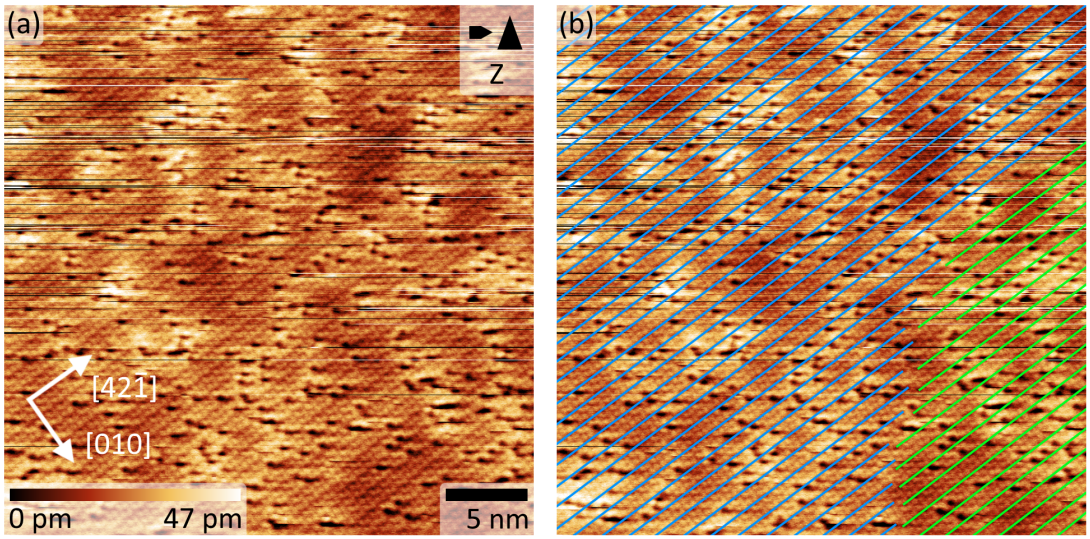

Figure 58: Same image data as in figure 44(c) (Calcite-03, Ra crystal). (b) Wide, dark rows along [4 2 $\bar{1}$] on the calcite surface are marked with lines. The sets of black and blue lines are not aligned to each other due to a domain boundary.

rows in [4 2 $\bar{1}$] direction have an alternating apparent width and can be identified as small and wide rows. Some of the bright protrusions are substituted by dark depressions. These are identified as CO molecules. These molecules are imaged with an elongation on the right side, which is due to a slow feedback response time. In addition CO molecules are often manipulated by the tip, which is apparent as "scratches" in the image. The blue and green lines in figure 58(a) have been aligned with the wide dark rows along the [4 2 $\bar{1}$] direction. Interestingly, the marked rows fall into two separate sets: The set of rows in the left and in the right side of the image cannot be extended to match each other; instead a shift by half a unit cell is found. Such a shift indicates the presence of a domain boundary.

During the experiments of this thesis, domain boundaries are found for CO-covered calcite(104) (figure 58) as well as for H_2O-covered calcite(104) (subchapter 7.2). Control experiments mapping large areas of pristine calcite(104) surfaces did so far not reveal any domain boundary. Although the precise mechanism for domain boundary generation is unclear so far, it could be speculated that an adsorbate-induced effect is present.

6.6 Conclusion: Adsorption properties of CO molecules on calcite(104) at 5 K

In this chapter the adsorption geometry of CO molecules on calcite(104) at 5 K is investigated. At first, it is shown that the CO molecules adsorb exclusively on the calcium atoms of the calcite surface. Therefore, CO molecules can be used as marker molecule to identify the

calcium positions on the calcite(104) surface. Second, the CO molecules show in the NC-AFM images two different adsorption geometries, each with a glide plane reflected counterpart. The geometry of the adsorbed CO molecules follow the chequerboard-like pattern of the calcium atoms. Third, according to the slice data the CO molecules adsorb in a tilted geometry. The tilt direction is different for the two types of CO molecules. Fourth, CO molecules in a dimer can express an apparent bond. It is shown, that only CO dimers with a length smaller (0.49 ± 0.03) nm are imaged with such an apparent bond. Hence, it can be assumed that these bonds are a tip induced effect of proximity and not a chemical bond. This assumption is further confirmed by manipulation of CO molecules, where apparent bonds can be formed or dispersed. Last, it is shown, that domain boundaries can be found on the calcite(104) if CO molecules were dosed on this surface.

7 NC-AFM investigations of water on calcite(104) in the coverage regime up to 1 ML

In the last chapter the adsorption geometry of CO molecules on calcite(104) at 5 K was exterminated, and it was found that the CO molecules follow the glide plane symmetry of the (2×1) reconstructed calcite surface. In this chapter, it is analysed whether the adsorption geometry of water molecules in the coverage regime up to 1 ML also follow the symmetry of the calcite surface at temperatures of 5 K (LT system) and 110 K to 140 K (VT system).

The chapter is organised as follows: First, a concise literature overview describing the atomic properties of single water molecules and small water assemblies on calcite(104) (subchapter 7.1). Second, NC-AFM measurements of 0.09 ML water on calcite(104) at 5 K are presented. Under these conditions the water molecules show preferred adsorption positions within the (2×1) unit cell while no differences are noticeable in the NC-AFM images in the appearance of water molecules on positions adjacent in $[0\,\overline{1}\,0]$ direction. A glide plane symmetry relation is found for water molecules adjacent in $[4\,2\,\overline{1}]$ direction (subchapter 7.2). Third, measurement results acquired for water coverage in the range of 0.18 ML to 1 ML at temperatures between 110 K to 140 K are given, highlighting a clear influence of the (2×1) reconstruction at coverages smaller than 0.5 ML (subchapter 7.3).

7.1 Literature review: Properties of water on calcite(104)

A large body of work is available in literature, where the adsorption properties of water on calcite(104) by a number of different simulation techniques has been studied [23, 24, 25, 33, 34, 35, 36, 37, 38, 40, 43, 49, 54, 57, 210, 211, 212, 213, 214, 215, 216]. For the case of a single water molecule adsorbed on a (1×1) calcite surface, most simulations find a similar adsorption geometry with only minor differences as described in the following. A sketch of this prevalent structure is shown in figure 59(a) that follows the adsorption geometry from reference [212].

The water molecule lies almost flat on the calcite surface and the oxygen atom of the water molecule is located at a calcium site. In turn, the hydrogen atoms form hydrogen bonds to the topmost oxygen atoms of two carbonate groups that are adjacent in $[4\,2\,\overline{1}]$ direction to each other. The distance between the oxygen atom of the water molecule and the closest calcium atom (blue line in figure 59(a)) is in the range of 0.237 nm to 0.243 nm when using DFT calculations [35, 57, 212], 0.237 nm to 0.255 nm in atomistic calculations [23, 24, 25, 35, 37, 212] and between 0.242 nm and 0.251 nm for using molecular dynamics simulations performed at temperatures from 300 K to 900 K [212]. These calculated distances are in a range that is in agreement with best-fit models of X-ray reflectivity measurements from

Geissbühler *et al.* and Fenter *et al.* [34, 38], where the water molecules have been found to have a height from the topmost calcium plane of about 0.23 nm to 0.25 nm.

The two hydrogen bonds between the water molecule hydrogen atoms and two carbonate group oxygens have been calculated to have rather different lengths. The longer hydrogen bond, which is marked with an orange line in figure 59(a), has been found to have a length in the range of 0.233 nm to 0.242 nm in DFT calculations [35, 57], and 0.18 nm to 0.236 nm in atomistic simulations [23, 24, 25, 35, 37]. The shorter hydrogen bond, marked with a green line in figure 59(a), has been found to have a length in the range of 0.166 nm to 0.179 nm (DFT calculations, [35, 57]), and 0.168 nm to 0.189 nm (atomistic simulations, [23, 24, 25, 35]).

In the experiments of Stipp *et al.* [36, 49], and simulations of Lardge *et al.* [211, 212], Wright *et al.* [37], as well as Kerisit *et al.* [35], dissociated water molecules on the calcite(104) surface have been observed that were supposedly generated at step edges and defects. In contrast, on the pristine calcite surface, dissociated water molecules were found to be energetically very unfavourable.

On the fully hydrated surface (1 ML coverage), each calcium atom of the surface has been found to bind to one water molecule, and each of the topmost surface oxygen atoms has been identified to be coordinated to two hydrogen atoms from two neighbouring H_2O molecules

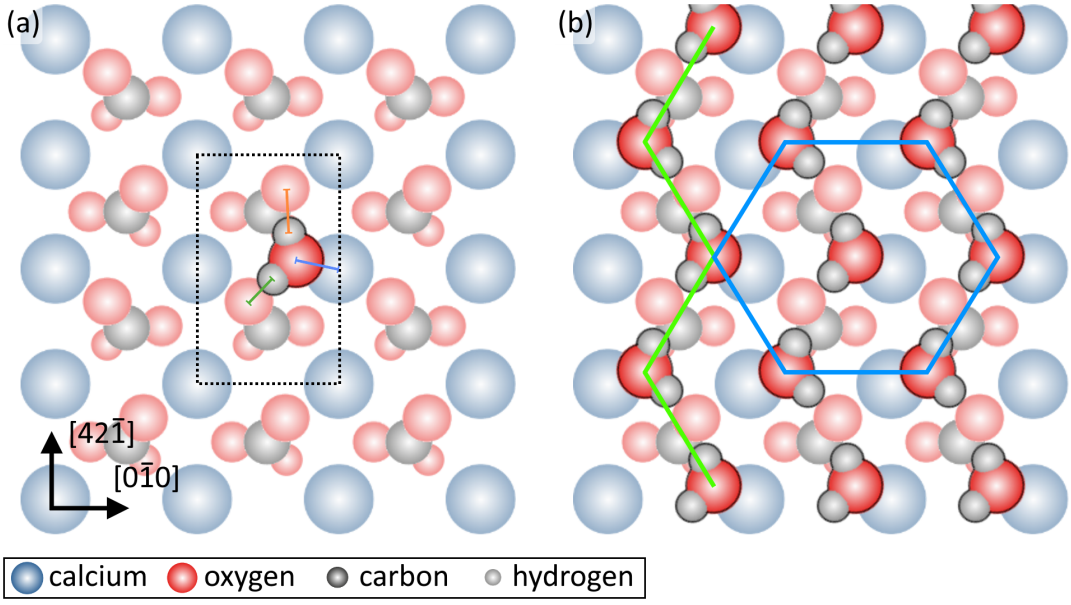

Figure 59: Model of the calcite(104) surface in top view with (a) one single H_2O molecule and (b) with 1 ML water coverage. The water molecule in (a) is drawn according to the adsorption geometry from reference [212]. The orange, green, and blue lines are between the atoms centres, additionally a (1×1) unit cell is marked by the black dotted rectangle. The water molecules in (b) are drawn according to the adsorption geometry from reference [25].

[23, 24, 25, 35, 57, 211, 212, 215]. This adsorption geometry express a (1×1) glide plane symmetry; an example is drawn in figure 59(b) that follows the geometry from reference [25]. As marked by the blue line, the water oxygen atoms have a rather hexagonal (1×1) pattern (the internal angles of the blue hexagon are not 120°) with a zig-zag arrangement in $[4\,2\,\overline{1}]$ direction (light green line).

The (1×1) reconstruction found in the simulations of water on calcite [23, 24, 33, 35, 37, 38, 54, 57, 212, 25, 211] is in agreement with AFM measurements from Ohnesorge *et al.* [43] and Liang *et al.* [40, 216], XPS and LEED experiments from Stipp *et al.* [49], and best-fit models of X-ray reflectivity measurements performed by Geissbühler *et al.* [34]. In contrast, second study measurements from Stipp *et al.* [36] found a (2×1) reconstruction, and Fenter *et al.* [38] found in best-fit models of X-ray reflectivity measurements that a (1×1) reconstruction cannot fully explain their experimental data.

The geometry of the relaxed calcite surface under the influence of adsorbed water is still a matter of discussion in the literature. De Leeuw *et al.* [23, 24] found in their atomistic simulations of partially covered calcite(104) surfaces that the two carbonate groups relax due to the hydrogen bonds with highest oxygen atom protruding 35 pm from the plane spanned by the topmost surface oxygen atoms of the un-relaxed carbonate groups. This finding is similar to the atomistic simulations from Wright *et al.* [37], who found a rather bulk-like calcite structure under the influence of water, with a slight rotation of the carbonate groups out of the surface. The observation of protruding topmost surface oxygen atoms from De Leeuw *et al.* and Wright *et al.* are supported by LEED experiments from Stipp *et al.* [49], by the newer X-ray reflectivity measurements performed by Fenter *et al.* [210], and the best-fit models of grazing incidence X-ray diffraction of Magdans *et al.* [33], who found a tilt of the carbonate groups of 10.9° around the surface normal vector and 5.3° around the vector in $[0\,\overline{1}\,0]$ direction that brings the topmost carbonate oxygen slightly out of the surface. In contrast, Geissbühler *et al.* [34] found in their best-fit models for X-ray reflectivity measurements a rotation of the carbonate groups of 11.3° around the vector in $[0\,\overline{1}\,0]$ direction and that results in flatter lying carbonate groups. This angle is supported by the older best-fit models of X-ray reflectivity measurements performed from Fenter *et al.* [38].

In the above mentioned literature, only a (1×1) reconstruction of the calcite(104) surface is considered when the adsorption geometry of water on calcite(104) is discussed. In contrast, in subchapter 5.1 of this thesis it is shown that a (2×1) reconstruction with a glide plane symmetry is a surface property of the calcite(104) surface. Hence, this symmetry could explain some of the discrepancies of the geometry of water on calcite(104) in literature, and high-resolution NC-AFM experiments as well as simulations considering the reconstructed surface are necessary. In the following it is shown that the (2×1) reconstruction influences

the adsorption geometry of single water molecules.

7.2 NC-AFM investigation of individual water molecules on calcite(104) at 5 K

The adsorption geometry of single water molecules on calcite(104) at 5 K is investigated with NC-AFM and CO-terminated tips in this subchapter. The data situation for this sample system is still scarce, therefore, this section will mainly focus on the adsorption position of water molecules within the (2×1) unit cell of the calcite(104) surface.

For the measurements presented in this subchapter, the calcite crystal (Calcite-004, Ra crystal) is prepared by cleaving and heating (see subchapter 4.2). Ensuing, water is dosed for 60 s and additional for 20 s, both times at a pressure of 1×10^{-9} mbar with the sample held at 150 K as described in section 4.3.2. Last, CO is dosed into the cold scan head for 20 s at a pressure of 4×10^{-8} mbar as explained in section 4.3.1.

Preferred adsorption positions of single water molecules

An overview topography image after dosing a submonolayer coverage of water on calcite(104) is shown in figure 60(a). After water dosing, two types of bright features with a darker spot at the side (one feature of each kind is marked by a light blue and a dark green circle) appear and are, therefore, identified as water molecules. A total of 186 water molecules were counted in this image; this corresponds to a water coverage of about 0.09 ML (1 ML corresponds to one water molecule per Ca atom). The 42 dark depressions in the image (one is marked by a dark green arrow) are assigned to CO molecules by following the results from subchapter 6.2. Consequently, a CO coverage of about 0.02 ML is present. The calcite lattice is faintly visible. In particular, the (2×1) reconstruction is apparent in areas without water or CO molecules.

Two types of water molecules can be identified as shown in the detail images in figure 60(c) and (d) (same image data as in figure 63(a) and (b)). These images are acquired at the position marked by the black rectangle in figure 60(a) in topography (figure 60(c)) and constant-height (figure 60(d)) mode. In the constant-height frequency-shift image (figure 60(d)), the water molecules are imaged as almost round dark (more attractive) features with a bright (less attractive) spot at one side. Notably, this dark spot is located on either the right or the left side of a dark feature with respect to the $[4\,2\,\overline{1}]$ axis. In the following the dark features with the bright spot on the right side are named type A (green triangles) while the features with the bright spot on the left side are named type B (blue triangles). The different brightness of these colours additionally indicates different positions within a (2×1) grid as will be explained later.

The bright protrusion in the lower left corner of figure 60(d) (marked by a green arrow) is located at the position of a dark depression in the topography images figure 60(a) and (c) (green arrows) and is, therefore, identified as a CO molecule. This molecule is used as a reference point to copy the triangle positions from figure 60(d) to (c). Such a reference is necessary because the images are acquired at slightly different lateral positions due to thermal drift.

In topography mode imaging (figure 60(c)), the water molecules are apparent as bright features with a dark spot at the side, while the calcite surface is only barely visible at this interaction strength. Increasing the Δf setpoint usually caused lateral manipulation of the surface-adsorbed molecules. The positions of the copied triangles, which are aligned to the CO molecule in this image, match with the positions of the dark spots of the water molecules. Similar to figure 60(d), dark spots located at the right side of bright features (with respect to the $[4\,2\,\overline{1}]$ axis) are marked by green triangles and, consequently, named type A while dark spots on the left side of a feature are indicated by blue triangles and named type B.

The two types of water molecules are also distinguishable in figure 60(a). All water molecules with a dark spot on the right side are marked by a green triangle in figure 60(b) (same image data as in (a)) while all water molecules with a dark spot on the left side are marked by a blue triangle. Additional, to analyse if the two types of water molecules are related to the (2×1) reconstruction of the calcite(104) surface a black (2×1) grid is overlaid to figure 60(b). This grid has been aligned to the calcite lattice by the Fourier-based strategy (section 6.2.1). All four maxima ((020), $(0\overline{2}0)$, $(42\overline{1})$, and $(\overline{42}1)$) are used from the 2D Fourier transform to align both the $[0\,\overline{1}\,0]$ as well as the $[4\,2\,\overline{1}]$ direction of the (2×1) grid. The resulting grid was translated in such a way that the CO molecules always lie in a grid corner (similar criterium as for figure 45(b)). With this alignment, the grid lines in $[4\,2\,\overline{1}]$ direction represent every second row of carbonate groups while the grid corners indicate the positions of the calcium atoms.

It is found that the water molecules of type A (light and dark green triangles) are always found in the upper half of the (2×1) grid cells (with respect to the $[4\,2\,\overline{1}]$ axis), while the molecules of type B (light and dark blue triangles) are always in the lower half. Additional, the water molecules can be classified whether they are in the right or the left half of a (2×1) grid cell, with respect to the $[4\,2\,\overline{1}]$ axis. Consequently, four different kinds of water molecules can be distinguished (see inset in figure 60(b)): Water molecules that are imaged in topography mode with a dark spot on the right side and located in the upper left half of a grid cell (marked by dark green triangles in figure 60(b)), water molecules that are imaged with a dark spot on the left side and located in the lower left half of a grid cell (light blue triangles), water molecules that are imaged with a dark spot on the right side and located

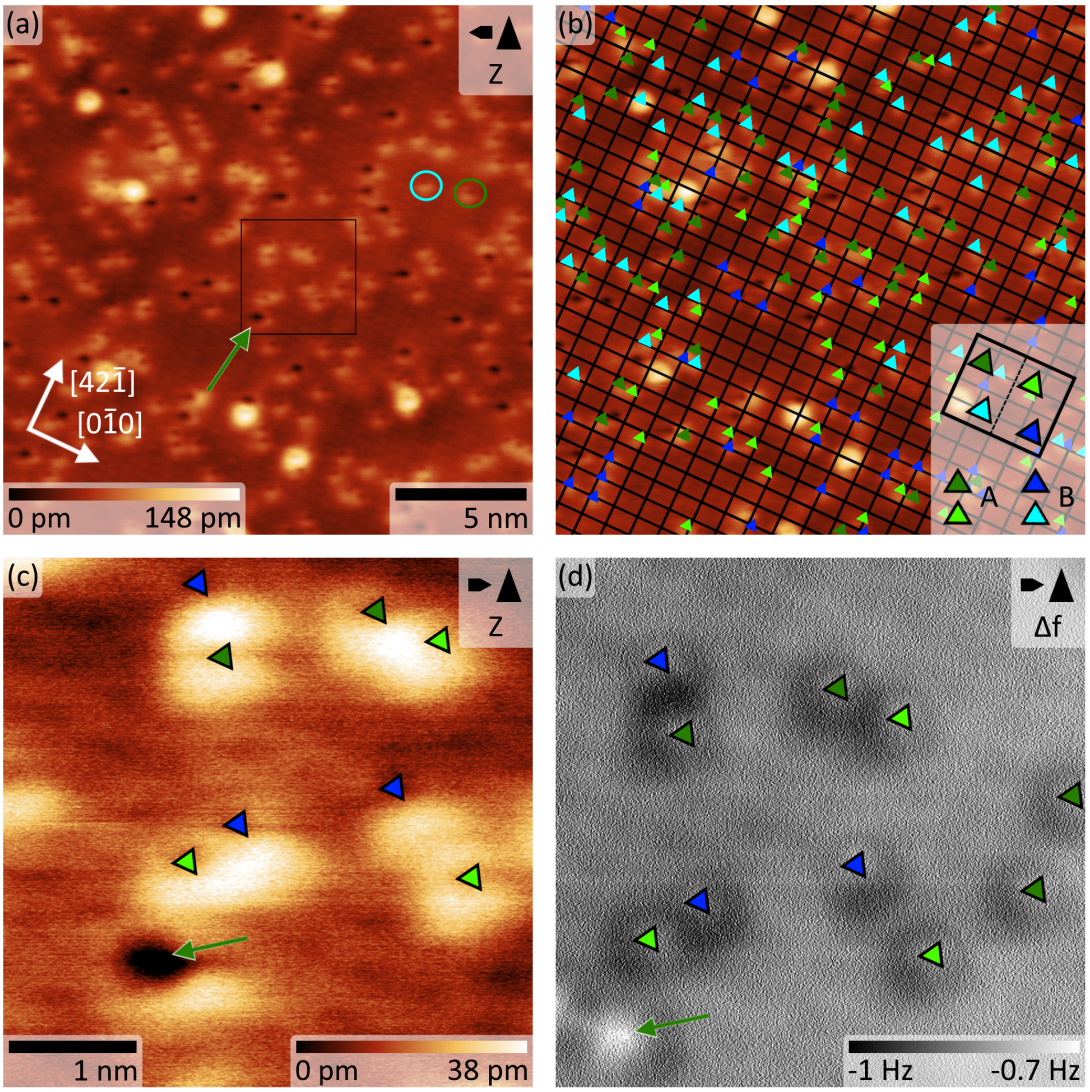

Figure 60: NC-AFM images acquired after dosing 0.08 ML water on calcite(104) (Calcite-004, Ra crystal). (a) Topography image acquired at $\Delta f = -0.9\,\mathrm{Hz}$ and $U_{tip} = 10\,\mathrm{V}$. (b) Same image data as in (a) with overlaid (2×1) grid. H_2O molecules of similar shape and on equivalent grid positions are marked by triangles of similar colour. (c) and (d) NC-AFM images of a group of H_2O molecules (positions marked in figure 60(a) by a black rectangle). The topography image in (c) is acquired at $U_{tip} = 10\,\mathrm{V}$ and $\Delta f = -0.9\,\mathrm{Hz}$. The tapered side of the CO feature (green arrow) is due to an artefact of the topography feedback loop. The corrugation of the calcite surface is only barely visible between the molecules. (d) Constant-height frequency-shift data ($U_{tip} = 10\,\mathrm{V}$) of the group of water molecules shown in (c).

in the upper right half of a grid cell (light green triangles), and water molecules that are imaged with a dark spot on the left side and located in lower right half of a grid cell (dark blue triangles).

The data in figure 60(b) give the visual appearance that the water molecules in the lower left of a (2×1) grid cell and imaged with a dark spot on the right side (marked by light

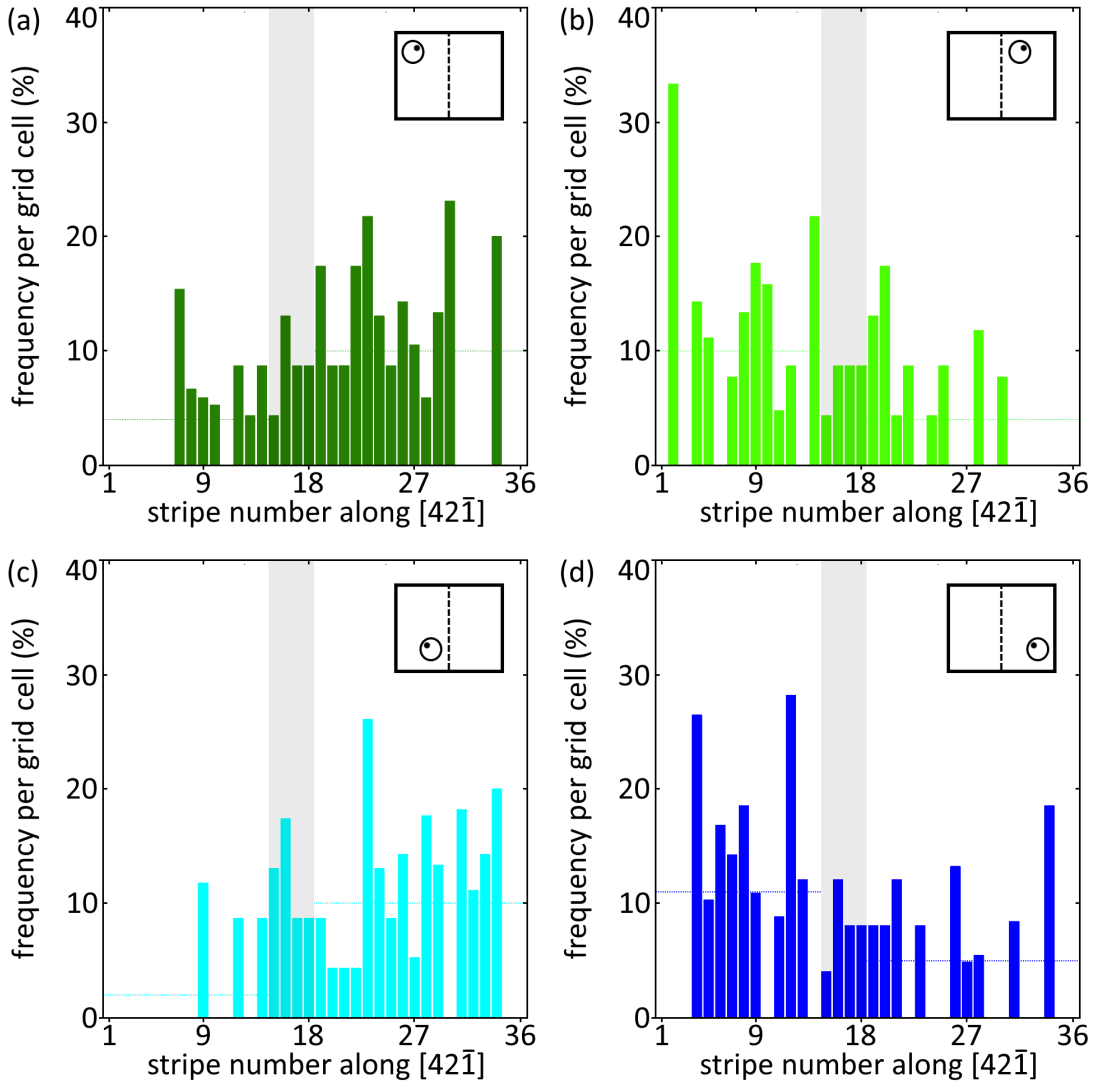

Figure 61: Number frequency of water molecules of the four positions within a (2×1) grid cell, analysed along stripes along the $[0\,\bar{1}\,0]$ direction: (a) upper left (2×1) grid cell corner (type A, marked with dark green triangles), (b) upper right (2×1) grid cell corner (type A, light green triangles), (c) lower left (2×1) grid cell corner (type B, light blue triangles), and (d) lower right (2×1) grid cell corner (type B, dark blue triangles). Range of the domain boundary is marked by a grey background. The dotted lines indicate the averaged frequency for the bars within each domain. An abstraction of a water molecule on one of the four adsorption positions is inserted in the figures for each kind of water molecule.

blue triangles) are more frequent in the upper than in in the lower image half. To further investigate this observation, the distribution of the four water molecule kinds in figure 60(b) is determined. For this purpose the grid in figure 60(b) is first sub-divided into stripes of (2×1) grid cells along $[0\,\bar{1}\,0]$ direction. Second, the frequency per grid cell for each stripe is determined for each kind of water molecule. In particular, the total number of one kind of H_2O molecules is counted for each stripe and the sum is divided by the total number of grid

cells in this stripe. A total of 36 stripes is evaluated with the first stripe being located in the lower left corner of image figure 60(b), and the 36^{th} stripe is in the upper right corner. The resulting frequencies plottet against the stripe number are presented separately for the four kinds of water molecules in figure 61. A tendency is apparent from the data in figure 61(a) and (c): a preference of occupying the left grid cell halves is found for stripes located at large index number, while the water molecules appear to prefer the right (2×1) grid cell halve in stripes with small index number, see also figure 61(b) and (d).

Two observations are made from this analysis: First, the data suggest that water at sub-monolayer coverage prefers to occupy only specific positions within the (2×1) grid cell. Second, this preference differs within the image data of figure 60(b). The latter observation might be explained by a (2×1) domain boundary which can be identified in this image. The existence of this domain boundary is highlighted in figure 62. These images reproduce the same image data as in figure 60(a), but with a different colour mapping to highlight the structure of the calcite surface. The blue and green lines in figure 62(b) have been aligned with the darker rows in $[4\,2\,\overline{1}]$ direction that are visible in the areas of the pristine calcite surface. Interestingly, the marked rows in the lower (domain I) and upper (domain II) half of the image do not match to each other, but instead express a transition by half a unit cell. Such a shift is an expression of a domain boundary, here located across the middle of the image.

The stripe index number range within the domain boundary is marked by a grey background in figure 61. The bars with small stripe index numbers located left of this grey area represents domain I, while bars with large stripe index numbers represents domain II. It is more likely to find water molecules in the domain I in the right (2×1) grid cell half (on average 10 ± 10 % for type A and 11 ± 9 % for type B) than in the left half (4 ± 5 % for type A and 2 ± 4 % for type B). In contrast, it is more likely to find water molecules in the left grid cell half (10 ± 8 % for type A and type B) in domain II than in the right half (4 ± 6 % for type A and 5 ± 6 % for type B). Consequently, the water molecules have preferred adsorption position within the (2×1) unit cells. These positions are different in the grid cells of domain I and domain II due to the domain boundary.

The preferred adsorption position within one half of the (2×1) unit cell is very likely a consequence of the (2×1) reconstruction. In particular, it seems to be an effect related to the different carbonate group orientation previously identified by P and Q in figure 41(b). This suggestion is based on the fact that similar adsorption positions are found in rows along the $[4\,2\,\overline{1}]$ direction. In contrast, if water molecules would prefer one kind of calcium atom previous identified S and R in figure 41(c), a chequerboard-like pattern would be expected. While this is found for the CO adsorption positions in subchapter 6.2, the previous analysis

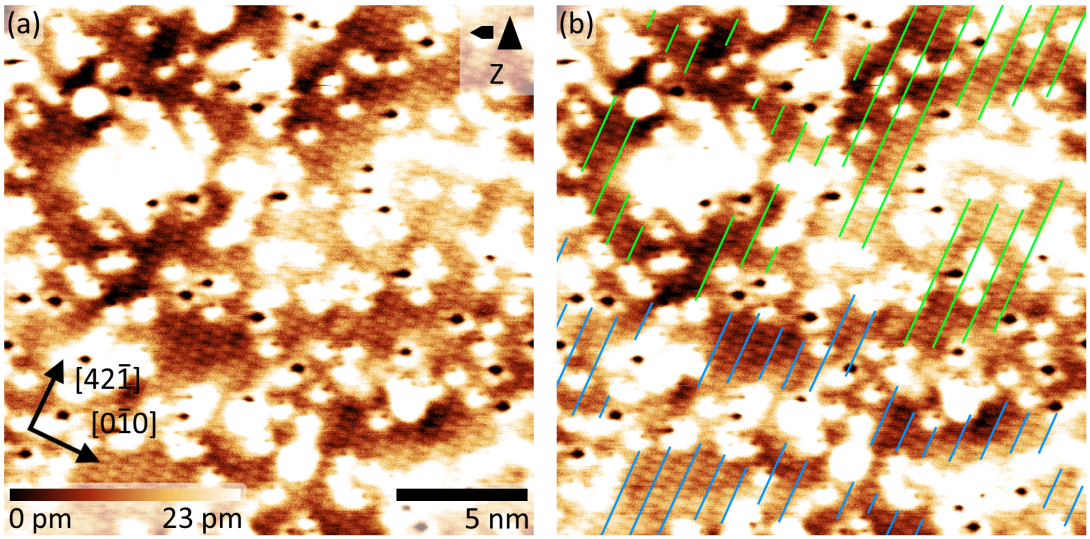

Figure 62: Same image data as in figure 60(a) but with different contrast to highlight the bare calcite surface. (b) similar features of the calcite surface are marked with lines. The blue and green lines are not aligned to each other due to a domain boundary.

for H_2O does not support such an arrangement.

In conclusion, this subchapter demonstrates, that single water molecules have two preferred adsorption positions within a single (2×1) unit cell of calcite(104). The difference seems to be related to the different carbonate group orientation previous denoted as P and Q. The finding of a domain boundary further confirms the assumption from subchapter 6.5, that most of the domain boundaries are induced by the molecules that are adsorbed on the calcite(104) surface.

Visual glide plane symmetry of the water molecules on calcite(104)

Figure 63 presents a series of constant-height NC-AFM images of a few water molecules and one CO molecule on calcite(104), acquired at the position marked by a black rectangle in figure 60(a). The topography image in figure 63(a) (same image as figure 60(c)) is acquired at large tip-sample distances to avoid tip induced manipulation of the CO and water molecules.

The image series in figure 63(b–f) is generated by successively reducing the tip-sample distance. After each image the distance controller was switched on to measure the vertical drift in order to adjust the atom-tracking system. Due to this adjustment the height difference between the images are not known. Before the measurements on calcite CO was picked up on Ag(111), but during the measurements on the calcite sample the tip changed several times, likely dropping and picking up calcite-adsorbed CO molecules. However, due

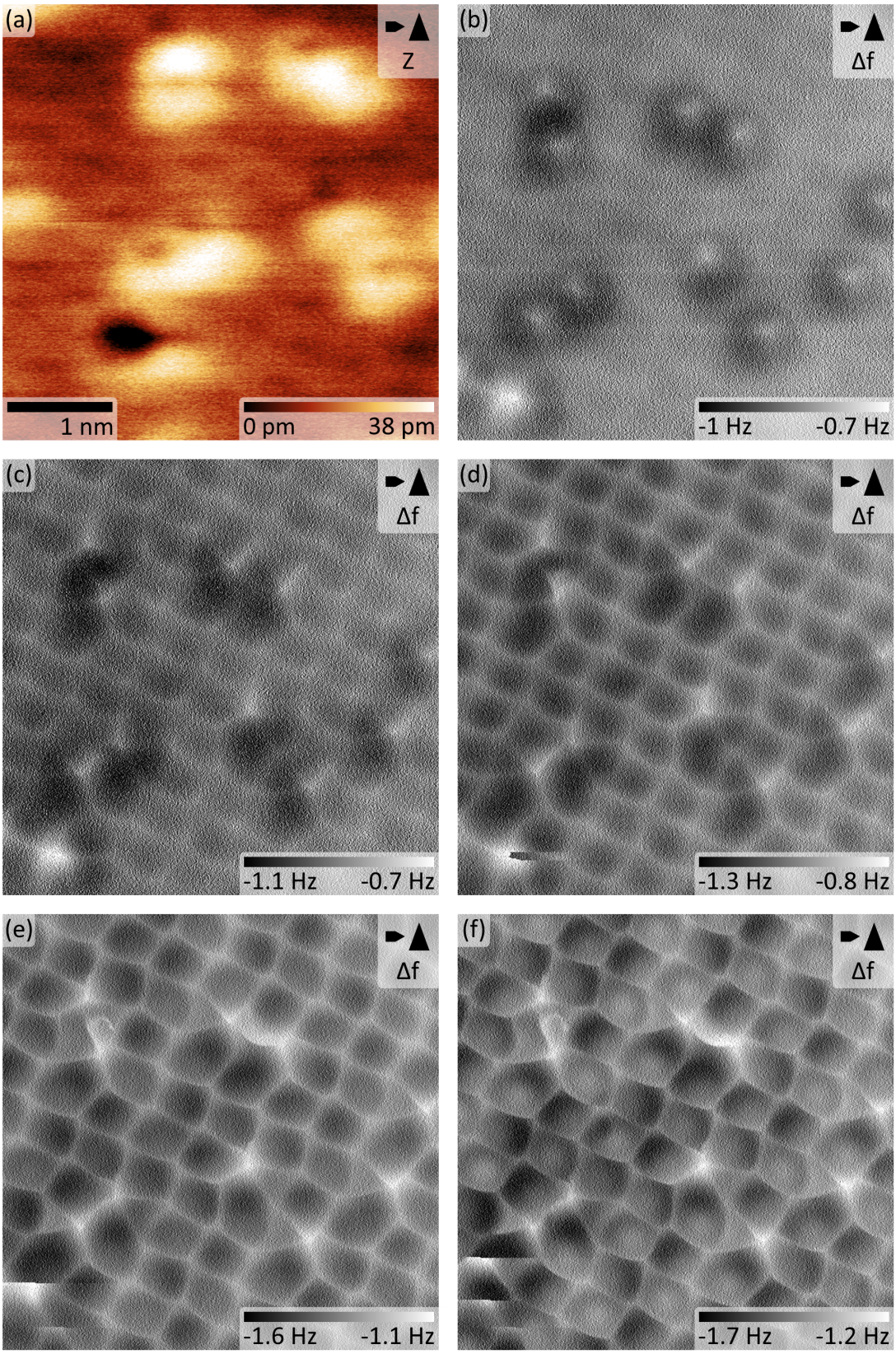

Figure 63: NC-AFM images of the H_2O assembly marked by a black rectangle in figure 60(a). The six images are acquired at $U_{tip} = 10\,\mathrm{V}$ and at slightly shifted lateral positions due to residual drift. (a) Topography image ($\Delta f = -0.9\,\mathrm{Hz}$). (b–f) Constant-height frequency-shift images acquired at different tip-sample distances.

to the clear imaging of the calcite lattice that closely resembles the contrast achieved with a CO-terminated tip (see figure 63 and figure 32) it can be assumed that the image series in figure 63 is also acquired with a CO terminated tip.

With decreasing distance, the brighter spot of each water molecules evolves into a sharp bright maximum with bright linkers to the calcite lattice, while the dark surrounding almost disappears. The bright lines running in $[4\,2\,\bar{1}]$ and $[0\,\bar{1}\,0]$ direction representing the calcite lattice. In particular, the carbonate groups at the crossing points, become sharper with decreasing tip-sample distance and show a similar appearance as in figure 32.

At smaller tip-sample distances (figure 64(e) and (f)), the appearance of the water molecules does not change significantly further. Instead, a contrast inversion of the calcite lattice occur as the dark pores of the calcite lattice become brighter. As the CO molecule is manipulated by the tip at closer tip-sample distances (figure 63(d–f)), it is not used as a reference within these images.

The imaging contrast of the calcite lattice in figure figure 63(e) suggests a similar interaction strength as used before in figure 37(c). Therefore, figure 63(e) is used as a representative image of water on calcite(104) for the further analysis in figure 64. Additional markers are included in figure 64(b) to highlight the different features as discussed in the following. First, it is already known from subchapter 5.1 that the dark pores of the calcite lattice are

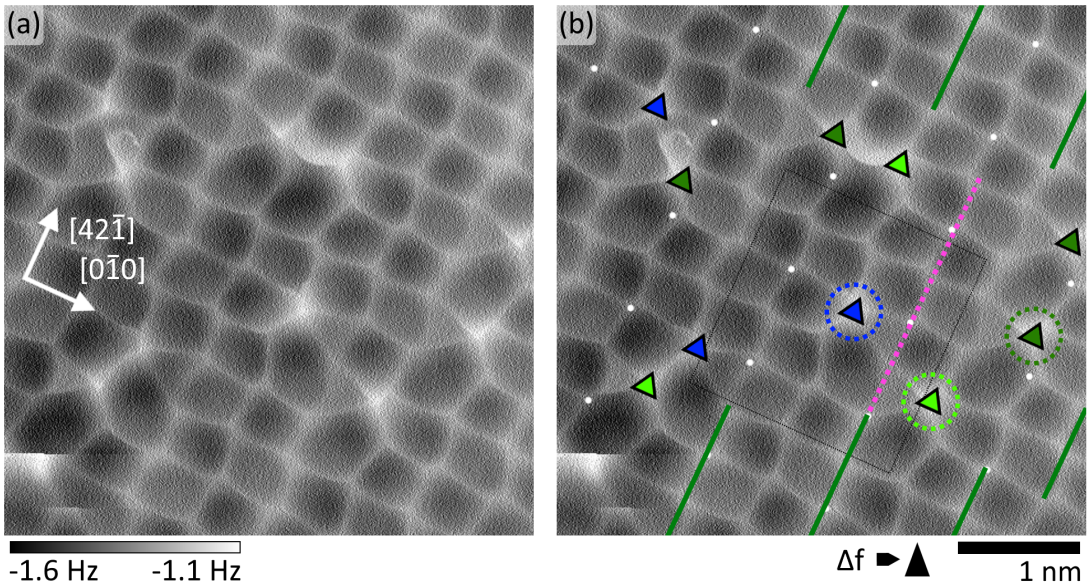

Figure 64: Detail examination of figure 63(e) ($U_{tip} = 10\,\mathrm{V}$). (a) Same image data as in figure 63(e). (b) The wide lines running in $[4\,2\,\bar{1}]$ are marked by dark green lines. H_2O molecules on equivalent (2×1) lattice sites are marked with triangles of the same colour. The white dots are positioned in a (2×1) pattern.

the positions of the calcium atoms, while the intersections of the bright lines indicate the positions of the carbonate groups.

Second, this image is acquired across the domain boundary identified before. This domain boundary is identified from the positions of the wider bright lines (marked by dark green lines): The lines in the upper half are displaced by a half (2×1) unit cell in $[0\,\bar{1}\,0]$ direction when compared to the lines in the lower half. Thus, the adsorption of H_2O is a second example for generating adsorbate-induced (2×1) domain boundaries on calcite(104).

Third, the positions of the bright centres of the water molecules (marked with coloured triangles in figure 64(b)) have remarkable similarity to the water adsorption position from the literature review in figure 59(a). This similarity is analysed in figure 65. The image data in the black dotted rectangle in figure 64(b) are reproduced in figure 65(a) with $[4\,2\,\bar{1}]$ pointing upwards. The bright centre of a water molecule is visible in the centre of the image. This centre is close to a bright line in $[0\,\bar{1}\,0]$ direction of the calcite lattice (light blue dotted line) and close to a bright line in $[4\,2\,\bar{1}]$ direction (magenta dotted line). Both lines indicate rows of carbonate groups as known from chapter 5. The model in figure 59(a) is reproduced in figure 65(b). The position of the water molecule is close to rows of carbonate groups that run in $[0\,\bar{1}\,0]$ (light blue dotted line) and $[4\,2\,\bar{1}]$ (magenta dotted line) direction. Under the

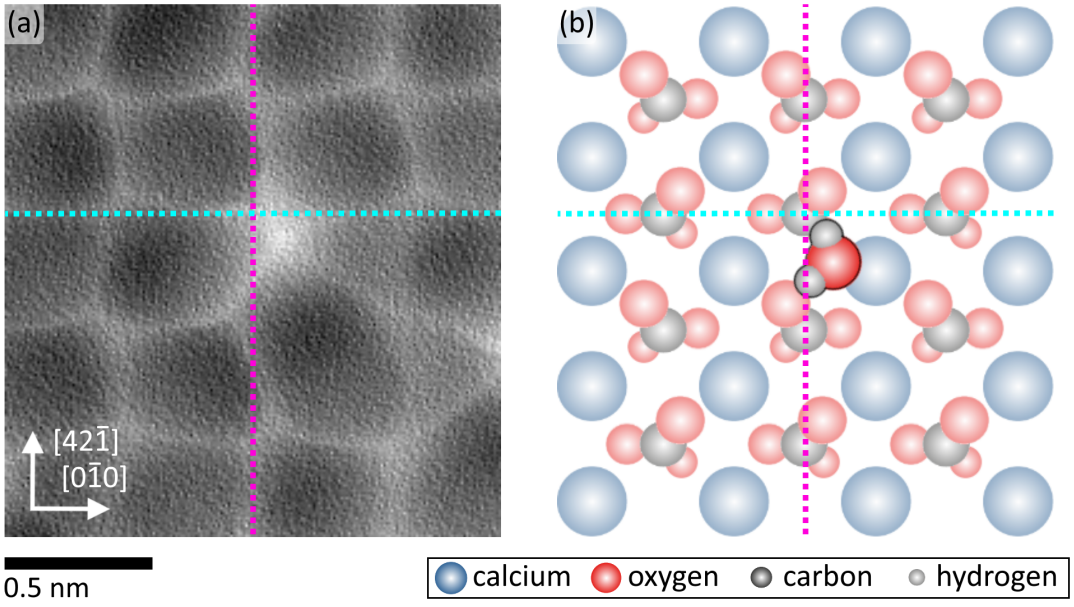

Figure 65: Comparison between the adsorption position of H_2O on calcite(104) (a) in a constant-height frequency-shift image with the model from the literature review. (a) Reproduced image data from the area marked by the black dotted rectangle in figure 64(b). (b) as in figure 63(e). (b) Same model as in figure 59(a). The dotted lines indicate rows of carbonate groups in $[0\,\bar{1}\,0]$ direction (light blue dotted lines) and in $[4\,2\,\bar{1}]$ direction (magenta dotted line).

assumption that the bright centre of the water molecules in the NC-AFM image indicate the position of the water oxygen atom, both, the constant-height frequency-shift image as well as the model indicate a similar position for this atom.

Fourth, water molecules adsorbed on lattice positions adjacent in $[4\,2\,\overline{1}]$ direction (light green and dark blue dashed circles, type A and type B, respectively) seem to be related by the glide plane symmetry. The algorithmic symmetry test can not applied to the water molecules in figure 64, because no separated water molecule can be found that is on an equivalent (2×1) lattice position to one of the water molecules that are marked by a dotted circle. Due to the scarce data situation other images are yet not available.

Five, if the adsorption positions of the water molecules are influenced by the (2×1) reconstruction of the calcite surface, it would be expected that the adsorption geometry of molecules adjacent in $[0\,\overline{1}\,0]$ direction are not related to each other (figure 41). In figure 64, no difference is visible in the appearance of water molecules on lattice positions adjacent in $[0\,\overline{1}\,0]$ direction (light and dark green dotted circles, both type A). Hence, visual follow the water molecules a (1×1) reconstruction. In contrast, from figure 61 it is known, that the water molecules prefer adsorption positions that follow the (2×1) reconstruction.

In conclusion, it is demonstrated in this subchapter, that single water molecules have preferred adsorption positions on the calcite(104) surface. These positions follow the (2×1) reconstruction. In the NC-AFM images water molecules adsorbed on positions adjacent in $[0\,\overline{1}\,0]$ direction are imaged similar and seem, therefore, to follow a (1×1) reconstruction. A glide plane symmetry is found visual for water molecules adsorbed on positions adjacent in $[4\,2\,\overline{1}]$.

7.3 NC-AFM investigation of water on calcite(104) at varied coverage in the range of 110 K to 140 K

In the last subchapter it is demonstrated that single water molecules on calcite(104) have preferred adsorption positions within the calcite (2×1) unit cell at water coverage of the order of 0.1 ML. Now, the coverage is stepwise increased up to 1 ML and the finding of preferred adsorption positions is also demonstrated in the temperature range of 110 K to 140 K.

All AFM measurements in this subchapter are performed together with Simon Aeschlimann at a variable-temperature atomic force microscope (type VT AFM XA from Omicron, Taunusstein, Germany, group of Prof. Dr. A. Kühnle), operated at 140 K (liquid nitrogen) or 110 K (helium cooling).

The calcite crystal (samples from the calcite block Ku) is cleaved, by a sharp blade in UHV

to generate a pristine (104) surface. After cleaving, the calcite crystal is heated up to about 326 °C for 1 h. For these experiments, a higher temperature was selected, because annealing to 200 °C (subchapter 4.2) was observed to be not sufficient to reduce surface charges to an acceptable low level. Next, the calcite(104) surface is imaged by NC-AFM to ensure surface cleanliness. Next, water deposition is performed on a freshly prepared calcite(104) surface in the same way as described in section 4.3.2 with a water dosing unit identical to the unit explained in this section. Deposition is performed at a pressure in the preparation chamber of about 1×10^{-9} mbar and with varied deposition times.

Figure 66 presents a series of AFM images of calcite surfaces, prepared with increasing water coverage. All images are corrected for thermal drift by comparing the positions of features in two sequential images as described in subchapter 3.6.

Figure 66(a) shows a typical NC-AFM image of a clean calcite(104) surface at room temperature. The surface shows bright protrusions arranged along the $[4\,2\,\overline{1}]$ and $[0\,\overline{1}\,0]$ directions, a (2×1) reconstruction and the row-pairing reconstruction is apparent, while no foreign adatoms are visible. One exemplary (2×1) unit cell is marked by the white rectangle in this image.

Image data for the smallest water coverage investigated within this series is shown in figure 66(b) as a result of dosing water for 40 s. Before these experiments, the freshly prepared calcite(104) surface exhibits large surface charges that prevented stable NC-AFM measurements. Therefore, in order to reduce these charges by desorbing H_2O molecules, the calcite surface was cleaned from a higher water coverage (dosed for 60 s) by annealing to 300 K for about 20 min before the 40 s dosing step. Due to the desorption temperature of −10 °C [57] it can be assumed that water was completely desorbed.

Elongated dark areas with an internal (2×1) row pattern along the $[4\,2\,\overline{1}]$ direction are clearly visible in the NC-AFM images (figure 66(b)). The area coverage of these features is $(36 \pm 7)\,\%$ as determined with the Gwyddion tool "Mark Grains by Threshold" [140]. This tool calculates the total percentage of pixels that have data values above or below a given threshold in relation to the entire number of image pixels. It is challenging to precisely determine the area coverage of these dark features by finding an appropriate threshold because the boundaries of these features are irregular. Hence, a compromise is made, see also figure 72 in the appendix and a rather large error results.

A higher water coverage is found after dosing water for 50 s on a freshly cleaved calcite(104) sample (figure 66(c)). Small dark dots are visible that are arranged in a zig-zag pattern along the $[4\,2\,\overline{1}]$ direction. The separation along the $[0\,\overline{1}\,0]$ direction amounts to about 1 nm

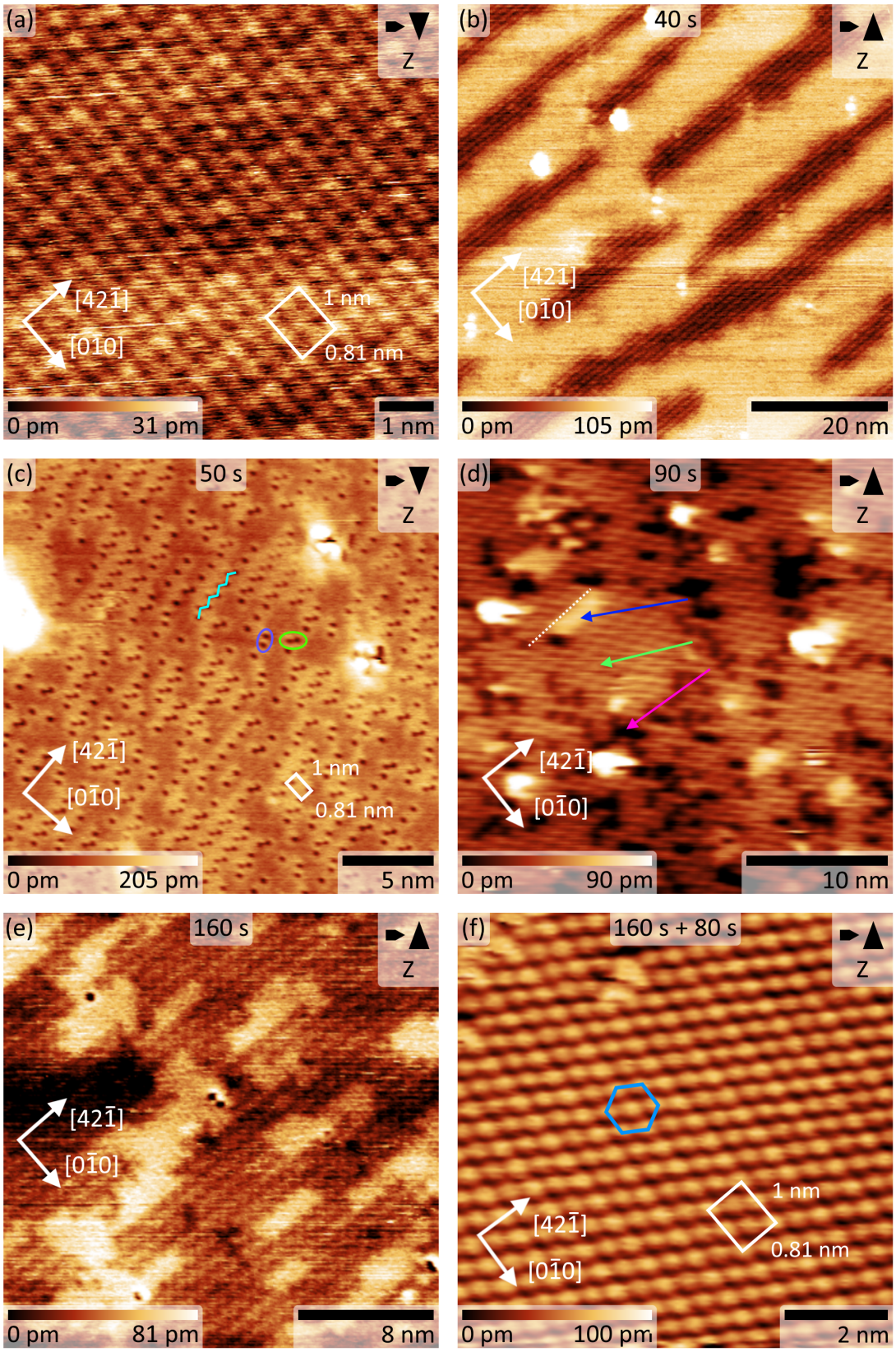

Figure 66: NC-AFM images of calcite(104) acquired at different temperatures and after increasing water coverages. (a) Pristine surface ($T_{\text{imaging}} = 300\,\text{K}$, $\Delta f = -38.6\,\text{Hz}$, $U_{tip} = 2\,\text{V}$). (b) Image of the calcite surface for $t = 40\,\text{s}$ (110 K, $-2.2\,\text{Hz}$, $-2.5\,\text{V}$), (c) 50 s (140 K, $-8.4\,\text{Hz}$, 0 V), (d) 90 s (110 K, $-4\,\text{Hz}$, $-2.4\,\text{V}$), (e) 160 s (140 K, $-15\,\text{Hz}$, 4 V), and (f) 240 s (140 K, $-25.2\,\text{Hz}$, 4 V).

Therefore, each (2×1) unit cell is only filled at maximum by two dark dots. One exemplary (2×1) unit cell with two dark dots is marked in figure 66(c).

The zig-zag pattern of the dark dots is not complete across the image, most likely because the water coverage after dosing for 50 s is to low to fill all (2×1) unit cells by half. One exemplary section of a complete zig-zag row is marked by a light blue line in figure 66(c). The shape of the zig-zag lines in figure 66(c) is asymmetric, some of the dark dots adjacent in the zig-zag lines are clockwise rotated (light green oval), while others are counter-clockwise rotated (blue oval). During the experiments it was observed that this asymmetry depends on the orientation of the fast scan direction (see appendix figure 71). Hence, this asymmetry is not a property of the adsorbed water molecules but a tip induced effect. Hence, it is concluded that a dark spot in figure 66(c) is one water molecule, because the surface structure resulting from filling only half of a (2×1) unit cell as well as the imaged zig-zag pattern is very similar to the arrangement in the model of a complete hydrated calcite surface in figure 59(b) if only every second (1×1) unit cell along $[0\,\overline{1}\,0]$ is filled with water molecules.

To determine the water coverage of the sample of figure 66(c), a grid of (2×1) unit cells is overlaid on the image and the number of dark spots with respect to the number of unit cells is determined. Hereby, unit cells containing surface defects (bright areas in figure 66(c)) were neglected. It is found that 25 % of the (2×1) unit cells are unoccupied, 45 % have one dark spot, and 30 % have two spots. Under the assumption that one dark spot is one water molecule and one (2×1) unit cell can contain at maximum four water molecules (subchapter 7.1) the water coverage for this deposition time is (0.26 ± 0.02) ML (evaluated from two consecutively acquired images).

It is so far not clear why the H_2O molecules in figure 66(b) (40 s deposition time) form elongated features, while the water molecules in figure 66(c) (50 s) do not. A reason for the formation of this features could be an intermittent higher temperature of the surface during the 40 s water dosing step or during sample transfer. In this case, the water molecules could gain enough energy to cross the diffusion barrier and achieve an energetically preferred position. The history of the surface of figure 66(b) does not seem to be the reason for the formation of the elongated features: Ataman *et al.* [57] found in X-ray photoelectron spectroscopy (XPS) that water molecules desorb from the calcite(104) surface at about −10 °C. Hence, it is expected that all water molecules are desorbed from the calcite surface after holding the surface for 20 min at room temperature.

After 90 s water deposition, three different phases covering the calcite surface are found in the NC-AFM images (figure 66(d)). Phase A covers most areas in the image and is visible as corrugated rows along $[4\,2\,\overline{1}]$ direction (exemplary area marked by green arrow). Phase B

(one example marked by pink arrow) is embedded in phase A in the form of dark areas and has an area coverage of $(21 \pm 3)\,\%$ of the surface area (average coverage of six consecutively acquired images, each evaluated using the "Mark Grains by Threshold" tool in Gwyddion [140], threshold 7 pm). Phase C is also embedded in phase A and is identified as protruding (bright) areas (one example is marked by a blue arrow). The edges of these areas seem to be aligned along the $[4\,2\,\overline{1}]$ direction with the pattern of phase A as indicated by a white dotted line. This phase is not considered in the following, because it only covers a small area. Furthermore, the presence of foreign adatoms deposited on the surface during water dosing cannot be excluded. Hence, phase A is the prevalent phase and exhibits an area coverage of about $(79 \pm 3)\,\%$ within this image.

After deposition of water for 160 s, two different phases are observed as shown in figure 66(e). Phase 1 exhibits areas with dark rows along the $[4\,2\,\overline{1}]$ direction and has an area coverage of $(67.0 \pm 0.2)\,\%$ (average from two consecutively acquired images using the "Mark Grains by Threshold" tool in Gwyddion [140] with threshold 62 pm). Phase 2 is identified as islands embedded in phase 1 which are imaged to protrude the areas of phase 1 in the topography image. These islands (area coverage of $(33.0 \pm 0.2)\,\%$) do not show a clear inner structure in these image data.

When water is dosed for additional 80 s on the sample shown in figure 66(e), the structure imaged in figure 66(f) evolves. This structure consists of bright protrusions arranged in a (1×1) reconstruction. The row-pairing reconstruction is visible from a modulation of the imaged height along the $[4\,2\,\overline{1}]$ direction. Four protrusions are located within one (2×1) unit cell (one example is marked by a white rectangle) and are arranged in a rather hexagonal as highlighted by a light blue hexagon. This hexagonal structure is similar to the model of a fully hydrated calcite(104) (see literature review, figure 59(b)) if the imaging is dominated by the oxygen atoms of the water molecules [25]. Therefore, it is assumed that figure 66(f) represents a fully covered calcite surface (water coverage 1 ML) and each bright protrusion represents one water molecule.

Determining the water coverage of the phases visible figure 66

In order to determine how water molecules arrange on the calcite(104) surface at different water coverage it is crucial to determine the respective water content within each image and of each phase of figure 66. However, the different AFM imaging contrast complicates the interpretation: In figure 66(b), (d) and (e) it is not straightforward to determine the water coverage of the different phases by counting the water molecules.

Therefore, the water coverage of the different phases in figure 66 is at first set as a free

variable. For a single (2×1) unit cell and in the coverage regime up to one full monolayer, this free variable can be either 0 ML for unoccupied (2×1) unit cells, 0.25 ML for unit cells containing one water molecule, 0.5 ML for containing two molecules, 0.75 ML for containing three, or 1 ML for containing four water molecules. These values follow from the literature review (subchapter 7.1) in particular from the finding that one water molecule binds to one calcium surface atom [25]. The resulting water coverage $C_{p,d}$ for given water dosing time d of a calcite crystal is given by the formula:

$$C_{p,d} = v \cdot 0\,\mathrm{ML} + w \cdot 0.25\,\mathrm{ML} + x \cdot 0.5\,\mathrm{ML} + y \cdot 0.75\,\mathrm{ML} + z \cdot 1\,\mathrm{ML}, \tag{19}$$

whereby v (w, x, y, z) is the area coverage of a phase that has zero (one, two, three, four) water molecules in a (2×1) unit cell, with $v + w + x + y + z = 100\,\%$. p is the index of a permutation, and d indicates the water dosing time. At first, all possible permutations of the area coverage to v, w, x, y, and z are considered. To reduce the number of permutations only the physically reasonable cases are considered. These cases result from making following three assumptions:

I) Only two different phases are clearly visible in figure 66(b), (d) and (e), therefore, only permutations considering two different phases are considered for these data.

II) At a deposition time of 40 s, the water coverage is 0.26 ML while the coverage is 1 ML after 240 s (figure 66(c) and (f)).

III) The amount of water increases linearly with the deposition time.

As an example of this determination process, the data in figure 66(b) are analysed in detail. From the previous analysis it was determined that the darker features in figure 66(b) cover 36 % of the surface area while the brighter areas cover 64 %. There are a total of 20 possibilities to set (v, w, x, y, z) to either 36 % or 64 % coverage, these are listed in table 9. Next, the respective phase area coverages are inserted into formula 19 for each case and the resulting $C_{p,40\,\mathrm{s}}$ are listed in the sixth column of table 9. The errors of $C_{p,40\,\mathrm{s}}$ are calculated by Gaussian error propagation. Following assumption II), the water coverage after 40 s water dosing can not be higher than 0.26 ML, which was determined for a water dosing time of 50 s. Therefore, all $C_{p,40\,\mathrm{s}}$ higher than 0.26 ML can be neglected as marked in column 7.

This evaluation is performed also for the images in figure 66(d) with the results presented in the appendix, tables 14 and 15, respectively. $C_{p,d}$, which are in agreement with assumption I to III are plotted over the water dosing time (d) in figure 67, together with the coverage values determined from figure 66(c) and (f) as fix points.

Since a linear relationship is expected between the water deposition time and the water

v [%]	w [%]	x [%]	y [%]	z [%]	$C_{p,40\,\mathrm{s}}$ [ML]	forbidden by II)
36	64	0	0	0	0.16±0.02	no
36	0	64	0	0	0.32±0.04	yes
36	0	0	64	0	0.48±0.05	yes
36	0	0	0	64	0.64±0.07	yes
64	36	0	0	0	0.09±0.02	no
0	36	64	0	0	0.41±0.04	yes
0	36	0	64	0	0.57±0.06	yes
0	36	0	0	64	0.73±0.07	yes
64	0	36	0	0	0.18±0.04	no
0	64	36	0	0	0.34±0.04	yes
0	0	36	64	0	0.66±0.06	yes
0	0	36	0	64	0.82±0.08	yes
64	0	0	36	0	0.27±0.05	yes
0	64	0	36	0	0.43±0.06	yes
0	0	64	36	0	0.59±0.06	yes
0	0	0	36	64	0.91±0.09	yes
64	0	0	0	36	0.36±0.07	yes
0	64	0	0	36	0.52±0.07	yes
0	0	64	0	36	0.68±0.08	yes
0	0	0	64	36	0.84±0.09	yes

Table 9: All assignments of surface phases to water density for figure 66(b) (40 s dosing time) with resulting total coverage $C_{p,40\,\mathrm{s}}$. The last column indicate if a permutation is forbidden by assumption II).

coverage (assumption III)), and the NC-AFM images acquired for 50 s and 160 s+80 s allow to count the absolute number of water molecules, it is reasonable to interpolate these two measurements by a linear function (red line in figure 67), yielding a water deposition rate of about $0.004\,\mathrm{ML\,s^{-1}}$ with an offset of 0.07 ML. While the slope is determined by the water partial pressure during dosing, the offset is explained by residual water molecules in the vacuum system after water dosing, leading to additional water deposition.

From this linear interpolation, the most likely assignment can be derived for the other three images. These are marked by red squares in figure 67 and also listed in table 10. Based on this analysis, the bright areas in figure 66(b) (40 s deposition time) are unoccupied (2×1) unit cells, while the elongated dark features are unit cells filled with two water molecules. This would be in agreement with the observations in subchapter 7.2, where two preferred adsorption positions were found within the (2×1) unit cell. The dark rows within the dark features can be assigned to the positions of the water molecules. Hence, the molecules are imaged dark, similar to the water molecules in figure 66(c).

For figure 66(d) (90 s deposition time), there are three possible assignments. Two of these

have in common that the areas of phase A can be assigned to a (2×1) unit cell with two water molecules, while the areas with phase B can be assigned to having either zero or one water molecule within each (2×1) unit cell. For the third assignment, phase B consists of completely filled (2×1) unit cells, while phase A are unit cells contain only one water molecule. When considered figure 66(c), where more (2×1) unit cells are found to be filled with one water molecule than to be unoccupied, and where no completely filled unit cells are found, it seems to be more likely that phase A in figure 66(d) consists of half filled unit cells, while phase B contains single occupied (2×1) unit cells. Hence, the water molecules in figure 66(d) seem to be imaged with an attractive interaction, because of the observation that a half filled (2×1) unit cell is imaged brighter in this image than a single occupied unit cells.

For figure 66(e) (160 s deposition time), there are also three possible assignments. In the first case, phase 1 contains two water molecules within each (2×1) unit cell, while phase 2 consists of fully filled (2×1) unit cells. In the second case, phase 1 contains three H_2O molecules within each (2×1) unit cell while two molecules per cell are found for phase 2. In the third case, the areas with phase 1 consist of fully occupied (2×1) unit cells, while phase 2 are unit cells containing one water molecule. Still, the first assignment seems preferable when comparing the structures with figure 66(b) and (f). The rows in phase 1 in figure 66(e) are similar to the rows in figure 66(b), while the smooth surface of phase 2 in figure 66(e) have a similar appearance such as the surface in figure 66(f).

In conclusion, following behaviour when increasing the water coverage on calcite(104) in the range of 0 ML to 1 ML and at a temperature between 110 K and 140 K can be inferred from the experimental data: At first, the water molecules occupy each (2×1) unit cell with two molecules, resulting in rows along $[4\,2\,\overline{1}]$ direction. A similar behaviour is found at 5 K where the water molecules prefer to fill every (2×1) unit cell half at water coverages of the order

water deposition time [s]	v [%]	w [%]	x [%]	y [%]	z [%]	C [%]
40	64	0	36	0	0	18±4
50	25	45	30	0	0	26±2
90	21	0	79	0	0	40±1
90	0	79	0	0	21	41±3
90	0	21	79	0	0	45±2
160	0	0	67	0	33	66.5±0.2
160	0	0	33	67	0	66.8±0.2
160	33	0	0	0	67	67±0.2
240	0	0	0	0	100	100±0

Table 10: Coverage information of the red marked values in figure 67. Water phases and total coverage for increasing water deposition times. Three cases are found for 90 s and 160 s.

of 0.1 ML. Hence, it can be assumed that such a half filled (2×1) unit cell is energetically favourable, probably because the (2×1) reconstruction of the pristine calcite(104) influences the adsorption positions of the water molecules.

With increasing deposition time, the (2×1) unit cells get fully covered by four molecules and the surface express a (1×1) super structure with a rather hexagonal geometry. This super structure is in agreement with the simulations presented in literature [25], if only the positions of the water oxygens dominate the imaging contrast (figure 59(b)).

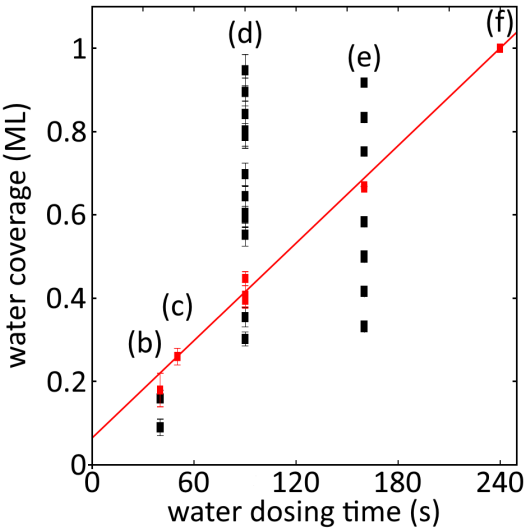

Figure 67: Determined water coverages of the phases in figure 66. 1 ML defined as four H_2O molecules per (2×1) unit cell.

8 Conclusion

This thesis delivers a detailed investigation of the pristine as well as CO and H_2O-covered calcite(104) surface. The experiments are mainly performed with high-resolution non-contact atomic force microscopy (NC-AFM) at 5 K with CO-terminated tips, while H_2O on calcite(104) is additionally studied in the temperature range of 110 K to 140 K.

A key improvement for the NC-AFM measurements at 5 K is the development of a double sample holder, which supports both a metal and a calcite sample. The metal sample is used to sharpen the tip apex, to terminate the tip with a CO molecule, and to characterise the tip. This so prepared and pre-characterised tip is then used for the high-resolution measurements of the calcite(104) surface. Based on the experiences made in these experiments, a tip preparation protocol based on several preparation methods systematically organised via a flowchart is developed.

High-resolution NC-AFM images acquired with symmetric as well as CO-terminated tips at 5 K enable a detailed study of the imaging mechanisms and the surface structure of calcite(104). In topography NC-AFM data, the calcite(104) surface is imaged in the form of bright protrusions that are arranged along the $[4\,2\,\overline{1}]$ and $[0\,\overline{1}\,0]$ surface directions. These bright protrusions are separated by dark rows that run along both surface directions and express a zig-zag shape. A (2×1) reconstruction is apparent in these data from both a modulation of the protrusion height, forming chequerboard-like pattern, and from a modulation of the with of the dark lines along the $[4\,2\,\overline{1}]$ direction, whereby every second row is imaged in wider form. Due to the exclusive adsorption of CO molecules on the calium atoms of calcite(104), the bright protrusions can be assigned to the positions of the calcium atoms [55]. Consequently, the dark lines represent the positions of the carbonate group rows. The calcite(104) surface is furthermore studied using the constant-height AFM mode with CO-terminated tips. In the resulting constant-height frequency-shift images, the calcium atoms are imaged as dark pores arranged along the $[4\,2\,\overline{1}]$ and $[0\,\overline{1}\,0]$ direction, while the rows of carbonate groups are imaged as bright lines. Every second bright line along the $[4\,2\,\overline{1}]$ direction is imaged wider, again reflecting the (2×1) reconstruction.

The development and application of an algorithmic symmetry test identifies a glide plane symmetry in the NC-AFM images of the calcite(104) surface acquired with sharp tips. In particular, this test finds that the symmetry axes run along the rows of carbonate groups in $[4\,2\,\overline{1}]$ direction.

The identification of a (2×1) reconstruction, the evidence for presence of a glide plane symmetry, and the location of symmetry axes allow to derive conclusions for the geometrical structure of the calcite(104) surface. Based on this analysis, carbonate groups adjacent in

$[4\,2\,\overline{1}]$ direction are linked via the glide plane symmetry, while carbonate groups adjacent in $[0\,\overline{1}\,0]$ direction are independent. In turn, calcium atoms diagonally adjacent in the (2×1) unit cell are linked by glide reflection, while calcium atoms adjacent in $[4\,2\,\overline{1}]$ or $[0\,\overline{1}\,0]$ direction are independent. These relation are in excellent agreement with the experimentally-observed chequerboard-like pattern of the calcium atoms and row structure of the carbonate groups.

In contrast, the row-pairing effect and violations of the glide plane symmetry are only found for ill-characterised and blunt tips. Therefore, this thesis highlights that the row-pairing reconstruction is not a surface property, but an AFM tip artefact.

Thus, in conclusion, the surface structure of calcite(104) in UHV and at 5 K can be described by calcite(104)-(2×1)pg.

Going beyond the study of the pristine calcite(104)-(2×1)pg surface, the adsorption characteristics of CO are investigated by imaging with CO-terminated tips at 5 K. It is found that the CO molecules interact weakly attractive with the tip at large tip-sample distances, while the interaction swiftly turns repulsive with decreasing tip-sample distance. The NC-AFM data reveal that the CO geometry at the four adsorption sites inside one (2×1) unit cell are influenced by the glide plane symmetry. In particular, the adsorption geometry of CO molecules on adsorption sites adjacent in $[4\,\overline{4}\,\overline{1}]$ and $[\overline{4}\,\overline{8}\,1]$ is found to be mirrored, according to the glide plane symmetry. In contrast, the CO adsorption geometry for molecules at two sites adjacent in $[4\,2\,\overline{1}]$ or $[0\,\overline{1}\,0]$ is found to be different. This difference is visible in a total of three measurements: (a) in $\Delta f(z_p)$-curves systematically acquired along the surface directions. These slice data show that the CO molecules are tilted compared to the surface normal and that the tilt of the CO molecules at the two different sites is different. (b) in topography images. At large tip-sample distance, the CO molecules are imaged as dark centres with bright rims, whereby the fine structure of the rims differs for molecules adsorbed at the different adsorption positions. (c) by apparent bonds in constant height NC-AFM data. In particular, apparent bonds are found in NC-AFM image data of for CO molecules adsorbed at adjacent positions. It is furthermore demonstrated that the occurrence of such an image feature does not point towards the existence of a real chemical bond, but rather towards an effect of the proximity of the CO molecules, occurring for CO–CO distances below (0.49 ± 0.03) nm.

The identification of two different adsorption positions for CO molecules within the (2×1) unit cell of calcite(104) demonstrates that the (2×1) reconstruction is an important surface property when the adsorption of molecules is investigated on this surface in UHV. This importance is further highlighted by the outlook of studying the adsorption properties of submonolayer coverage of water on calcite(104). part of the experimental study is performed at

5 K with a CO-terminated tip, while a second series at increasing water coverage is performed in the temperature range of 110 K to 140 K. From both experiments, evidence is given that the water molecules have preferred adsorption positions within the (2×1) unit cell. These preferred adsorption positions seem to be related to the different carbonate group orientation in the (2×1) unit cell. Instead, the NC-AFM images of the adsorbed water film highlight a (1×1) superstructure at water coverage of about one monolayer.

9 Bibliography

References

[1] W.A. Deer, R.A. Howie, and J. Zussman, *Calcite CaCO3*, page 453, Mineralogical Society of Great Britain and Ireland, 2013.

[2] H. R. Wenk, Hu Meisheng, T. Lindsey, and J. W. Morris, Physics and Chemistry of Minerals **17**, 527 (1991).

[3] J. Aizenberg, A. Tkachenko, S. Weiner, L. Addadi, and G. Hendler, Nature **412**, 819 (2001).

[4] Emilie M. Pouget, Paul H. H. Bomans, Jeroen A. C. M. Goos, Peter M. Frederik, Gijsbertus de With, and Nico A. J. M. Sommerdijk, Science **323**, 1455 (2009).

[5] Giuseppe Falini, Shira Albeck, Steve Weiner, and Lia Addadi, Science **271**, 67 (1996).

[6] Heinz A. Lowenstam, Science **211**, 1126 (1981).

[7] L. Addadi and S. Weiner, Angewandte Chemie-International Edition in English **31**, 153 (1992).

[8] M. Isabel Carretero and Manuel Pozo, Applied Clay Science **47**, 171 (2010).

[9] Ulli G. Limpitlaw, International Geology Review **52**, 726 (2010).

[10] Ramesh Raliya, Avik Som, Nishit Shetty, Nathan Reed, Samuel Achilefu, and Pratim Biswas, RSC Advances **6**, 54331 (2016).

[11] P. Hlubina and W. Urbanczyk, Measurement Science & Technology **16**, 1267 (2005).

[12] Sarah M. Walker, Maria C. Marcano, Sooyeon Kim, Sandra D. Taylor, and Udo Becker, Journal of Physical Chemistry C **121**, 28017 (2017).

[13] Helmut Cölfen, Current Opinion in Colloid & Interface Science **8**, 23 (2003).

[14] Li-Bo Mao, Huai-Ling Gao, Hong-Bin Yao, Lei Liu, Helmut Colfen, Gang Liu, Si-Ming Chen, Shi-Kuo Li, You-Xian Yan, Yang-Yi Liu, and Shu-Hong Yu, Science **354**, 107 (2016).

[15] Kyubock Lee, Wolfgang Wagermaier, Admir Masic, Krishna P. Kommareddy, Mathieu Bennet, Inderchand Manjubala, Seung-Woo Lee, Seung B. Park, Helmut Colfen, and Peter Fratzl, Nature Communications **3** (2012).

[16] Steve Weiner and Lia Addadi, Annual Review of Materials Research **41**, 21 (2011).

[17] Hirotaka Maeda, Haruki Imaizumi, and Emile Hideki Ishida, Journal of Environmental Management **92**, 2881 (2011).

[18] Min-Gu Lee, Dongwoo Kang, Yunsung Yoo, Hoyong Jo, Ho-Jun Song, and Jinwon Park, Industrial & Engineering Chemistry Research **55**, 11795 (2016).

[19] A. Sanna, M. Uibu, G. Caramanna, R. Kuusik, and M.M. Maroto-Valer, Chemical Society Reviews **43**, 8049 (2014).

[20] Ribooga Chang, Semin Kim, Seungin Lee, Soyoung Choi, Minhee Kim, and Youngjune Park, Frontiers in Energy Research **5**, 17 (2017).

[21] Helmut Schröcke and Karl-Ludwig Weiner, *Nitrate, Carbonate, Borate*, page 956, de Gruyter, 1981.

[22] R. Kristensen, S. L. S. Stipp, and K. Refson, Journal of Chemical Physics **121**, 8511 (2004).

[23] N. H. de Leeuw and S. C. Parker, Journal of the Chemical Society-Faraday Transactions **93**, 467 (1997).

[24] N. H. de Leeuw and S. C. Parker, Journal of Physical Chemistry B **102**, 2914 (1998).

[25] Nora H. de Leeuw, American Mineralogist **87**, 679 (2002).

[26] Richard J. Reeder, *Chapter 1. CRYSTAL CHEMISTRY of the RHOMBOHEDRAL CARBONATES*, Carbonates: Mineralogy and Chemistry, De Gruyter, 1983.

[27] Stefan Kuhn, Markus Kittelmann, Yoshiaki Sugimoto, Masayuki Abe, Angelika Kühnle, and Philipp Rahe, Physical Review B **90**, 195405 (2014).

[28] Philipp Rahe, Stefan Kuhn, and Angelika Kühnle, Journal of Unresolved Questions **3**, 21 (2013).

[29] Philipp Rahe, Jens Schütte, and Angelika Kühnle, Journal of Physics: Condensed Matter **24**, 084006 (2012).

[30] Toru Akiyama, Kohji Nakamura, and Tomonori Ito, Physical Review B **84** (2011).

[31] J. Schütte, P. Rahe, L. Tröger, S. Rode, R. Bechstein, M. Reichling, and A. Kühnle, Langmuir **26**, 8295 (2010).

[32] Dino Spagnoli, S. Kerisit, and S. C. Parker, Journal of Crystal Growth **294**, 103 (2006).

[33] Uta Magdans, Hermann Gies, Xavier Torrelles, and Jordi Rius, European Journal of Mineralogy **18**, 83 (2006).

[34] P. Geissbühler, P. Fenter, E. DiMasi, G. Srajer, L. B. Sorensen, and N. C. Sturchio, Surface Science **573**, 191 (2004).

[35] S. Kerisit, S. C. Parker, and J. H. Harding, Journal of Physical Chemistry B **107**, 7676 (2003).

[36] S. L. S. Stipp, Molecular Simulation **28**, 497 (2002).

[37] K. Wright, R. T. Cygan, and B. Slater, Physical Chemistry Chemical Physics **3**, 839 (2001).

[38] P. Fenter, P. Geissbühler, E. DiMasi, G. Srajer, L. B. Sorensen, and N. C. Sturchio, Geochimica et Cosmochimica Acta **64**, 1221 (2000).

[39] S. L. S. Stipp, Geochimica et Cosmochimica Acta **63**, 3121 (1999).

[40] Y. Liang, A. S. Lea, D. R. Baer, and M. H. Engelhard, Surface Science **351**, 172 (1996).

[41] S. L. S. Stipp, C. M. Eggleston, and B. S. Nielsen, Geochimica et Cosmochimica Acta **58**, 3023 (1994).

[42] G. Raina, R. W. Gauldie, S. K. Sharma, and C. E. Helsley, Ferroelectrics Letters Section **17**, 65 (1994).

[43] F. Ohnesorge and G. Binnig, Science **260**, 1451 (1993).

[44] Alan L. Rachlin, Grant S. Henderson, and M. Cynthia Goh, American Mineralogist **77**, 904 (1992).

[45] Hiroki Nada, Polymer Journal **47**, 84 (2015).

[46] R. M. Hazen, T. R. Filley, and G. A. Goodfriend, Proceedings of the National Academy of Sciences **98**, 5487 (2001).

[47] Robert M. Hazen, American Mineralogist **91**, 1715 (2006).

[48] M. X. Jin, E. Shimada, and Y. Ikuma, Journal of the Ceramic Society of Japan **107**, 1166 (1999).

[49] Susan L. Stipp and Michael F. Hochella, Geochimica et Cosmochimica Acta **55**, 1723 (1991).

[50] L. Gross, F. Mohn, N. Moll, P. Liljeroth, and G. Meyer, Science **325**, 1110 (2009).

[51] Qigang Zhong, Xuechao Li, Haiming Zhang, and Lifeng Chi, Surface Science Reports **75**, 100509 (2020).

[52] Henry Chessin, Walter C. Hamilton, and Ben Post, Acta Crystallographica **18**, 689 (1965).

[53] H. Winchell, American Journal of Science **254**, 65 (1956).

[54] Jian Zhao, Jiamin M. Wang, Xinzhan Z. Qin, and Yu Cao, Solid State Communications **313** (2020).

[55] Tahereh Mohammadi Hafshejani, Weijia Wang, Jonas Heggemann, Alexei Nefedov, Stefan Heissler, Yuemin Wang, Philipp Rahe, Peter Thissen, and Christof Wöll, Physical Chemistry Chemical Physics **23**, 7696 (2021).

[56] Lin Tao, Zhi Li, Guo-Cheng Wang, Bao-Yu Cui, Xi-Tao Yin, and Qi Wang, Materials Research Express **6**, 025035 (2019).

[57] E. Ataman, M. P. Andersson, M. Ceccato, N. Bovet, and S. L. S. Stipp, Journal of Physical Chemistry C **120**, 16586 (2016).

[58] Doris Schattschneider, The American Mathematical Monthly **85**, 439 (1978).

[59] Friedhelm Bechstedt, *Symmetry*, pages 1–44, Springer Berlin Heidelberg, Berlin, Heidelberg, 2003.

[60] Hirotake Imada, Kenjiro Kimura, and Hiroshi Onishi, Chemical Physics **419**, 193 (2013).

[61] Andrew L. Rohl, Kate Wright, and Julian D. Gale, American Mineralogist **88**, 921 (2003).

[62] Kari Reksten, American Mineralogist **75**, 807 (1990).

[63] John Tracey, Keisuke Miyazawa, Peter Spijker, Kazuki Miyata, Bernhard Reischl, Filippo Federici Canova, Aandrew L. Rohl, Takeshi Fukuma, and Adam S. Foster, Nanotechnology **27** (2016).

[64] Sebastian Rode, Noriaki Oyabu, Kei Kobayashi, Hirofumi Yamada, and Angelika Kühnle, Langmuir **25**, 2850 (2009).

[65] P. Geissbühler, P. Fenter, E. DiMasi, G. Srajer, L. B. Sorensen, and N. C. Sturchio, Surface Science **573**, 191 (2004).

[66] Franz J. Giessibl, Phys. Rev. B: Condens. Matter **56**, 16010 (1997).

[67] Franz J. Giessibl, Reviews of Modern Physics **75**, 949 (2003).

[68] Hagen Söngen, Ralf Bechstein, and Angelika Kühnle, Journal of Physics-Condensed Matter **29** (2017).

[69] W. Melitz, J. Shen, A. C. Kummel, and S. Lee, Surface Science Reports **66**, 1 (2011).

[70] C. Argento and R. H. French, Journal of Applied Physics **80**, 6081 (1996).

[71] H. C. Hamaker, Physica (The Hague) **4**, 1058 (1937).

[72] Franz J. Giessibl, Florian Pielmeier, Toyoaki Eguchi, Toshu An, and Yukio Hasegawa, Physical Review B **84**, 125409 (2011).

[73] F.J. Giessibl, S. Hembacher, M. Herz, C. Schiller, and J. Mannhart, Nanotechnology **15**, S79 (2004).

[74] Franz J. Giessibl, Review of Scientific Instruments **90**, 011101 (2019).

[75] Jannis Lübbe, Matthias Temmen, Philipp Rahe, and Michael Reichling, Beilstein Journal of Nanotechnology **7**, 1885 (2016).

[76] M. J. Rost, *High-Speed Electrochemical STM*, pages 180–198, Elsevier, Oxford, 2018.

[77] Georg Hermann Simon, Markus Heyde, and Hans-Peter Rust, Nanotechnology **18**, 255503 (2007).

[78] Z. Majzik, M. Setvín, A. Bettac, A. Feltz, V. Cháb, and P. Jelínek, Beilstein Journal of Nanotechnology **3**, 249 (2012).

[79] J. E. Sader and S. P. Jarvis, Applied Physics Letters **84**, 1801 (2004).

[80] Matthias Temmen and Lübbe Jannis, RHK Technology Application Note , 1 (2015).

[81] Daniel Heile, Reinhard Olbrich, Michael Reichling, and Philipp Rahe, Physical Review B **103**, 075409 (2021).

[82] Julian C. Chen, *Tunneling Phenomenon*, book section 2, page 1, Oxford University Press, Oxford, 2007.

[83] Y. Sugimoto, Y. Nakajima, D. Sawada, K. Morita, M. Abe, and S. Morita, Physical Review B **81**, 245322 (2010).

[84] Scienta Omicron GmbH, *Multiprobe LT System User's Guide, Project 151801*, info@scientaomicron.com, 22.09.2017.

[85] Rostislaw Baurichter, Laborbericht zur Temperaturkalibration der Probenheizstation im UHV-System, 2021.

[86] L. Tröger, J. Schütte, F. Ostendorf, A. Kühnle, and M. Reichling, Rev. Sci. Instrum. **80**, 063703 (2009).

[87] Scienta Omicron GmbH, *LT STM User's Guide, Version 4.3*, services@scientaomicron.com, 10.11.2016.

[88] Franz J. Giessibl, Appl. Phys. Lett. **73**, 3956 (1998).

[89] *MATRIX 3.2 Application Manual for Scanning probe Microscopy*, Version 3.2, 04 November 2014, German headquarters and Service Centre: Scienta Omicron GmbH, Limburger Str. 75, 65232 Taunusstein Germany.

[90] Philipp Rahe, Jens Schütte, Werner Schniederberend, Michael Reichling, Masayuki Abe, Yoshiaki Sugimoto, and Angelika Kühnle, Review of Scientific Instruments **82**, 063704 (2011).

[91] Guangxi Zhou, Mengqi Tian, and Miao Song, *The influence of the tip shape on the STM scans*, Band 9449 of *The International Conference on Photonics and Optical Engineering and the Annual West China Photonics Conference (icPOE 2014)*, SPIE, 2015.

[92] Thomas Hofmann, Florian Pielmeier, and Franz J. Giessibl, Phys. Rev. Lett. **115**, 066101 (2015), Supplemental information.

[93] Jean-Benoît Lalanne, William Paul, David Oliver, and Peter H. Grütter, Rev. Sci. Instrum. **82**, 116105 (2011).

[94] J. Skibinski, J. Rebis, T. Wejrzanowski, K. Rozniatowski, K. Pressard, and K. J. Kurzydlowski, Micron **66**, 23 (2014).

[95] Masahiko Tomitori, Keiichi Sugata, Goro Okuyama, and Hideki Kimata, Surf. Sci. **355**, 21 (1996).

[96] Dehuan H. Huang, Fumiko Yamaguchi, and Yoshihisa Yamamoto, Japanese Journal of Applied Physics Part 1-Regular Papers Short Notes & Review Papers **37**, 3824 (1998).

[97] Wolfgang Demtröder, *Experimentalphysik 3 : Atome, Moleküle und Festkörper*, Springer-Lehrbuch, Springer Berlin Heidelberg, Berlin, Heidelberg, 2010.

[98] Ralph Howard Fowler and L. Nordheim, Proceedings of the Royal Society London **119**, 173 (1928).

[99] Wolfgang Demtröder, *Experimentalphysik 2 : Elektrizität und Optik*, Springer-Lehrbuch, Springer Berlin Heidelberg, Berlin, Heidelberg, 2012.

[100] Naoki Yokoi, Satoshi Ueda, Susumu Namba, and Mikio Takai, Japanese Journal of Applied Physics Part 2-Letters & Express Letters **32**, L129 (1993).

[101] O. Nishikawa, M. Tomitori, and F. Katsuki, Journal of Microscopy-Oxford **152**, 637 (1988).

[102] Michael Drechsler, Zeitschrift Fur Elektrochemie **61**, 48 (1957).

[103] Vu Thien Binh, Journal of Microscopy **152**, 355 (1988).

[104] Xin Ge, *Scanning tunneling microscopy and spectroscopy of functional molecules on metal surfaces*, Thesis, 2006.

[105] H. Mehrez, S. Ciraci, C. Y. Fong, and Ş. Erkoc, Journal of Physics-Condensed Matter **9**, 10843 (1997).

[106] Pablo Z. Coura, Sergio B. Legoas, Anderson S. Moreira, Fernando Sato, Varlei Rodrigues, Sócrates O. Dantas, Daniel Ugarte, and Douglas S. Galvao, Nano Letters **4**, 1187 (2004).

[107] J. I. Pascual, J. Méndez, J. Gómez-Herrero, A. M. Baró, N. Garcia, U. Landman, W. D. Luedtke, E. N. Bogachek, and H. P. Cheng, Science **267**, 1793 (1995).

[108] Saw-Wai Hla, Kai-Felix Braun, Violeta Iancu, and Aparna Deshpande, Nano Lett. **4**, 1997 (2004).

[109] L. Limot, J. Kroger, R. Berndt, A. Garcia-Lekue, and W. A. Hofer, Physical Review Letters **94**, 126102 (2005).

[110] Fabian Mohn, Bruno Schuler, Leo Gross, and Gerhard Meyer, Applied Physics Letters **102**, 073109 (2013).

[111] Joachim Welker and Franz J. Giessibl, Science **336**, 444 (2012).

[112] N. Fournier, C. Wagner, C. Weiss, R. Temirov, and F. S. Tautz, Physical Review B **84**, 035435 (2011).

[113] Wolfgang Haiss, Harm van Zalinge, Simon J. Higgins, Donald Bethell, Horst Höbenreich, David J. Schiffrin, and Richard J. Nichols, Journal of the American Chemical Society **125**, 15294 (2003).

[114] Leif Lafferentz, Francisco Ample, Hao Yu, Stefan Hecht, Christian Joachim, and Leonard Grill, Science **323**, 1193 (2009).

[115] L. Bartels, G. Meyer, K. H. Rieder, D. Velic, E. Knoesel, A. Hotzel, M. Wolf, and G. Ertl, Physical Review Letters **80**, 2004 (1998).

[116] N. Moll, L. Gross, F. Mohn, A. Curioni, and G. Meyer, New Journal of Physics **12**, 125020 (2010).

[117] L. Bartels, G. Meyer, and K. H. Rieder, Appl. Phys. Lett. **71**, 213 (1997).

[118] Björn Neu, Gerhard Meyer, and Karl-Heinz Rieder, Modern Physics Letters B **9**, 963 (1995).

[119] Hiroki Andoh, Naoki Yokoi, and Mikio Takai, Journal of Applied Physics **79**, 3348 (1996).

[120] Adam Sweetman, Neil R. Champness, and Alex Saywell, Chem. Soc. Rev. **49**, 4189 (2020).

[121] Fei Hui and Mario Lanza, Nat Electron **2**, 221 (2019).

[122] Takeshi Fukuma and Ricardo Garcia, ACS Nano **12**, 11785 (2018).

[123] Clemens Barth, Adam S. Foster, Claude R. Henry, and Alexander L. Shluger, Adv. Mater. **23**, 477 (2011).

[124] Shigeki Kawai, Adam S. Foster, Torbjorn Björkman, Sylwia Nowakowska, Jonas Björk, Filippo Federici Canova, Lutz H. Gade, Thomas A. Jung, and Ernst Meyer, Nat. Commun. **7**, 11559 (2016).

[125] Leo Gross, Bruno Schuler, Niko Pavliček, Shadi Fatayer, Zsolt Majzik, Nikolaj Moll, Diego Peña, and Gerhard Meyer, Angew. Chem. Int. Edit **57**, 3888 (2018).

[126] Martin Setvin, Michele Reticcioli, Flora Poelzleitner, Jan Hulva, Michael Schmid, Lynn A. Boatner, Cesare Franchini, and Ulrike Diebold, Science **359**, 572 (2018).

[127] Y. Yury Illarionov, Alexander G. Banshchikov, Dmitry K. Polyushkin, Stefan Wachter, Theresia Knobloch, Mischa Thesberg, Lukas Mennel, Matthias Paur, Michael Stoger-Pollach, Andreas Steiger-Thirsfeld, Mikhail I. Vexler, Michael Walt, Nikolai S. Sokolov, Thomas Mueller, and Tibor Grasser, Nat. Electron. **2**, 230 (2019).

[128] Masakazu Aono, Ataru Kobayashi, Francois Grey, Hironaga Uchida, and De-Huan Huang, Jpn. J. Appl. Phys. 1 **32**, 1470 (1993).

[129] Heinrich Adenstedt, Ann. Phys. **418**, 69 (1936).

[130] K. V. Krishna Rao, S. V. Naidu Naidu, and K. Satyanarayana Murthy, J. Phys. Chem. Solids **29**, 245 (1968).

[131] Robert J. Corruccini and John J. Gniewek, *Thermal expansion of technical solids at low temperatures; a compilation from the literature*, National Bureau of Standards. Monograph 29, U.S. Dept. of Commerce, National Bureau of Standards, Washington, 1961.

[132] P. E. Bradley and R. Radebaugh, CRC Handbook of Chemistry and Physics **Chap. 12** (2013).

[133] H. H. Pieper, C. Barth, and M. Reichling, Appl. Phys. Lett. **101**, 051601 (2012).

[134] Alexander Gustafsson, Norio Okabayashi, Angelo Peronio, Franz J. Giessibl, and Magnus Paulsson, Phys. Rev. B **96**, 085415 (2017).

[135] F. Calleja, J. J. Hinarejos, A. L. V. de Parga, S. M. Suturin, N. S. Sokolov, and R. Miranda, Surf. Sci. **582**, 14 (2005).

[136] Daniel W. Thompson, Michael J. DeVries, Thomas E. Tiwald, and John A. Woollam, Thin Solid Films **313**, 341 (1998).

[137] Jonas Heggemann, Linda Laflör, and Philipp Rahe, Rev. Sci. Instrum. **92**, 053705 (2021).

[138] *LT STM User's Guide*, Version 4.3, 10 November 2016, German headquarters and Service Centre: Scienta Omicron GmbH, Limburger Str. 75, 65232 Taunusstein Germany.

[139] Jieqiong Q. Zhang, Junzhi Z. Cui, Zihao H. Yang, and Shangkun K. Shen, Computational Mechanics **65**, 989 (2020).

[140] David Nečas and Petr Klapetek, Central European Journal of Physics **10**, 181 (2011).

[141] Felix Kling Universität Mainz, Unit cell correction program: I12c (I want to see) (2015).

[142] P. Rahe, R. Bechstein, and A. Kühnle, J. Vac. Sci. Technol. B **28**, C4E31 (2010).

[143] Felix Kling Universität Mainz, Drift correction program: Alpha Drift 1.18 (2015).

[144] S. Rusponi, C. Boragno, and U. Valbusa, Physical Review Letters **78**, 2795 (1997).

[145] G. Costantini, S. Rusponi, F. B. de Mongeot, C. Boragno, and U. Valbusa, Journal of Physics-Condensed Matter **13**, 5875 (2001).

[146] J. Wollbrandt, W. Linke, and U. Brückner, Exp Tech Phys **23**, 65 (1975).

[147] C. Barth and C. R. Henry, Nanotechnology **17**, 155 (2006).

[148] W. Hansen, M. Bertolo, and K. Jacobi, Surface Science **253**, 1 (1991).

[149] Daniel P. Engelhart, Roman J. V. Wagner, Artur Meling, Alec M. Wodtke, and Tim Schafer, Surface Science **650**, 11 (2016).

[150] Dr. Ralf Bechstein (Universität Bielefeld), private communication (2017).

[151] William Henry, Phil. Trans. R. Soc. **93**, 29 (1803).

[152] Inc. Global Headquarters MKS Instruments, *Mass Spectrometry Solutions, e-Vision 2*, www.mksinst.com, 2018.

[153] Thomas Lehmann, *Massenspektrometrie*, pages https://www.bcp.fu–berlin.de/chemie/chemie/studium/ocpraktikum/_Unterlagen_Spektroskopie/ms.pdf, Freie Universität Berlin, 2010.

[154] Jiang-Tao Li, Zhen-Bin Wang, Da-Wei Hu, and Yi-Kang Pu, *Mass Spectroscopy Study of Hydrocarbon Removal by an Argon-Oxygen DC-Glow Discharge*, http://www.ispc-conference.org/ispcproc/ispc20/658.pdf, 2022.

[155] Pfeiffer Vacuum GmbH, *Residual gas composition*, https://www.pfeiffer-vacuum.com/en/know-how/introduction-to-vacuum-technology/influences-in-real-vacuum-systems/residual-gas-composition/, 2022.

[156] Yu-long Tang, Yu-ling He, Yan-song Meng, Wei-wei Wang, Rong-yan Zhang, Er-wang Du, and Li-jun Du, *Study on residual gas composition in 316L stainless steel-quartz glass hybrid ultra-high vacuum sealed tube*, Band 11887 of *International Conference on Sensors and Instruments 2021*, SPIE, wei wei and fengjie cen Auflage, 2021.

[157] U.S. Secretary of Commerce on behalf of the United States of America, *Hydrogen*, https://webbook.nist.gov/cgi/cbook.cgi?ID=C1333740&Units=SI&Mask=200#Mass-Spec, 2021.

[158] U.S. Secretary of Commerce on behalf of the United States of America, *Methane*, https://webbook.nist.gov/cgi/cbook.cgi?ID=C74828&Units=SI&Mask=200#Mass-Spec, 2021.

[159] U.S. Secretary of Commerce on behalf of the United States of America, *Ethane*, https://webbook.nist.gov/cgi/cbook.cgi?ID=C74840&Units=SI&Mask=200#Mass-Spec, 2021.

[160] U.S. Secretary of Commerce on behalf of the United States of America, *Carbon monoxide*, https://webbook.nist.gov/cgi/cbook.cgi?ID=C630080&Units=SI&Mask=200#Mass-Spec, 2021.

[161] U.S. Secretary of Commerce on behalf of the United States of America, *Nitrogen*, https://webbook.nist.gov/cgi/cbook.cgi?ID=C7727379&Units=SI&Mask=200#Mass-Spec, 2021.

[162] U.S. Secretary of Commerce on behalf of the United States of America, *Oxygen*, https://webbook.nist.gov/cgi/cbook.cgi?ID=C7782447&Units=SI&Mask=200#Mass-Spec, 2021.

[163] U.S. Secretary of Commerce on behalf of the United States of America, *Carbon dioxide*, https://webbook.nist.gov/cgi/cbook.cgi?ID=C124389&Units=SI&Mask=200#Mass-Spec, 2021.

[164] W. Seelmann-Eggebert, G. Pfennig, H. Münzel, and H. Klewe-Nebenius, *KARLSRUHER NUKLIDKARTE 5. Auflage*, Kernforschungszentrum Karlsruhe GmbH, Institut für Radiochemie, 1981.

[165] U.S. Secretary of Commerce on behalf of the United States of America, *Water*, https://webbook.nist.gov/cgi/cbook.cgi?ID=C7732185&Units=SI&Mask=200#Mass-Spec, 2021.

[166] Adam S. Foster, Alexander L. Shluger, and Risto M. Nieminen, Applied Surface Science **188**, 306 (2002).

[167] Tomas Hofmann, Florian Pielmeier, and Franz J. Giessibl, Physical Review Letters **112**, 066101 (2014).

[168] Adam S. Foster, Clemens Barth, Alexander L. Shluger, Risto M. Nieminen, and Michael Reichling, Physical Review B **66**, 235417 (2002).

[169] P. Pou, S. A. Ghasemi, P. Jelínek, T. Lenosky, S. Goedecker, and R. Perez, Nanotechnology **20**, 264015 (2009).

[170] Chun-Sheng Guo, Michel A. Van Hove, Rui-Qin Zhang, and Christian Minot, Langmuir **26**, 16271 (2010).

[171] Michael Ellner, Niko Pavliček, Pablo Pou, Bruno Schuler, Nikolaj Moll, Gerhard Meyer, Leo Gross, and Rubén Peréz, Nano Letters **16**, 1974 (2016).

[172] Michael Ellner, Pablo Pou, and Rubén Pérez, Physical Review B **96**, 075418 (2017).

[173] C. Weiss, C. Wagner, C. Kleimann, M. Rohlfing, F. S. Tautz, and R. Temirov, Physical Review Letters **105**, 086103 (2010).

[174] J. Zhang, P. C. Chen, B. K. Yuan, W. Ji, Z. H. Cheng, and X. H. Qiu, Science **342**, 611 (2013).

[175] A. M. Sweetman, S. P. Jarvis, Hongqian Sang, I. Lekkas, P. Rahe, Yu Wang, Jianbo Wang, N. R. Champness, L. Kantorovich, and P. Moriarty, Nature Communications **5**, 3931 (2014).

[176] Prokop Hapala, Georgy Kichin, Christian Wagner, F. Stefan Tautz, Ruslan Temirov, and Pavel Jelínek, Physical Review B **90**, 085421 (2014).

[177] Sampsa K. Hämäläinen, Nadine van der Heijden, Joost van der Lit, Stephan den Hartog, Peter Liljeroth, and Ingmar Swart, Physical Review Letters **113**, 186102 (2014).

[178] Matthias Emmrich, Ferdinand Huber, Florian Pielmeier, Joachim Welker, Thomas Hofmann, Maximilian Schneiderbauer, Daniel Meuer, Svitlana Polesya, Sergiy Mankovsky, Diemo Ködderitzsch, Hubert Ebert, and Franz J. Giessibl, Science **348**, 308 (2015).

[179] Christof Wöll, Acs Catalysis **10**, 168 (2020).

[180] H. Itoh and G. Ertl, Zeitschrift Fur Naturforschung Section a-a Journal of Physical Sciences **37**, 346 (1982).

[181] E. W. Plummer, W. R. Salaneck, and J. S. Miller, Physical Review B **18**, 1673 (1978).

[182] George Blyholder, The Journal of Physical Chemistry **68**, 2772 (1964).

[183] Alexander Gustafsson and Magnus Paulsson, Physical Review B **93**, 115434 (2016).

[184] Nicolas Néel and Jörg Kröger, NanoLett **21**, 2318 (2021).

[185] Zhixiang Sun, Mark P. Boneschanscher, Ingmar Swart, Daniël Vanmaekelbergh, and Peter Liljeroth, Physical Review Letters **106**, 046104 (2011).

[186] Alfred John Weymouth, Thomas Hofmann, and Franz J. Giessibl, Science **343**, 1120 (2014).

[187] H. J. Meyer, Journal of Crystal Growth **66**, 639 (1984).

[188] M. Menadakis, G. Maroulis, and P. G. Koutsoukos, Computational Materials Science **38**, 522 (2007).

[189] Xiandeng Hou, Renata S. Amais, Bradley T. Jones, and George L. Donati, *Inductively Coupled Plasma Optical Emission Spectrometry*, pages 1–25, American Cancer Society, 2016.

[190] Dr. Thomas Bergfeldt (Karlsruher Institut für Technologie), private communication (2021).

[191] GEOWiki@LMU, *Optische Emissionsspektrometrie mit induktiv gekoppeltem Plasma*, page https://geowiki.geo.lmu.de/wiki/Optische_Emissionsspektrometrie_mit_induktiv_gekoppeltem_Plasma, Ludwig-Maximilians-Universität München, version from 28.07.2021.

[192] Heinz Rüdel, Jan Kösters, and Josef Schörmann, *Bestimmung von Elementgehalten in Umweltproben durch ICP-OES*, pages https://www.ime.fraunhofer.de/content/dam/ime/de/documents/AE/UPB_SOP_ICP–OES_de.pdf, Fraunhofer-Institut für Molekularbiologie und Angewandte Oekologie, 2011.

[193] Korth Kristalle GmbH, *Kalzit*, https://www.korth.de/material/detail/Kalzit, 2019.

[194] C. A. Orme, A. Noy, A. Wierzbicki, M. T. McBride, M. Grantham, H. H. Teng, P. M. Dove, and J. J. DeYoreo, Nature **411**, 775 (2001).

[195] Hermann Haken and Hans Christoph Wolf, *Atom- und Quantenphysik: Einführung in die experimentellen und theoretischen Grundlagen*, Springer-Lehrbuch, Springer Berlin Heidelberg, Berlin, Heidelberg, 2004.

[196] Shin-ichi Ishi, Yuichi Ohno, and B. Viswanathan, Surface Science **161**, 349 (1985).

[197] Friedrich M. Hoffmann, Surface Science Reports **3**, 107 (1983).

[198] Yuemin Wang and Christof Wöll, Chemical Society Reviews **46**, 1875 (2017).

[199] Manish Kaushik, Ayodhya Singh, and Munesh Kumar, European Journal of Chemistry **3**, 367 (2012).

[200] Jeffrey B. Johnson and W. G. Klemperer, Journal of the American Chemical Society **99**, 7132 (1977).

[201] Winifred M. Huo, Journal of Chemical Physics **43**, 624 (1965).

[202] K. P. Huber and G. Herzberg, *Molecular Spectra and Molecular Structure: IV. Constants of Diatomic Molecules*, Springer Book Archive, Springer, Boston, MA, Boston, MA, 1979.

[203] A. Ortega, F. M. Hoffmann, and A. M. Bradshaw, Surface Science **119**, 79 (1982).

[204] Shuanglin Hu, Zhuo Wang, Andreas Mattsson, Lars Österlund, and Kersti Hermansson, The Journal of Physical Chemistry C **119**, 5403 (2015).

[205] P. A. Redhead, Vacuum **12**, 203 (1962).

[206] João P. Prates Ramalho, Francesc Illas, and José R. B. Gomes, Physical Chemistry Chemical Physics **19**, 2487 (2017).

[207] Martin J. Hÿtch, Jean-Luc Putaux, and Jean-Michel Penisson, Nature **423**, 270 (2003).

[208] Martin J. Hÿtch, E. Snoeck, and R. Kilaas, Ultramicroscopy **74**, 131 (1998).

[209] J. E. Bresenham, IBM Systems Journal **4**, 25 (1965).

[210] P. Fenter and N. C. Sturchio, Geochimica Et Cosmochimica Acta **97**, 58 (2012).

[211] Jennifer S. Lardge, Dorothy M. Duffy, Mike J. Gillan, and Matthew Watkins, Journal of Physical Chemistry C **114**, 2664 (2010).

[212] J. S. Lardge, D. M. Duffy, and M. J. Gillan, Journal of Physical Chemistry C **113**, 7207 (2009).

[213] A. Rahaman, V. H. Grassian, and C. J. Margulis, Journal of Physical Chemistry C **112**, 2109 (2008).

[214] S. Hwang, M. Blanco, and W. A. Goddard, Journal of Physical Chemistry B **105**, 10746 (2001).

[215] N. H. de Leeuw, S. C. Parker, and J. H. Harding, Physical Review B: Condensed Matter and Materials Physics **60**, 13792 (1999).

[216] Yong Liang, Donald R. Baer, James M. McCoy, James E. Amonette, and John P. Lafemina, Geochimica et Cosmochimica Acta **60**, 4883 (1996).

10 Acknowledgement

11 Publications and presentations

Publications in peer-reviewed journals:

Stephan Appelfeller, Jonas Heggemann, Tore Niermann, Michael Lehmann, and Mario Dähne, Refined structure model of rare earth silicide nanowires on Si(001), Appl. Phys. Lett. **114**, 093104 (2019)

Jonas Heggemann, Stephan Appelfeller, Tore Niermann, Michael Lehmann, and Mario Dähne, Internal atomic structure of terbium silicide nanowires on Si(001) capped by silicon, Surf. Sci. **696**, 121563 (2020)

Tahereh Mohammadi Hafshejani, Weijia Wang, Jonas Heggemann, Alexei Nefedov, Stefan Heissler, Yuemin Wang, Philipp Rahe, Peter Thissen, Christof Wöll, CO adsorption on the calcite(10.4) surface: a combined experimental and theoretical study, Phys. Chem. Chem. Phys. **23**, 7696 (2021)

Jonas Heggemann, Linda Laflör, Philipp Rahe, Note: Double sample holder for efficient high resolution studies of an insulator and a metal surface, Rev. Sci. Instrum. **92**, 053705 (2021)

Publications submitted:

Jonas Heggemann, Yashasvi Ranawat, Ondřej Krejčí, Adam S. Foster, and Philipp Rahe, "Differences in molecular adsorption emanating from the (2×1) reconstruction of calcite(104)

Presentations:

Jonas Heggemann, and Philipp Rahe, Accuracy and precision of amplitude calibration in NC-AFM: A comparison of methods, poster, NC-AFM 2018, Porvoo, Finland

Jonas Heggemann, Yashasvi Ranawat, Ondřej Krejčí, Adam S. Foster, and Philipp Rahe, The (2×1) reconstruction of calcite(104), talk, NC-AFM 2022, Nijmegen, Netherlands

12 Appendix

Glide plane reflected positions dependent on *A*, *A'*, *B*, and *B'*

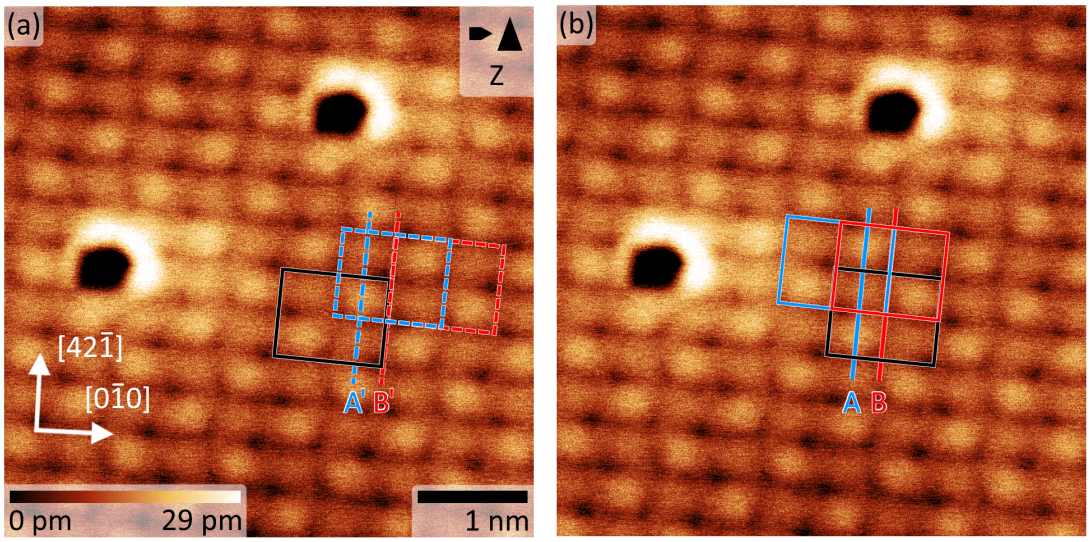

Figure 68: Same image data as in figure 27(a). (a) The glide plane reflected position of the black rectangle is at the position of the dashed blue rectangle if the row *A'* (calcium atom) is selected as the axis of glide reflection, and at the position of the dashed red rectangle if the row *B'* (carbonate groups) is selected. (b) If the row *A* is selected as the axis of glide reflection then the glide plane reflected position of the black rectangle is at the position of the solid blue rectangle, and at the position of the solid red rectangle if the row *B* is selected. The solid and dashed red (blue) rectangles are adjacent in $[0\,\bar{1}\,0]$ direction and, therefore, on equivalent (2×1) lattice positions.

Positions of unit cells for the algorithmic symmetry test applied to the image data of figure 40(d)

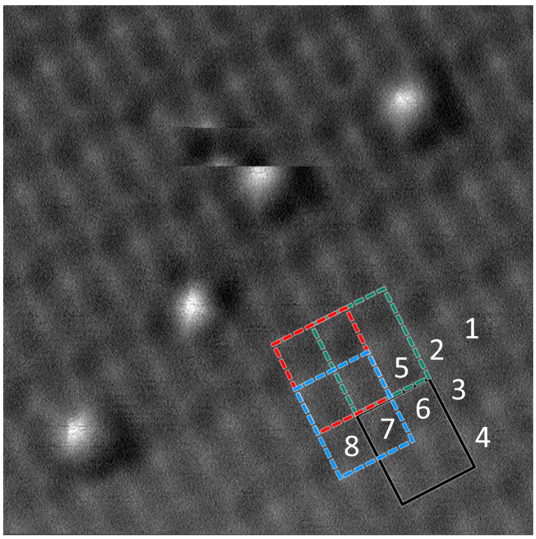

Figure 69: Same image data as shown in figure 40(c), but with positions of unit cells for the algorithmic symmetry test marked. The number indicates the lower right quadrate as shown exemplary for number 6. The results are listed in table 11.

Unit cell number	β (%)				Unit cell number	β (%)			
	S_1	S_1'	S_2	S_2'		S_1	S_1'	S_2	S_2'
1		2.7	0.8		5		1.1	1.6	
2		2.2	0.7		6	3.5			5.9
3	3.9			5.5	7	2.1			3.9
4		4.1	4.4		8	2.7			5.6
					Average	3 ± 1		4 ± 2	

Table 11: Results of algorithmic symmetry test applied to the unit cells marked in figure 69. The unit cell that is analysed in figure 40(d) corresponds to number 6.

Tilt of the single CO molecules on calcite(104)

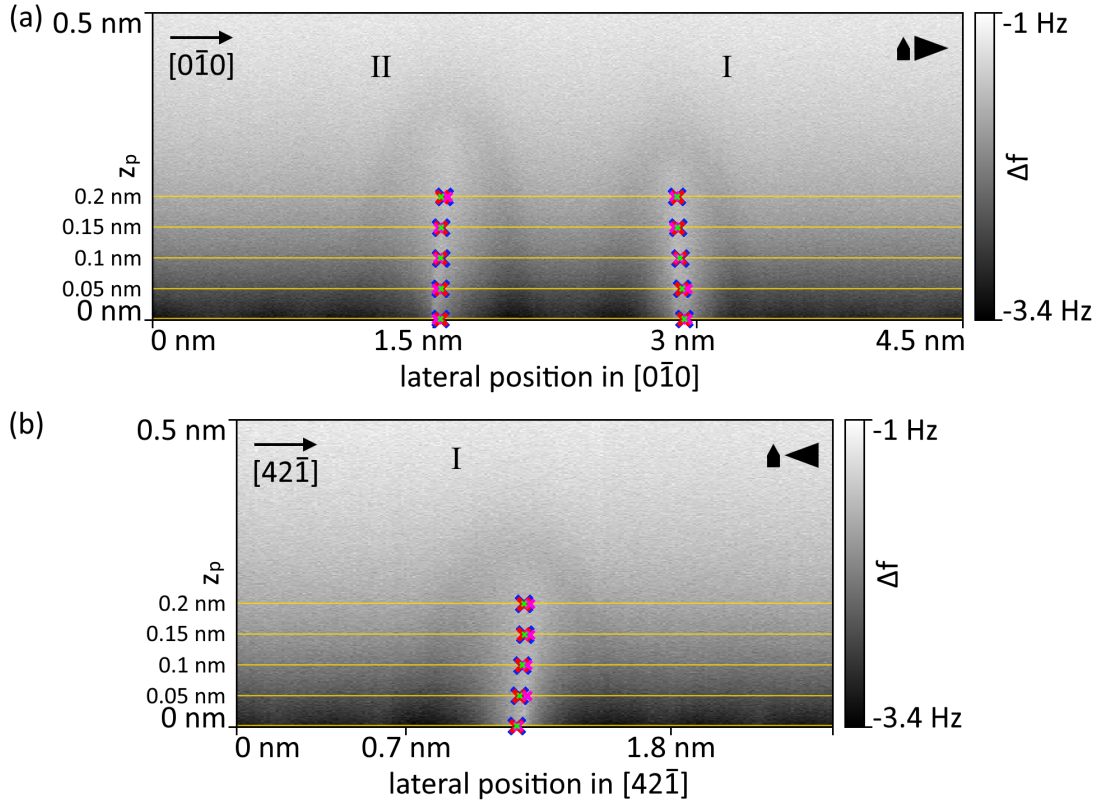

Figure 70: (a) Same slices as in figure 50(A). (b) Same slice as in figure 50(C). Marked with orange lines are the heights where line profiles were extracted. The centre of the features determined by the different methods (red – Gaussian, blue–Lorentz, green–Voigt, magenta–numerical maximum) are marked by crosses.

Method	Gaussian	Lorentz	Voigt	Numerical Maximum
α_I (°)	-12±2	-13±2	-13±2	-20±10
β_I (°)	-13±2	-14±2	-14±2	-20±10
β_{II} (°)	1±3	2±2	2±3	7±7

Table 12: Mean values of the results of the different methods for α_I, β_I, and β_{II}.

Dependence of the imaging of water on calcite(104) on the fast scan direction

Figure 71 shows two subsequent images of figure 66(c). The fast scan direction in these two images are perpendicular to each other. This direction is from left to right in figure 71(a), while it is from bottom to top in figure 71(b). Dark dots adjacent in the fast scan direction are imaged connected in figure 71(a), while in figure 71(b) the same molecules are imaged with a larger distance and separated from each other. Example of two water molecules, which are imaged different in the two images, are marked with green ovals.

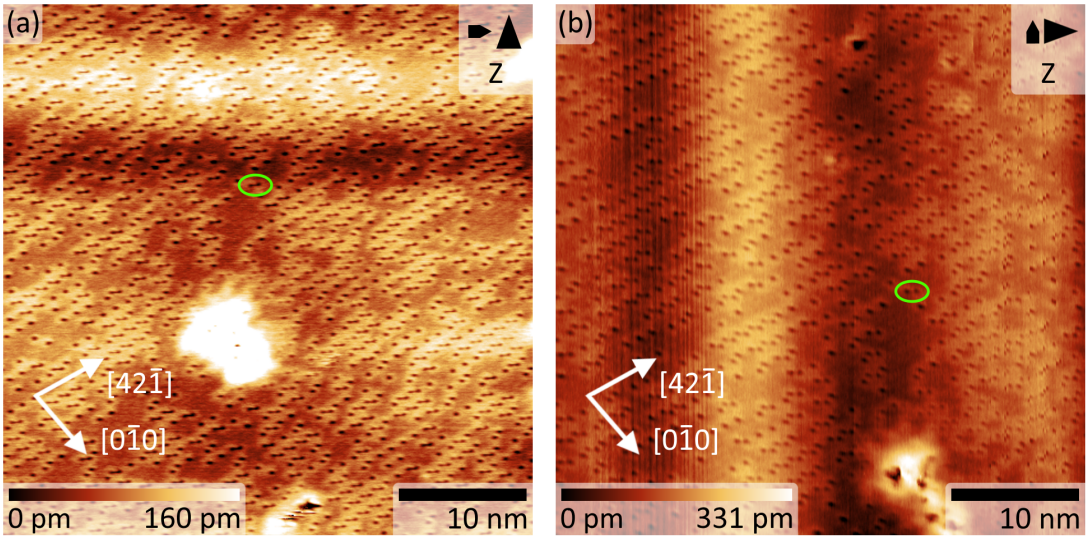

Figure 71: Subsequent images of figure 66(c) acquired with $\Delta f = -8.4\,\mathrm{Hz}$ and $U_{tip} = 0\,\mathrm{V}$. The green ovals indicate the same two water molecules. The images are not drift corrected.

Area coverage dependent on the threshold

The images in figure 72 shows the same image data as in figure 66(b), but every pixel with a value below a given threshold is coloured in blue. In figure 72(b), the threshold is set to 65.6 pm, which results in an area coverage of 31.98 %. The blue marked areas are slightly smaller than the dark features; around the "blue islands" a small dark rim is faintly visible, and smaller holes are within the blue coverage. Therefore, the threshold of this image is considered as a lower limit for the size of the dark features.

In figure 72(c), the threshold is set to 76.6 pm (42.89 % area coverage). In this image, the

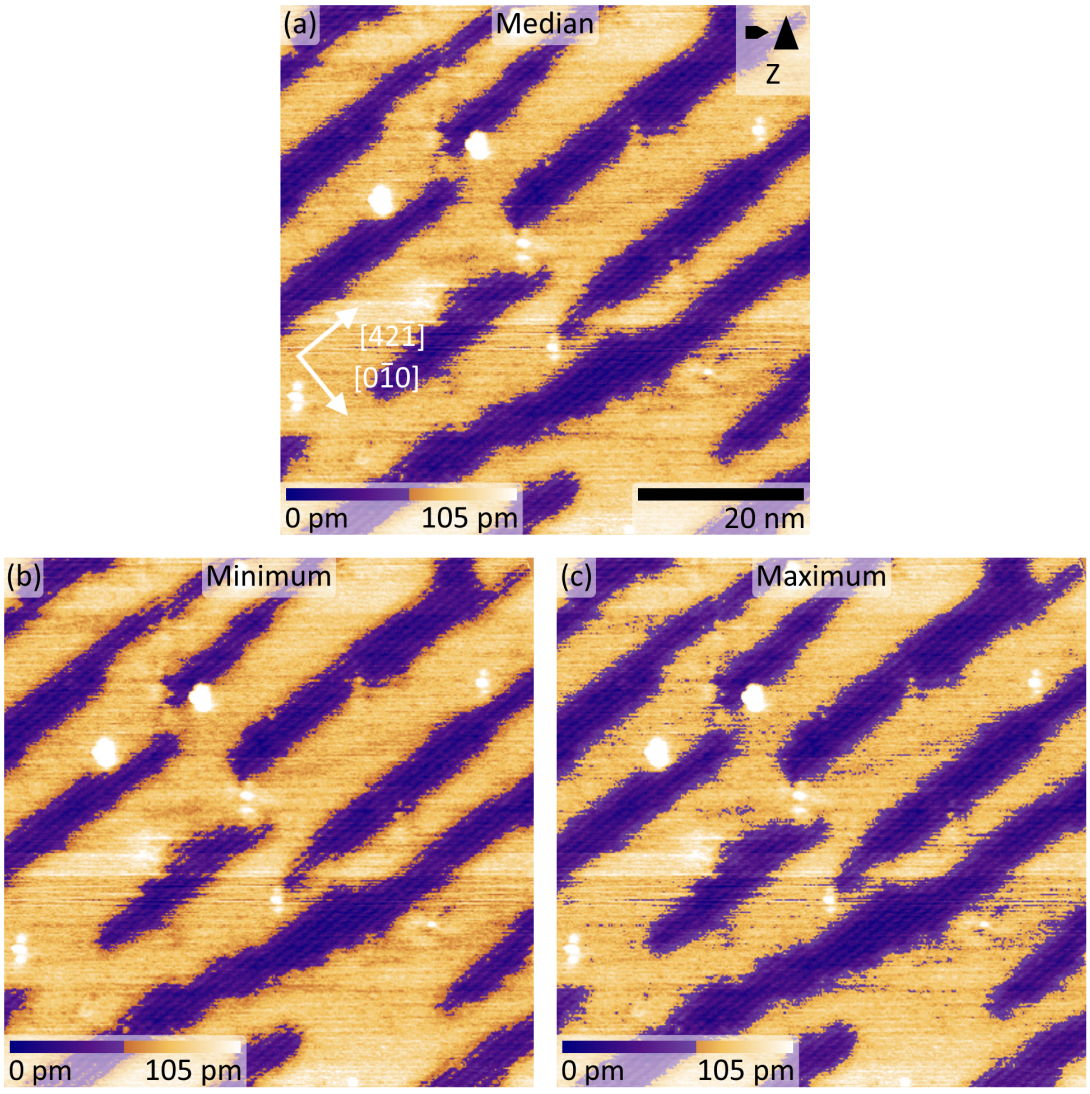

Figure 72: Same image data as in figure 66(b). Blue pixels indicate data values under a certain threshold. (a) The threshold is set to 71.1 pm, about 36 % of the image is covered by the blue islands. (b) At a threshold of 65.6 pm the blue coverage covers about 32 % of the image. (c) About 43 % of the image is covered if the threshold is set to 76.6 pm.

blue coverage are slightly larger than the dark islands and cover the dark features completely, while "scratches" in the image, which are clearly not belong to the dark features, are also marked blue. Hence, this threshold is considered as an upper limit.

A compromise between these minimum and maximum area coverages is the average of the thresholds (table 13). This threshold is 71.1 pm and the corresponding area coverage is 36 % (figure 72(a)) with a maximum error of 7 %.

	threshold value	area coverage
Minimum	76.6 pm	43 %
Median	71.1 pm	36 %
Maximum	65.6 pm	32 %

Table 13: Area coverage of the elongated dark features in figure 72 dependent on threshold value.

Permutations of the area coverages for figure 66(d)

v [%]	w [%]	x [%]	y [%]	z [%]	$C_{p,40\,\mathrm{s}}$ [ML]	forbidden by II)
21	79	0	0	0	0.198±0.008	yes
21	0	79	0	0	0.4±0.02	no
21	0	0	79	0	0.59±0.02	no
21	0	0	0	79	0.79±0.03	no
79	21	0	0	0	0.053±0.008	no
0	21	79	0	0	0.45±0.02	no
0	21	0	79	0	0.65±0.02	no
0	21	0	0	79	0.84±0.03	no
79	0	21	0	0	0.11±0.02	yes
0	79	21	0	0	0.3±0.02	no
0	0	21	79	0	0.7±0.03	no
0	0	21	0	79	0.9±0.03	no
79	0	0	21	0	0.16±0.02	yes
0	79	0	21	0	0.36±0.02	no
0	0	79	21	0	0.55±0.03	no
0	0	0	21	79	0.95±0.04	no
79	0	0	0	21	0.2±0.03	yes
0	79	0	0	21	0.41±0.03	no
0	0	79	0	21	0.61±0.03	no
0	0	0	79	21	0.8±0.04	no

Table 14: All assignments of surface phases to water density for figure 66(d) with resulting total coverage. The last column indicate if a permutation is forbidden by assumption II).

Permutations of the area coverages for figure 66(e)

v [%]	w [%]	x [%]	y [%]	z [%]	$C_{p,40\,\mathrm{s}}$ [ML]	forbidden by II)
67	33	0	0	0	0.0825±0.0005	yes
67	0	33	0	0	0.165±0.003	yes
67	0	0	33	0	0.248±0.002	yes
67	0	0	0	33	0.33±0.002	no
33	67	0	0	0	0.1675±0.0005	yes
0	67	33	0	0	0.333±0.001	no
0	67	0	33	0	0.415±0.002	no
0	67	0	0	33	0.498±0.002	no
33	0	67	0	0	0.335±0.001	no
0	33	67	0	0	0.418±0.001	no
0	0	67	33	0	0.583±0.002	no
0	0	67	0	33	0.665±0.002	no
33	0	0	67	0	0.503±0.002	no
0	33	0	67	0	0.585±0.002	no
0	0	33	67	0	0.668±0.002	no
0	0	0	67	33	0.838±0.003	no
33	0	0	0	67	0.67±0.002	no
0	33	0	0	67	0.753±0.002	no
0	0	33	0	67	0.835±0.002	no
0	0	0	33	67	0.918±0.003	no

Table 15: All assignments of surface phases to water density for figure 66(d) with resulting total coverage. The last column indicate if a permutation is forbidden by assumption II).